Technische Universität Braunschweig

CAMPUS FORSCHUNGSFLUGHAFEN

Eine Kooperation mit dem DLR

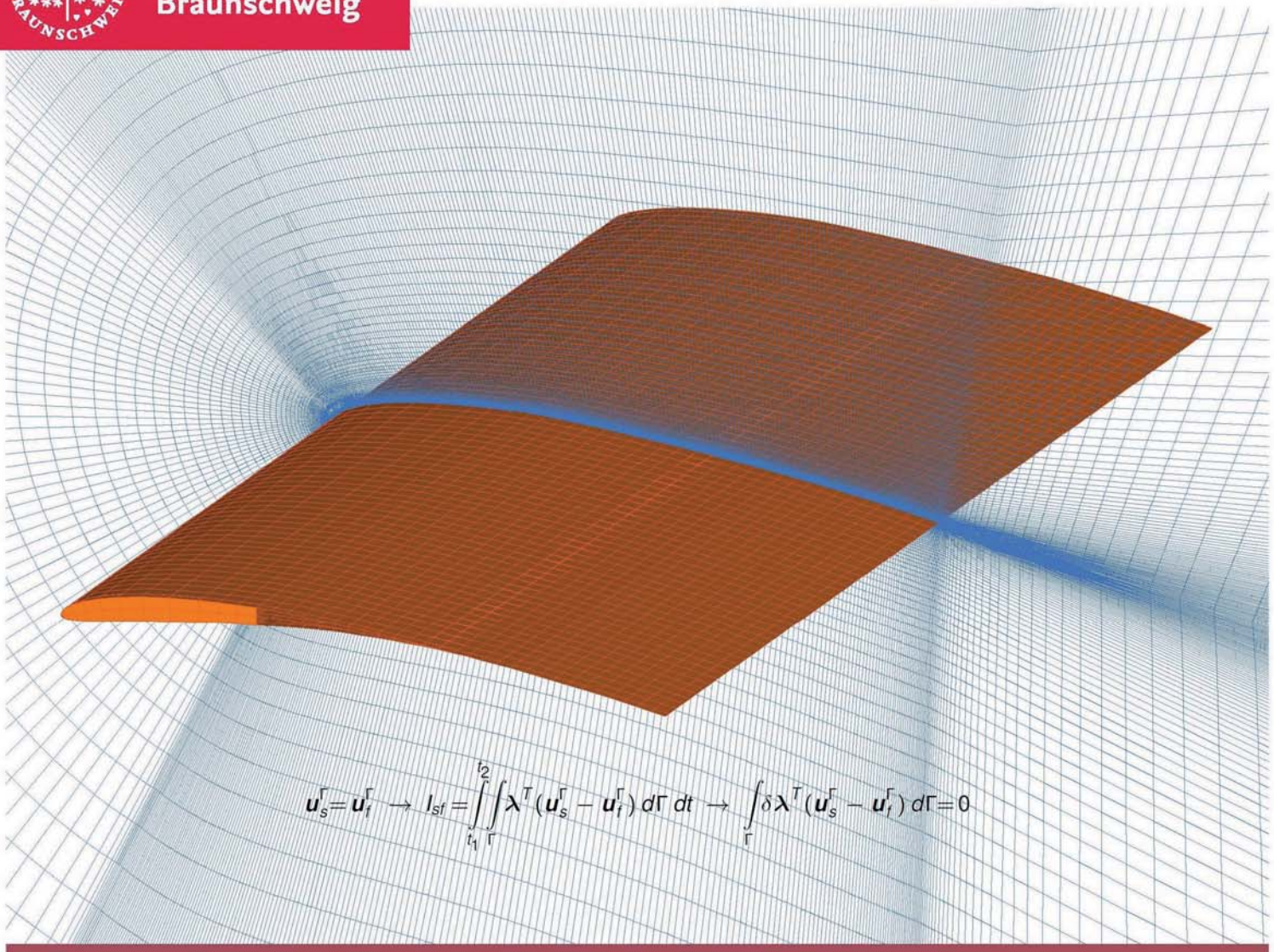

$$\mathbf{u}_s^\Gamma = \mathbf{u}_f^\Gamma \rightarrow I_{sf} = \int_{t_1}^{t_2}\int_\Gamma \boldsymbol{\lambda}^T (\mathbf{u}_s^\Gamma - \mathbf{u}_f^\Gamma)\, d\Gamma\, dt \rightarrow \int_\Gamma \delta\boldsymbol{\lambda}^T (\mathbf{u}_s^\Gamma - \mathbf{u}_f^\Gamma)\, d\Gamma = 0$$

Application of finite elements for computational aeroelasticity

Ralf Unger
TU Braunschweig, Institut für Flugzeugbau und Leichtbau

CFF - Forschungsbericht 2011-08

Cuvillier Verlag Göttingen
Internationaler wissenschaftlicher Fachverlag

TU Braunschweig - Campus Forschungsflughafen

Berichte aus der Luft- und Raumfahrttechnik

Forschungsbericht 2011-08

Application of finite elements for computational aeroelasticity

Ralf Unger

TU Braunschweig – Institut für Flugzeugbau und Leichtbau

Diese Arbeit erscheint gleichzeitig als von der Fakultät für Maschinenbau der Technischen Universität Carolo-Wilhelmina zu Braunschweig zur Erlangung des akademischen Grades eines Doktor-Ingenieurs genehmigte Dissertation.

Bibliografische Information der Deutschen Nationalbibliothek
Die Deutsche Nationalbibliothek verzeichnet diese Publikation in der Deutschen Nationalbibliographie; detaillierte bibliografische Daten sind im Internet über http://dnb.d-nb.de abrufbar.
1. Aufl. - Göttingen: Cuvillier, 2011
Zugl.: (TU) Braunschweig, Univ., 2011

978-3-86955-900-1

Diese Arbeit erscheint gleichzeitig als von der Fakultät für Maschinenbau der Technischen Universität Carolo-Wilhelmina zu Braunschweig zur Erlangung des akademischen Grades eines Doktor-Ingenieurs genehmigten Dissertation.

Herausgeber der CFF Forschungsberichte:
TU Braunschweig - Campus Forschungsflughafen
Hermann-Blenk-Straße 27 • 38108 Braunschweig
Tel: 0531-391-9822 • Fax: 0531-391-9808
Internet: www.campus-forschungsflughafen.de
Mail: cff@tu-braunschweig.de

© CUVILLIER VERLAG, Göttingen 2011
Nonnenstieg 8, 37075 Göttingen
Telefon: 0551-54724-0
Telefax: 0551-54724-21
www.cuvillier.de

1. Auflage, 2011
Gedruckt auf säurefreiem Papier

978-3-86955-900-1

Application of finite elements for computational aeroelasticity

Bei der Fakultät für Maschinenbau
der Technischen Universität Carolo-Wilhelmina zu Braunschweig

zur Erlangung der Würde

eines Doktor-Ingenieurs (Dr.-Ing.)

genehmigte Dissertation

von:	Dipl.-Ing. Ralf Unger
aus:	Finsterwalde

eingereicht am:	16. Dezember 2010
mündliche Prüfung am:	30. August 2011
Referenten:	Prof. Dr.-Ing. Peter Horst Prof. Dr.-Ing. Rolf Radespiel Prof. Dr.-Ing. Norbert Kroll
Vorsitzender:	Prof. Dr.-Ing. Peter Hecker

2011

Danksagung

Die vorliegende Arbeit entstand während meiner Tätigkeit als wissenschaftlicher Mitarbeiter am Institut für Flugzeugbau und Leichtbau der Technischen Universität Braunschweig in der Zeit von 2004 bis 2010. Während dieser Zeit hatte ich die Gelegenheit an verschiedensten wissenschaftlichen Projekten zusammen mit großartigen Kollegen, Mitstreiter und Studenten zusammenzuarbeiten.

Besonderen Dank gilt Prof. Dr.-Ing. Peter Horst, dem Leiter des Instituts, der mir stets die Möglichkeit und Freiheit gab, wissenschaftlichen Fragestellungen über das übliche Projekt-Tagesgeschäft hinaus nachzugehen. Für die fachliche Unterstützung und vielfältigen Anregungen während dieser Zeit danke ich ihm sehr.

Herrn Prof. Dr.-Ing. Rolf Radespiel möchte ich für die Übernahme des Koreferats danken. Die Zusammenarbeit mit ihm während der letzte Jahre im Rahmen eines DFG-Projektes war eine echte Bereicherung für mich. Herrn Prof. Dr.-Ing. Norbert Kroll danke ich für die Übernahme des Drittreferats und die wertvollen Anmerkungen zu dieser Arbeit.

Ohne das Wirken von Herrn Dr.-Ing. Matthias Haupt, dem Leiter der Numerik-Arbeitssgruppe am IFL, wäre diese Arbeit nicht zustande gekommen. Seine zahlreichen Anregungen und wertvollen Vorschläge haben in vielfältiger Weise zum Gelingen der Arbeit beigetragen. Unvergessen bleiben die gemeinsamen Reisen zu wissenschaftlichen Konferenzen und Projekttreffen.

Bedanken möchte ich mich auch bei den heutigen und ehemaligen Kollegen am Institut für Flugzeugbau und Leichtbau für die großartige Zeit, dem freundschaftlichen Umgang miteinander und den gemeinsamen Kaffeepausen. Meinen ehemaligen Studenten danke ich für Unterstützung bei den vielseitigen Aufgaben während der anfallenden Projekten. Für die enge und spannende Zusammenarbeit danke ich auch den Kollegen vom Institut für Strömungsmechanik (ISM), die sowohl bei der numerischen Aerodynamik als auch bei der experimentellen Windkanalversuchen wertvolle Arbeit und Unterstützung geleistet haben. Die in dieser Arbeit dargestellten Ergebnisse aus Strömungsmessungen stammen vom ISM und für deren Bereitstellung danke ich sehr.

Meiner Familie und besonders meiner Frau Antje danke ich für die bewundernswerte Geduld und Verständnis, die sie für mich aufgebracht haben. Alexandra Smith, danke ich für die Durchsicht des englischen Textes und für die Verbesserungsvorschläge.

Overview

In this thesis, the classical aeroelastic panel flutter problem, where a compressible fluid flows over a thin elastic plate, is investigated in detail. A non-linear modeling is necessary when flutter is analyzed in the transonic flow regime and here inviscid as well as turbulent viscous air flows are considered. For these purposes, a consistent unified coupling approach is developed based on an energetic variational formulation, where the structural as well as the fluid subsystem are described by Hamilton's principle. With this procedure, the classical direct two-field approach and a novel indirect three-field approach can be employed. By discretization of the entire coupled system consistently with finite elements, the fluid subsystem can be treated with the characteristic based split (CBS) scheme independently of a classical structural discretization. In this context, the established continuous Galerkin form of the CBS scheme is advanced and a discontinuous version is proposed, which is an attractive approach due to its local element edge flux conservation. The Spalart-Allmaras turbulence model in conjunction with the CBS scheme and unsteady Reynolds-averaged Navier-Stokes equations is considered within this topic. With the separated discretization of the fluid and structural subsystem, a data transfer scheme over the non-matched interface grids is mandatory and based on the variational formulation, several energy and load conservative transmission schemes are employed.

These methods and further coupling aspects, in particular time integration and equilibrium iteration as well as the fluid grid deformation, are assessed with the aid of several examples and the panel flutter problem at transonic flow conditions. Especially, the three-field approach yields an attractive smooth transfer of the interface values with being load and energy conservative at the same time, which results in a more accurate and improved fluid flow solution. Consequently, the flutter phenomenon is studied in detail for sub-, super-, and transonic flows including the evaluation of stability boundary for different parameters.

Übersicht

In dieser Arbeit soll das klassische aeroelastische Panelflattern, bei dem ein kompressibles Fluid über eine dünne elastische Platte strömt, detailliert untersucht werden. Um das Flatterphänomen in transonischer Strömung zu analysieren, ist dazu eine nichtlineare Modellierung notwendig. Sowohl reibungsfreie als auch turbulente, reibungsbehaftete Luftströmungen werden dabei berücksichtigt. Zu diesem Zwecke wird ein konsistenter, einheitlicher Kopplungsansatz entwickelt, welcher auf einer energetischen Variationsformulierung beruht, bei dem das strukturelle und fluiddynamische Teilsystem mittels dem Hamilton-Prinzip beschrieben werden. Mit diesem Vorgehen kann die klassische, direkte Zwei-Feld- aber auch eine neuartige indirekte Drei-Feld-Formulierung entwickelt werden. Um eine einheitliche Diskretisierung mit finiten Elementen zu erreichen, wird das fluiddynamische Teilgebiet mit dem *characteristic based split* (CBS) Schema unabhängig von einer konventionellen Strukturdiskretisierung behandelt. In diesem Zusammenhang wird die etablierte kontinuierliche Galerkin-Form des CBS Schemas erweitert und eine diskontinuierliche Version erarbeitet, welche sich durch eine lokale Konservativität der Kantenflüsse über benachbarte Elemente auszeichnet. Das Spalart-Allmaras Turbulenzmodell im Zusammenhang mit dem CBS Schema und der instationären, Reynolds-gemittelten Navier-Stokes Gleichungen wird ebenfalls innerhalb dieser Arbeit berücksichtigt. Aufgrund der getrennten Diskretisierung des strukturellen und fluiddynamischen Teilgebietes, wird ein Datentransferverfahren über nicht konforme Oberflächengitter notwendig. Mit Hilfe der Variationsformulierung können dazu verschiedene energie- und lasterhaltende Transferverfahren entwickelt werden.

Diese Methoden und weitere Kopplungsaspekte, wie beispielsweise die Zeitintegration und die Gleichgewichtsiteration aber auch die Deformation des Fluidgitters, werden anhand verschiedener Beispiele und des Plattenflattern bei transonischer Strömung bewertet. Besonders die neuartige Drei-Feld-Formulierung führt zu einem vorteilhaften glatten Transfer der Oberflächengrößen bei gleichzeitiger Erhaltung der Gesamtlast und -energy, welcher zu einer genaueren und verbesserten Strömungssimulation beiträgt. Infolgedessen, wird das Flatternverhalten des Panels detailliert im Unter-, Über- und Transschall untersucht. Dies beinhaltet auch die Berechnung der Flatter-Stabilitätsgrenze für verschiedene Parameter.

Contents

List of Figures

List of Tables

Nomenclature

In the nomenclature, every used symbol is named and the following conventions are generally made:

- vectors and matrices are marked with bold characters
- discrete values, vectors and matrices are labeled with a sans-serif font (except for Greek symbols)
- a quantity denoted with a lower character gets labeled with its upper counterpart, when multiplied with the density
- thus, with the example of the velocity:
  - v is the velocity or a velocity component
  - $\boldsymbol{v}$ is the velocity vector
  - $\boldsymbol{V}$ is the velocity vector times the density, i.e. $\boldsymbol{V} = \rho\boldsymbol{v}$
  - $\mathbf{v}$ is the vector of nodal velocity values
  - v is a certain nodal velocity
- a calligraphic font is used for operators

Roman Symbols

a	general diffusion coefficient
$\mathbf{a}$	vector of nodal acceleration values
A	nodal associated area
$\mathcal{A}$	spatial derivative operator
$b, \boldsymbol{b}$	body force, body force vector
$\mathbf{B}$	strain displacement matrix
c	speed of sound
c_p, c_v	specific heat at constant pressure and volume, respectively
C	hydrostatic, temperature dependent part of the Cauchy stress vector
C_d, C_f, C_l, C_p	drag, friction, lift and pressure coefficient
$C_{b1}, C_{b2}, C_\sigma^\nu$	Spalart-Allmaras turbulence model constants
C_{w1}, C_{w2}, C_{w3}	Spalart-Allmaras turbulence model constants
$C_\kappa, C_{v1}, C_{t3}, C_{t4}$	Spalart-Allmaras turbulence model constants
$C^k_{\sigma 1}, C^\omega_{\sigma 1}, C^\omega_{\beta 1}, C_{\gamma 1}$	BSL and SST turbulence model constants (inner set)
$C^k_{\sigma 2}, C^\omega_{\sigma 2}, C^\omega_{\beta 2}, C_{\gamma 2}$	BSL and SST turbulence model constants (outer set)
C^k_β, C_κ	BSL and SST turbulence model constants
$\mathbf{C}$	convective matrix

$\boldsymbol{C}$	CBS solver operator
d_w	wall distance
$\mathbf{d}$	vector of nodal displacement values
D	plate stiffness
$\mathcal{D}$	strain-displacement operator
$e, E, \mathbf{E}$	specific total energy, specific total energy × density, vector of nodal E-values
$\hat{e}^0$	prescribed initial conditions for the specific total energy
E_K	total kinetic energy
$\boldsymbol{E}$	stress-strain matrix
f	scalar variable / frequency
f_{v1}, f_{v2}, f_w	Spalart-Allmaras turbulence model parameters
f_{t2}, g, r	Spalart-Allmaras turbulence model parameters
$\mathbf{f}$	vector of nodal values of the scalar quantity f / discrete force vector
F_1, F_2	blending functions for the two-equation turbulence models
$\mathbf{F}$	element edge flux
$\mathcal{F}$	fluid solver operator
B_x	in-plane membrane force of the plate
G	shear module
$\mathbf{G}$	gradient matrix
$\mathcal{G}$	fluid grid deformation operator
h, h	characteristic length, characteristic length of a finite element
h_s	step height
H, h_0, H_0	Hamiltonian of a system, specific Hamiltonian, Hamiltonian density
I, I_i, I_{ij}	action functional, action functional of a single field i, connectivity action functional between two subdomains i and j
$I_\Lambda, I_{\Lambda 2}, I_{\Lambda 3}$	action functional subject to a constraint function, action functional of the two- and three-field approach
$\boldsymbol{I}, \boldsymbol{I}_0$	unit matrix, diagonal matrix used for stress expression
$J_{\boldsymbol{x}\boldsymbol{\chi}}$	Jacobi determinant of the ALE mapping ($\boldsymbol{x} \rightarrow \boldsymbol{\chi}$)
k	turbulent kinetic energy
K	reduced frequency / conservative turbulent kinetic energy ($K = \rho k$)
$\mathbf{K}$	stiffness matrix / vector of nodal values of the conservative turbulent kinetic energy
l, l_c, l_e	reference length, chord length, edge length
L, l_0, L_0	Lagrangian of a system, specific Lagrangian, Lagrangian density
$\mathbf{L}$	strain displacement vector
m	mass
$\boldsymbol{m}$	Kronecker like vector ($= [1, 1, 1, 0, 0, 0]^T$)
M	element mass
Ma	Mach number
$\mathbf{M}$	mass matrix
$\mathcal{M}$	data transfer operator
n	time step index
$\boldsymbol{n}$	normal vector
$N_d, N_{DOF}, N_{\text{edges}}$	number of subdomains, degrees of freedom, edges of an element
N_{gp}, N_e, N_n, N_t	number of Gaussian points, finite elements, nodes, time steps
N_{crit}	critical N-factor
$\mathsf{N}, \mathbf{N}, \mathbf{N}_v$	shape function, shape function vector, velocity shape function matrix
$p, \mathsf{p}, \mathbf{p}$	pressure, nodal pressure value, vector of nodal pressure values

$\boldsymbol{p}, \boldsymbol{p}_0$	Hamiltonian and specific Hamiltonian momentum density
$\mathbf{p}_{,x}$	nodal pressure derivatives
P	potential energy
Pr	Prandtl number
$\mathbf{P}, \mathsf{P}$	general coupling matrix and its entry
$\boldsymbol{q}$	heat flux
Q	general source term
$\boldsymbol{Q}$	velocity matrix containing the velocity entries in consistent form
r	radius
r_m, r_p	non-dimensional mass ratio and dynamic pressure
$\boldsymbol{r}$	vector of generalized coordinates
R	specific gas constant
Re	Reynolds number
$\mathbf{R}$	residual function
$\boldsymbol{s}, \mathbf{s}$	convective velocity vector ($\boldsymbol{s} = \boldsymbol{v} - \boldsymbol{w}$) and its nodal vector
S	Sutherland temperature
St	Strouhal number
$\check{S}$	modified vorticity
$\mathbf{S}$	smoothing matrix
$\mathcal{S}$	structural solver operator
t	time
$\boldsymbol{t}$	traction forces
T	temperature / time of one period
$\mathbf{T}, \mathbf{T}_{,x}$	vector of nodal temperature values and its nodal derivatives
$\hat{\boldsymbol{u}}^0, \dot{\hat{\boldsymbol{u}}}^0$	prescribed initial conditions for the displacements and for their first substantial derivative
$\boldsymbol{u}$	displacement vector
U, U_0	strain energy and strain energy density
$v, \boldsymbol{v}, \mathbf{v}$	velocity, velocity vector in the Eulerian frame of reference, vector of nodal velocity values
$\hat{\boldsymbol{v}}^0$	prescribed initial conditions for the velocity
$\boldsymbol{V}, \check{\boldsymbol{V}}, \mathbf{V}, \check{\mathbf{V}}$	velocity vector $\boldsymbol{v}$ times density ρ, its intermediate and their nodal representatives
$\boldsymbol{w}, \mathbf{w}$	velocity of the ALE frame of reference in the Eulerian frame of reference and its nodal vector
$\mathcal{W}$	fluid grid velocity operator
x_t	transition location in x-direction
$\boldsymbol{x}, \boldsymbol{X}$	coordinates in the Eulerian and Lagrangian frame of reference
y^+	dimensionless wall distance

Greek Symbols

α	angle of attack
β	artificial compressibility parameter
γ	ratio of specific heats $\gamma = c_p/c_v$
$\Gamma, \Gamma^N, \Gamma^D$	general, Neumann and Dirichlet boundary
Γ_{fs}	interface between fluid and structure
Γ_c, Γ_{ci}	connectivity frame boundary, part of the connectivity frame boundary shared by the domain i
ϵ	specific internal energy

$\boldsymbol{\varepsilon}, \dot{\boldsymbol{\varepsilon}}, \boldsymbol{\varepsilon}^0$	strain and strain rate vector, non-displacement caused strain vector
ζ	damping ratio
θ_1, θ_2	first and second relaxation parameter for the CBS scheme
θ_s	rotation of a plate section
ϑ	logarithmic decrement
κ	thermal conductivity
$\lambda, \boldsymbol{\lambda}, \acute{\boldsymbol{\lambda}}$	Lagrange multiplier, vector of Lagrange multipliers and its nodal values
$\boldsymbol{\lambda}_i, \boldsymbol{\lambda}_{ij}$	vector of Lagrange multipliers on the boundary of the domain i and between two subdomains i and j
$\Lambda, \boldsymbol{\Lambda}$	constraint function, vectorial constraint function
$\mu, \mu_a, \mu_T, \breve{\mu}, \breve{\boldsymbol{\mu}}$	dynamic, artificial, eddy and modified eddy viscosity as well as its nodal representative
$\nu, \nu_T, \breve{\nu}, \breve{\boldsymbol{\nu}}$	kinematic, kinematic eddy and modified eddy viscosity as well as its nodal representative
ν_g	Poisson's ratio of the fluid grid
ξ	local coordinate within a finite element
Π	total potential energy
$\rho, \hat{\rho}^0, \boldsymbol{\rho}$	density, its prescribed initial conditions, nodal density vector
ς_c	lower bound artificial compressibility parameter β
ς_{RI}	relaxation parameter for the Richardson iteration
ς_s	smoothing parameter
ς_{SN}	stiffness matrix weight for the Sobolev-norm based transfer
ς_T	data transfer tolerance
ς_t	safety factor for the local time stepping
$\varsigma_\beta, \varsigma_\gamma$	Newmark parameters for the displacements and velocities
$\boldsymbol{\sigma}$	Cauchy stress vector
$\boldsymbol{\tau}, \breve{\boldsymbol{\tau}}$	viscous stress vector and its nodal representation
$\boldsymbol{\Upsilon}$	matrix containing entries of the normal vector
ϕ	scalar variable
ϕ^g	gravitational potential
$\boldsymbol{\chi}$	coordinates in the ALE frame of reference
ψ_{gp}	weight of Gaussian points
$\omega, \breve{\boldsymbol{\omega}}$	specific turbulent dissipation and its nodal representation
Ω	domain

Mathematical Notation

Δ	difference
$\frac{d}{dt}$	substantial time derivative
$\frac{\partial}{\partial t}$	partial derivative with respect to time t
$\dot{(\cdot)}, \ddot{(\cdot)}$	first and second substantial time derivative
$(\cdot)^+$	Moore-Penrose pseudo-inverse
∇	nabla operator
δ	variational operator
δ_{ij}	Kronecker delta
$\det(\cdot)$	determinant
$\lim(\cdot)$	limit
$\emptyset, \cap, \cup$	empty set, intersection and union of two sets
$\bigcup$	union of several sets
$(\cdot)^T$	transposed
$(\cdot)\|_{\boldsymbol{x}}, (\cdot)\|_{\boldsymbol{X}}, (\cdot)\|_{\boldsymbol{\chi}}$	evaluated at constant $\boldsymbol{x}$, $\boldsymbol{X}$, $\boldsymbol{\chi}$, respectively

Superscripts, Subscripts and Accents

$(\cdot)^0$	inital quantity
$(\cdot)^{\text{conv}}, (\cdot)^{\text{diff}}$	convective and diffusive quantity
$(\cdot)^e$	quantity calculated for a finite element
$(\cdot)^F$	Favre averaged quantity
$(\cdot)^m, (\cdot)^n$	quantity at real time instance m and at time n
$(\cdot)^R$	real time specific quantity
$(\cdot)^\star$	non-dimensional quantity
$(\cdot)', (\cdot)''$	turbulent fluctuation of a quantity
$(\cdot)^\Omega, (\cdot)^\Gamma$	domain and interface values
$(\cdot)_c$	connectivity frame quantity
$(\cdot)_D$	diagonal quantity
$(\cdot)_{\text{eff}}$	effective
$(\cdot)_E$	energy specific quantity
$(\cdot)_e$	element specific quantity
$(\cdot)_{\text{ext}}$	external quantity
$(\cdot)_f$	fluid quantity
$(\cdot)_g$	grid specific value
$(\cdot)_{gp}$	Gaussian point specific value
$(\cdot)_i$	ith component of the vector $(\cdot)$
$(\cdot)_{\text{int}}$	internal quantity
$(\cdot)_K$	turbulent kinetic energy specific quantity
$(\cdot)_L$	lumped quantity
$(\cdot)_p$	pressure specific quantity
$(\cdot)_s$	structural quantity / convective velocity specific quantity
$(\cdot)_T$	turbulent specific quantity
$(\cdot)_{te}$	trailing edge specific quantity
$(\cdot)_u$	displacement specific quantity
$(\cdot)_v$	velocity specific quantity
$(\cdot)_V$	density $\times$ velocity specific quantity
$(\cdot)_w$	grid velocity specific quantity
$(\cdot)_\infty$	reference quantity
$(\cdot)_\rho$	density specific quantity
$(\cdot)_\tau$	stress specific quantity
$(\cdot)_\lambda$	Lagrange multiplier specific value
$(\cdot)_{\breve{\mu}}, (\cdot)_{\breve{\nu}}$	dynamic and kinematic eddy viscosity specific quantity
$(\cdot)_{\breve{\omega}}$	turbulent dissipation specific quantity
$\hat{(\cdot)}$	prescribed quantity
$\breve{(\cdot)}$	modified quantity
$\grave{(\cdot)}$	amplitude of a quantity
$\tilde{(\cdot)}$	mass averaged quantity
$\overline{(\cdot)}$	time averaged quantity / general mean value
$\acute{(\cdot)}$	blended quantity

Acronyms

AGARD	Advisory Group for Aerospace Research and Development
ALE	arbitrary Lagrangian-Eulerian

BSL	baseline turbulence model
CBS	characteristic based split
CFD	computational fluid dynamics
CG	characteristic Galerkin
DFG	German research foundation (Deutsche Forschungsgemeinschaft)
DGCL	discrete geometric conservation law
DG	discontinuous Galerkin
DN	Dirichlet-Neumann
FEM	finite elements method
SUPG	streamline upwind Petrov Galerkin
GCL	geometric conservation law
GMRES	generalized minimal residual method
LCO	limit cycle oscillation
NURBS	non-uniform rational B-splines
RANS	Reynolds-averaged Navier-Stokes
SA	Spalart-Allmaras
SG04	seagull airfoil with a camber of 4%
SPP	priority program (Schwerpunktprogramm)
SST	shear stress transport turbulence model
URANS	unsteady Reynolds-averaged Navier-Stokes

1 Introduction

1.1 Motivation

The dynamic interaction of a fluid flow with an elastic structure plays an important part in engineering science. Interesting applications can also be found in biomechanical engineering, where for example the blood flow interacting with the abdominal aorta is investigated to prevent an aneurysm, [FVJ+06, SF07]. In civil engineering, wind induced vibrations of bridges need to be suppressed, [BS06]. A fluid-structure interaction (FSI) analysis, may help to find an engineering solution for this demand. A further application of FSI in civil engineering is the computation of a dam failure caused by a seismic excitation [RFPS08, RSFP09]. Such applications are of interest due to the enormity of the destructive power of the water flood wave, which is released after the failure of a dam.

In engineering science the field of *aeroelasticity* mainly driven by aeronautical engineering has been developed for such FSI problems. Quoting [WC07], "Aeroelasticity is the subject that describes the interaction of aerodynamic, inertia and elastic forces for a flexible structure and the phenomena that can result". Aircraft structures in particular are subjected to massively deflect under aerodynamic and inertia loads. Modern lightweight structures and increasing flight speeds amplify the aeroelastic behavior. Aeroelastic problems can mainly be divided into two classes [CD04, Foe74, WC07]:

1. static aeroelasticity
2. dynamic aeroelasticity

Inertia forces can be neglected for the first class and typical problems are: torsional divergence, control reversal, static stability. Typical problems for the second class are: *flutter*, dynamic flight stability, buffeting. Thereby, flutter is a critical aeroelastic problem, which can lead to the damage of the structure. A typical flutter phenomenon is the *panel flutter problem*, Figure 1.1(a), which shows - depending on the flow conditions - a limited flutter amplitude. Such *limit cycle oscillation* (LCO) is caused by a non-linear structural deflection. Furthermore, simplified linear aerodynamic models, in particular strip theory or panel method aerodynamics, are unable to predict shocks in the flow field. Thus, the prediction of the stability in the transonic flow regime becomes inaccurate as shown in Figure 1.1(b), where the flutter speed versus the Mach number for a typical panel flutter problem is plotted. The flutter speed is defined as the lowest flow speed at which flutter occurs. In the transonic flow regime, a significant reduction of this characteristic aeroelastic value can be observed from Figure 1.1(b). Such transonic dip cannot be predicted with linear aerodynamic models and modern fluid dynamics modeling techniques need thus to be used, which solve the Euler or Navier-Stokes equation of fluid motion. Moreover, depending on the flow conditions other long term system responses of the panel might be static deflection, i.e. divergence or an undeflected panel. Thus, the panel flutter problem can serve as a significant model problem for aeroelastic applications to study several numerical schemes, which are going to be discussed in this thesis.

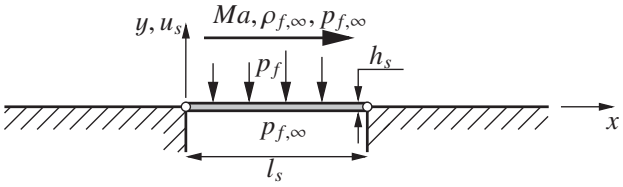

(a) panel flutter problem

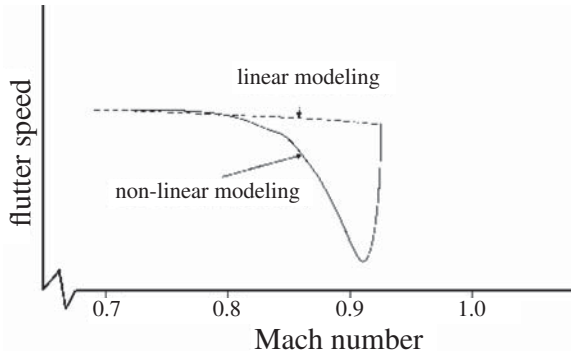

(b) typical flutter behavior of a panel in a transonic flow regime (taken from [WC07])

Figure 1.1: Description of the panel flutter problem and the typical flutter behavior in a transonic flow regime

Although several non-linear *structural* approaches for the panel flutter problem can be found in literature, [Dow70, ACM99], only some attention has been paid to the non-linear *fluid* part of the panel flutter problem, [DB93]. To consider shock waves in the transonic flow regime, often the Euler equations of fluid motion are solved, [GM00, Mas02]. In [Dow73], a simplified shear layer fluid model is used to incorporate the effect of viscosity. A full Navier-Stokes fluid solver was used in [GV02] for the panel flutter problem, but the flow was assumed to be laminar at a Reynolds number of 10^5 based on the panel length. Some results for the panel flutter problem with a turbulent Navier-Stokes fluid solver can be found in [GV02, Hur01, HAN09, BS08]. That a turbulent boundary layer affects the flutter behavior depending significantly on a supersonic Mach number of the overflowing fluid could be shown in [HAN09].

1.2 Methodology

In the previous section, it could be shown, that aeroelasticity describes a subset of fluid-structure interaction problems and this multidisciplinarity is an important aspect for aeronautical engineering. In this thesis, *computational aeroelasticity* (CA) is understood as the numerical treatment of aeroelastic problems with accurate simulation methods [Far04, Ben04]. Several approaches exist here. In the so-called monolithic coupling approach, one computational algorithm is developed for both - the fluid and the structural subsystem - and the governing equations are treated simultaneously, [Blo98]. Such a method often requires a new code development and is frequently applied only for academic problems, [Hei04]. Since the coupled physical system is treated with one numerical scheme, the *monolithic* approach might show better and more robust computational behavior, [BC10]. However, the most common method to numerically treat an aeroelastic problem is the so-called *partitioned* approach, which is discussed in the next subsection.

1.2.1 Partitioned coupling approach

Applying the partitioned coupling approach each participating subdomain is computationally solved by its own solver [FLM95, Pip97, FL00, MS03, GBD+03, vZB05, DP06, VLDV07, SMU+10, DSVP+10]. Thus, a framework is necessary, into which the fluid and structural solver are integrated. Numerical data have to be transferred from one to the other simulation code to ensure the computational coupling. Moreover and due to the use of separate solvers, the aerodynamic forces and the structural deformations need to be intrinsically in an equilibrium, which requires an iteration procedure.

Frequently, for the second demand of the *equilibrium iteration*, a straightforward Richardson iteration is applied, where the coupled problem is treated as a Dirichlet-Neumann-decomposition, i.e. the structural deformations are set as boundary conditions on the fluid and the aerodynamic forces are imposed on the structural side. However, this simple Richardson iteration procedure might show an unstable behavior or slow convergence rate for strong coupled problems, where a high density fluid acts on a high flexible structure, [CGN05, FWR07]. Thus, high-order iteration schemes, like Netwon-Raphson, Newton-GMRES, etc. are applied for these kinds of applications, which is an active research field, [vZB05, VLDV07]. The most typical aeroelastic problems are weakly coupled, i.e. a relative stiff structure interacts with an airflow. For those weakly coupled applications, a *simple staggered iteration* procedure, where the force and deformation data transmission is accomplished only once in a time step, is generally sufficient [FL00]. The accuracy of this simple staggered scheme can be improved by the usage of *structural predictors*, where the structural deformation of the next time level is estimated based on the structural solution at the actual time level [Pip97, FvdZG06].

While the equilibrium iteration is extensively studied in literature, the topic of data transmission over computational meshes is often treated without significant attention. A comprehensive overview of this essential coupling aspect can be found in [JH04, JJGL05, dBvdSB07, Kim10]. The problem of the numerical data transfer arises due to the usage of different computational grids for the fluid flow and the structural simulations. Thus, the interface is represented by different surface grids which are generally *non-matched*, i.e. the nodes and elements are non-coincident. Several methods exist and an appropriate transfer scheme should not only satisfy accuracy but also load and energy conservation, i.e. neither artificial load nor energy should be generated when transmitting data from one to the other interface grid, [dBvZB08, dB08]. Furthermore, the accuracy of the structural displacements transfer is frequently disregarded. In [dB08], an example of an unsatisfied deformation transfer and its effect on the accuracy of the solution are given by a problem of a flexible flap coupled with an incompressible fluid. For multiphysical problems involving a compressible fluid, an inaccurate displacement transmission can lead to unintentional artificial shocks close to the interface when the fluid interface grid is much better resolved than the structural counterpart [UHH07b].

The most common transfer method is the nearest neighbour interpolation, [TBU00], where the datum of a node from mesh one is simply set to the nearest node of mesh two. Obviously, such a procedure is neither load nor energy conservative. A further class of transfer schemes are projection methods like the conservative node interpolation, [FLL98] or *quadrature point interpolation*, [CL97]. A variation of the quadrature point interpolation was proposed within the field of contact mechanics by Puso in [Pus04], which uses *dual-Lagrange multipliers* to obtain more efficient transfer schemes. Furthermore, geometric splines are frequently used for the data transmission across non-matching interface meshes, [SCH00].

1.2.2 Finite-element methodology for the fluid flow

Another difficulty of using a partitioned coupling approach arises due to the application of inconsistent numerical schemes to simulate aeroelastic phenomena. For example, often a *finite volume* scheme for the computation of the fluid flow, [Bla06, FP01], is utilized in conjunction with a *finite element* methodology (FEM) for the structural part, [Hug00, ZTZ05, Bat96]. Due to this fact, difficulties might be encountered to design a mathematically correct transfer scheme. Therefore and for reasons of numerical consistency, a numerical coupling scheme is employed, where the fluid subdomain is also discretized with finite elements. In the context of the *discontinuous Galerkin* method such finite element approximation becomes a key method for solving the governing fluid equations in the near future, [BO99, ZTSP03, Coc03, BCRS05, Har06, LBL08, HHLP10].

The finite element method for fluid flow problems has been established in the last twenty years, while first attempts were made by Zienkiewicz, [ZC65], Oden, [Ode72], or Chung, [CC76] with a *continuous Galerkin* method. To use the standard Petrov-Galerkin form (weight functions are equal to interpolation functions), stability terms need to be added to suppress instabilities caused by the convective terms of the fluid equations. Such stability terms are introduced naturally by the *characteristic based split* (CBS) scheme proposed by Zienkiewicz and Codina [ZC95, ZMS+95], which uses a local Taylor expansion to design a computational effective scheme. A comprehensive overview of this scheme is provided by Nithiarasu in [NCZ06] and nowadays the CBS scheme is widely used to solve the compressible and incompressible fluid flows. In [Nit03, NMWM04] incompressible flows are treated via an *artificial compressibility* method. Turbulent incompressible flow with the aid of the CBS scheme is investigated in [NHM+08]. Inviscid compressible flows treated with the CBS scheme is analyzed for a wide range of Mach numbers in [TN05].

In the context of FSI problems, the concept of artificial compressibility is advantageous, due to the observation of the so-called *added mass effect* when simulating an elastic structure coupled to a pure incompressible fluid flow, [CGN05, FWR07]. With an incompressible fluid, Poisson's equation is solved for the pressure unknown and thus a disturbance caused by the elasticity of the structure can propagate with infinite velocity, i.e. the speed of sound is infinity. This infinite velocity is responsible for the added mass effect, which cause numerical difficulties. Recently, it could be proven, that this fact is responsible for the requirement of an equilibrium iteration with slow convergence rates, [vB09]. In the same paper, it was revealed, that with a finite speed of sound a simple staggered iteration procedure is possible and the added mass effect can be reduced by a smaller time step. With the artificial compressibility, the infinite value for the speed of sound is replaced by a finite numerical value and thus the CBS scheme can be used for incompressible fluid without any restrictions. This is motivated by the findings in [FRWB10], where a stable and robust simple staggered scheme could be designed as long as the fluid is basically modeled as a compressible fluid.

The discontinuous Galerkin method has been developed mainly for problems in fluid mechanics and combines features of the finite element and the finite volume schemes. Indeed, the finite element method is frequently criticized to violate local conservation of the primary fluid quantities, [HSBB06]. The discontinuous Galerkin method can ensure such *local conservation* by a proper treatment of the element edge flux. A good overview of this methodology can be found in [Coc03, Li06, BCRS05] and the references therein. One noteworthy advantage of the discontinuous Galerkin method is the possibility of easy parallelization of the algorithm since this method allows an element-by-element solution procedure. However, each node belongs to several elements and therefore multiple solutions for each node need to be stored, which results in a large memory requirement. Further, additional edge fluxes for each element have to be computed, which makes the discontinuous methodology usually more computationally expensive than its continuous Galerkin counterpart. On the other hand, solving a large system of linear algebraic equations

necessary for the continuous Galerkin CBS scheme is needless for the explicit discontinuous version, proposed in this thesis. In [TNB08], the discontinuous Galerkin method to the CBS scheme for laminar incompressible fluids was applied and the accuracy for typical testcases shown.

Finally, a consistent usage of finite elements as the spatial discretization method is motivated by the geometric flexibility of this method and the inherent possibility to impose physical boundary conditions, [GSE98, Loe08]. A further advantage of the FEM is the straightforward development of higher order spatial discretizations. In this context and from the mathematical point of view, a rigorous convergence theory is available, e.g. [Hug00, ZTZ05, Bat96]. Furthermore, in [GSE98, Chu02] the finite element method is seen as a generalized finite volume method, which underlines the general character of the FEM.

1.3 Research aim

Two different points of view are considered for the research aim in this thesis.

From the numerical standpoint, consistency is an important requirement for a system's convergence, especially when a system should be analyzed as accurately as possible with modern computational tools. Consistency of a numerical scheme is usually defined as the property, that the discretized equations converge to the underlying differential equations if the time step as well as the element size approach zero [Bla06]. Therefore, a unified coupling approach is developed in this thesis, which is in its discrete form spatially as well as temporally consistent. The question arises whether such unified coupling approach can be designed in a partitioned way so that existing and well-established algorithms can furthermore be used. Thus, a continuous energy based, variational principle for coupled problems is employed, which serves as the fundament for the consistent spatial discretization with finite elements. The choice of the FEM is motivated by a long history of this scheme in structural mechanics and by recent numerous research activities of Galerkin methods in fluid dynamics. The partitioning of the system leads to the consideration of several coupling aspects, e.g. data transfer, fluid grid deformation, equilibrium iteration and time integration.

With the requirement of keeping the consistency of the discrete system and with the variational principles as the fundament, some new ideas regarding these coupling aspects are considered and existing schemes are revisited and improved. Especially with the three-field approach, an attractive smooth transfer of the interface values can be employed to overcome unphysical numerical effects in the fluid flow solution. Further, the development of the CBS scheme for moving and deforming fluid domains is a topic to be answered in this thesis. To obtain a temporal consistency of the simulation, a classical fluid time integration scheme is adapted to the structural subdomain of an aeroelastic system. Finally, the question arises whether with higher order finite elements, an improvement of a simulation's accuracy can be reached. In this context, a discontinuous Galerkin form of the CBS scheme is required to implement, which yields a matrix-free scheme for the fluid part of the coupled simulation.

From the aeroelastic point of view, the transonic panel flutter problem is still an interesting and important model problem, which is characterized by structural as well as aerodynamic nonlinearities. As already mentioned, many of the simulations found in literature have been conducted with an inviscid fluid flow model. The effect of a boundary layer is the topic to be answered in this thesis and therefore, the panel flutter problem is investigated with a modern CFD algorithm, which solves the fluid equations in the framework of the Reynolds-averaged Navier-Stokes model. The proposed numerical methods (three-field approach, consistent time integration) are used to ensure accurate simulations and a turbulence model needs further to be applied for compressible flows in the context of the CBS scheme. Some insights into the importance of a viscous fluid boundary

layer on the stability boundary should be provided and thus the panel's LCO is also intensively investigated with an inviscid flow.

1.4 Thesis outline

To draw the introduction to a close, this thesis is divided into two parts: in a first, the continuous coupling approach and its discretization with finite elements are presented. Within the second part numerical examples and verification are shown. More precisely, a unified coupling approach based on a classical variational principle of stationary action is introduced in chapter 2. This principle is known as Hamilton's principle and it is used to consistently express the structural and fluid subsystem by a variational principle. The fluid subsystem itself is described by Hamiltonian fluid dynamics in an Arbitrary-Lagrangian-Eulerian frame of reference. The interaction of both subsystems is then further expressed via a weak formulation of the interface displacement equality.

The spatial and temporal discretization of the fluid and structural subsystem as well as the interface displacement transfer are discussed in chapters 3 and 4. Thereby, the discretization of the fluid subsystem is dedicated to an extra chapter (chapter 3), where the characteristic based split scheme is used to numerically treat the Navier-Stokes equation for the ALE frame of reference. A discontinuous version of this scheme is furthermore proposed in this chapter. The discretization of the whole coupled aeroelastic system is discussed in chapter 4, where an operational view of the system is introduced. This operational view is used to express the equilibrium iteration and the time integration of the coupled system. Further, data transfer methods over non-matching interface grids as well as a constistent time integration for the structural subsystem are proposed.

Within the second part of this thesis, the fluid solver is verified for several flow problems ranging from inviscid, viscous and turbulent as well as compressible and incompressible fluid flows, chapter 5. The whole coupling environment is verified and assessed in terms of the fluid grid deformation algorithm, the data interface approach in chapter 6 and the equilibrium iteration procedure. A smooth data transfer is proposed here, which use the three-field approach in conjunction with a higher order spatial discretization of the interface frame.

Finally, the methods proposed in this thesis are examined for the panel flutter problem, which shows a limit cycle oscillation at various flow conditions in chapter 7. Moreover, the panel flutter behavior is investigated in a transonic flow regime and additionally for turbulent flows.

In chapter 8, this thesis is summarized with a conclusion and an indication of future work is discussed. In the appendix A, some further informations are provided, where some mathematical notations are explained and the turbulence modeling with the aid of the CBS scheme are discussed in detail.

Part I

Numerical Schemes

2 A Unified Coupling Approach

In this thesis, coupled problems involving interaction of a fluid with a structure are derived from a variational formulation of the physical system. Variation principles have been an important basis in mechanics because many mechanical problems require finding an extremum (minima or maxima) by nature and thus can be natively formulated in terms of a variational statement. Other physical problems can only be expressed by partial differential equations, but can also be transformed to a variational principle equivalent to the original corressponding partial differential equations. These variational principles, naturally defined or derived from differential equations, are the basis for obtaining approximate solutions like finite element models. Such approximations of variational statements and their application to a broad range of physical problems were mainly investigated at the beginning of the twentieth century by Ritz [Rit08], Rayleigh [Ray77] and Galerkin [Gal15] to name a few. In the middle of the twentieth century new ideas in the field of variational principles were developed by Hellinger [Hel14] and Reissner [Rei50] for structural mechanics to describe continuum systems with mixed formulations and their approximation. With the appearance of modern computer systems, also variational principles for fluid systems have been developed, e.g. Seliger [SW68], Additionally, the spatial approximation with finite elements has been derived.

A more general approach to treat the dynamics of a system is Hamilton's principle, which uses the kinetic and potential energy as the basis for the variation [Ham34]. Hamilton's principle has been well established in the field of elastodynamics and dynamics of particles. In structural mechanics, Hamilton's principle reduces to the principle of virtual displacement for systems that are in static equilibrium. Due to the generalization of Hamilton's principle, in this thesis, physical phenomena involving fluid-structure interaction are formulated based on an expression of the scalar energy functional of the coupled system utilizing this principle. For an introduction to variational principle applied to interaction problems the reader is refered to [ACD09] and the various references therein.

2.1 System of reference

Before deriving the governing equations for the structure and fluid, a few comments on the system of reference should be made. Two systems of reference are usually used in continuum mechanics, distinguished in the way the kinematics are observed. Structural systems and their displacements are most frequently described in the so-called Lagrangian frame of reference, in which each material point is observed as it moves through the space. The coordinate system for the Lagrangian frame of reference is denoted as $\boldsymbol{X}$ and is associated with the material points. On the other hand, single fluid systems are commonly described in the Eulerian frame of reference, where the motion is observed from a fixed reference in space, while the fluid flow is passing. The coordinate system for the Eulerian frame of reference is denoted as $\boldsymbol{x}$. The Eulerian and Lagrangian frame of reference, Figure 2.1, are related by the time derivatives, see [DH03] for a derivation:

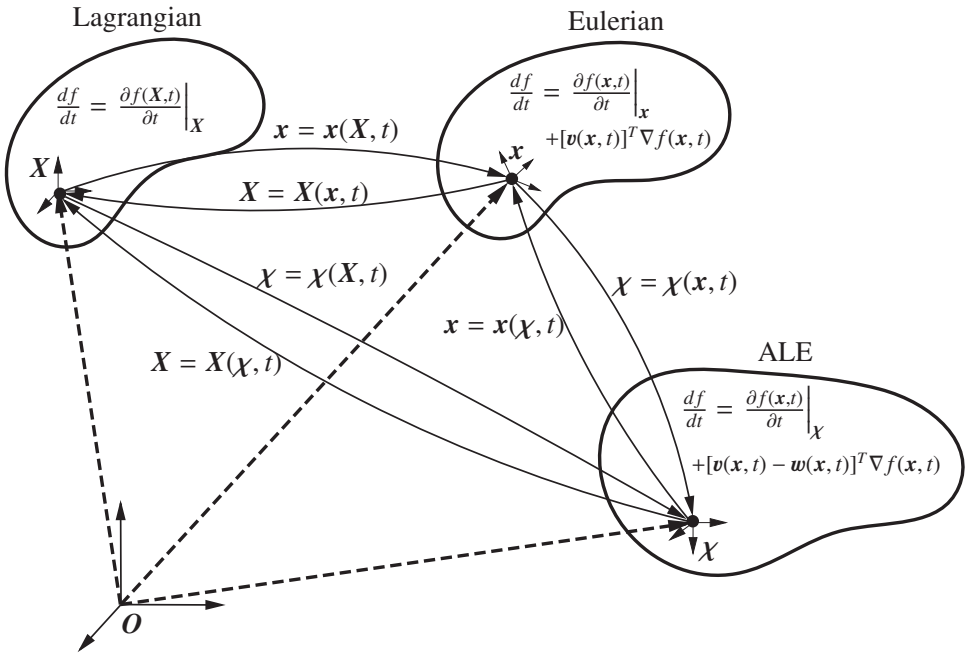

Figure 2.1: Frame of references used in continuousc mechanics and their substantial derivative

$$\begin{aligned} \dot{f} = \frac{df}{dt} &= \frac{\partial f(\boldsymbol{X},t)}{\partial t}\bigg|_{\boldsymbol{X}} && \text{(Lagrangian)} \\ &= \frac{\partial f(\boldsymbol{x},t)}{\partial t}\bigg|_{\boldsymbol{x}} + [\boldsymbol{v}(\boldsymbol{x},t)]^T \nabla f(\boldsymbol{x},t) && \text{(Eulerian)}\,, \end{aligned} \tag{2.1.1}$$

where d/dt is called either the advective, convective, substantial, Lagrangian or material derivative and is the time rate of change following a moving material particle The vector $\boldsymbol{v}(\boldsymbol{x},t) = \dot{\boldsymbol{x}} = \partial \boldsymbol{x}(\boldsymbol{X},t)/\partial t\,|_{\boldsymbol{X}}$ is the velocity of the material point given in the Eulerian frame of reference and f is some physical property. Furthermore, in Cartesian coordinates, the vector operator $\nabla = \partial/\partial \boldsymbol{x} = [\frac{\partial}{\partial x_1}, \frac{\partial}{\partial x_2}, \frac{\partial}{\partial x_3}]^T$ is the nabla operator in the Eulerian frame of reference.

In the context of fluid-structure interaction, the domain, where the fluid flow passes through, needs to be time-dependent. Therefore, a third frame of reference is introduced as the arbitrary Lagrangian-Eulerian (ALE) frame of reference, denoted by $\boldsymbol{\chi}$, Figure 2.1. The ALE frame of reference was first introduced in the context of fluid flow for finite difference methods in [Noh64, HAC74] and later for finite element schemes in [HLZ81, HL88]. For the ALE frame of reference, the motion is neither observed in Lagrangian nor in the Eulerian frame of reference, but is a mixture between the two of them, where the ALE frame of reference follows the structural motion at the boundaries while deforming arbitrarily within it. For the ALE frame of reference the substantial derivative can be written in a mixed form as, see [DH03] or [Li06] for details:

$$\begin{aligned} \dot{f} = \frac{df}{dt} &= \frac{\partial f(\boldsymbol{x},t)}{\partial t}\bigg|_{\boldsymbol{\chi}} + [\boldsymbol{v}(\boldsymbol{x},t) - \boldsymbol{w}(\boldsymbol{x},t)]^T \nabla f(\boldsymbol{x},t) \\ &= \frac{\partial f(\boldsymbol{x},t)}{\partial t}\bigg|_{\boldsymbol{\chi}} + [\boldsymbol{s}(\boldsymbol{x},t)]^T \nabla f(\boldsymbol{x},t)\,, \end{aligned} \tag{2.1.2}$$

where the $\boldsymbol{w}$ is the velocity of the ALE frame of reference in the Eulerian frame of reference:

$$\boldsymbol{w} = \frac{\partial \boldsymbol{x}(\boldsymbol{\chi},t)}{\partial t}\bigg|_{\boldsymbol{\chi}} \tag{2.1.3}$$

and $\boldsymbol{s} = \boldsymbol{v} - \boldsymbol{w}$ is known as the convective velocity and is the difference between the material velocity and the ALE frame velocity. Eq. (2.1.2) is often denoted as the fundamental ALE function, [DH03]. If $\boldsymbol{\chi} = \boldsymbol{X}$, clearly the velocity $\boldsymbol{v}$ and $\boldsymbol{w}$ are the same and Eq. (2.1.2) reduces to the equation of the substantial derivative for the Lagrangian frame of reference. If on the other hand $\boldsymbol{\chi} = \boldsymbol{x}$, then $\boldsymbol{w} = 0$ and the equation of the substantial derivative for the Eulerian frame of reference is obtained.

2.2 Hamilton's principle for continuum systems

Hamilton's principle states that a physical system undergoes that particular trajectory between t_1 and t_2, whose action has a stationary value (optimal path in time), see [Red02]. The system's action, which has the physical meaning of 'energy x time' can be described by a functional subject to be minimized:

$$I(\,t, \boldsymbol{r}(t)\,) = \int_{t_1}^{t_2} L(\,t, \boldsymbol{r}(t), \dot{\boldsymbol{r}}(t)\,)\,dt = \int_{t_1}^{t_2} \int_{\Omega} L_0(\,t, \boldsymbol{r}(t), \dot{\boldsymbol{r}}(t)\,)\,d\Omega\,dt \quad \rightarrow \quad \text{minimize}\,. \tag{2.2.1}$$

The quantity L is usually denoted as the Lagrangian of the system with the generalized coordinates $\boldsymbol{r}$ and can be expressed as:

$$L = E_K - \Pi = E_K - U - P\,, \tag{2.2.2}$$

where E_K is the total kinetic and Π is the total potential energy to which the strain energy U and the potential energy P contribute. With Eq. (2.2.2) it follows that the quantity L_0 is the Lagrangian density. Minimizing the functional I is equivalent to the first variation of this functional to be equal zero:

$$\delta I \;= \delta \int_{t_1}^{t_2} L(\,t, \boldsymbol{r}(t), \dot{\boldsymbol{r}}(t)\,)\,dt = \delta \int_{t_1}^{t_2} (E_K - \Pi)\,dt = \delta \int_{t_1}^{t_2} (E_K - U - P)\,dt = 0\,, \tag{2.2.3}$$

where δ is the variational operator. This states, that the difference between the kinetic and potential energies will be stationary, which is equivalent to the solution of the Euler-Lagrange equations:

$$\frac{\partial L}{\partial \boldsymbol{r}} - \frac{d}{dt}\frac{\partial L}{\partial \dot{\boldsymbol{r}}} = \boldsymbol{0}\,. \tag{2.2.4}$$

Before applying Hamilton's principle to a coupled system like FSI problems, the variational formulation for each single field needs to be investigated.

2.3 Hamiltonian structural dynamics

Using Hamilton's formalism, the standard displacement-based action functional for a non-linear single structural mechanical system may be written as follows, [Red02, ZT05]:

$$\begin{aligned} I_s(\boldsymbol{u}_s) = \int_{t_1}^{t_2} \Bigg[& \int_{\Omega_s} \frac{1}{2}\rho_s \dot{\boldsymbol{u}}_s^T \dot{\boldsymbol{u}}_s\,d\Omega_s - \int_{\Omega_s} U_0(\mathcal{D}\boldsymbol{u}_s)\,d\Omega_s \\ & + \int_{\Omega_s} \boldsymbol{u}_s^T \hat{\boldsymbol{b}}_s\,d\Omega_s + \int_{\Gamma_s^N} \boldsymbol{u}_s^T \hat{\boldsymbol{t}}_s\,d\Gamma_s^N \Bigg] dt\,, \end{aligned} \tag{2.3.1}$$

where $\boldsymbol{u}_s = [u_1, u_2, u_3]_s^T$ is the displacement field vector, $\dot{\boldsymbol{u}}_s = d\boldsymbol{u}_s/dt$ is the material time derivative of the displacement field vector, ρ_s is the density and $U_0(\mathcal{D}\boldsymbol{u}_s)$ is the strain-energy density function to model non-linear elastic material behavior from which the stress vector $\boldsymbol{\sigma}_s = [\sigma_{11}, \sigma_{22}, \sigma_{33}, \sigma_{12}, \sigma_{23}, \sigma_{31}]_s^T$ is calculated as:

$$\boldsymbol{\sigma}_s = \frac{\partial U_0}{\partial \mathcal{D}\boldsymbol{u}_s}\,, \tag{2.3.2}$$

in which $\mathcal{D}$ is the three-dimensional strain-displacement operator given by:

$$\mathcal{D}^T = \begin{bmatrix} \frac{\partial}{\partial x_1} & 0 & 0 & \frac{\partial}{\partial x_2} & 0 & \frac{\partial}{\partial x_3} \\ 0 & \frac{\partial}{\partial x_2} & 0 & \frac{\partial}{\partial x_1} & \frac{\partial}{\partial x_3} & 0 \\ 0 & 0 & \frac{\partial}{\partial x_3} & 0 & \frac{\partial}{\partial x_2} & \frac{\partial}{\partial x_1} \end{bmatrix} \tag{2.3.3}$$

to calculate the strain vector $\boldsymbol{\varepsilon}_s = [\varepsilon_{11}, \varepsilon_{22}, \varepsilon_{33}, \varepsilon_{12}, \varepsilon_{23}, \varepsilon_{31}]_s^T$ by:

$$\boldsymbol{\varepsilon}_s = \mathcal{D}\boldsymbol{u}_s\,. \tag{2.3.4}$$

It should be noted here, that the stress and the strain are already assumed to be symmetric throughout this thesis, i.e. $\sigma_{ij} = \sigma_{ji}$ and $\varepsilon_{ij} = \varepsilon_{ji}$. For linear elasticity, the strain-energy density function is:

$$U_0 = \frac{1}{2}\boldsymbol{\varepsilon}_s^T \boldsymbol{E}\boldsymbol{\varepsilon}_s - \boldsymbol{\varepsilon}_s^T \boldsymbol{E}\boldsymbol{\varepsilon}_s^0 \tag{2.3.5}$$

and the constitutive equation provided by Eq. (2.3.2) then becomes:

$$\boldsymbol{\sigma}_s = \frac{\partial U_0}{\partial \mathcal{D}\boldsymbol{u}_s} = \frac{\partial U_0}{\partial \boldsymbol{\varepsilon}_s} = \boldsymbol{E}(\boldsymbol{\varepsilon}_s - \boldsymbol{\varepsilon}_s^0)\,, \tag{2.3.6}$$

where $\boldsymbol{E}$ is the 6x6 material stress-strain matrix and $\boldsymbol{\varepsilon}_s^0$ are strains caused by non-displacement sources, e.g. temperature strain.

With reference to Eq. (2.2.2) the first term in Eq. (2.3.1) represents the kinetic energy, whereas the second term stands for the potential energy of the inner forces, which is equivalent to the strain energy. The last two terms account for potential energy of external forces, where $\hat{\boldsymbol{b}}_s = [\hat{b}_1, \hat{b}_2, \hat{b}_3]_s^T$ are the body forces and $\hat{\boldsymbol{t}}_s = [\hat{t}_1, \hat{t}_2, \hat{t}_3]_s^T$ are the traction or surface forces.

Now, taking the first variation of Eq. (2.3.1) with respect to $\boldsymbol{u}_s$ gives:

$$\begin{aligned} \delta I_s = \int_{t_1}^{t_2} \Bigg[&- \int_{\Omega_s} \rho_s \delta\boldsymbol{u}_s^T \ddot{\boldsymbol{u}}_s \, d\Omega_s - \int_{\Omega_s} \delta(\mathcal{D}\boldsymbol{u}_s)^T \frac{\partial U_0}{\partial \mathcal{D}\boldsymbol{u}_s} \, d\Omega_s \\ &+ \int_{\Omega_s} \delta\boldsymbol{u}_s^T \hat{\boldsymbol{b}}_s \, d\Omega_s + \int_{\Gamma_s^N} \delta\boldsymbol{u}_s^T \hat{\boldsymbol{t}}_s \, d\Gamma_s^N \Bigg] dt = 0\,, \end{aligned} \tag{2.3.7}$$

where $\ddot{\boldsymbol{u}}_s$ is the second material time derivative of the displacement field. Integration by parts and using Eq. (2.3.2) and (2.3.4) leads to:

$$\delta I_s = \int_{t_1}^{t_2} \left[\int_{\Omega_s} \delta\boldsymbol{u}_s^T \left(-\rho_s \ddot{\boldsymbol{u}}_s + \mathcal{D}^T \boldsymbol{\sigma}_s + \hat{\boldsymbol{b}}_s \right) d\Omega_s + \int_{\Gamma_s^N} \delta\boldsymbol{u}_s^T \left(\hat{\boldsymbol{t}}_s - \boldsymbol{\Upsilon}^T \boldsymbol{\sigma}_s \right) d\Gamma_s^N \right] dt = 0\,, \tag{2.3.8}$$

where $\boldsymbol{\Upsilon}^T$ contains the entries of the boundary normal vector:

$$\boldsymbol{\Upsilon}^T = \begin{bmatrix} n_1 & 0 & 0 & n_2 & 0 & n_3 \\ 0 & n_2 & 0 & n_1 & n_3 & 0 \\ 0 & 0 & n_3 & 0 & n_2 & n_1 \end{bmatrix}. \tag{2.3.9}$$

Cleary, the Euler-Lagrange equation corresponding to the double integral Eq. (2.3.1) is:

$$\mathcal{D}^T \boldsymbol{\sigma}_s + \hat{\boldsymbol{b}}_s = \rho_s \ddot{\boldsymbol{u}}_s \,, \tag{2.3.10}$$

which is the well-known equation of (linear) momentum conservation for a structural systems. Further, as seen from the second term of Eq. (2.3.8), the natural boundary condition - or Neumann boundary condition - for the traction are obtained by the variation of the functional:

$$\boldsymbol{t}_s = \boldsymbol{\Upsilon}^T \boldsymbol{\sigma}_s = \hat{\boldsymbol{t}}_s \quad \text{on} \quad \Gamma_s^N \,, \tag{2.3.11}$$

where Γ_s^N is called Neumann boundary subset.

Boundary conditions for displacement - the Dirichlet boundary conditions - on the Dirichlet boundary subset Γ_s^D:

$$\boldsymbol{u}_s = \hat{\boldsymbol{u}}_s \quad \text{on} \quad \Gamma_s^D \,, \tag{2.3.12}$$

where $\Gamma_s^D \cap \Gamma_s^N = \emptyset$ and $\Gamma_s^D \cup \Gamma_s^N = \Gamma_s$ holds, as well as initial conditions for transient problems:

$$\boldsymbol{u}_s(\boldsymbol{X}_s, t = 0) = \hat{\boldsymbol{u}}_s^0(\boldsymbol{X}_s) \quad \text{and} \quad \dot{\boldsymbol{u}}_s(\boldsymbol{X}_s, t = 0) = \hat{\dot{\boldsymbol{u}}}_s^0(\boldsymbol{X}_s) \tag{2.3.13}$$

are required to be applied.

It should be noted here, that the variation of Eq. (2.3.8) is the simplest form and only requires the displacement field to be considered. More general variational principles, including also the constitutive equation Eq. (2.3.2) and all boundary condition, is the Hu-Washizu variational principle [Was75], which is often used for mixed formulation in structural elasticity.

2.4 Hamiltonian fluid dynamics

Hamilton's principle can also be applied to problems in fluid mechanics. As Hamilton's formulation is based on an energy expression, two problems arise when formulating a proper Lagrangian density L_0. First, viscous fluids are dissipative in terms of energy due to friction or heat conduction and second, the equations of choice in fluid dynamics are usually given in a Eulerian frame of reference, where the flow quantities are expressed as a function of fixed position and time since the fluid motion is observed from a fixed reference in space. As it was pointed out in [Mue98], the fluid equations of motion in a Eulerian frame of reference are non-canonical, while the equations of motion in a Lagrangian frame of reference are canonical and can therefore be derived from a Lagrangian density L_0 by using Hamilton's principle. Or as expressed in [Sal88], in the Lagrangian frame of reference the equations of motion are coupled in the sense that the location together with velocities of particles are governed by them. This is in contrast to the equations in a Eulerian frame of reference, which are closed, meaning that the velocity, density and a fifth thermodynamic variable, e.g. entropy or energy, can be solved without finding the trajectory of the fluid particle.

In the following, the three equations describing fluid motion in the Eulerian frame of reference are derived with the aid of Hamiltonian fluid dynamics before the governing equations are obtained in the ALE frame of reference. These are the equation of mass, momentum and energy conservation. Without going unneccessarily into detail, good introductions on this topic can be found in [Lee77, Sal88, Sal98, Mue98, Lyn02, Swa00, Mor06, Pal06].

2.4.1 Mass conservation

As it was pointed out in [Sal88, Lyn02, Mor06], the equation of mass conservation is implicit given by switching from the Lagrangian to the Eulerian frame of reference. In these references

an infinitesimal fixed volume $d\Omega_{\boldsymbol{X}}$ with a constant density is assumed, where the Lagrangian coordinates are assigned in a way that:

$$dm = dX_1 dX_2 dX_3 = d\Omega_{\boldsymbol{X}} \tag{2.4.1}$$

holds. On the other hand, for the Eulerian frame of reference this infinitesimal mass can be expressed as:

$$dm = \rho_f dx_1 dx_2 dx_3 = \rho d\Omega_x \,, \tag{2.4.2}$$

where the coordinates in the Eulerian frame of reference, $\boldsymbol{x}_f = [x_1, x_2, x_3]_f^T$, are a function of the Lagrangian coordinates and the time:

$$\boldsymbol{x}_f = \boldsymbol{x}_f(\boldsymbol{X}_f, t) \,. \tag{2.4.3}$$

Therefore, both expressions for the mass are related by the well-known Jacobian, which gives:

$$\rho_f = \det\left[\frac{\partial \boldsymbol{x}_f}{\partial \boldsymbol{X}_f}\right] . \tag{2.4.4}$$

A direct application of the substantial derivative, d/dt, to this equation and using $d\boldsymbol{x}_f/dt = \dot{\boldsymbol{x}}_f = \boldsymbol{v}_f$ lead to (see [Sal98]):

$$\frac{d\rho_f}{dt} + \rho_f \nabla^T \boldsymbol{v}_f = 0 \tag{2.4.5}$$

and with the use of Eq. (2.1.1) and the product rule:

$$\nabla^T (f\boldsymbol{g}) = \boldsymbol{g}^T \nabla f + f \nabla^T \boldsymbol{g} \,, \tag{2.4.6}$$

this can be rewritten to obtain the equation of mass conservation in conservative form and in the Eulerian frame of reference as:

$$\frac{\partial \rho_f}{\partial t} + \nabla^T (\rho_f \boldsymbol{v}_f) = 0 \,, \tag{2.4.7}$$

where:

$$\left.\frac{\partial f}{\partial t}\right|_{\boldsymbol{x}} = \frac{\partial f}{\partial t} \tag{2.4.8}$$

is used as an abbreviation. Nevertheless, the mass conservation equation for the fluid flow can also be derived from the condition, that the Lagrangian density is constant over the time, [Pal06]:

$$\frac{d\,L_0}{d\,t} = \dot{L}_0 = 0 \quad \Rightarrow \quad \frac{\partial \rho_f}{\partial t} + \nabla^T (\rho_f \boldsymbol{v}_f) = 0 \,. \tag{2.4.9}$$

2.4.2 Hamilton's canonical equations

To derive now the equations of momentum and energy conservation, it is first convenient to use Hamilton's canonical equations, which introduce a new variable $\boldsymbol{p} = \partial L/\partial \dot{\boldsymbol{r}}$ and define a new function by a Legendre transformation. The Hamiltonian of the system is then be written as:

$$H = H(\boldsymbol{r}, \boldsymbol{p}, t) = \int_\Omega \boldsymbol{p}^T \dot{\boldsymbol{r}}\, d\Omega - L = \int_\Omega \boldsymbol{p}^T \dot{\boldsymbol{x}}_f\, d\Omega - L = \int_\Omega \boldsymbol{p}^T \boldsymbol{v}_f\, d\Omega - L \,, \tag{2.4.10}$$

which forms the second order differential equations of Eq. (2.2.4) to a first order differential equations.

With a Lagrangian density $L_0 = \rho_f l_0$, the action functional for a fluid can be expressed as:

$$I_f = \int_{t_1}^{t_2} \int_{\Omega_f} (\boldsymbol{p}^T \boldsymbol{v}_f - H_0)\, d\Omega_f\, dt = \int_{t_1}^{t_2} \int_{\Omega_f} \rho_f (\boldsymbol{p}_0^T \boldsymbol{v}_f - h_0)\, d\Omega_f\, dt\,, \tag{2.4.11}$$

where l_0 is the specific Lagrangian, H_0 and h_0 are the Hamiltonian density and the specific Hamiltonian, respectively, and the variable $\boldsymbol{p}_0$ is defined as $\boldsymbol{p}_0 = \partial l_0 / \partial \dot{\boldsymbol{r}} = \partial l_0 / \partial \boldsymbol{v}_f$. The equation of momentum conservation is now obtained by taking the first variation of this action functional while the equation of energy conservation is derived from the assumption, that the Hamiltonian density will not change with time, thus $dH_0/dt = 0$. A distinction for the different fluid model is required, which is discussed further in the following subsections.

2.4.3 Inviscid fluid

For an inviscid fluid, the Lagrangian density L_0 and the specific Lagrangian l_0 can be expressed as:

$$L_0 = L_0(\boldsymbol{x}_f, \boldsymbol{v}_f, \rho_f, t) = \frac{1}{2}\rho_f \boldsymbol{v}_f^T \boldsymbol{v}_f - \rho_f \epsilon_f(\rho_f) - \rho_f \phi_f^g(\boldsymbol{x}_f) \tag{2.4.12}$$

$$\Rightarrow \quad l_0 = l_0(\boldsymbol{x}_f, \boldsymbol{v}_f, \rho_f, t) = \frac{1}{2}\boldsymbol{v}_f^T \boldsymbol{v}_f - \epsilon_f(\rho_f) - \phi_f^g(\boldsymbol{x}_f)\,, \tag{2.4.13}$$

where $\frac{1}{2}\rho_f \boldsymbol{v}_f^T \boldsymbol{v}_f$ is the kinetic energy density, $\rho_f \epsilon_f(\rho_f)$ is the potential energy density with $\epsilon_f(\rho_f)$ being the specific internal energy of the fluid and $\phi_f^g(\boldsymbol{x}_f)$ is a given gravitational potential, which depends on the position in such a way that:

$$\hat{\boldsymbol{b}}_f = -\nabla \phi_f^g = -\frac{\phi_f^g}{\partial \boldsymbol{x}_f}\,, \tag{2.4.14}$$

where $\hat{\boldsymbol{b}}_f$ is the external body force per unit mass caused for example by gravitation. The Hamiltonian density H_0 as well as the specific Hamiltonian h_0 can therefore be obtained as:

$$H_0 = H_0(\boldsymbol{x}_f, \boldsymbol{v}_f, \rho_f, t) = \frac{1}{2}\rho_f \boldsymbol{v}_f^T \boldsymbol{v}_f + \rho_f \epsilon_f(\rho_f) + \rho_f \phi_f^g(\boldsymbol{x}_f) \tag{2.4.15}$$

$$\Rightarrow \quad h_0 = h_0(\boldsymbol{x}_f, \boldsymbol{v}_f, \rho_f, t) = \frac{1}{2}\boldsymbol{v}_f^T \boldsymbol{v}_f + \epsilon_f(\rho_f) + \phi_f^g(\boldsymbol{x}_f)\,, \tag{2.4.16}$$

where it is easy to verify, that $\boldsymbol{p}_0 = \boldsymbol{v}_f$ holds. The action functional for an inviscid fluid can then be written as:

$$I_f(\boldsymbol{x}_f, \boldsymbol{v}_f, \rho_f, t) = \int_{t_1}^{t_2} \left[\int_{\Omega_f} \rho_f (\boldsymbol{v}_f^T \boldsymbol{v}_f - h_0)\, d\Omega_f + \int_{\Gamma_f^N} \boldsymbol{x}_f^T \hat{\boldsymbol{t}}_f\, d\Gamma_f^N \right] dt\,, \tag{2.4.17}$$

where analogue to Eq. (2.3.1) the surface traction integral is added.

2.4.3.1 Momentum conservation

According to [Pal06], the first variation of the action functional, Eq. (2.4.17), results in:

$$\begin{aligned} \delta I_f = \int_{t_1}^{t_2} \Bigg\{ & \int_{\Omega_f} \delta \boldsymbol{x}_f^T \left[-\frac{d}{dt}(\rho_f \boldsymbol{p}_0) - \rho_f \boldsymbol{p}_0\, \nabla^T \boldsymbol{v}_f - \rho_f \frac{\partial h_0}{\partial \boldsymbol{x}_f} - \nabla \left(\rho_f^2 \frac{\partial h_0}{\partial \rho_f} \right) \right] d\Omega_f \\ & + \int_{\Gamma_f^N} \delta \boldsymbol{x}_f^T \left[\hat{\boldsymbol{t}}_f - \left(\rho_f^2 \frac{\partial h_0}{\partial \rho_f} \right) \boldsymbol{n} \right] d\Gamma_f^N \Bigg\} dt = 0\,, \end{aligned} \tag{2.4.18}$$

where $\boldsymbol{n}$ is the outward normal vector. This equation is only valid, if the volume and the surface integral vanishes. With the pressure definition for a perfect fluid:

$$p_f = -\frac{\partial \epsilon_f}{\partial (1/\rho_f)} = \rho_f^2 \frac{\partial \epsilon_f}{\partial \rho_f} \tag{2.4.19}$$

and with the given specific Hamiltonian of Eq. (2.4.16), the equation of momentum conservation in the Eulerian frame of reference for an inviscid fluid is obtained from the integrand of the volume integral as:

$$\frac{\partial (\rho_f \boldsymbol{v}_f)}{\partial t} + [\nabla^T (\rho_f \boldsymbol{v}_f \boldsymbol{v}_f^T)]^T = -\nabla p_f + \rho_f \hat{\boldsymbol{b}}_f \,, \tag{2.4.20}$$

where the definition of the Eq. (2.4.14), the product rule Eq. (2.4.6) and the definition of the Eq. (2.1.1) are used. The Neumann boundary conditions are obtained directly from the surface integral as:

$$\hat{\boldsymbol{t}}_f - \left(\rho_f^2 \frac{\partial h_0}{\partial \rho_f} \right) \boldsymbol{n} = \boldsymbol{0} \quad \Rightarrow \quad \hat{\boldsymbol{t}}_f = p_f \boldsymbol{n} \quad \text{on} \quad \Gamma_f^N \,. \tag{2.4.21}$$

Further, the initial condition for the velocity field needs to be prescribed:

$$\boldsymbol{v}_f(\boldsymbol{x}_f, t = 0) = \hat{\boldsymbol{v}}_f^0(\boldsymbol{x}_f) \tag{2.4.22}$$

as well as the boundary conditions for inviscid fluid flow on the Dirichlet boundary subset Γ_f^D:

$$\boldsymbol{v}_f = \hat{\boldsymbol{v}}_f \quad \text{on} \quad \Gamma_f^D \,, \tag{2.4.23}$$

including the slip boundary condition on walls:

$$\boldsymbol{v}_f^T \boldsymbol{n} = \hat{\boldsymbol{v}}_f^T \boldsymbol{n} \quad \text{on} \quad \Gamma_f^D \,, \tag{2.4.24}$$

where $\Gamma_f^D \cap \Gamma_f^N = \emptyset$ and $\Gamma_f^D \cup \Gamma_f^N = \Gamma_f$ holds.

2.4.3.2 Energy conservation

The equation of energy conservation is, like the equation of mass conservation, automatically fulfilled by the action functional. According to [Pal06], the energy equation is obtained from the specific Hamiltonian by generating its total derivative with respect to the time, dh_0/dt, which leads to:

$$\frac{dH_0}{dt} + H_0 \, \nabla^T \boldsymbol{v}_f + \nabla^T \left(\rho_f^2 \frac{\partial h_0}{\partial \rho_f} \boldsymbol{v}_f \right) = 0 \,. \tag{2.4.25}$$

With the Hamiltonian density and specific Hamiltonian of the inviscid fluid provided by Eq. (2.4.15) and Eq. (2.4.16), the equation of energy conservation can be obtained as:

$$\frac{\partial}{\partial t} \left(\frac{1}{2} \rho_f \boldsymbol{v}_f^T \boldsymbol{v}_f + \rho_f \epsilon_f \right) + \nabla^T \left[\left(\frac{1}{2} \rho_f \boldsymbol{v}_f^T \boldsymbol{v}_f + \rho_f \epsilon_f + \rho_f \phi_f^g \right) \boldsymbol{v}_f \right] + \nabla^T (p_f \boldsymbol{v}_f) = 0 \,, \tag{2.4.26}$$

where the definition of the fluid pressure, Eq. (2.4.19), and of the substantial derivative, Eq. (2.1.1), as well as the product rule, Eq. (2.4.6), are utilized. Introducing the specific total energy:

$$e_f = \epsilon_f + \tfrac{1}{2} \boldsymbol{v}_f^T \boldsymbol{v}_f \,, \tag{2.4.27}$$

the equation of energy conservation for an inviscid fluid in a Eulerian frame of reference can be rewritten as:

$$\frac{\partial (\rho_f e_f)}{\partial t} + \nabla^T (\rho_f e_f \boldsymbol{v}_f) = -\nabla^T (p_f \boldsymbol{v}_f) + \rho_f \hat{\boldsymbol{b}}_f^T \boldsymbol{v}_f \,. \tag{2.4.28}$$

2.4.3.3 Closure of the conservation equations

To summarize, the only fluid governing equation obtained directly by a variational principle is the equation of momentum conservation, Eq. (2.4.20), together with the Neumann boundary conditions. The equation of mass and energy conservation, Eq. (2.4.7) and Eq. (2.4.28), are derived from conditions, which are valid for the general form of the action functional. These conditions can be seen as constraints for the equation of momentum conservation, which has to be considered when solving it. In order to close the set of equations, the equation of state for a perfect fluid:

$$p_f = \rho_f R T_f \tag{2.4.29}$$

and the thermodynamic relation:

$$\epsilon_f = c_v T_f \tag{2.4.30}$$

are additionally needed as well as proper boundary conditions for the density and temperature:

$$\rho_f = \hat{\rho}_f \quad \text{on} \quad \Gamma_f^{\rho} \qquad \text{and} \qquad T_f = \hat{T}_f \quad \text{on} \quad \Gamma_f^{T}\,, \tag{2.4.31}$$

where R and c_v are the specific gas constant and the specific heat at constant volume, respectively. Further, initial conditions for equation of mass and energy conservation need to be applied:

$$\rho_f(\boldsymbol{x}_f, t=0) = \hat{\rho}_f^0(\boldsymbol{x}_f) \quad \text{and} \quad e_f(\boldsymbol{x}_f, t=0) = \hat{e}_f^0(\boldsymbol{x}_f)\,. \tag{2.4.32}$$

2.4.4 Viscous fluid

To describe the viscous fluid by Hamiltonian fluid dynamics, the dissipative processes need to be taken into account. Two sources of dissipative processes arise in viscous fluids. The first is viscosity due to internal friction of fluid particles and the second is the thermal conductivity due to temperature gradients within the fluid.

The equations of momentum and energy conservation for a viscous fluid are obtained in the same way from a Hamiltonian density and the corresponding action integral as for the inviscid fluid. The difference to the inviscid fluid consists in the specific internal energy ϵ_f, which for the viscous fluid flow depends on the deviatoric strain rate $\dot{\boldsymbol{\varepsilon}}_f = [\dot{\varepsilon}_{11}, \dot{\varepsilon}_{22}, \dot{\varepsilon}_{33}, 2\dot{\varepsilon}_{12}, 2\dot{\varepsilon}_{23}, 2\dot{\varepsilon}_{31}]_f^T$ according to Eq. (2.3.4) given by:

$$\dot{\boldsymbol{\varepsilon}}_f = \mathcal{D}\boldsymbol{v}_f\,, \tag{2.4.33}$$

where $\mathcal{D}$ is given in Eq. (2.3.3). Further and related to Eq. (2.3.2), the Cauchy stress in a viscous fluid is obtained by:

$$\boldsymbol{\sigma}_f = \frac{\partial \epsilon_f(\dot{\boldsymbol{\varepsilon}}_f)}{\partial \dot{\boldsymbol{\varepsilon}}_f}\,, \tag{2.4.34}$$

which can then be decomposed into a hydrostatic and a viscous part:

$$\boldsymbol{\sigma}_f = -(p_f + C_f)\boldsymbol{m} + \boldsymbol{\tau}_f\,, \tag{2.4.35}$$

where $C_f = C_f(T_f)$ is a temperature depended function, $\boldsymbol{\tau}_f = [\tau_{11}, \tau_{22}, \tau_{33}, \tau_{12}, \tau_{23}, \tau_{31}]_f^T$ is the viscous stress vector and $\boldsymbol{m}^T = [1,1,1,0,0,0]$ gives the functionality of the Kronecker delta to the stress vector. For a linear, isotropic (Newtonian) fluid, the entries of the viscous stress vector can be written as:

$$\tau_{ij} = 2\mu_f\left(\dot{\varepsilon}_{ij} - \frac{1}{3}\delta_{ij}\dot{\varepsilon}_{kk}\right) = \mu_f\left[\left(\frac{\partial v_i}{\partial x_j} + \frac{\partial v_j}{\partial x_i}\right) - \frac{2}{3}\delta_{ij}\frac{\partial v_k}{\partial x_k}\right]\,, \tag{2.4.36}$$

where μ_f is the dynamic viscosity of the fluid and δ_{ij} is the Kronecker delta ($\delta_{ij} = 1$ if $i = j$ and $\delta_{ij} = 0$ otherwise). In vector notation this can be rewritten as:

$$\boldsymbol{\tau}_f = \mu_f \left(\boldsymbol{I}_0 - \frac{2}{3} \boldsymbol{m}\boldsymbol{m}^T \right) \dot{\boldsymbol{\varepsilon}}_f = \mu_f \left(\boldsymbol{I}_0 - \frac{2}{3} \boldsymbol{m}\boldsymbol{m}^T \right) \mathcal{D}\boldsymbol{v}_f \,, \tag{2.4.37}$$

with $\boldsymbol{I}_0$ being a diagonal matrix:

$$\boldsymbol{I}_0 = \begin{bmatrix} 2 & 0 & 0 & 0 & 0 & 0 \\ 0 & 2 & 0 & 0 & 0 & 0 \\ 0 & 0 & 2 & 0 & 0 & 0 \\ 0 & 0 & 0 & 1 & 0 & 0 \\ 0 & 0 & 0 & 0 & 1 & 0 \\ 0 & 0 & 0 & 0 & 0 & 1 \end{bmatrix} . \tag{2.4.38}$$

Now, the Hamiltonian density H_0 and the specific Hamiltonian h_0 can be expressed similarly to Eq. (2.4.15) and Eq. (2.4.16) as:

$$H_0 = H_0(\boldsymbol{x}_f, \boldsymbol{v}_f, \dot{\boldsymbol{\varepsilon}}_f, t) = \frac{1}{2} \rho_f \boldsymbol{v}_f^T \boldsymbol{v}_f + \rho_f \epsilon_f(\dot{\boldsymbol{\varepsilon}}_f) + \rho_f \phi_f^g(\boldsymbol{x}_f) \tag{2.4.39}$$

$$\Rightarrow \quad h_0 = h_0(\boldsymbol{x}_f, \boldsymbol{v}_f, \dot{\boldsymbol{\varepsilon}}_f, t) = \frac{1}{2} \boldsymbol{v}_f^T \boldsymbol{v}_f + \epsilon_f(\dot{\boldsymbol{\varepsilon}}_f) + \phi_f^g(\boldsymbol{x}_f) \,. \tag{2.4.40}$$

The action functional is similar to functional for the inviscid fluid given in Eq. (2.4.17), but has a different dependency:

$$I_f(\boldsymbol{x}_f, \boldsymbol{v}_f, \dot{\boldsymbol{\varepsilon}}_f, t) = \int_{t_1}^{t_2} \left[\int_{\Omega_f} \rho_f (\boldsymbol{v}_f^T \boldsymbol{v}_f - h_0) \, d\Omega_f + \int_{\Gamma_f^N} \boldsymbol{x}_f^T \hat{\boldsymbol{t}}_f \, d\Gamma_f^N \right] dt \,. \tag{2.4.41}$$

2.4.4.1 Momentum conservation

Related to Eq. (2.4.18), the first variation of the action functional can be derived as, see [Pal06]:

$$\begin{aligned} \delta I_f = \int_{t_1}^{t_2} \Bigg\{ & \int_{\Omega_f} \delta \boldsymbol{x}_f^T \left[-\frac{d}{dt}(\rho_f \boldsymbol{p}_0) - \rho_f \boldsymbol{p}_0 \, \nabla^T \boldsymbol{v}_f - \rho_f \frac{\partial h_0}{\partial \boldsymbol{x}_f} + \mathcal{D}^T \left(\frac{\partial h_0}{\partial \dot{\boldsymbol{\varepsilon}}_f} \right) \right] d\Omega_f \\ & + \int_{\Gamma_f^N} \delta \boldsymbol{x}_f^T \left[\hat{\boldsymbol{t}}_f - \boldsymbol{\Upsilon}^T \left(\frac{\partial h_0}{\partial \dot{\boldsymbol{\varepsilon}}_f} \right) \right] d\Gamma_f^N \Bigg\} dt = 0 \,, \end{aligned} \tag{2.4.42}$$

where again $\boldsymbol{p}_0 = \boldsymbol{v}_f$ holds and $\boldsymbol{\Upsilon}$ is given in Eq. (2.3.9).

This variation is only valid, if both integrals vanish and with the given Hamiltonian density the following equation of momentum conservation in the Eulerian frame of reference is obtained from the integrand of the first space-time integral:

$$\frac{\partial (\rho_f \boldsymbol{v}_f)}{\partial t} + [\nabla^T (\rho_f \boldsymbol{v}_f \boldsymbol{v}_f^T)]^T = -\nabla p_f + \mathcal{D}^T \boldsymbol{\tau}_f + \rho_f \hat{\boldsymbol{b}}_f \,, \tag{2.4.43}$$

where the product rule Eq. (2.4.6) and the definition of the Eq. (2.1.1) as well as the constitutive relation Eq. (2.4.34) and the decomposition of the stress in Eq. (2.4.35) are used. From the integrand of the surface integral the Neumann boundary conditions are obtained as:

$$\hat{\boldsymbol{t}}_f - \boldsymbol{\Upsilon}^T \left(\frac{\partial h_0}{\partial \dot{\boldsymbol{\varepsilon}}_f} \right) = \boldsymbol{0} \quad \Rightarrow \quad \hat{\boldsymbol{t}}_f = \boldsymbol{\Upsilon}^T \boldsymbol{\sigma}_f \quad \text{on} \quad \Gamma_f^N \,. \tag{2.4.44}$$

The initial conditions:

$$\boldsymbol{v}_f(\boldsymbol{x}_f, t = 0) = \hat{\boldsymbol{v}}_f^0(\boldsymbol{x}_f) \tag{2.4.45}$$

as well as the velocity boundary conditions for viscous fluid flow:

$$\boldsymbol{v}_f = \hat{\boldsymbol{v}}_f \quad \text{on} \quad \Gamma_f^D\,, \tag{2.4.46}$$

where again $\Gamma_f^D \cap \Gamma_f^N = \emptyset$ and $\Gamma_f^D \cup \Gamma_f^N = \Gamma_f$ holds, are further required to apply. Eq. (2.4.46) incorporates the no-slip condition on viscous walls, where the normal and tangential velocity components are set to zero. Other velocity boundary conditions could be the symmetry condition, which is similar to the slip boundary condition of Eq. (2.4.24).

2.4.4.2 Energy conservation

As for the case of the inviscid fluid, the third conservation equation, the equation of energy conservation, can similarly be obtained by generating the total derivative of the specific Hamiltonian with respect to the time, i.e. dh_0/dt, and thus:

$$\frac{dH_0}{dt} + H_0\,\nabla^T \boldsymbol{v}_f - \nabla^T \left(\boldsymbol{Q}_f^T \frac{\partial h_0}{\partial \dot{\boldsymbol{\varepsilon}}_f} \right) = 0\,, \tag{2.4.47}$$

where $\boldsymbol{Q}_f$ is a 6x3 matrix, which has the same structure as $\mathcal{D}$ or Υ but contains the fluid velocities as:

$$\boldsymbol{Q}_f^T = \begin{bmatrix} v_1 & 0 & 0 & v_2 & 0 & v_3 \\ 0 & v_2 & 0 & v_1 & v_3 & 0 \\ 0 & 0 & v_3 & 0 & v_2 & v_1 \end{bmatrix}_f . \tag{2.4.48}$$

Thus, with the given Hamiltonian density and with the constitutive relation Eq. (2.4.34), the equation of energy conservation is obtained as:

$$\frac{\partial}{\partial t}\left(\frac{1}{2}\rho_f \boldsymbol{v}_f^T \boldsymbol{v}_f + \rho_f \epsilon_f \right) + \nabla^T \left[\left(\frac{1}{2}\rho_f \boldsymbol{v}_f^T \boldsymbol{v}_f + \rho_f \epsilon_f + \rho_f \phi_f^g \right) \boldsymbol{v}_f \right] - \nabla^T (\boldsymbol{Q}_f^T \boldsymbol{\sigma}_f) = 0\,, \tag{2.4.49}$$

where again the definition of the substantial derivative, Eq. (2.1.1), and the product rule Eq. (2.4.6) are used. With $e_f = \epsilon_f + \frac{1}{2}\boldsymbol{v}_f^T \boldsymbol{v}_f$ and Eq. (2.4.35) and Eq. (2.4.14), this can be rewritten as:

$$\frac{\partial(\rho_f e_f)}{\partial t} + \nabla^T(\rho_f e_f \boldsymbol{v}_f) = \nabla^T(\kappa_f \nabla T_f) + \nabla^T(\boldsymbol{Q}_f^T \boldsymbol{\tau}_f) - \nabla^T(p_f \boldsymbol{v}_f) + \rho_f \hat{\boldsymbol{b}}_f^T \boldsymbol{v}_f\,, \tag{2.4.50}$$

where the heat flux $\boldsymbol{q}_f$ was introduced by (see [Pal06]):

$$\boldsymbol{q}_f = C_f \boldsymbol{v}_f = -\kappa_f \nabla T_f\,, \tag{2.4.51}$$

with κ_f being the thermal conductivity of the fluid and the relation $\boldsymbol{q}_f = -\kappa_f \nabla T_f$ known as Fouriers's law.

2.4.4.3 Closure of the conservation equations

With the equation of mass conservation, Eq. (2.4.7), the equation of momentum and energy conservation, Eq. (2.4.43) and Eq. (2.4.50), the three governing equations describing a viscous fluid in a Eulerian frame of reference are found, where the only equation derived from a variational formalism is, like for the structural domain, the momentum equation. As also stated for the inviscid fluid, the mass and energy conservation can be viewed as constraint conditions to the momentum equation, which arise due to the general form of the action functional. Furthermore, this set of

equations needs to be closed by the equation of state, Eq. (2.4.29), and the thermodynamic relation, Eq. (2.4.30), as well as boundary conditions for ρ_f and T_f, Eq. (2.4.31), and the initial condition Eq. (2.4.32). Finally, the values for viscosity, μ_f, and the thermal conductivity, κ_f, are a function of the temperature. For air, these values are provided by Sutherland's relation through, [Ian06]:

$$\frac{\mu}{\mu_0} = \left(\frac{T}{T_0}\right)^{\frac{3}{2}} \frac{T_0 + S_\mu}{T + S_\mu} \quad \text{and} \quad \frac{\kappa}{\kappa_0} = \left(\frac{T}{T_0}\right)^{\frac{3}{2}} \frac{T_0 + S_k}{T + S_k} \tag{2.4.52}$$
$$T_0 = 273.15\,\mathrm{K}, \quad \mu_0 = 1.7161 \cdot 10^{-5}\,\frac{\mathrm{kg}}{\mathrm{m\,s}}, \quad \kappa_0 = 2.3360 \cdot 10^{-2}\,\frac{\mathrm{J}}{\mathrm{m\,s\,K}},$$
$$S_\mu = 110.4\,\mathrm{K}, \quad S_\kappa = 112.0\,\mathrm{K},$$

where S is called Sutherland temperature, which is slightly different for the viscosity and conductivity expression. This relation remains valid for $T < 2000\,\mathrm{K}$.

2.4.5 Conservation equation in the ALE frame of reference

In the previous two subsections, the governing equations for an inviscid as well as for a viscous fluid are derived from Hamilton's principle. As Hamilton's principle is based on an energy expression, the variational principle is in general invariant in terms of the frame of reference. Therefore, the governing equations in the ALE frame of reference are obtained by consequently substituting Eq. (2.1.1) through Eq. (2.1.2). This ALE version of the governing equations is needed due to the deforming fluid domain in the context of fluid-structure interaction.

With the fundamental ALE equation (2.1.2), the equation of mass conservation, Eq. (2.4.5), can be rewritten in the ALE frame of reference as:

$$\frac{\partial \rho_f}{\partial t} + (\boldsymbol{v}_f^T - \boldsymbol{w}_f^T)\nabla\rho_f + \rho_f \nabla^T \boldsymbol{v}_f = 0 \tag{2.4.53}$$
$$\text{or} \quad \frac{\partial \rho_f}{\partial t} + \nabla^T(\rho_f \boldsymbol{v}_f) - \boldsymbol{w}_f^T \nabla\rho_f = 0\,, \tag{2.4.54}$$

where:

$$\left.\frac{\partial f}{\partial t}\right|_\chi = \frac{\partial f}{\partial t} \tag{2.4.55}$$

is used as an abbreviation.

From the first variation of the action functional for a viscous fluid, Eq. (2.4.42), the equation of momentum conservation is obtained by using Eq. (2.1.2) as:

$$\frac{\partial(\rho_f \boldsymbol{v}_f)}{\partial t} + [(\boldsymbol{v}_f^T - \boldsymbol{w}_f^T)\nabla(\rho_f \boldsymbol{v}_f^T)]^T + \rho_f \boldsymbol{v}_f \nabla^T \boldsymbol{v}_f = -\nabla p_f + \mathcal{D}^T \boldsymbol{\tau}_f + \rho_f \hat{\boldsymbol{b}}_f \tag{2.4.56}$$
$$\text{or} \quad \frac{\partial(\rho_f \boldsymbol{v}_f)}{\partial t} + [\nabla^T(\rho_f \boldsymbol{v}_f \boldsymbol{v}_f^T)]^T - [\boldsymbol{w}_f^T \nabla(\rho_f \boldsymbol{v}_f^T)]^T = -\nabla p_f + \mathcal{D}^T \boldsymbol{\tau}_f + \rho_f \hat{\boldsymbol{b}}_f\,. \tag{2.4.57}$$

Finally, the equation of energy conservation in the ALE frame is derived from Eq. (2.4.47) by again using Eq. (2.1.2) as:

$$\begin{aligned} &\frac{\partial(\rho_f e_f)}{\partial t} + (\boldsymbol{v}_f^T - \boldsymbol{w}_f^T)\nabla(\rho_f e_f) + \rho_f e_f \nabla^T \boldsymbol{v}_f = \\ &\qquad \nabla^T(\kappa_f \nabla T_f) + \nabla^T(\boldsymbol{Q}_f^T \boldsymbol{\tau}_f) - \nabla^T(p_f \boldsymbol{v}_f) + \rho_f \hat{\boldsymbol{b}}_f^T \boldsymbol{v}_f \end{aligned} \tag{2.4.58}$$
$$\begin{aligned} \text{or} \quad &\frac{\partial(\rho_f e_f)}{\partial t} + \nabla^T(\rho_f e_f \boldsymbol{v}_f) - \boldsymbol{w}_f^T \nabla(\rho_f e_f) = \\ &\qquad \nabla^T(\kappa_f \nabla T_f) + \nabla^T(\boldsymbol{Q}_f^T \boldsymbol{\tau}_f) - \nabla^T(p_f \boldsymbol{v}_f) + \rho_f \hat{\boldsymbol{b}}_f^T \boldsymbol{v}_f\,. \end{aligned} \tag{2.4.59}$$

This ALE-form of the conservation equations is the same as derived in [DGH82]. Comparing these equations with Eq. (2.4.7), (2.4.43) and (2.4.50), obviously, an additional advection term $-\boldsymbol{w}_f^T \nabla(\rho_f f)$ is added to the governing equations in the Eulerian frame of reference, where f is either 1, $\boldsymbol{v}_f$ or e_f for Eq. (2.4.54), (2.4.57) and (2.4.59), respectively.

The velocity $\boldsymbol{w}_f$ needs to be calculated, which is provided by Eq. (2.1.3) or otherwise expressed as:

$$\boldsymbol{w}_f = \left.\frac{\partial \boldsymbol{u}_f}{\partial t}\right|_{\chi} , \tag{2.4.60}$$

where the displacement $\boldsymbol{u}_f$ of the fluid domain is introduced. Then clearly, the Hamiltonian density H_0 or the specific Hamiltonian h_0 can be expressed as:

$$H_0 = H_0(\boldsymbol{u}_f, \boldsymbol{v}_f, \dot{\boldsymbol{\varepsilon}}_f, t) = \frac{1}{2}\rho_f \boldsymbol{v}_f^T \boldsymbol{v}_f + \rho_f \epsilon_f(\dot{\boldsymbol{\varepsilon}}_f) + \rho_f \phi_f^g(\boldsymbol{u}_f) \tag{2.4.61}$$

$$\Rightarrow \quad h_0 = h_0(\boldsymbol{u}_f, \boldsymbol{v}_f, \dot{\boldsymbol{\varepsilon}}_f, t) = \frac{1}{2}\boldsymbol{v}_f^T \boldsymbol{v}_f + \epsilon_f(\dot{\boldsymbol{\varepsilon}}_f) + \phi_f^g(\boldsymbol{u}_f) , \tag{2.4.62}$$

without changing the results. It follows, that the action functional for a viscous fluid in the ALE frame of reference is:

$$I_f = I_f(\boldsymbol{u}_f, \boldsymbol{v}_f, \dot{\boldsymbol{\varepsilon}}_f, t) . \tag{2.4.63}$$

Again, the set of equations needs to be closed by the equation of state, Eq. (2.4.29), the thermodynamic relation, Eq. (2.4.30) and Sutherland's law, Eq. (2.4.52). Furthermore, boundary conditions for the velocity $\boldsymbol{v}_f$, Eq. (2.4.46), for the boundary stress $\hat{\boldsymbol{t}}_f$, Eq. (2.4.44), and for the density ρ_f and temperature T_f, Eq. (2.4.31) need to be applied. The initial conditions for the basic unknowns, ρ_f, $\boldsymbol{v}_f$, e_f are required as already provided by Eq. (2.4.45) and (2.4.32).

2.4.6 Geometric conservation law

The usage of the ALE form of the governing equations instead of the conservation equations in the Eulerian frame of reference should not influence the exact solution of the fluid flow. The minimum requirement for the calculation of the flow field on moving domains is that a uniform flow should be preserved. This requirement was first pointed out by Thomas and Lombard in [TL79] and leads to the so-called geometric conservation law (GCL), which can be seen as a further constraint equation to the governing flow equations linking the position and the velocity of the ALE frame of reference together. Considerable research was conducted by Farhat et al. in [FLM95] or LeTallec and Mani in [LM99] in this field, who has shown the importance of the GCL for the accuracy and stability of the flow field on moving meshes. The GCL in continuum space can be written as, [LM99]:

$$\nabla^T \boldsymbol{w}_f = \frac{1}{J_{x\chi}} \frac{\partial J_{x\chi}}{\partial t} \quad \text{with} \quad J_{x\chi} = \det\left[\frac{\partial \boldsymbol{x}}{\partial \boldsymbol{\chi}}\right] , \tag{2.4.64}$$

which has to be discretized in time leading to the discrete geometric conservation law (DGCL).

2.5 A weak formulation for fluid-structure interaction

In the previous subsections, it was shown, that a variational principle based on Hamilton's principle for a single fluid and a single structural system exist. The first variation of the action functionals results in the equation of momentum conservation for a single structural system, Eq. (2.3.10), and in the equation of momentum conservation for a single fluid system, Eq. (2.4.43) or Eq. (2.4.57), as well as their Neumann boundary conditions. These momentum equations are completed by

various additional conditions, e.g. constitutive equations for both - the fluid and the structure - or equations of mass and energy conservation in the case of the fluid system.

With the existence of a variational principle for a fluid as well as for a structural problem, it is now possible to express a coupled system involving FSI by an action functional and to derive the governing equations by its first variation. Here, only surface coupled problems should be considered, where the system's domains share a common boundary - the interface. Describing a coupled problem via an action functional can then be done by defining constraints for the common boundary of the systems to be coupled. In general, a functional to be minimized:

$$I(\,t, \boldsymbol{r}(t)\,) = \int_{t_1}^{t_2} L(\,t, \boldsymbol{r}(t), \dot{\boldsymbol{r}}(t)\,)\,dt \quad \rightarrow \quad \text{minimize} \tag{2.2.1}$$

and subject to the following constraint:

$$\Lambda(\,\boldsymbol{r}(t)\,) = 0 \tag{2.5.1}$$

can be treated by the Lagrange multiplier method, see [Red02], which results in a modified functional:

$$I_\Lambda(\,t, \boldsymbol{r}(t), \lambda\,) = \int_{t_1}^{t_2} (L + \lambda\Lambda)\,dt \quad \rightarrow \quad \text{minimize}\,, \tag{2.5.2}$$

where the so-called Lagrange multiplier λ is introduced. The Lagrange multiplier is initially an arbitrary parameter, which weights the constraint, Eq. (2.5.1), so that the first variation of the functional I_Λ with respect to the Lagrange multiplier leads to this constraint equation. Having multiple constraints:

$$\boldsymbol{\Lambda}(\,\boldsymbol{r}(t)\,) = \boldsymbol{0}\,, \tag{2.5.3}$$

the modified functional can be rewritten as:

$$I_\Lambda(\,t, \boldsymbol{r}(t), \boldsymbol{\lambda}\,) = \int_{t_1}^{t_2} (L + \boldsymbol{\lambda}^T\boldsymbol{\Lambda})\,dt \quad \rightarrow \quad \text{minimize}\,, \tag{2.5.4}$$

where $\boldsymbol{\lambda}$ is the vector of Lagrange multipliers.

In the following subsection, two different approaches will be introduced, which use the equality of system's variables on the interface. In the case of fluid-structure interaction, obviously, the constraint condition is, that the displacements along the interface are equal, that is to say:

$$\boldsymbol{u}_f = \boldsymbol{u}_s \quad \text{or} \quad \boldsymbol{u}_f - \boldsymbol{u}_s = \boldsymbol{0} \quad \text{on} \quad \Gamma_{fs}\,. \tag{2.5.5}$$

It should be taken into account here, that some formulations in the field of FSI use the equality of fluid and structural velocities at the interface. Clearly, the equation above is equivalent to this statement. Moreover, the equality of the displacements at the interface also ensures the geometry to be consistent at the interface, which is not given *per se* when stipulating the equality of the displacement's first temporal derivative. Further, for an inviscid fluid, only the equality of fluid and structural velocities along the normal to the interface, $\boldsymbol{v}_f^T\boldsymbol{n} = \boldsymbol{v}_s^T\boldsymbol{n}$, is required from the fluid equation point of view, which also leaves the geometric consistency out of consideration. Therefore, the equality of the fluid and structural interface displacements, Eq. (2.5.5), is used throughout this thesis, which also ensures the equality of fluid and structural interface velocities. It is then the matter of the fluid formulation to use the appropriate boundary conditions on the interface, i.e. the slip for inviscid fluids or the no-slip boundary condition for a viscous fluid.

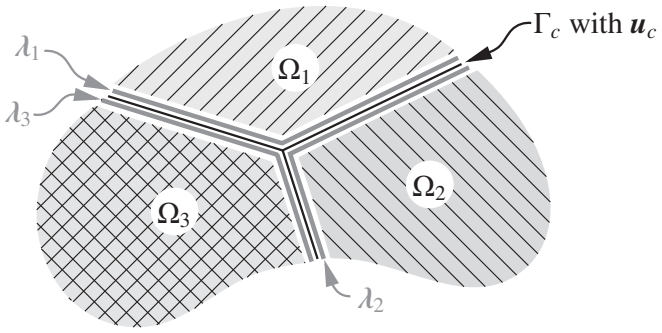

Figure 2.2: Three-field approach of a continuum system

2.5.1 Three-field approach

For the action functional of the three-field approach, an additional connectivity frame is used to which each physical field is connected only. Thus, there exists no direct connection of the fields but the they are indirectly coupled with the aid of the frame. Thereby the name *three-field* is derived from the minimal case, where a fluid field is coupled with a structural field via a connectivity frame field, i.e. the three fields - structure, fluid and frame - need to be considered. The action functional of the whole coupled system can then be divided into an interior and connectivity functional for each participating system or more precisely for each participating subdomain:

$$I_{\Lambda 3} = \sum_{i=1}^{N_d} (I_i - I_{ci}) \,, \tag{2.5.6}$$

where I_i is the action functional of a single fluid or structure, I_f or I_s and I_{ci} denotes the appropriate connectivity functional to the connectivity frame, Figure 2.2. The sum in Eq. (2.5.6) runs from 1 to the number of all subdomains N_d. The connectivity functional for each subdomain is expressed as:

$$I_{ci} = \int_{t_1}^{t_2} \int_{\Gamma_{ci}} \boldsymbol{\lambda}_i^T (\boldsymbol{u}_c - \boldsymbol{u}_i) \, d\Gamma_{ci} \, dt \,, \tag{2.5.7}$$

where $\boldsymbol{u}_c$ is the displacement of the frame. For each set of I_i and I_{ci} a Lagrange multiplier field $\boldsymbol{\lambda}_i$ is defined on Γ_{ci}, which means according to [PF00], that $\boldsymbol{\lambda}_i$ is localized to each I_i, Figure 2.2. Thus, each subdomain is associated with one appropriate Lagrange multiplier field to connect the displacements to the frame. The sum of the interfaces Γ_{ci} forms the complete connectivity frame:

$$\Gamma_c = \Gamma_{c1} \cup \Gamma_{c2} \cup \ldots \cup \Gamma_{ci} = \bigcup_{i=1}^{N_d} \Gamma_{ci} \,. \tag{2.5.8}$$

From Eq. (2.3.1) or Eq. (2.4.17), it can be discovered, that the Lagrange multiplier has the same physical meaning as $\boldsymbol{t}_s$ or $\boldsymbol{t}_f$. Thus, the Lagrange multiplier acts as a force flux gluing the subdomain and the connectivity frame together.

The variation of the three-field action functional, Eq. (2.5.6), related to the unknowns yields:

$$\begin{aligned}\delta I_{\Lambda 3} &= \sum_{i=1}^{N_d} [\delta I_i - \delta I_{ci}] \\ &= \sum_{i=1}^{N_d} \Bigg\{ \delta I_i + \int_{t_1}^{t_2} \Bigg[\int_{\Gamma_{ci}} \boldsymbol{\lambda}_i^T \, \delta \boldsymbol{u}_i \, d\Gamma_{ci} - \int_{\Gamma_{ci}} \boldsymbol{\lambda}_i^T \, \delta \boldsymbol{u}_c \, d\Gamma_{ci} \\ &\quad - \int_{\Gamma_{ci}} \delta \boldsymbol{\lambda}_i^T \, (\boldsymbol{u}_c - \boldsymbol{u}_i) \, d\Gamma_{ci} \Bigg] dt \Bigg\} = 0 \, .\end{aligned} \tag{2.5.9}$$

The third integral is only valid, if the integrand becomes zero, which results in the interface displacements equality for each subdomain. The second integral is the contribution of the force equilibrium on the interface frame, that is to say:

$$\sum_{i=0}^{N_d} \int_{t_1}^{t_2} \int_{\Gamma_{ci}} \boldsymbol{\lambda}_i^T \, \delta \boldsymbol{u}_c \, d\Gamma_{ci} \, dt = 0 \, . \tag{2.5.10}$$

Thus, Newton's third law is represented through this term. With the first integral, the single field problem is now transformed to be:

$$\delta I_i + \int_{t_1}^{t_2} \int_{\Gamma_{ci}} \boldsymbol{\lambda}_i^T \, \delta \boldsymbol{u}_i \, d\Gamma_{ci} \, dt = 0 \, , \tag{2.5.11}$$

where the second term has to be considered within the single field problem due the variation with respect to $\boldsymbol{u}_i$. Therefore, the variation of the structural subdomain becomes with the aid of Eq. (2.3.8):

$$\begin{aligned}\delta I_s + \int_{t_1}^{t_2} \int_{\Gamma_{cs}} \boldsymbol{\lambda}_s^T \, \delta \boldsymbol{u}_s \, d\Gamma_{cs} \, dt = \int_{t_1}^{t_2} \Bigg[&\int_{\Omega_s} \delta \boldsymbol{u}_s^T \left(-\rho_s \ddot{\boldsymbol{u}}_s + \mathcal{D}^T \boldsymbol{\sigma}_s + \hat{\boldsymbol{b}}_s \right) d\Omega_s \\ &+ \int_{\Gamma_s^N} \delta \boldsymbol{u}_s^T \left(\hat{\boldsymbol{t}}_s - \boldsymbol{\Upsilon}^T \boldsymbol{\sigma}_s \right) d\Gamma_s^N \\ &+ \int_{\Gamma_{cs}} \delta \boldsymbol{u}_s^T \left(\boldsymbol{\lambda}_s - \boldsymbol{\Upsilon}^T \boldsymbol{\sigma}_s \right) d\Gamma_{cs} \Bigg] dt = 0\end{aligned} \tag{2.5.12}$$

and in the same way, the variation of the fluid subdomain is rewritten as:

$$\begin{aligned}\delta I_f + \int_{t_1}^{t_2} \int_{\Gamma_{cf}} \boldsymbol{\lambda}_f^T \delta \boldsymbol{u}_f \, d\Gamma_{cf} \, dt = \int_{t_1}^{t_2} \Bigg[&\int_{\Omega_f} \delta \boldsymbol{u}_f^T \left(-\frac{d}{dt}(\rho_f \boldsymbol{v}_f) - \rho_f \boldsymbol{v}_f \, \nabla^T \boldsymbol{v}_f + \rho_f \hat{\boldsymbol{b}}_f + \mathcal{D}^T \boldsymbol{\sigma}_f \right) d\Omega_f \\ &+ \int_{\Gamma_f^N} \delta \boldsymbol{u}_f^T \left(\hat{\boldsymbol{t}}_f - \boldsymbol{\Upsilon}^T \boldsymbol{\sigma}_f \right) d\Gamma_f^N \\ &+ \int_{\Gamma_{cf}} \delta \boldsymbol{u}_f^T \left(\boldsymbol{\lambda}_f - \boldsymbol{\Upsilon}^T \boldsymbol{\sigma}_f \right) d\Gamma_{cf} \Bigg] dt = 0 \, ,\end{aligned} \tag{2.5.13}$$

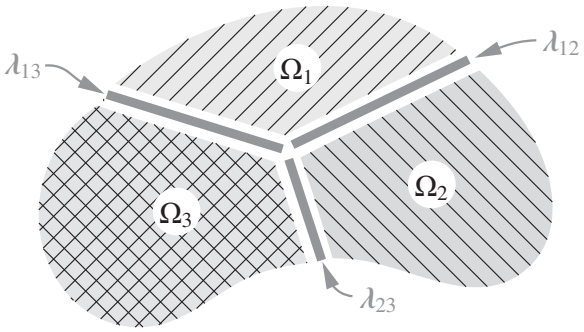

Figure 2.3: Two-field approach of a continuum system

where Eq. (2.4.42) is used with the substitution provided in section 2.4.4.

Using a partitioned coupling approach, the structure is usually treated as a Neumann problem, that is, the Lagrange multiplier $\boldsymbol{\lambda}_s$ is prescribed on the interface Γ_{cs} and transformed to internal stresses as given by the third integral on the right hand side in Eq. (2.5.12):

$$\boldsymbol{\Upsilon}^T \boldsymbol{\sigma}_s = \boldsymbol{\lambda}_s \quad \text{on} \quad \Gamma_{cs}\,, \tag{2.5.14}$$

which then gives - according to the first integral - the displacement $\boldsymbol{u}_s$ on the interface.

In contrast, the fluid is usually treated as Dirichlet problem. Thus, the displacement $\boldsymbol{u}_f$ is prescribed on the interface Γ_{cf} and the resulting Lagrange multiplier $\boldsymbol{\lambda}_f$ is obtained from the third integral in Eq. (2.5.13) as:

$$\boldsymbol{\lambda}_f = \boldsymbol{\Upsilon}^T \boldsymbol{\sigma}_f \quad \text{on} \quad \Gamma_{cf}\,. \tag{2.5.15}$$

These different points of view cause difficulties in the case of three-field approach as discussed later in this thesis. Treating the fluid as a Neumann problem can also be done, when two fluid subdomains are linked together.

2.5.2 Two-field approach

Using the two-field approach, the connectivity frame is omited and the subdomains are coupled directly via one Lagrange multiplier field for each inter-connection, Figure 2.3. The action functional of the whole coupled system is then expressed as:

$$I_{\Lambda 2} = \sum_{i=1}^{N_d} I_i - \sum_{i=1}^{N_d} \sum_{j=i+1}^{N_d} I_{ij}\,, \tag{2.5.16}$$

where I_i is again the action functional of a single fluid or structure, I_f or I_s and I_{ij} denotes the appropriate connectivity functional, which can be expressed as:

$$I_{ij} = \int_{t_1}^{t_2} \int_{\Gamma_{ij}} \boldsymbol{\lambda}_{ij}^T (\boldsymbol{u}_i - \boldsymbol{u}_j)\, d\Gamma_{ij}\, dt\,, \tag{2.5.17}$$

where Γ_{ij} is the interface between subdomain i and j. This equation also includes the case, where $\Gamma_{ij} = \emptyset$ holds and from which $I_{ij} = 0$ follows.

The variation of the action functional (2.5.16) is obtained as:

$$\delta I_{\Lambda 2} = \sum_{i=1}^{N_d} \delta I_i + \sum_{i=1}^{N_d} \sum_{j=i+1}^{N_d} \int_{t_1}^{t_2} \Bigg[\int_{\Gamma_{ij}} \boldsymbol{\lambda}_{ij}^T \delta \boldsymbol{u}_j \, d\Gamma_{ij} - \int_{\Gamma_{ij}} \boldsymbol{\lambda}_{ij}^T \delta \boldsymbol{u}_i \, d\Gamma_{ij} - \int_{\Gamma_{ij}} \delta \boldsymbol{\lambda}_{ij}^T \left(\boldsymbol{u}_i - \boldsymbol{u}_j \right) d\Gamma_{ij} \Bigg] dt = 0 \,. \tag{2.5.18}$$

Here again, the third integral under the double sum results in the interface displacement equality and the first and the second integral are the interface force flux for each interface Γ_{ij}. If the minimal case is assumed, where only a fluid subdomain (index 1) and a structural domain (index 2) are coupled via the two-field approach, Eq. (2.5.18) simplifies to:

$$\delta I = \delta I_f + \delta I_s + \int_{t_1}^{t_2} \Bigg[\int_{\Gamma_{fs}} \boldsymbol{\lambda}_{fs}^T \delta \boldsymbol{u}_s \, d\Gamma_{fs} - \int_{\Gamma_{fs}} \boldsymbol{\lambda}_{fs}^T \delta \boldsymbol{u}_f \, d\Gamma_{fs} - \int_{\Gamma_{fs}} \delta \boldsymbol{\lambda}_{fs}^T \left(\boldsymbol{u}_f - \boldsymbol{u}_s \right) d\Gamma_{fs} \Bigg] dt = 0 \,. \tag{2.5.19}$$

Similar to Eq. (2.5.12), the variation of the structural subdomain becomes:

$$\begin{aligned} \delta I_s + \int_{t_1}^{t_2} \int_{\Gamma_{fs}} \boldsymbol{\lambda}_{fs}^T \delta \boldsymbol{u}_s \, d\Gamma_{fs} \, dt = \int_{t_1}^{t_2} \Bigg[& \int_{\Omega_s} \delta \boldsymbol{u}_s^T \left(-\rho_s \ddot{\boldsymbol{u}}_s + \mathcal{D}^T \boldsymbol{\sigma}_s + \hat{\boldsymbol{b}}_s \right) d\Omega_s \\ & + \int_{\Gamma_s^N} \delta \boldsymbol{u}_s^T \left(\hat{\boldsymbol{t}}_s - \boldsymbol{\Upsilon}^T \boldsymbol{\sigma}_s \right) d\Gamma_s^N \\ & + \int_{\Gamma_{fs}} \delta \boldsymbol{u}_s^T \left(\boldsymbol{\lambda}_{fs} - \boldsymbol{\Upsilon}^T \boldsymbol{\sigma}_s \right) d\Gamma_{fs} \Bigg] dt = 0 \end{aligned} \tag{2.5.20}$$

and for the fluid subdomain it is obtained:

$$\begin{aligned} \delta I_f - \int_{t_1}^{t_2} \int_{\Gamma_{fs}} \boldsymbol{\lambda}_{fs}^T \delta \boldsymbol{u}_f \, d\Gamma_{fs} \, dt = \int_{t_1}^{t_2} \Bigg[& \int_{\Omega_f} \delta \boldsymbol{u}_f^T \left(-\frac{d}{dt}(\rho_f \boldsymbol{v}_f) - \rho_f \boldsymbol{v}_f \, \nabla^T \boldsymbol{v}_f + \rho_f \hat{\boldsymbol{b}}_f + \mathcal{D}^T \boldsymbol{\sigma}_f \right) d\Omega_f \\ & + \int_{\Gamma_f^N} \delta \boldsymbol{u}_f^T \left(\hat{\boldsymbol{t}}_f - \boldsymbol{\Upsilon}^T \boldsymbol{\sigma}_f \right) d\Gamma_f^N \\ & + \int_{\Gamma_{fs}} \delta \boldsymbol{u}_f^T \left(-\boldsymbol{\lambda}_{fs} - \boldsymbol{\Upsilon}^T \boldsymbol{\sigma}_f \right) d\Gamma_{fs} \Bigg] dt = 0 \,. \end{aligned} \tag{2.5.21}$$

The structural domain is again treated as a Neumann problem. The Lagrange multiplier $\boldsymbol{\lambda}_{fs}$ is applied on the fluid-structure interface Γ_{fs} with:

$$\boldsymbol{\Upsilon}^T \boldsymbol{\sigma}_s = \boldsymbol{\lambda}_{fs} \quad \text{on} \quad \Gamma_{fs} \tag{2.5.22}$$

to obtain the displacements $\boldsymbol{u}_s$ with the aid of the conservation of momentum, i.e. with the integrand of the first integral.

The Lagrange multiplier prescribed on the structure is obtained from the fluid with the aid of the integrand of the third integral of Eq. (2.5.21) as:

$$\boldsymbol{\lambda}_{fs} = -\boldsymbol{\Upsilon}^T \boldsymbol{\sigma}_f \quad \text{on} \quad \Gamma_{fs} \tag{2.5.23}$$

under the constraint of the interface problem obtained from the integrand of the third integral in Eq. (2.5.19):

$$\boldsymbol{u}_f = \boldsymbol{u}_s \quad \text{on} \quad \Gamma_{fs}\,. \tag{2.5.24}$$

This two-field approach is the most often used formulation for FSI problems due to the natural use of the Dirichlet-Neumann cycle here. However, by using more then two fields, e.g. fluid-fluid-structure interaction, this scheme can be challenging in conjunction with a partitioned coupling approach. For more than two connecting domains, it might be advantageous to use the three-field approach, because here each domain is only connected to the connectivity frame, i.e. there is no direct inter-domain coupling.

2.6 Chapter summary

In this chapter, the three systems of references - the Eulerian, the Lagrangian and the ALE system of reference - are introduced, which are needed to describe and distinguish the usually used physical natures of problem description. These systems of references differ basically in their expression of the substantial derivative and are essential to describe the structural and fluid subsystems with the aid of an energy principle, i.e. with Hamilton's principle. Hamilton's principle as a variational scheme is well established for pure structural systems, but some assumption are needed to apply this principle to the fluid subsystem. The three conservation laws (mass, momentum and energy conservation) of a fluid flow can be derived by Hamiltonian fluid dynamics using Hamilton's canonical form. In this chapter, both basic fluid model equations - inviscid and viscous fluid models - are employed with this weak variational energy principle.

Finally, as a unified coupling approach on continuum mechanics level, the two- and three-field approach are obtained, which use Lagrange multipliers in terms of a weak formulation to connect the fluid and structural subsystem. While the three-field approach utilizes an intermediate connectivity frame, the two-field approach connects directly the fluid and structural domain. The main advantage of the indirect three-field approach is the property, that each physical subdomain is only connected to an intermediate frame. Thus, the communication of each participating subdomain is only accomplished with that frame. Another important benefit of the three-field approach, which is used for the first time in this thesis, is the possibility of an independent and high-order discretization of the frame.

3 Characteristic Based Split Methodology for the Fluid Flow

In this chapter, the method to spatially discretize the governing fluid equations is presented. In this thesis, the finite elements method (FEM) is used, which is the third major method to solve the fluid conservation equations numerically, apart from finite difference and finite volume methods. The finite element method for fluid flow problems was established within the last twenty years, while first attempts were made by Zienkiewicz, [ZC65], Oden, [Ode72], or Chung, [CC76]. For appropriate textbooks on the introduction of the finite element method see, Hughes [Hug00], Bathe [Bat96] and the three volume set of Zienkiewicz and Taylor [ZTZ05, ZT05, ZBN05]. The third volume of the latter set of books also covers the characteristic based split scheme for fluid dynamics.

In the context of the finite element method, it is usually advisable to use the standard Galerkin form (weight functions are equal to interpolation functions) of the FEM method as a numerical method, which leads to symmetric matrices for self-adjoint problems, e.g. diffusion dominated problems. Due to the convective term - the second term on the left hand side in Eq. (2.4.54), (2.4.57), (2.4.59) - the resulting matrices from this non self-adjoint term are asymmetric, which can lead to instability, if the fluid problem to be solved is convective dominated. Therefore, the variational integral statements of the last chapter obtained from Hamilton's principle cannot be used directly, because stability schemes need to be used to suppress this instability caused by the standard Galerkin form. Several stability schemes have been proposed, including the streamline upwind Petrov Galerkin (SUPG) method [BH82], the Galerkin least square method [HFH89] or the characteristic Galerkin (CG) method [LMZ84, LPZ87]. While the SPUG method uses modified weight functions for the convective term, the CG method modifies the governing equations, whereby the temporal derivative is discretized along the problem characteristic, [LMZ84], by using the wave nature of the governing equations. The resulting equations are now self-adjoint and the standard Galerkin scheme can be applied as the optimal scheme. The characteristic based split (CBS) method is a variant of the CG method first proposed by Zienkiewicz and Codina [ZC95, ZMS$^+$95], which utilizes a local Taylor expansion to design a computational more effective scheme. A comprehensive overview of this scheme is provided by Nithiarasu in [NCZ06] and nowadays the CBS scheme is widely used to solve the compressible and incompressible fluid flows.

In the following sections, the CBS scheme is applied to the ALE version of the compressible conservation equations.

3.1 Characteristic Galerkin method

The characteristic Galerkin (CG) method forms the basis of the CBS scheme presented in the next sections. Several variants of this scheme are in existence and discussed in the context of the CBS

procedure in [NCZ06]. For the CBS method, the *simple explicit characteristic Galerkin* procedure is applied due to its simplicity, [LMZ84]. Assuming a simple one-dimensional convection diffusion equation:

$$\frac{\partial f}{\partial t} + \frac{\partial (vf)}{\partial x} - \frac{\partial}{\partial x}\left(a\frac{\partial f}{\partial x}\right) + Q = 0\,, \tag{3.1.1}$$

where f is some scalar quantity, v is the velocity, a is the diffusion coefficient and Q is the source term. The simple explicit characteristic Galerkin procedure then leads to the following form, by using a local Taylor expansion, see [NCZ06] or [ZBN05]:

$$\begin{aligned}\frac{f^{n+1}-f^n}{\Delta t} = &-\left[\frac{\partial (vf)}{\partial x} - \frac{\partial}{\partial x}\left(a\frac{\partial f}{\partial x}\right) + Q\right]^n \\ &+ \frac{\Delta t}{2} v\frac{\partial}{\partial x}\left[\frac{\partial (vf)}{\partial x} - \frac{\partial}{\partial x}\left(a\frac{\partial f}{\partial x}\right) + Q\right]^n \\ &- \frac{\Delta t^2}{6} v^2 \frac{\partial^2}{\partial x^2}\left[\frac{\partial (vf)}{\partial x} - \frac{\partial}{\partial x}\left(a\frac{\partial f}{\partial x}\right) + Q\right]^n + O(\Delta t^3)\,.\end{aligned} \tag{3.1.2}$$

Usually the higher order terms are neglected. Rewriting this equation for the case of a multidimensional velocity leads to:

$$\begin{aligned}\frac{f^{n+1}-f^n}{\Delta t} = &-\left[\nabla^T(\boldsymbol{v}f) - \nabla^T(a\nabla f) + Q\right]^n \\ &+ \frac{\Delta t}{2}(\boldsymbol{v}^T\nabla)\left[\nabla^T(\boldsymbol{v}f) - \nabla^T(a\nabla f) + Q\right]^n + O(\Delta t^2)\,.\end{aligned} \tag{3.1.3}$$

This equation is used as the basis for the discretization of the fluid dynamics equations using the standard Galerkin form of the FEM. The second term on the right hand side forms the stability part for the spatial discretization, because it acts as an extra diffusion term. It should be noted here, when using linear elements, the second term in the second square brackets leads to no contribution in the resulting matrix system and can therefore also be neglected. However, this term has to be considered for the discretization, when higher order elements are used. Before applying Eq. (3.1.3) to the basic conservation equation for fluid flows, these equations are converted to a non-dimensional form, which is often done in computational fluid dynamics.

3.2 Non-dimensional form of the conservation equations

The conservation equations in ALE form derived from Hamilton's principle are rewritten first:

$$\frac{\partial \rho_f}{\partial t} + \nabla^T(\rho_f \boldsymbol{v}_f) - \boldsymbol{w}_f^T\nabla\rho_f = 0 \tag{2.4.54}$$

$$\frac{\partial(\rho_f \boldsymbol{v}_f)}{\partial t} + [\nabla^T(\rho_f \boldsymbol{v}_f \boldsymbol{v}_f^T)]^T - [\boldsymbol{w}_f^T\nabla(\rho_f \boldsymbol{v}_f^T)]^T = -\nabla p_f + \mathcal{D}^T\boldsymbol{\tau}_f + \rho_f\hat{\boldsymbol{b}}_f \tag{2.4.57}$$

$$\begin{aligned}\frac{\partial(\rho_f e_f)}{\partial t} + \nabla^T(\rho_f e_f \boldsymbol{v}_f) - \boldsymbol{w}_f^T\nabla(\rho_f e_f) = &\nabla^T(\kappa_f\nabla T_f) + \nabla^T(\boldsymbol{Q}_f^T\boldsymbol{\tau}_f) \\ &- \nabla^T(p_f\boldsymbol{v}_f) + \rho_f\hat{\boldsymbol{b}}_f^T\boldsymbol{v}_f\end{aligned}\,. \tag{2.4.59}$$

To reduce the parameter space, these equations are non-dimensionalized, i.e. all unknown quantities are written as ratios to reference values.Different non-dimensionalization schemes are possible and here a density-velocity based form is used, i.e. the reference quantities for the density and velocity are the respective free stream values. Thus, for most of the reference quantities, the free

variable		reference value	non-dimensional value	dimensional value
length, coordinate	x_i	l	$x_i^\star = \frac{x_i}{l}$	$x_i = x_i^\star \cdot l$
velocity	v_i	v_∞	$v_i^\star = \frac{v_i}{v_\infty}$	$v_i = v_i^\star \cdot v_\infty$
frame velocity	w_i	v_∞	$w_i^\star = \frac{w_i}{v_\infty}$	$w_i = w_i^\star \cdot v_\infty$
convective velocity	s_i	v_∞	$s_i^\star = \frac{s_i}{v_\infty}$	$s_i = s_i^\star \cdot v_\infty$
speed of sound	c	v_∞	$c^\star = \frac{c}{v_\infty}$	$c = c^\star \cdot v_\infty$
density	ρ	ρ_∞	$\rho^\star = \frac{\rho}{\rho_\infty}$	$\rho = \rho^\star \cdot \rho_\infty$
time	t	$\frac{l}{v_\infty}$	$t^\star = \frac{t v_\infty}{l}$	$t = \frac{t^\star l}{v_\infty}$
pressure	p	$\rho_\infty v_\infty^2$	$p^\star = \frac{p}{\rho_\infty v_\infty^2}$	$p = p^\star \cdot \rho_\infty v_\infty^2$
total specific energy	e	v_∞^2	$e^\star = \frac{e}{v_\infty^2}$	$e = e^\star \cdot v_\infty^2$
temperature	T	$\frac{v_\infty^2}{c_p}$	$T^\star = \frac{T c_p}{v_\infty^2}$	$T = \frac{T^\star v_\infty^2}{c_p}$
heat flux	q_i	$\frac{v_\infty^3}{l}$	$q_i^\star = \frac{q_i l}{v_\infty^3}$	$q_i = \frac{q_i^\star v_\infty^3}{l}$
thermal conductivity	κ	κ_∞	$\kappa^\star = \frac{\kappa}{\kappa_\infty}$	$\kappa = \kappa^\star \cdot \kappa_\infty$
body force	b_i	$\frac{v_\infty^2}{l}$	$b_i^\star = \frac{b_i l}{v_\infty^2}$	$b_i = \frac{b_i^\star v_\infty^2}{l}$
dynamic viscosity	μ	μ_∞	$\mu^\star = \frac{\mu}{\mu_\infty}$	$\mu = \mu^\star \cdot \mu_\infty$
dynamic eddy viscosity	μ_T	μ_∞	$\mu_T^\star = \frac{\mu_T}{\mu_\infty}$	$\mu_T = \mu_T^\star \cdot \mu_\infty$
kinematic viscosity	ν	ν_∞	$\nu^\star = \frac{\nu}{\nu_\infty}$	$\nu = \nu^\star \cdot \nu_\infty$
kinematic eddy viscosity	ν_T	ν_∞	$\nu_T^\star = \frac{\nu_T}{\nu_\infty}$	$\nu_T = \nu_T^\star \cdot \nu_\infty$
modified eddy viscosity	$\breve{\nu}$	ν_∞	$\breve{\nu}^\star = \frac{\breve{\nu}}{\nu_\infty}$	$\breve{\nu} = \breve{\nu}^\star \cdot \nu_\infty$

Table 3.1: Fluid values and their references used for non-dimensionalization and re-dimensionalization

stream values can be taken, but for some the references need to be calculated from other values to provide a coherent non-dimensionalization. In Table 3.1, the references for the several fluid variables used for non-dimensionalization are listed, where the superscript $(\cdot)^\star$ denotes a non-dimensional value. Inserting the dimensional quantity of the last row into the conservation equations, the non-dimensional form of the governing equations are obtained as:

- equation of mass conservation:

$$\frac{\partial \rho_f^\star}{\partial t^\star} + \nabla_\star^T (\rho_f^\star \boldsymbol{v}_f^\star) - \boldsymbol{w}_f^{\star T} \nabla_\star \rho_f^\star = 0 \tag{3.2.1}$$

- equation of momentum conservation:

$$\frac{\partial(\rho_f^\star \boldsymbol{v}_f^\star)}{\partial t^\star} + [\nabla_\star^T(\rho_f^\star \boldsymbol{v}_f^\star \boldsymbol{v}_f^{\star T})]^T - [\boldsymbol{w}_f^{\star T} \nabla_\star(\rho_f^\star \boldsymbol{v}_f^{\star T})]^T = -\nabla_\star p_f^\star + \frac{1}{Re}\mathcal{D}^{\star T}\boldsymbol{\tau}_f^\star + \rho_f^\star \hat{\boldsymbol{b}}_f^\star \tag{3.2.2}$$

- equation of energy conservation:

$$\begin{aligned}\frac{\partial(\rho_f^\star e_f^\star)}{\partial t^\star} + \nabla_\star^T(\rho_f^\star e_f^\star \boldsymbol{v}_f^\star) - \boldsymbol{w}_f^{\star T}\nabla_\star(\rho_f^\star e_f^\star) = -\nabla_\star^T(p_f^\star \boldsymbol{v}_f^\star) + \frac{1}{Re}\nabla_\star^T(\boldsymbol{Q}_f^{\star T}\boldsymbol{\tau}_f^\star) \\ + \frac{1}{Re\,Pr}\nabla_\star^T(\kappa_f^\star \nabla_\star T_f^\star) + \rho_f^\star \hat{\boldsymbol{b}}_f^{\star T}\boldsymbol{v}_f^\star\,,\end{aligned} \tag{3.2.3}$$

where the Reynolds and Prandtl number are introduced as:

$$Re = \frac{\rho_\infty v_\infty l}{\mu_\infty} = \frac{v_\infty l}{\nu_\infty} \tag{3.2.4}$$

$$Pr = \frac{\mu_\infty c_p}{\kappa_\infty}\,, \tag{3.2.5}$$

and $\nabla_\star$ is the nabla operator in the Eulerian frame of reference using the non-dimensional coordinates. The free stream kinematic viscosity is defined as $\nu_\infty = \mu_\infty/\rho_\infty$ and c_p is the specific heat at constant pressure. The non-dimensional viscous stress vector is given by:

$$\boldsymbol{\tau}_f^\star = \mu_f^\star\left(\boldsymbol{I}_0 - \tfrac{2}{3}\boldsymbol{m}\boldsymbol{m}^T\right)\mathcal{D}^\star \boldsymbol{v}_f^\star\,, \tag{3.2.6}$$

the thermodynamic relation by:

$$\epsilon_f^\star = \frac{1}{\gamma}T_f^\star \quad \text{with} \quad \gamma = \frac{c_p}{c_v}\,, \tag{3.2.7}$$

and the equation of state by:

$$p_f^\star = \rho_f^\star R^\star T_f^\star \quad \text{with} \quad R^\star = \frac{R}{c_p} = \frac{\gamma - 1}{\gamma}\,. \tag{3.2.8}$$

With the definition of the specific total energy, Eq. (2.4.27), the non-dimensional temperature is obtained as:

$$T_f^\star = \gamma\left(e_f^\star - \frac{1}{2}\boldsymbol{v}_f^{\star T}\boldsymbol{v}_f^\star\right), \tag{3.2.9}$$

and further useful fluid values are the speed of sound:

$$c_f^\star = \sqrt{\gamma R^\star T_f^\star} = \sqrt{(\gamma - 1)T_f^\star}\,, \tag{3.2.10}$$

and the local Mach number:

$$Ma = \frac{\sqrt{\boldsymbol{v}_f^{\star T}\boldsymbol{v}_f^\star}}{c_f^\star}\,. \tag{3.2.11}$$

The above set of equations is also valid for the flow in the Eulerian frame of reference or for inviscid flows by setting the velocity of the ALE frame of reference to zero and the Reynolds number to infinity, respectively.

For the CBS scheme, it is appropriate to introduce the conservative variables $\boldsymbol{V}_f^\star = \rho_f^\star \boldsymbol{v}_f^\star$ and $E_f^\star = \rho_f^\star e_f^\star$. Further, for clarity the superscript $(\cdot)^\star$ is omitted in the following, but it should be

evident, when the dimensional or non-dimensional form of the governing equations are used. The conservation equations are then rewritten as:

$$\frac{\partial \rho_f}{\partial t} + \nabla^T \boldsymbol{V}_f - \boldsymbol{w}_f^T \nabla \rho_f = 0 \tag{3.2.12}$$

$$\frac{\partial \boldsymbol{V}_f}{\partial t} + [\nabla^T (\boldsymbol{v}_f \boldsymbol{V}_f^T)]^T - [\boldsymbol{w}_f^T \nabla \boldsymbol{V}_f^T]^T = -\nabla p_f + \frac{1}{Re} \mathcal{D}^T \boldsymbol{\tau}_f + \rho_f \hat{\boldsymbol{b}}_f \tag{3.2.13}$$

$$\begin{aligned} \frac{\partial E_f}{\partial t} + \nabla^T (\boldsymbol{v}_f E_f) - \boldsymbol{w}_f^T \nabla E_f = &-\nabla^T (p_f \boldsymbol{v}_f) + \frac{1}{Re} \nabla^T (\boldsymbol{Q}_f^T \boldsymbol{\tau}_f) \\ &+ \frac{1}{Re\, Pr} \nabla^T (\kappa_f \nabla T_f) + \rho_f \hat{\boldsymbol{b}}_f^T \boldsymbol{v}_f \,. \end{aligned} \tag{3.2.14}$$

These equations together with the proper boundary and initial conditions are the starting point for the discretization using the CBS scheme.

3.3 The CBS scheme

The CBS procedure is an application of the characteristic Galerkin method to the fluid conservation equations with a subsequent split regarding the momentum conservation equation to decouple the pressure term. Two different split possibilities can be found in literature and the way known as *split A* from [ZBN05] is modified in the present thesis. Further, it is desirable from the computational point of view, to create a matrix free scheme, which can be derived with the full explicit version the CBS scheme. The CBS scheme has been chosen in this thesis due to its broad range of applicability ranging from inviscid to viscous, from laminar to turbulent or from incompressible to compressible fluid problems. Further, this scheme and its properties are well-documented in literature and an extension of this method to the ALE frame of reference is straightforward. Moreover, the CBS scheme is similar computional efficient as state-of-the-art finite volume codes, which is an important property to compute time-resolved aeroelastic problems [ZBN05].

3.3.1 Temporal discretization and splitting

For the characteristic based split, the conservation of momentum, Eq. (3.2.13), is first considered. Using the temporal discretization provided by the characteristic Galerkin method, the question arises, which velocity should be used in Eq. (3.1.3). Solving the fluid equations in the Eulerian frame of reference, this velocity is identical to the local fluid velocity, but using the ALE frame of reference, this velocity is equal to the convective velocity $\boldsymbol{s}_f = \boldsymbol{v}_f - \boldsymbol{w}_f$. Therefore, the following can be obtained with the aid of Eq. (3.1.3):

$$\begin{aligned} \Delta \boldsymbol{V}_f = \boldsymbol{V}_f^{n+1} - \boldsymbol{V}_f^n = -\Delta t \Bigg[[\nabla^T (\boldsymbol{v}_f \boldsymbol{V}_f^T)]^T - [\boldsymbol{w}_f^T \nabla \boldsymbol{V}_f^T]^T - \frac{1}{Re} \mathcal{D}^T \boldsymbol{\tau}_f - \rho_f \hat{\boldsymbol{b}}_f \Bigg]^n \\ - \Delta t \nabla p_f^{n+\theta_2} + \frac{\Delta t^2}{2} \Bigg[(\boldsymbol{s}_f^T \nabla) \Bigg([\nabla^T (\boldsymbol{v}_f \boldsymbol{V}_f^T)]^T - [\boldsymbol{w}_f^T \nabla \boldsymbol{V}_f^T]^T \\ - \frac{1}{Re} \mathcal{D}^T \boldsymbol{\tau}_f - \rho_f \hat{\boldsymbol{b}}_f + \nabla p_f \Bigg) \Bigg]^n , \end{aligned} \tag{3.3.1}$$

where everything is computed at time t^n except the pressure gradient in the second term of the right hand side, which is evaluated at time $t^{n+\theta_2}$. The value θ_2 is a user specified value, which is in the range of $(0 \leq \theta_2 \leq 1)$. Setting $\theta_2 = 0$ the temporal discretization is full explicit and semi-implicit else. The pressure gradient is expressed as:

$$\nabla p_f^{n+\theta_2} = \nabla p_f^n + \theta_2 \nabla (\Delta p_f) \,, \tag{3.3.2}$$

where $\Delta p_f = p_f^{n+1} - p_f^n$ holds. The concept of the CBS scheme is now to split the calculation of $\boldsymbol{V}_f^{n+1}$ into two steps. In a first, an intermediate value for the quantity $\boldsymbol{V}_f$ without the second term - the primary pressure term - of the right hand is evaluated, followed by the calculation of the pressure using the equation of mass conservation (Eq. (3.2.12)). With the pressure quantity available, $\boldsymbol{V}_f^{n+1}$ can then finally be obtained. Thus, the intermediate momentum quantity, $\check{\boldsymbol{V}}_f^{n+1}$, is primarily calculated as:

$$\begin{aligned}\Delta\check{\boldsymbol{V}}_f = \check{\boldsymbol{V}}_f^{n+1} - \boldsymbol{V}_f^n = -\Delta t\Bigg[[\nabla^T(\boldsymbol{v}_f\boldsymbol{V}_f^T)]^T - [\boldsymbol{w}_f^T\nabla\boldsymbol{V}_f^T]^T - \frac{1}{Re}\mathcal{D}^T\boldsymbol{\tau}_f - \rho_f\hat{\boldsymbol{b}}_f\Bigg]^n \\ + \frac{\Delta t^2}{2}\Bigg[(\boldsymbol{s}_f^T\nabla)\Bigg([\nabla^T(\boldsymbol{v}_f\boldsymbol{V}_f^T)]^T - [\boldsymbol{w}_f^T\nabla\boldsymbol{V}_f^T]^T - \frac{1}{Re}\mathcal{D}^T\boldsymbol{\tau}_f \\ - \rho_f\hat{\boldsymbol{b}}_f + \nabla p_f\Bigg)\Bigg]^n .\end{aligned} \tag{3.3.3}$$

This is in contrast to the split A of [ZBN05], where all pressure terms are removed from Eq. (3.3.1). Once, the pressure is known, $\boldsymbol{V}_f^{n+1}$ can be completed by:

$$\begin{aligned}\Delta\boldsymbol{V}_f &= \Delta\check{\boldsymbol{V}}_f - \Delta t\nabla p_f^{n+\theta_2} \\ &= \Delta\check{\boldsymbol{V}}_f - \Delta t\nabla\left[p_f^n + \theta_2(\Delta p_f)\right] .\end{aligned} \tag{3.3.4}$$

The pressure is calculated with the equation of mass conservation, which is discretized as:

$$\Delta\rho_f = \rho_f^{n+1} - \rho_f^n = \left(\frac{1}{c_f^2}\right)^n\Delta p_f = \left(\frac{1}{c_f^2}\right)^n(p_f^{n+1} - p_f^n) = -\Delta t\,\nabla^T\boldsymbol{V}_f^{n+\theta_1} + \Delta t\,\boldsymbol{w}_f^T\nabla\rho_f^n , \tag{3.3.5}$$

where from classical mechanics:

$$c_f^2 = \frac{\partial p_f}{\partial\rho_f} \tag{3.3.6}$$

is used and:

$$\boldsymbol{V}_f^{n+\theta_1} = \boldsymbol{V}_f^n + \theta_1\Delta\boldsymbol{V}_f \tag{3.3.7}$$

holds, i.e. the first term on the right hand side is taken implicitly. The user specified value for θ_1 has a range of $(0.5 \leq \theta_1 \leq 1)$. By using Eq. (3.3.4) and (3.3.7), the density and pressure difference, Eq. (3.3.5), are rewritten as:

$$\begin{aligned}\Delta\rho_f = \left(\frac{1}{c_f^2}\right)^n\Delta p_f = -\Delta t\left[\nabla^T\boldsymbol{V}_f^n + \theta_1\nabla^T(\Delta\check{\boldsymbol{V}}_f) - \boldsymbol{w}_f^T\nabla\rho_f^n\right] \\ + \Delta t^2\theta_1\nabla^T\left[\nabla p_f^n + \theta_2\nabla(\Delta p_f)\right] .\end{aligned} \tag{3.3.8}$$

The temporal discretization of the energy conservation equation, Eq. (3.2.14), is obtained by applying the characteristic Galerkin scheme, Eq. (3.1.3), by keeping all terms explicit and thus:

$$\begin{aligned}\Delta E_f = E_f^{n+1} - E_f^n = -\Delta t\Bigg[\nabla^T(\boldsymbol{v}_f E_f) - \boldsymbol{w}_f^T\nabla E_f + \nabla^T(p_f\boldsymbol{v}_f) - \frac{1}{Re}\nabla^T(\boldsymbol{Q}_f^T\boldsymbol{\tau}_f) \\ - \frac{1}{Re\,Pr}\nabla^T(\kappa_f\nabla T_f) - \rho_f\hat{\boldsymbol{b}}_f^T\boldsymbol{v}_f\Bigg]^n \\ + \frac{\Delta t^2}{2}\Bigg[(\boldsymbol{s}_f^T\nabla)\Bigg(\nabla^T(\boldsymbol{v}_f E_f) - \boldsymbol{w}_f^T\nabla E_f + \nabla^T(p_f\boldsymbol{v}_f) \\ - \frac{1}{Re}\nabla^T(\boldsymbol{Q}_f^T\boldsymbol{\tau}_f) - \frac{1}{Re\,Pr}\nabla^T(\kappa_f\nabla T_f) - \rho_f\hat{\boldsymbol{b}}_f^T\boldsymbol{v}_f\Bigg)\Bigg]^n .\end{aligned} \tag{3.3.9}$$

With these equations, the iterative solution procedure using the CBS scheme can be summarized in terms of the temporal discretization as:

1. solve Eq. (3.3.3) for $\Delta\check{\boldsymbol{V}}_f$
2. solve Eq. (3.3.8) for $\Delta\rho_f$ in the case of a compressible fluid or for Δp_f in the case of an incompressible fluid
3. solve Eq. (3.3.4) for $\Delta\boldsymbol{V}_f$
4. solve Eq. (3.3.9) for ΔE_f

where the unknowns are iterated to a steady state solution.

3.3.2 Spatial discretization

The temporal discretized equations of the previous subsection now need to be discretized in space by using the FEM and the standard Galerkin procedure. For a comprehensive introduction to this procedure, the textbooks by Bathe [Bat96], Hughes [Hug00] and Zienkiewicz [ZTZ05] are recommended to consult.

Using the spatial Galerkin discretization, the fluid domain is divided into a mesh of non-overlapping cells - the finite elements - connected at nodes, at which the fluid values are to be evaluated. The fluid variables are approximated with the aid of shape functions as:

$$f \approx \mathbf{N}\mathbf{f}\,, \tag{3.3.10}$$

where $\mathbf{f} = [\mathsf{f}_1, \mathsf{f}_2, \ldots, \mathsf{f}_m]^T$ contains the nodal values of the quantity f and $\mathbf{N} = [\mathsf{N}_1, \mathsf{N}_2, \ldots, \mathsf{N}_m]$ is the vector of shape functions at the nodes with m being the number of nodes. The strong form of the temporal discretized equations is transformed to an integral weak form by introducing a weight, which in the case of the standard Galerkin procedure is equal to the shape functions. Although an independent discretization can be taken for each fluid variable, all primary fluid quantities are discretized by using the same shape functions in this thesis. Therefore, it is:

$$\begin{aligned} \rho_f &\approx \mathbf{N}\boldsymbol{\rho}_f; \qquad p_f \approx \mathbf{N}\mathbf{p}_f; \qquad \boldsymbol{v}_f \approx \mathbf{N}_v\mathbf{v}_f; \qquad \boldsymbol{w}_f \approx \mathbf{N}_v\mathbf{w}_f; \\ \boldsymbol{s}_f &\approx \mathbf{N}_v\mathbf{s}_f; \qquad \boldsymbol{V}_f \approx \mathbf{N}_v\mathbf{V}_f; \qquad E_f \approx \mathbf{N}\mathbf{E}_f; \qquad T_f \approx \mathbf{N}\mathbf{T}_f; \end{aligned} \tag{3.3.11}$$

where each component of the fluid velocity is approximated with the shape functions, which are also used for each other quantity and thus:

$$\mathbf{N}_v = \begin{bmatrix} \mathsf{N}_1 & 0 & 0 & \mathsf{N}_2 & 0 & 0 & \ldots & \mathsf{N}_m & 0 & 0 \\ 0 & \mathsf{N}_1 & 0 & 0 & \mathsf{N}_2 & 0 & \ldots & 0 & \mathsf{N}_m & 0 \\ 0 & 0 & \mathsf{N}_1 & 0 & 0 & \mathsf{N}_2 & \ldots & 0 & 0 & \mathsf{N}_m \end{bmatrix}$$

$$\mathbf{V}_f = [\mathsf{V}_{11}, \mathsf{V}_{12}, \mathsf{V}_{13}, \mathsf{V}_{21}, \mathsf{V}_{22}, \mathsf{V}_{23} \ldots, \mathsf{V}_{m1}, \mathsf{V}_{m2}, \mathsf{V}_{m3}]_f^T\,.$$

3.3.2.1 Step 1: intermediate velocity

With the shape function matrix given above, the Galerkin form of Eq. (3.3.3) leads to:

$$\begin{aligned}\int_{\Omega_f} \mathbf{N}_v^T \Delta\check{\boldsymbol{V}}_f \, d\Omega_f = -\Delta t \Bigg[& \int_{\Omega_f} \mathbf{N}_v^T [\nabla^T (\boldsymbol{v}_f \boldsymbol{V}_f^T)]^T \, d\Omega_f - \int_{\Omega_f} \mathbf{N}_v^T [\boldsymbol{w}_f^T \nabla \boldsymbol{V}_f^T]^T \, d\Omega_f \\ & + \int_{\Omega_f} (\mathcal{D}\mathbf{N}_v)^T \frac{1}{Re} \boldsymbol{\tau}_f \, d\Omega_f - \int_{\Omega_f} \mathbf{N}_v^T \rho_f \hat{\boldsymbol{b}}_f \, d\Omega_f - \int_{\Gamma_f} \mathbf{N}_v^T \frac{1}{Re} \boldsymbol{\Upsilon}^T \boldsymbol{\tau}_f \, d\Gamma_f \Bigg]^n \\ & + \frac{\Delta t^2}{2} \Bigg[- \int_{\Omega_f} (\boldsymbol{s}_f^T \nabla) \mathbf{N}_v^T [\nabla^T (\boldsymbol{v}_f \boldsymbol{V}_f^T)]^T \, d\Omega_f + \int_{\Omega_f} (\boldsymbol{s}_f^T \nabla) \mathbf{N}_v^T [\boldsymbol{w}_f^T \nabla \boldsymbol{V}_f^T]^T \, d\Omega_f \\ & - \int_{\Omega_f} \mathbf{N}_v^T (\boldsymbol{s}_f^T \nabla)(\rho_f \hat{\boldsymbol{b}}_f) \, d\Omega_f - \int_{\Omega_f} (\boldsymbol{s}_f^T \nabla) \mathbf{N}_v^T \nabla p_f \, d\Omega_f \\ & + \int_{\Gamma_f} \mathbf{N}_v^T [\nabla^T (\boldsymbol{v}_f \boldsymbol{V}_f^T)]^T (\boldsymbol{s}_f^T \boldsymbol{n}) \, d\Gamma_f - \int_{\Gamma_f} \mathbf{N}_v^T [\boldsymbol{w}_f^T \nabla \boldsymbol{V}_f^T]^T (\boldsymbol{s}_f^T \boldsymbol{n}) \, d\Gamma_f \\ & + \int_{\Gamma_f} \mathbf{N}_v^T \nabla p_f (\boldsymbol{s}_f^T \boldsymbol{n}) \, d\Gamma_f \Bigg]^n , \end{aligned} \tag{3.3.12}$$

where integration by parts (or the product rule) on the second order terms are used and third order terms are neglected. The surface integrals of the stabilizing terms are equal to zero for most fluid problems because either the convective velocity on the wall is zero (no-slip boundary condition), the scalar product of convective velocity and the wall normal is zero (slip conditions) or the velocity and pressure gradient is zero (farfield boundary condition). Therefore, these surface integrals can be neglected. Further, the contributions resulting from body forces are excluded in this thesis, but can be included without difficulty. By replacing the continuous fields with the approximations of Eq. (3.3.11), the final matrix form of the above equation is obtained as:

$$\Delta\check{\mathbf{V}}_f = \mathbf{M}_v^{-1} \Delta t \Big[(-\mathbf{C}_{vV}\mathbf{V}_f + \mathbf{C}_{wV}\mathbf{V}_f - \mathbf{K}_\tau \mathbf{v}_f + \mathbf{f}_\tau) + \Delta t(-\mathbf{K}_{vV}\mathbf{V}_f + \mathbf{K}_{wV}\mathbf{V}_f - \mathbf{K}_{pV}\mathbf{p}_f) \Big]^n , \tag{3.3.13}$$

where:

$$\mathbf{M}_v = \int_{\Omega_f} \mathbf{N}_v^T \mathbf{N}_v \, d\Omega_f ; \qquad \mathbf{C}_{vV} = \int_{\Omega_f} \mathbf{N}_v^T \mathbf{B}_v \, d\Omega_f ; \qquad \mathbf{C}_{wV} = \int_{\Omega_f} \mathbf{N}_v^T \mathbf{B}_w \, d\Omega_f ;$$

$$\mathbf{K}_\tau = \int_{\Omega_f} \mathbf{B}_\tau^T \frac{\mu_f}{Re} \left(\boldsymbol{I}_0 - \tfrac{2}{3} \boldsymbol{m}\boldsymbol{m}^T \right) \mathbf{B}_\tau \, d\Omega_f ; \qquad \mathbf{f}_\tau = \int_{\Gamma_f} \mathbf{N}_v^T \boldsymbol{\Upsilon}^T \left[\frac{\mu_f}{Re} \left(\boldsymbol{I}_0 - \tfrac{2}{3} \boldsymbol{m}\boldsymbol{m}^T \right) \mathbf{B}_\tau \mathbf{v}_f \right] d\Gamma_f ;$$

$$\mathbf{K}_{vV} = \frac{1}{2} \int_{\Omega_f} \mathbf{B}_s^T \mathbf{B}_v \, d\Omega_f ; \qquad \mathbf{K}_{wV} = \frac{1}{2} \int_{\Omega_f} \mathbf{B}_s^T \mathbf{B}_w \, d\Omega_f ; \qquad \mathbf{K}_{pV} = \frac{1}{2} \int_{\Omega_f} \mathbf{B}_s^T (\nabla \mathbf{N}) \, d\Omega_f .$$

The $\mathbf{B}$-matrices are expressed as:

$$\mathbf{B}_{[v,w,s]} = \begin{bmatrix} \mathsf{b}_{a1} & 0 & 0 & \mathsf{b}_{a2} & 0 & 0 & \dots & \mathsf{b}_{am} & 0 & 0 \\ 0 & \mathsf{b}_{a1} & 0 & 0 & \mathsf{b}_{a2} & 0 & \dots & 0 & \mathsf{b}_{am} & 0 \\ 0 & 0 & \mathsf{b}_{a1} & 0 & 0 & \mathsf{b}_{a2} & \dots & 0 & 0 & \mathsf{b}_{am} \end{bmatrix} ;$$

$$\mathsf{b}_{vi} = \nabla^T (\boldsymbol{v}_f \mathsf{N}_i); \quad \mathsf{b}_{wi} = \boldsymbol{w}_f^T \nabla \mathsf{N}_i ; \quad \mathsf{b}_{si} = (\boldsymbol{s}_f^T \nabla) \mathsf{N}_i ;$$

$$\mathbf{B}_\tau = \mathcal{D}\mathbf{N}_v ;$$

where for $\mathbf{B}_v$, $\mathbf{B}_w$ and $\mathbf{B}_s$ the velocities $\boldsymbol{v}_f$, $\boldsymbol{w}_f$, $\boldsymbol{s}_f$ are needed to be discretized for the integration. The most obvious way is to use the nodal values of these velocities for the $\mathbf{B}$-matrices, [ZBN05]. Thus, one can write for b_{vi}, b_{wi} and b_{si}:

$$\mathsf{b}_{vi} = \mathbf{v}_i^T(\nabla \mathsf{N}_i); \quad \mathsf{b}_{wi} = \mathbf{w}_i^T(\nabla \mathsf{N}_i); \quad \mathsf{b}_{si} = \mathbf{s}_i^T(\nabla \mathsf{N}_i); \tag{3.3.14}$$

where $\mathbf{v}_i = [\mathsf{v}_{i1}, \mathsf{v}_{i2}, \mathsf{v}_{i3}]_f^T$, $\mathbf{w}_i = [\mathsf{w}_{i1}, \mathsf{w}_{i2}, \mathsf{w}_{i3}]_f^T$, $\mathbf{s}_i = [\mathsf{s}_{i1}, \mathsf{s}_{i2}, \mathsf{s}_{i3}]_f^T$ are the values of the fluid, the mesh and the convective velocity at a node i, respectively. Therefore, with $\mathbf{B}_s = \mathbf{B}_v - \mathbf{B}_w$, the matrix equation of Eq. (3.3.13) simplifies to:

$$\Delta\check{\mathbf{V}}_f = \mathbf{M}_v^{-1}\Delta t\Big[(-\mathbf{C}_{sV}\mathbf{V}_f - \mathbf{K}_\tau \mathbf{v}_f + \mathbf{f}_\tau) + \Delta t(-\mathbf{K}_{sV}\mathbf{V}_f - \mathbf{K}_{pV}\mathbf{p}_f)\Big]^n, \tag{3.3.15}$$

where:

$$\mathbf{C}_{sV} = \int_{\Omega_f} \mathbf{N}_v^T \mathbf{B}_s \, d\Omega_f; \qquad \mathbf{K}_{sV} = \frac{1}{2}\int_{\Omega_f} \mathbf{B}_s^T \mathbf{B}_s \, d\Omega_f \, .$$

3.3.2.2 Step 2: density/pressure

The weak form of the density/pressure equation, Eq. (3.3.8), can be expressed as:

$$\begin{aligned}
\int_{\Omega_f} \mathbf{N}^T \Delta\boldsymbol{\rho}_f \, d\Omega_f &= \int_{\Omega_f} \mathbf{N}^T \left(\frac{1}{c_f^2}\right)^n \Delta \boldsymbol{p}_f \, d\Omega_f \\
&= \Delta t \Bigg[\int_{\Omega_f} (\nabla \mathbf{N})^T (\boldsymbol{V}_f^n + \theta_1 \Delta\check{\boldsymbol{V}}_f) \, d\Omega_f + \int_{\Omega_f} \mathbf{N}^T (\boldsymbol{w}_f^T \nabla \rho_f^n) \, d\Omega_f \\
&\qquad - \int_{\Gamma_f} \mathbf{N}^T [\boldsymbol{V}_f^n + \theta_1 \Delta\check{\boldsymbol{V}}_f]^T \boldsymbol{n} \, d\Gamma_f \Bigg] \\
&\quad + \Delta t^2 \theta_1 \Bigg[\int_{\Omega_f} -(\nabla \mathbf{N})^T [\nabla p_f^n + \theta_2 \nabla(\Delta p_f)] \, d\Omega_f \\
&\qquad + \int_{\Gamma_f} \mathbf{N}^T [\nabla p_f^n + \theta_2 \nabla(\Delta p_f)]^T \boldsymbol{n} \, d\Gamma_f \Bigg].
\end{aligned} \tag{3.3.16}$$

In the last surface integral on the right hand side, the gradient of the term $\theta_2 \Delta p_f$ is omitted, which is reasonable as shown in [NCZ06]. Substituting the continuous field variables with the approximations of Eq. (3.3.11), the final matrix system is obtained either for the density as:

$$\Delta\boldsymbol{\rho}_f = (\mathbf{M} + \Delta t^2 \theta_1 \theta_2 \mathbf{K}_\rho)^{-1} \Delta t \Big[\mathbf{G}(\mathbf{V}_f^n + \theta_1 \Delta\check{\mathbf{V}}_f) + \mathbf{C}_{w\rho}\boldsymbol{\rho}_f^n - \mathbf{f}_V + \Delta t \theta_1 (-\mathbf{K}_p \mathbf{p}_f^n + \mathbf{f}_p) \Big], \tag{3.3.17}$$

or for the pressure as:

$$\Delta\mathbf{p}_f = (\mathbf{M}_p + \Delta t^2 \theta_1 \theta_2 \mathbf{K}_p)^{-1} \Delta t \Big[\mathbf{G}(\mathbf{V}_f^n + \theta_1 \Delta\check{\mathbf{V}}_f) + \mathbf{C}_{w\rho}\boldsymbol{\rho}_f^n - \mathbf{f}_V + \Delta t \theta_1 (-\mathbf{K}_p \mathbf{p}_f^n + \mathbf{f}_p) \Big], \tag{3.3.18}$$

where the matrices and vectors are expressed as:

$$\mathbf{M} = \int_{\Omega_f} \mathbf{N}^T \mathbf{N}\, d\Omega_f; \qquad \mathbf{M}_p = \int_{\Omega_f} \mathbf{N}^T \left(\frac{1}{c_f^2}\right)^n \mathbf{N}\, d\Omega_f; \qquad \mathbf{K}_p = \int_{\Omega_f} (\nabla \mathbf{N})^T (\nabla \mathbf{N})\, d\Omega_f;$$

$$\mathbf{K}_\rho = \int_{\Omega_f} (\nabla \mathbf{N})^T (c_f^2)^n (\nabla \mathbf{N})\, d\Omega_f; \qquad \mathbf{G} = \int_{\Omega_f} (\nabla \mathbf{N})^T \mathbf{N}_v\, d\Omega_f; \qquad \mathbf{f}_p = \int_{\Gamma_f} \mathbf{N}^T (\nabla \mathbf{N} \mathbf{p}_f^n)^T \boldsymbol{n}\, d\Gamma_f;$$

$$\mathbf{C}_{w\rho} = \int_{\Omega_f} \mathbf{N}^T \mathbf{L}_w\, d\Omega_f; \qquad \mathbf{f}_V = \int_{\Gamma_f} \mathbf{N}^T (\mathbf{N}_v [\mathbf{V}_f^n + \theta_1 \Delta \check{\mathbf{V}}_f])^T \boldsymbol{n}\, d\Gamma_f;$$

with $\mathbf{L}_w$ being:

$$\mathbf{L}_w = [\mathsf{b}_{w1}, \mathsf{b}_{w2}, \ldots, \mathsf{b}_{wm}]$$

and b_{wi} given in Eq. (3.3.14) at the time n.

3.3.2.3 Step 3: velocity correction

Having calculated the pressure or density update, Eq. (3.3.4) is used in its weak form to correct the intermediate velocity:

$$\int_{\Omega_f} \mathbf{N}_v^T \Delta \boldsymbol{V}_f\, d\Omega_f = \int_{\Omega_f} \mathbf{N}_v^T \Delta \check{\boldsymbol{V}}_f\, d\Omega_f + \Delta t \int_{\Omega_f} -\mathbf{N}_v^T \nabla [p_f^n + \theta_2 (\Delta p_f)]\, d\Omega_f\,, \tag{3.3.19}$$

which results in the final matrix form:

$$\Delta \mathbf{V}_f = \Delta \check{\mathbf{V}}_f + \mathbf{M}_v^{-1} \Delta t \left[-\mathbf{G}^T (\mathbf{p}_f^n + \theta_2 \Delta \mathbf{p}_f) \right]. \tag{3.3.20}$$

3.3.2.4 Step 4: energy

Analogous to the first step (intermediate velocity), the weak form of the energy equation (3.3.9) can be expressed as:

$$\begin{aligned}
\int_{\Omega_f} \mathbf{N}^T \Delta E_f\, d\Omega_f = -\Delta t \Bigg[& \int_{\Omega_f} \mathbf{N}^T \nabla^T (\boldsymbol{v}_f (E_f + p_f))\, d\Omega_f - \int_{\Omega_f} \mathbf{N}^T \boldsymbol{w}_f^T \nabla E_f\, d\Omega_f \\
& + \int_{\Omega_f} (\nabla \mathbf{N})^T \frac{1}{Re} \left(\boldsymbol{Q}_f^T \boldsymbol{\tau}_f + \frac{1}{Pr} \kappa_f \nabla T_f \right) d\Omega_f - \int_{\Omega_f} \mathbf{N}^T \rho_f \hat{\boldsymbol{b}}_f^T \boldsymbol{v}_f\, d\Omega_f \\
& - \int_{\Gamma_f} \mathbf{N}^T \frac{1}{Re} \left[\boldsymbol{Q}^T \boldsymbol{\tau}_f + \frac{1}{Pr} \kappa_f \nabla T_f \right]^T \boldsymbol{n}\, d\Gamma_f \Bigg]^n \\
& + \frac{\Delta t^2}{2} \Bigg[- \int_{\Omega_f} (\boldsymbol{s}_f^T \nabla) \mathbf{N}^T \nabla^T (\boldsymbol{v}_f (E_f + p_f))\, d\Omega_f + \int_{\Omega_f} (\boldsymbol{s}_f^T \nabla) \mathbf{N}^T (\boldsymbol{w}_f^T \nabla E_f)\, d\Omega_f \\
& - \int_{\Omega_f} \mathbf{N}^T (\boldsymbol{s}_f^T \nabla)(\rho_f \hat{\boldsymbol{b}}_f^T \boldsymbol{v}_f)\, d\Omega_f \Bigg]^n,
\end{aligned} \tag{3.3.21}$$

where again integration by parts on the second order terms are used and third order terms are neglected. Further, the surface integrals arising due to the integration by parts of the stabilization

terms are again omitted, because they are equal to zero due to boundary conditions. The matrix form is then obtained by substituting the approximations of Eq. (3.3.11) into the above equation as:

$$\Delta \mathbf{E}_f = \mathbf{M}^{-1}\Delta t\Big[(-\mathbf{C}_{sE}\mathbf{E}_f - \mathbf{C}_{vE}\mathbf{p}_f - \mathbf{K}_{\tau E}\mathbf{v}_f - \mathbf{K}_T\mathbf{T}_f + \mathbf{f}_E) + \Delta t(-\mathbf{K}_{sE}\mathbf{E}_f - \mathbf{K}_{vE}\mathbf{p}_f)\Big]^n, \quad (3.3.22)$$

with the matrices and vectors:

$$\mathbf{C}_{sE} = \int_{\Omega_f} \mathbf{N}^T\mathbf{L}_s\, d\Omega_f; \qquad \mathbf{C}_{vE} = \int_{\Omega_f} \mathbf{N}^T\mathbf{L}_v\, d\Omega_f; \qquad \mathbf{K}_T = \int_{\Omega_f} (\nabla\mathbf{N})^T \frac{\kappa_f}{Re\,Pr}(\nabla\mathbf{N})\, d\Omega_f;$$

$$\mathbf{K}_{\tau E} = \int_{\Omega_f} (\nabla\mathbf{N})^T \boldsymbol{Q}_f^T \frac{\mu_f}{Re}\left(\boldsymbol{I}_0 - \tfrac{2}{3}\boldsymbol{m}\boldsymbol{m}^T\right)\mathbf{B}_\tau\, d\Omega_f; \quad \mathbf{K}_{sE} = \frac{1}{2}\int_{\Omega_f} \mathbf{L}_s^T\mathbf{L}_s\, d\Omega_f;$$

$$\mathbf{f}_E = \int_{\Gamma_f} \mathbf{N}^T \frac{1}{Re}\left(\boldsymbol{Q}^T\left[\mu_f\left(\boldsymbol{I}_0 - \tfrac{2}{3}\boldsymbol{m}\boldsymbol{m}^T\right)\mathbf{B}_\tau\mathbf{v}_f\right] + \frac{\kappa_f}{Pr}(\nabla\mathbf{N})\mathbf{T}_f\right)^T \boldsymbol{n}\, d\Gamma_f; \quad \mathbf{K}_{vE} = \frac{1}{2}\int_{\Omega_f} \mathbf{L}_s^T\mathbf{L}_v\, d\Omega_f;$$

where:

$$\mathbf{L}_s = [\mathsf{b}_{s1}, \mathsf{b}_{s2}, \ldots, \mathsf{b}_{sm}]; \qquad \mathbf{L}_v = [\mathsf{b}_{v1}, \mathsf{b}_{v2}, \ldots, \mathsf{b}_{vm}]\,.$$

The entries of $\mathbf{L}_s$ and $\mathbf{L}_v$ are given in Eq. (3.3.14).

3.3.2.5 Final CBS scheme

The matrix equations derived in the last subsections are summarized here due to its importance in this thesis. By using the CBS scheme, a steady state solution for compressible fluid problems is obtained by the following iterative procedure:

- preprocess (read grid, form mass matrices, initialize $\mathbf{V}_f^0$, $\boldsymbol{\rho}_f^0$, $\mathbf{E}_f^0$, and secondary fluid quantities (temperature, velocity, viscosity, etc.))
- loop over N_t time steps or until convergence is reached
  - intermediate velocity:

$$\Delta\check{\mathbf{V}}_f = \mathbf{M}_v^{-1}\Delta t\Big[(-\mathbf{C}_{sV}\mathbf{V}_f - \mathbf{K}_\tau\mathbf{v}_f + \mathbf{f}_\tau) + \Delta t(-\mathbf{K}_{sV}\mathbf{V}_f - \mathbf{K}_{pV}\mathbf{p}_f)\Big]^n \quad (3.3.15)$$

  - density:

$$\Delta\boldsymbol{\rho}_f = (\mathbf{M} + \Delta t^2\theta_1\theta_2\mathbf{K}_\rho)^{-1}\Delta t\Big[\mathbf{G}(\mathbf{V}_f^n + \theta_1\Delta\check{\mathbf{V}}_f) + \mathbf{C}_{w\rho}\boldsymbol{\rho}_f - \mathbf{f}_V + \Delta t(-\theta_1\mathbf{K}_p\mathbf{p}_f^n + \mathbf{f}_p)\Big] \quad (3.3.17)$$

  - correct velocity:

$$\Delta\mathbf{V}_f = \Delta\check{\mathbf{V}}_f + \mathbf{M}_v^{-1}\Delta t\Big[-\mathbf{G}^T(\mathbf{p}_f^n + \theta_2\Delta\mathbf{p}_f)\Big] \quad (3.3.20)$$

  - energy:

$$\Delta\mathbf{E}_f = \mathbf{M}^{-1}\Delta t\Big[(-\mathbf{C}_{sE}\mathbf{E}_f - \mathbf{C}_{vE}\mathbf{p}_f - \mathbf{K}_{\tau E}\mathbf{v}_f - \mathbf{K}_T\mathbf{T}_f + \mathbf{f}_E) + \Delta t(-\mathbf{K}_{sE}\mathbf{E}_f - \mathbf{K}_{vE}\mathbf{p}_f)\Big]^n \quad (3.3.22)$$

  - update solution and calculate secondary fluid quantities (temperature, velocity, viscosity, etc.)

  - set boundary conditions (slip, no-slip, farfield, symmetry, etc.)
  - check for convergence

- postprocess (write solution, calculate lift and drag, etc.)

With this CBS scheme, a powerful tool is available, which can be used to calculate a wide range of problems in fluid dynamics, ranging from inviscid to laminar or turbulent viscous as well as from compressible to incompressible flows. The treatment of these different fluid flow types is the topic of the next section. However, with the scheme above the basic steps are derived to calculate the fluid flow in the ALE frame of reference.

3.4 Additional computational techniques

The CBS scheme to solve fluid problems via finite elements is in its basic form of general applicability and some aspects for compressible and incompressible fluids need to be addressed. Further, some techniques to save computational time or to acquire a faster solution will be covered in next few subsections.

3.4.1 Matrix free, explicit form

As mentioned above, the full explicit version is obtained by setting $\theta_2 = 0$. Then, for the density or pressure equation, Eq. (3.3.17) or (3.3.18), only the inversion of the consistent mass matrix $\mathbf{M}$ or $\mathbf{M}_p$ is required[1]. In this thesis, the most numerical examples are carried out with the full explicit CBS scheme unless indicated differently. Especially, when a compressible fluid is considered, this explicit CBS scheme is advantageous since by using Eq. (3.3.17), $\mathbf{M}$ needs to be inverted, which is - unlike $\mathbf{M}_p$ - constant throughout the solution procedure. But as noted in [NCZ06], better convergence can be achieved for incompressible flows, if the implicit scheme for the pressure equation (3.3.18) is used, i.e. $0 < \theta_2 \leq 1$.

Further, a matrix free scheme can be obtained, by setting $\theta_2 = 0$ and diagonalization (or lumping) of the mass matrix. From the computational point of view, such matrix free scheme is attractive since the solution of the system becomes trivial. A lumped mass matrix $\mathbf{M}_L$ is usually obtained by summing up the mass matrix entries of each row and placing the sum on the diagonal, while setting the non-diagonal entries to zero. This is equivalent to distributing the mass of the element to the nodes, which is sketched on the left hand side of Figure 3.1 for linear triangles. However, this is only possible for linear or bilinear elements. For quadratic elements, zero sums are obtained, which prevents a solution. Therefore, for triangular quadratic elements a suggestion for lumping the mass matrix is shown on the right side of Figure 3.1, where the quadratic element is virtually divided into four linear triangles and the same lumping rule as for linear triangles is applied. For other quadratic elements, similar lumping procedures can be found. However, the nodal decoupling by using a lumped mass matrix can lead to unphysical oscillations. Another method to avoid a large system of linear equations invoked by the consistent mass matrix is the usage of a discontinuous characteristic based split scheme, where each finite element is treated independently and the element-by-element linking is considered by the elemental edge flux. This discontinuous characteristic based split scheme is the topic of section 3.5.

[1] The term mass matrix comes from the finite element method in structural mechanics, where the consistent mass matrix is calculated as: $\mathbf{M} = \int_\Omega \mathbf{N}^T \rho \mathbf{N} \, d\Omega$.

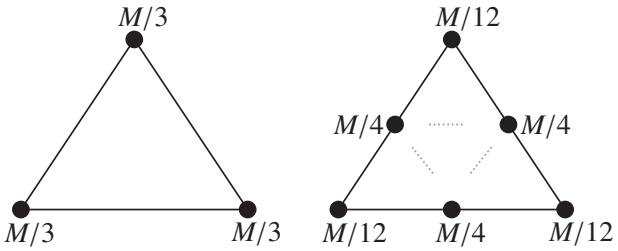

Figure 3.1: Mass lumping of linear (left) and quadratic triangle elements (right), where M indicates the whole mass of the element

3.4.2 Variable smoothing

In computational fluid dynamics, the use of a residual smoothing scheme is a common computational method [Bla06]. In this work, the fluid residuals are smoothed in each iteration of the CBS procedure. Adapted from [TN05, Loe08], the residual is smoothed by a Laplace operator approach, whereas the Laplacian coefficients are approximated with the aid of the consistent mass matrix as:

$$\mathbf{r}_S^{n+1} = \mathbf{S}\mathbf{r}^{n+1}\,, \tag{3.4.1}$$

where $\mathbf{r}_S^{n+1}$ is the smoothed residual and $\mathbf{S}$ is the is symmetric smoothing matrix, whose each row sum is equal to one.

The smoothing matrix, which represents the Laplacian coefficients, can be obtained from the consistent mass matrix as (see [Loe08]):

$$\mathbf{S} = (1 - \varsigma_s)\boldsymbol{I} + \varsigma_s \check{\mathbf{M}}_L^{-1}\check{\mathbf{M}}\,, \tag{3.4.2}$$

where $\check{\mathbf{M}}$ is the consistent mass matrix with diagonal elements set to zero, i.e. $\check{\mathbf{M}} = \mathbf{M} - \mathbf{M}_D$ with $\mathbf{M}_D$ being the diagonal of the consistent mass matrix. The matrix $\check{\mathbf{M}}_L$ denotes the lumped version of $\check{\mathbf{M}}$ and ς_s is a user specified smoothing parameter which varies between 0 and 0.03. Thus, an increasing value of ς_s means, that the influence of the nodes surrounding the node in question is decreased. To account for solid walls, a distance based linear dependency of ς_s is considered for $\mathbf{S}$, i.e. along a transition wall distance, ς_s decreases linearly to zero at wall points.

3.4.3 Incompressible fluid - artificial compressibility

The CBS scheme presented can also be used for incompressible fluids in the ALE frame of reference. Incompressible fluids are characterized by a constant density and therefore the pressure equation (3.3.18) instead of Eq. (3.3.17) needs to be used. On the other hand, for incompressible fluids the speed of sound c_f (or wave speed) becomes very large or even infinity, which results in a stiff solution scheme. Therefore, c_f is replaced by an artificial compressibility parameter β in the matrix $\mathbf{M}_p$ of (3.3.18). Still, the whole set of equations of the CBS scheme is used to iterate to steady state and it could be shown, that the parameter β does not affect the solution, [DGP94, Nit03, NMWM04, NCZ06, MLN02]. The parameter β makes sure that $\mathbf{M}_p$ does not reach zero, which is important, when the full explicit version ($\theta_2 = 0$) of the CBS scheme is used. According to [Liu05], β (in its non-dimensional form) is locally calculated as:

$$\beta = \max(\varsigma_c,\, v_f^{\text{conv}},\, v_f^{\text{diff}}) = \max\left(\varsigma_c,\, \sqrt{\boldsymbol{v}_f^T\boldsymbol{v}_f},\, \frac{2\nu_f}{h\,Re}\right), \tag{3.4.3}$$

where ς_c is a user specified lower bound, $v_f^{\text{conv}} = \sqrt{\boldsymbol{v}_f^T\boldsymbol{v}_f}$ is the convective velocity and $v_f^{\text{diff}} = \frac{2\nu_f}{h\,Re}$ is the diffusive velocity.

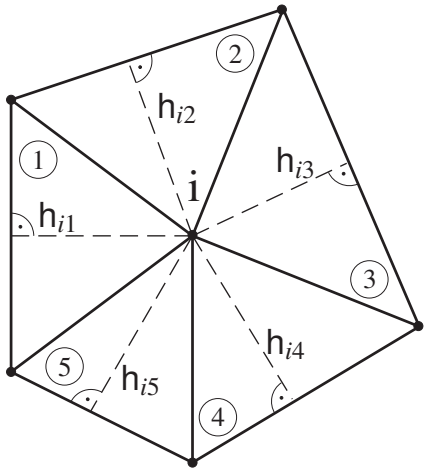

Figure 3.2: Calculation of h_i for the node i, surrounded by $N_{ie} = 5$ triangular elements, $\mathsf{h}_i = \min(\mathsf{h}_{i1}, \mathsf{h}_{i2}, \mathsf{h}_{i3}, \mathsf{h}_{i4}, \mathsf{h}_{i5})$

The quantity h denotes a characteristic length, which is derived from the local element size h_e. Since the value β is calculated for every node of the computational mesh, the local element size needs to be evaluated for each node, i.e. a value h_i for each node i is required. Therefore, h_i at a node is taken as the minimum of sizes of each element connecting to the node, that is for triangular elements, see also Figure 3.2:

$$\mathsf{h}_i = \min(\mathsf{h}_{ie})_{N_{ie}} = \min\left(\frac{2\text{Area}}{\text{Length of the opposite side}}\right)_{N_{ie}}, \tag{3.4.4}$$

where N_{ie} is the number of elements connecting to the node i. For tetrahedral elements, one can find:

$$\mathsf{h}_i = \min\left(\frac{3\text{Volume}}{\text{Area of the opposite face}}\right)_{N_{ie}}. \tag{3.4.5}$$

For quadrilateral and hexahedral elements, a similar calculation can be made considering here that the minimal orthogonal distance from all opposite edges or areas to the node in question needs to be taken. An alternative evaluation of the characteristic length based on the streamline vector is given in [Sha89] and applied and investigated in the context of the CBS scheme in [TN05]. Clearly, the characteristic length computed by a streamline based calculation would change during the iteration to steady state and is therefore more computational expensive than the static calculation of h given above. Thus, such a streamline based calculation of h is not considered here.

3.4.4 Inviscid flow problems

For inviscid flow problems, the Reynolds number Re is infinity, which results in solving the so-called Euler equations for fluid flow problems. Thus, the first step of calculating the intermediate velocity can be obtained as:

$$\Delta\check{\mathbf{V}}_f = \mathbf{M}_v^{-1}\Delta t\Big[(-\mathbf{C}_{sV}\mathbf{V}_f + \Delta t(-\mathbf{K}_{sV}\mathbf{V}_f - \mathbf{K}_{pV}\mathbf{p}_f)\Big]^n \tag{3.4.6}$$

and the fourth step of calculating the energy becomes:

$$\Delta\mathbf{E}_f = \mathbf{M}^{-1}\Delta t\Big[(-\mathbf{C}_{sE}\mathbf{E}_f - \mathbf{C}_{vE}\mathbf{p}_f + \Delta t(-\mathbf{K}_{sE}\mathbf{E}_f - \mathbf{K}_{vE}\mathbf{p}_f)\Big]^n. \tag{3.4.7}$$

The rest of the CBS scheme remains unchanged.

3.4.5 Local time stepping

Since the CBS scheme is used for flow problems to iterate to steady state, different local time steps can be used to accelerate the iteration, i.e. different time steps at the nodes and elements are used. These local time steps depend on the characteristic length as:

$$\Delta t = \varsigma_t \min(\Delta t^{\text{conv}}, \Delta t^{\text{diff}}), \tag{3.4.8}$$

where:

$$\Delta t^{\text{conv}} = \begin{cases} \frac{h}{v_f^{\text{conv}} + c_f} = \frac{h}{\sqrt{\boldsymbol{v}_f^T \boldsymbol{v}_f} + c_f} & \text{for compressible flows} \\ \frac{h}{v_f^{\text{conv}} + \beta} = \frac{h}{\sqrt{\boldsymbol{v}_f^T \boldsymbol{v}_f} + \beta} & \text{for incompressible flows} \end{cases} \tag{3.4.9}$$

and:

$$\Delta t^{\text{diff}} = \frac{h^2 Re}{2\nu_f} \tag{3.4.10}$$

and ς_t denotes a user specified safety factor ranging from 0.1 to 1.0 depending on the flow problem and used mesh. For the nodal value of the time step, $\Delta \mathsf{t}_i$, again the nodal value of the element size h_i from Eq. (3.4.4) as well as nodal velocities and nodal viscosities are needed. An elemental time step, $\Delta \mathsf{t}_e$, is calculated then as the mean of the nodes adjacent to the element in question. For inviscid problems, Δt^{diff} is not considered and the local time step is only calculated from the convective time step Δt^{conv}.

3.4.6 Unsteady flow problems

The CBS scheme is used to iterate a solution to steady state, i.e. $t \to \infty$. Most fluid problems - especially when structural interaction takes place - are unsteady in nature. For such time accurate (or transient) problems, it is common in CFD to use a dual time stepping approach, [Jam91], where in each real time step Δt^R, an iterative procedure is carried out, in which the pseudo time t goes to infinity. Thus, the unsteady flow problem becomes a pseudo-steady state problem within each real time step.

In order to recover a transient solution, real time terms need to be added to the CBS equations (3.3.15), (3.3.17)/(3.3.18), (3.3.20) and (3.3.22). The velocity real time term can be added to step 1, Eq. (3.3.15), or to step 3, Eq. (3.3.20). Here, the velocity real time term is added to step 3, which results in the following modified third term:

$$\Delta \mathbf{V}_f = \Delta \check{\mathbf{V}}_f + \mathbf{M}_v^{-1} \Delta t \left[-\mathbf{G}^T (\mathbf{p}_f^n + \theta_2 \Delta \mathbf{p}_f) \right] - \frac{\Delta t}{\Delta t^R} \Delta \mathbf{V}_f^R, \tag{3.4.11}$$

where $\Delta \mathbf{V}_f^R$ is the velocity real time term, which is implicitly approximated with a second order time-accurate three-point backward difference scheme as:

$$\begin{aligned} \Delta \mathbf{V}_f^R &= [\mathbf{M}_v^{m+1}]^{-1} \left(\frac{3}{2} \mathbf{M}_v^{m+1} \mathbf{V}_f^{m+1} - 2\, \mathbf{M}_v^m \mathbf{V}_f^m + \frac{1}{2} \mathbf{M}_v^{m-1} \mathbf{V}_f^{m-1} \right) \\ &= \frac{3}{2} \mathbf{V}_f^n + \mathbf{M}_v^{-1} \left(-2\, \mathbf{M}_v^m \mathbf{V}_f^m + \frac{1}{2} \mathbf{M}_v^{m-1} \mathbf{V}_f^{m-1} \right), \end{aligned} \tag{3.4.12}$$

where $\mathbf{V}_f^{m+1}$ is the desired solution at the new real time level $m+1$ equal to the nth pseudo time level value within the n-iteration (and thus $\mathbf{M}_v^{m+1} = \mathbf{M}_v$), $\mathbf{V}_f^m$ is the solution at the last real time level m and $\mathbf{V}_f^{m-1}$ denotes the solution at the real time level $m-1$. Here, a constant real time step Δt^R is assumed. Due to the use of an implicit real time stepping scheme, the real time step size is unrestricted in terms of stability.

For compressible flow, the density real time term is added to step 2 resulting in:

$$\Delta\boldsymbol{\rho}_f = (\mathbf{M} + \Delta t^2\theta_1\theta_2\mathbf{K}_\rho)^{-1}\Delta t\Big[\mathbf{G}(\mathbf{V}_f^n + \theta_1\Delta\check{\mathbf{V}}_f) + \mathbf{C}_{w\rho}\boldsymbol{\rho}_f^n - \mathbf{f}_V + \Delta t(-\theta_1\mathbf{K}_p\mathbf{p}_f^n + \mathbf{f}_p)\Big] - \frac{\Delta t}{\Delta t^R}\Delta\boldsymbol{\rho}_f^R, \tag{3.4.13}$$

where $\Delta\boldsymbol{\rho}_f^R$ is similar approximated as $\Delta\mathbf{V}_f^R$:

$$\Delta\boldsymbol{\rho}_f^R = \frac{3}{2}\boldsymbol{\rho}_f^n + \mathbf{M}^{-1}\Big(-2\,\mathbf{M}^m\boldsymbol{\rho}_f^m + \frac{1}{2}\mathbf{M}^{m-1}\boldsymbol{\rho}_f^{m-1}\Big). \tag{3.4.14}$$

For incompressible flow, a pressure real time term is added to step 2 resulting in:

$$\Delta\mathbf{p}_f = (\mathbf{M}_p + \Delta t^2\theta_1\theta_2\mathbf{K}_p)^{-1}\Delta t\Big[\mathbf{G}(\mathbf{V}_f^n + \theta_1\Delta\check{\mathbf{V}}_f) + \mathbf{C}_{w\rho}\boldsymbol{\rho}_f^n - \mathbf{f}_V + \Delta t(-\theta_1\mathbf{K}_p\mathbf{p}_f^n + \mathbf{f}_p)\Big] - \frac{\Delta t}{\Delta t^R}\Delta\mathbf{p}_f^R, \tag{3.4.15}$$

with $\Delta\mathbf{p}_f^R$ being:

$$\Delta\mathbf{p}_f^R = \frac{3}{2}\mathbf{p}_f^n + \mathbf{M}^{-1}\Big(-2\,\mathbf{M}^m\mathbf{p}_f^m + \frac{1}{2}\,\mathbf{M}^{m-1}\mathbf{p}_f^{m-1}\Big). \tag{3.4.16}$$

Finally, an energy real time term is added to the energy equation (3.3.22), which results in the following modified energy equation:

$$\Delta\mathbf{E}_f = \mathbf{M}^{-1}\Delta t\Big[(-\mathbf{C}_{sE}\mathbf{E}_f - \mathbf{C}_{vE}\mathbf{p}_f - \mathbf{K}_{\tau E}\mathbf{v}_f - \mathbf{K}_T\mathbf{T}_f + \mathbf{f}_E) + \Delta t(-\mathbf{K}_{sE}\mathbf{E}_f - \mathbf{K}_{vE}\mathbf{p}_f)\Big]^n - \frac{\Delta t}{\Delta t^R}\Delta\mathbf{E}_f^R, \tag{3.4.17}$$

with

$$\Delta\mathbf{E}_f^R = \frac{3}{2}\mathbf{E}_f^n + \mathbf{M}^{-1}\Big(-2\,\mathbf{M}^m\mathbf{E}_f^m + \frac{1}{2}\,\mathbf{M}^{m-1}\mathbf{E}_f^{m-1}\Big). \tag{3.4.18}$$

It should be noted here, that after each real time step the solution vectors at the time level m and $m-1$ need to be appropriately stored and the vectors $\Delta\mathbf{V}_f^R$, $\Delta\boldsymbol{\rho}_f^R$ or $\Delta\mathbf{p}_f^R$, and $\Delta\mathbf{E}_f^R$ need to be recalculated after each inner (pseudo time) iteration.

3.4.7 Geometric conservation law

In section 2.4.6, the geometric conservation law is introduced, which is a requirement for predicting exactly the trivial solution of a uniform flow on deforming meshes. A very comprehensive overview on this topic using different numerical schemes is given in the paper [EGP09] and the reference therein. Some literature references pointed out the importance of the GCL for the stability of the resulting numerical ALE scheme. But this is still a controversial topic of current research as the two papers - [FGG01] and [BG04] - show. While the first paper states that the GCL is a sufficient and necessary condition for stability up to second order accuracy in time, the second shows that through the GCL accuracy is likely to improve and stability is enhanced in some cases.

Mostly, the GCL is used to find a rule for the derivation of the discrete mesh velocity $\mathbf{w}_f$. In [LF96], a first temporary order scheme to calculate the mesh velocity is given by $\mathbf{w}_f^{m+1/2} = (\mathbf{x}_f^{m+1} - \mathbf{x}_f^m)/\Delta t^R$, where $\mathbf{x}_f$ is the position of the fluid grid nodes. To calculate the mesh velocity, in this thesis and according to [BG04, Bla06, Foe07] the same second order approximation is used as for the other primary fluid quantities in Eq. (3.4.12), (3.4.14)/(3.4.16) and (3.4.18), that is:

$$\mathbf{w}_f^{m+1} = \frac{\Delta\mathbf{x}_f^R}{\Delta t^R} = \frac{3\mathbf{x}_f^{m+1} - 4\mathbf{x}_f^m + \mathbf{x}_f^{m-1}}{2\Delta t^R}. \tag{3.4.19}$$

This equation automatically satisfied Eq. (2.4.64), [Bla06, Foe07]. Further, it should be noted here, that by using a partitioned coupling approach for fluid-structure interaction after each real time step, the fluid solver is restarted with the mesh at time level $m+1$ and its node positions $\mathbf{x}_f^{m+1}$. Therefore, the mass matrix $\mathbf{M}$ is calculated at each real time step according to the mesh at time level $m+1$.

3.5 Discontinuous Galerkin form

Mass matrix lumping as described in section 3.4.1 is not applicable, when the implicit form of the CBS scheme is applied, i.e. when $\theta_2 > 0$. Also, as noted in [ZBN05], the usage of mass matrix lumping can lead to serious errors, when used for time accurate problems. Further, it could be observed, that unphysical oscillations appear in the solution, when mass matrix lumping is applied for quadratic and higher order elements, i.e. for elements with quadratic and higher order shape function interpolation. Such oscillations are caused by a nodal decoupling, when a lumped mass matrix is used. Therefore, a consistent mass matrix should be applied in such situations, which is computational expensive with many degrees of freedom. Alternatively, an elemental discontinuous Galerkin (DG) form of the CBS scheme can be used, which was proposed for incompressible fluid flow problems in [Tho06, TNB08].

The DG method has been developed mainly for problems in fluid mechanics and combines features of finite element and the finite volume schemes. A good overview of this methodology can be found in [Coc03, Li06] and the references therein. One important advantage of the DG method is the possibility of an easy parallization of the algorithm since this method allows an element-by-element solution procedure. However, each node belongs to several elements and multiple solutions for each node need therefore to be stored, which results in a large memory requirement. Further, additional edge fluxes for each element have to be computed, which makes the computation of the residual for the discontinuous methodology more expensive than for the continuous Galerkin counterpart.

In this thesis, a discontinuous form of the characteristic based split (DG-CBS) scheme for the ALE frame of reference is employed, which has the same structure as the continuous Galerkin form of the CBS scheme. This has the advantages, that only minor modifications to the CBS scheme are necessary and that computational effort is reduced, [HSBB06]. The standard finite element assembly of the continuous Galerkin form is removed and the element-by-element linking is done by the edge flux, which ensures continuity between the elements. This edge flux also can be used to satisfy a local or elemental conservation, if this flux is equal for the common boundary of two adjoining elements. Due to the avoidance of a global matrix system, the necessity of solving a system of linear algebraic equations is omitted. As noted in [TNB08], the DG-CBS scheme is not only globally but also locally conservative in terms of the fluid variables.

To show the concept of the discontinuous Galerkin form, plots of a primary variable over a patch of three two-dimensional finite elements using continuous and discontinuous spatial shape function interpolation are shown in Figure 3.3. While for the continuous case the spatial evolution of a primary variable shows no steps over the element edges (C^0 continuous), this continuity requirement is abandoned with the discontinuous spatial discretization, Figure 3.3(b). Due to the avoidance of a global matrix system, the necessity of solving a system of linear algebraic equation is omitted for an explicit scheme.

3.5.1 Discontinuous Galerkin spatial discretization

The discretization of the DG-CBS scheme starts with the same weak statement as the continuous Galerkin form of Eq. (3.3.12). Using non-overlapping finite elements Ω_f^e, one can write for *each* of these elements:

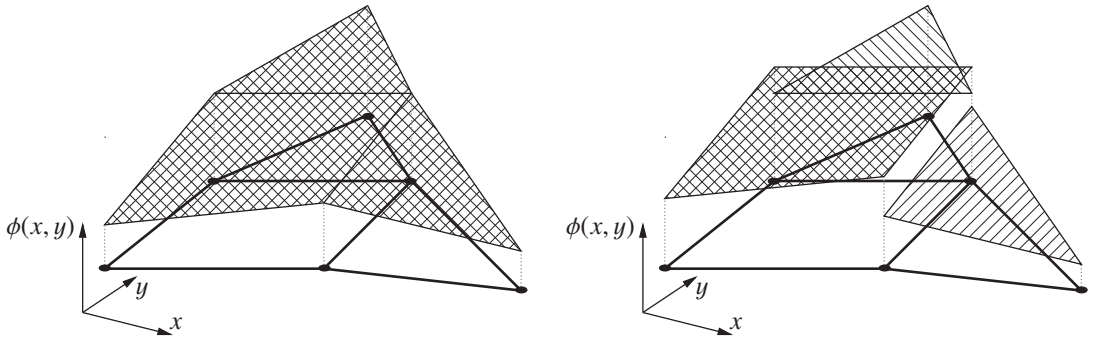

(a) continuous shape function interpolation (b) discontinuous shape function interpolation

Figure 3.3: Plot of a primary variable over a patch of two-dimensional finite elements using continuous and discontinuous spatial shape function interpolation

$$
\begin{aligned}
\int_{\Omega_f^e} \mathbf{N}_v^T \Delta\check{\boldsymbol{V}}_f \, d\Omega_f^e = \Delta t \Bigg[& \int_{\Omega_f^e} [(\boldsymbol{v}_f^T \nabla)\mathbf{N}_v^T] \boldsymbol{V}_f \, d\Omega_f^e - \int_{\Omega_f^e} [(\boldsymbol{w}_f^T \nabla)\mathbf{N}_v^T] \boldsymbol{V}_f \, d\Omega_f^e \\
& - \int_{\Gamma_f^e} \mathbf{N}_v^T [\boldsymbol{n}(\boldsymbol{v}_f \boldsymbol{V}_f^T)]^T \, d\Gamma_f^e + \int_{\Gamma_f^e} \mathbf{N}_v^T [\boldsymbol{w}_f^T \boldsymbol{n} \boldsymbol{V}_f^T]^T \, d\Gamma_f^e \\
& - \int_{\Omega_f^e} (\mathcal{D}\mathbf{N}_v)^T \frac{1}{Re} \boldsymbol{\tau}_f \, d\Omega_f^e + \int_{\Omega_f^e} \mathbf{N}_v^T \rho_f \hat{\boldsymbol{b}}_f \, d\Omega_f^e + \int_{\Gamma_f^e} \mathbf{N}_v^T \frac{1}{Re} \boldsymbol{\Upsilon}^T \boldsymbol{\tau}_f \, d\Gamma_f^e \Bigg]^n \\
+ \frac{\Delta t^2}{2} \Bigg[& - \int_{\Omega_f^e} (\boldsymbol{s}_f^T \nabla)\mathbf{N}_v^T [\nabla^T (\boldsymbol{v}_f \boldsymbol{V}_f^T)]^T \, d\Omega_f^e + \int_{\Omega_f^e} (\boldsymbol{s}_f^T \nabla)\mathbf{N}_v^T [\boldsymbol{w}_f^T \nabla \boldsymbol{V}_f^T]^T \, d\Omega_f^e \\
& - \int_{\Omega_f^e} \mathbf{N}_v^T (\boldsymbol{s}_f^T \nabla)(\rho_f \hat{\boldsymbol{b}}_f) \, d\Omega_f^e - \int_{\Omega_f^e} (\boldsymbol{s}_f^T \nabla)\mathbf{N}_v^T \nabla p_f \, d\Omega_f^e \Bigg]^n ,
\end{aligned}
\tag{3.5.1}
$$

where an additional integration by parts for the convective terms is applied, which leads to the appearance of an additional edge flux. It should be further noted here, that the element boundary terms of the stabilization part are neglected, which is a valid approach, [TNB08]. With the same assumption as in section 3.3.2.1, the resulting matrix system for this one element is:

$$
\Delta\check{\mathbf{V}}_f = \mathbf{M}_v^{e,-1} \Delta t \Big[(\mathbf{C}_{sV}^e \mathbf{V}_f - \mathbf{K}_\tau^e \mathbf{v}_f - \mathbf{f}_{sV}^e + \mathbf{f}_\tau^e) + \Delta t (-\mathbf{K}_{sV}^e \mathbf{V}_f - \mathbf{K}_{pV}^e \mathbf{p}_f) \Big]^n , \tag{3.5.2}
$$

where

$$
\mathbf{M}_v^e = \int_{\Omega_f^e} \mathbf{N}_v^T \mathbf{N}_v \, d\Omega_f^e ; \qquad \mathbf{C}_{sV}^e = \int_{\Omega_f^e} \mathbf{B}_s^T \mathbf{N}_v \, d\Omega_f^e ; \qquad \mathbf{K}_{sV}^e = \frac{1}{2} \int_{\Omega_f^e} \mathbf{B}_s^T \mathbf{B}_s \, d\Omega_f^e
$$

$$
\mathbf{K}_\tau^e = \int_{\Omega_f^e} \mathbf{B}_\tau^T \frac{\mu_f}{Re} \left(\boldsymbol{I}_0 - \tfrac{2}{3} \boldsymbol{m}\boldsymbol{m}^T \right) \mathbf{B}_\tau \, d\Omega_f^e ; \qquad \mathbf{f}_\tau^e = \int_{\Gamma_f^e} \frac{1}{Re} \mathbf{N}_v^T \boldsymbol{\Upsilon}^T \mathbf{N}_\tau \check{\boldsymbol{\tau}}_f \, d\Gamma_f^e ;
$$

$$
\mathbf{f}_{sV}^e = \int_{\Gamma_f^e} \mathbf{N}_v^T (\boldsymbol{s}_f^T \boldsymbol{n}) \mathbf{N}_v \mathbf{V}_f \, d\Gamma_f^e ; \qquad \mathbf{K}_{pV}^e = \frac{1}{2} \int_{\Omega_f^e} \mathbf{B}_s^T (\nabla \mathbf{N}) \, d\Omega_f^e .
$$

It is important to note, that for the boundary term $\mathbf{f}_\tau^e$ the nodal stress vector $\check{\boldsymbol{\tau}}_f$ is needed, which is spatially interpolated with the shape function matrix $\mathbf{N}_\tau$. This form ensures the local conservation of the edge flux and requires the nodal stress values to be computed in an additional post-processing step in each iteration.

The second step remains nearly unchanged and is rewritten for one finite element Ω_f^e as:

$$\Delta\boldsymbol{\rho}_f = (\mathbf{M}^e + \Delta t^2\theta_1\theta_2\mathbf{K}_\rho^e)^{-1}\Delta t\Big[\mathbf{G}_V^e(\mathbf{V}_f^n + \theta_1\Delta\check{\mathbf{V}}_f) + \mathbf{C}_{w\rho}^e\boldsymbol{\rho}_f^n - \mathbf{f}_V^e + \Delta t\theta_1(-\mathbf{K}_p^e\mathbf{p}_f^n + \mathbf{f}_p^e)\Big], \tag{3.5.3}$$

where

$$\mathbf{M}^e = \int_{\Omega_f^e}\mathbf{N}^T\mathbf{N}\,d\Omega_f^e; \qquad \mathbf{K}_\rho^e = \int_{\Omega_f^e}(\nabla\mathbf{N})^T(c_f^2)^n(\nabla\mathbf{N})\,d\Omega_f^e; \qquad \mathbf{G}_V^e = \int_{\Omega_f^e}(\nabla\mathbf{N})^T\mathbf{N}_v\,d\Omega_f^e;$$

$$\mathbf{f}_p^e = \int_{\Gamma_f^e}\mathbf{N}^T\boldsymbol{n}^T\mathbf{N}_v\mathbf{p}_{f,\boldsymbol{x}}\,d\Gamma_f^e; \quad \mathbf{C}_{w\rho}^e = \int_{\Omega_f^e}\mathbf{N}^T\mathbf{L}_w\,d\Omega_f^e; \quad \mathbf{f}_V^e = \int_{\Gamma_f^e}\mathbf{N}^T(\mathbf{N}_v[\mathbf{V}_f^n + \theta_1\Delta\check{\mathbf{V}}_f])^T\boldsymbol{n}\,d\Gamma_f^e.$$

Similar to the vector $\mathbf{f}_\tau^e$ from step 1, the nodal pressure derivatives $\mathbf{p}_{f,\boldsymbol{x}}$ interpolated with $\mathbf{N}_v$ are needed for $\mathbf{f}_p^e$ to ensure local conservation over the element boundaries. These nodal pressure derivatives are calculated in an extra step in each iteration. For incompressible flows, the pressure is calculated rather than the density as:

$$\Delta\mathbf{p}_f = (\mathbf{M}_p^e + \Delta t^2\theta_1\theta_2\mathbf{K}_p^e)^{-1}\Delta t\Big[\mathbf{G}_V^e(\mathbf{V}_f^n + \theta_1\Delta\check{\mathbf{V}}_f) + \mathbf{C}_{w\rho}^e\boldsymbol{\rho}_f^n - \mathbf{f}_V^e + \Delta t\theta_1(-\mathbf{K}_p^e\mathbf{p}_f^n + \mathbf{f}_p^e)\Big], \tag{3.5.4}$$

with the matrices:

$$\mathbf{M}_p^e = \int_{\Omega_f^e}\mathbf{N}^T\left(\frac{1}{c_f^2}\right)^n\mathbf{N}\,d\Omega_f^e; \qquad \mathbf{K}_p^e = \int_{\Omega_f^e}(\nabla\mathbf{N})^T(\nabla\mathbf{N})\,d\Omega_f^e.$$

In the next step the velocity is corrected with:

$$\Delta\mathbf{V}_f = \Delta\check{\mathbf{V}}_f + \mathbf{M}_v^{e,-1}\Delta t\Big[\mathbf{G}_p^e(\mathbf{p}_f^n + \theta_2\Delta\mathbf{p}_f) - \mathbf{f}_{V2}^e\Big], \tag{3.5.5}$$

where again integration by parts of Eq. (3.3.19) is used to obtain the elemental boundary flux $\mathbf{f}_{V2}^e$. The matrices and vectors are defined as:

$$\mathbf{G}_p^e = \int_{\Omega_f^e}\left(\begin{bmatrix}\partial/\partial x_1 & 0 & 0\\ 0 & \partial/\partial x_2 & 0\\ 0 & 0 & \partial/\partial x_3\end{bmatrix}\mathbf{N}_v\right)^T\mathbf{N}\,d\Omega_f^e; \qquad \mathbf{f}_{V2}^e = \int_{\Gamma_f^e}\mathbf{N}_v^T\boldsymbol{n}\mathbf{N}\mathbf{p}_f^n\,d\Gamma_f^e.$$

Finally and in analogy to step 1, the energy matrix-vector equation is obtained as

$$\begin{aligned}\Delta\mathbf{E}_f = \mathbf{M}^{e,-1}\Delta t\Big[&(\mathbf{C}_{sE}^e\mathbf{E}_f + \mathbf{C}_{vE}^e\mathbf{p}_f - \mathbf{K}_{\tau E}^e\mathbf{v}_f - \mathbf{K}_T^e\mathbf{T}_f - \mathbf{f}_{sE}^e - \mathbf{f}_{vE}^e + \mathbf{f}_E^e)\\ &+ \Delta t(-\mathbf{K}_{sE}^e\mathbf{E}_f - \mathbf{K}_{vE}^e\mathbf{p}_f)\Big]^n,\end{aligned} \tag{3.5.6}$$

with the matrices and vectors being:

$$\mathbf{C}_{sE}^e = \int_{\Omega_f^e}\mathbf{L}_s^T\mathbf{N}\,d\Omega_f^e; \quad \mathbf{C}_{vE}^e = \int_{\Omega_f^e}\mathbf{L}_v^T\mathbf{N}\,d\Omega_f^e; \quad \mathbf{K}_{sE}^e = \frac{1}{2}\int_{\Omega_f^e}\mathbf{L}_s^T\mathbf{L}_s\,d\Omega_f^e; \quad \mathbf{K}_{vE}^e = \frac{1}{2}\int_{\Omega_f^e}\mathbf{L}_s^T\mathbf{L}_v\,d\Omega_f^e;$$

$$\mathbf{K}_T^e = \int_{\Omega_f^e}(\nabla\mathbf{N})^T\frac{\kappa_f}{Re\,Pr}(\nabla\mathbf{N})\,d\Omega_f^e; \quad \mathbf{f}_{sE}^e = \int_{\Gamma_f^e}\mathbf{N}^T(\boldsymbol{s}_f^T\boldsymbol{n})\mathbf{N}\mathbf{E}_f\,d\Gamma_f^e; \quad \mathbf{f}_{vE}^e = \int_{\Gamma_f^e}\mathbf{N}^T(\boldsymbol{v}_f^T\boldsymbol{n})\mathbf{N}\mathbf{p}_f\,d\Gamma_f^e;$$

$$\mathbf{K}_{\tau E}^e = \int_{\Omega_f^e}(\nabla\mathbf{N})^T\boldsymbol{Q}_f^T\frac{\mu_f}{Re}\left(\boldsymbol{I}_0 - \tfrac{2}{3}\boldsymbol{m}\boldsymbol{m}^T\right)\mathbf{B}_\tau\,d\Omega_f^e; \quad \mathbf{f}_E^e = \int_{\Gamma_f^e}\mathbf{N}^T\frac{\boldsymbol{n}}{Re}\left(\boldsymbol{Q}^T\mathbf{N}_\tau\check{\boldsymbol{\tau}}_f + \frac{\kappa_f}{Pr}\mathbf{N}_v\mathbf{T}_{f,\boldsymbol{x}}\right)d\Gamma_f^e.$$

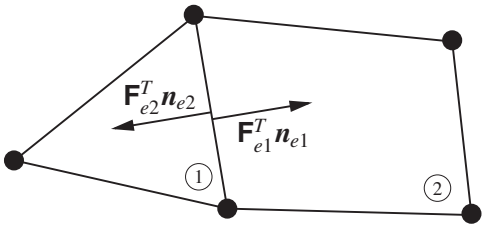

Figure 3.4: Triangular and quadrilateral element sharing a common boundary, where the flux is conserved

Again, the nodal temperature derivatives $\mathbf{T}_{f,\boldsymbol{x}}$ are needed for the element boundary flux to ensure local conservation and this vector is computed at the end of each iteration cycle.

3.5.2 Calculation of the edge fluxes and continuous solution

As already mentioned above, the DG-CBS scheme ensures a conservation of the flux crossing a common boundary of neighboring elements.

In Figure 3.4, a triangular (e1) and a quadrilateral (e2) element are depicted, which share a common edge. The condition for this flux conservation can be expressed with the aid of the boundary normals as:

$$\mathbf{F}_{e1}^T \boldsymbol{n}_{e1} = \mathbf{F}_{e2}^T \boldsymbol{n}_{e2} \,, \tag{3.5.7}$$

where $\mathbf{F}_{ei}$ is the flux and $\boldsymbol{n}_{ei}$ denotes the outward normal of the common boundary. Due to this equation, nodal values of the viscous stress vector and of the pressure and temperature derivatives are necessary, which are calculated from the surrounding elements of the node in question once a global continuous solution is obtained. For triangular elements, these derivatives are constant for each element and a mean value for specific nodes can be computed in a straightforward way. For quadrilateral elements and higher order elements, the derivatives are extrapolated from the Gaussian points of the element to the node and the nodal derivative is obtained by averaging these elemental derivatives. A patch of $N_{ie} = 5$ elements is shown in Figure 3.5 and the nodal derivative $(\nabla\phi)_i$ at a node i is calculated as:

$$(\nabla\phi)_i = \frac{1}{N_{ie}} \sum_{e=1}^{N_{ie}} (\nabla\phi)_{ei} \,. \tag{3.5.8}$$

In a similar way, the global continuous solution $(\boldsymbol{\rho}_f, \mathbf{V}_f, \mathbf{E}_f)$ is obtained by averaging the local elemental solution at the node in question, that is:

$$\phi_i = \frac{1}{N_{ie}} \sum_{e=1}^{N_{ie}} \phi_{ei} \,, \tag{3.5.9}$$

where ϕ_i is the global discrete solution at the node i and ϕ_{ei} the solution at the node i on element level.

After obtaining the global continuous solution, the calculation of the secondary fluid quantities like temperature, local Mach-Number, etc. is accomplished. For incompressible flow problems, the artificial compressibility scheme is available without restriction and a time accurate solution can again be recovered by the dual time-stepping approach employed in section 3.4.6.

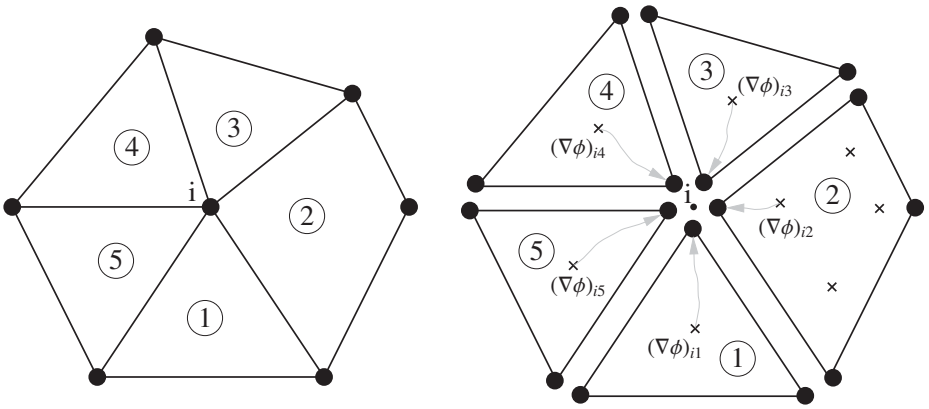

Figure 3.5: Patch of 5 finite elements and its discontinuous discretization - calculation of the nodal derivative $(\nabla\phi)_i$

3.6 Chapter summary

In this chapter, the CBS methodology is employed for the fluid domain described by the Navier-Stokes equation in ALE frame of reference. Thus, a spatial discretization scheme consistent to the structural solver is provided with CBS scheme. Modern discontinuous Galerkin developments are considered with the development of the DG-CBS scheme. The mathematical formulation of the CBS scheme uses a characteristic Galerkin expansion of the governing equations in non-dimensional form and the splitting is introduced during the temporal discretization. The full matrix scheme is then obtained by a spatial discretization with the aid of finite elements, which use a shape function interpolation of the unknown variables.

Since the fluid domain needs to be adapted according to the structural deformation the ALE form of the governing fluid equations is used in this thesis and this form is a novel extension compared to the work of Zienkiewicz [ZBN05] and Nithiarasu [NCZ06]. Furthermore, additional computational techniques, in particular a matrix free form, residual smoothing, artificial compressibility for incompressible fluids or local time stepping, are discussed in detail.

Additionally, an novel alternative spatial discretization is introduced in section 3.5, which uses a discontinuous Galerkin formulation of the CBS scheme. In this variant, it is circumvented to solve a system with a global coefficient mass matrix. A more important advantage of this DG-CBS scheme is the property that the element edge flux can be designed to be locally conservative.

Further, turbulence modeling with the aid of CBS the scheme is included in the appendix A.2. In appendix A.2, the Favre and Reynolds averaging to the governing fluid equations is applied and two models to determine the eddy viscosity are introduced. The first model is the well-known Spalart-Allmaras (SA) turbulence model as a representative of an one-equation turbulence model. In section A.2.4.2 the discretization of the k-ω baseline (BSL) and shear stress transport (SST) model of Menter using the CBS scheme are additionally shown. These models are two-equation turbulence models and like the Spalart-Allmaras model often used for aeronautical applications.

4 Discrete Coupling Scheme

In this chapter, the numerical aspects of the weak formulation for the coupled problem, which is presented in section 2.5, are discussed. For convenient reasons, an operational view will be introduced for each numerical ingredient, which also assists the partitioned coupling approach of the FSI problem.

4.1 Reduction on the coupling interface

To discuss the discrete coupling scheme, it is appropriate to reduce the discrete equation for each single field on the coupling interface. This reduction is naturally inspired by the use of the partitioned coupling approach, where distinguished solvers for each single field problem are combined to solve coupled problems. Thus operators are introduced, which provide the discrete forces on the coupling interface. This is physically reasonable as shown for the structural subdomain in the next subsection. For the fluid subdomain a similar operational view is introduced in a subsequent section.

4.1.1 Reduction on the coupling interface for the structural subdomain

For the structural domain, the first variation of the actions functional given in Eq. (2.3.8) can be directly discretized in space by using shape function interpolation as described in section 3.3.2. Thus, the structural displacement field as well as its first variation (Galerkin scheme) is interpolated as:

$$\boldsymbol{u}_s \approx \mathbf{N}_u \mathbf{u}_s; \quad \delta\boldsymbol{u}_s \approx \mathbf{N}_u \delta\mathbf{u}_s \,, \tag{4.1.1}$$

where the matrix of the shape functions is

$$\mathbf{N}_u = \begin{bmatrix} \mathsf{N}_1 & 0 & 0 & \mathsf{N}_2 & 0 & 0 & \dots & \mathsf{N}_m & 0 & 0 \\ 0 & \mathsf{N}_1 & 0 & 0 & \mathsf{N}_2 & 0 & \dots & 0 & \mathsf{N}_m & 0 \\ 0 & 0 & \mathsf{N}_1 & 0 & 0 & \mathsf{N}_2 & \dots & 0 & 0 & \mathsf{N}_m \end{bmatrix}.$$

Therefore, each component of the displacement field is interpolated with the same set of shape functions. With this interpolation, the first variation of the structural problem leads directly to, see [Hug00, ZTZ05, Bat96] for details:

$$\mathbf{M}_u \ddot{\mathbf{u}}_s + \mathbf{f}_{u,\text{int}}(\mathbf{u}_s) = \mathbf{f}_{u,\text{ext}} \,, \tag{4.1.2}$$

where:

$$\mathbf{M}_u = \int_{\Omega_s} \mathbf{N}_u^T \rho_s \mathbf{N}_u \, d\Omega_s; \quad \mathbf{f}_{u,\text{int}} = \int_{\Omega_s} (\mathcal{D}\mathbf{N}_u)^T \boldsymbol{\sigma}_s \, d\Omega_s; \quad \mathbf{f}_{u,\text{ext}} = \int_{\Omega_s} \mathbf{N}_u^T \hat{\boldsymbol{b}}_s \, d\Omega_s + \int_{\Gamma_s} \mathbf{N}_u^T \hat{\boldsymbol{t}}_s \, d\Gamma_s \,.$$

For non-linear structural problems, the internal forces $\mathbf{f}_{u,\text{int}}$ depend on the displacements. For linear problems, the constitutive relation of Eq. (2.3.6) is used and the spatial discretization leads to:

$$\mathbf{M}_u \ddot{\mathbf{u}}_s + \mathbf{K}_u \mathbf{u}_s = \mathbf{f}_{u,\text{ext}} \,, \tag{4.1.3}$$

with the stiffness matrix defined as:

$$\mathbf{K}_u = \int_{\Omega_s} \mathbf{B}_u^T \boldsymbol{E}\, \mathbf{B}_u \, d\Omega_s = \int_{\Omega_s} (\mathcal{D}\mathbf{N}_u)^T \boldsymbol{E}\, (\mathcal{D}\mathbf{N}_u) \, d\Omega_s \,.$$

The unknown displacements $\mathbf{u}_s$ as well as the forces $\mathbf{f}_u$ can be split into internal values and values on the coupling interface Γ_c as:

$$\mathbf{u}_s = \begin{pmatrix} \mathbf{u}_s^\Omega \\ \mathbf{u}_s^\Gamma \end{pmatrix}; \qquad \mathbf{f}_u = \begin{pmatrix} \mathbf{f}_u^\Omega \\ \mathbf{f}_u^\Gamma \end{pmatrix}. \tag{4.1.4}$$

With this splitting, it is convenient to introduce a structural operator $\mathcal{S}$ as:

$$\mathcal{S}\mathbf{u}_s^\Gamma = \mathbf{f}_{u,\text{ext}}^\Gamma = \mathbf{f}_s^\Gamma \,, \tag{4.1.5}$$

where $\mathbf{f}_{u,\text{ext}}^\Omega = \mathbf{0}$ is assumed, which implies $\hat{\boldsymbol{b}}_s = \mathbf{0}$. This operator is in general non-linear and depends on the displacements $\mathbf{u}_s$. In the case of a static linear structural problem, $\mathbf{K}_u \mathbf{u}_s = \mathbf{f}_{u,\text{ext}}$, this operator is identical to the Schur complement of $\mathbf{K}_u$:

$$\begin{bmatrix} \mathbf{K}_u^{\Omega\Omega} & \mathbf{K}_u^{\Omega\Gamma} \\ \mathbf{K}_u^{\Gamma\Omega} & \mathbf{K}_u^{\Gamma\Gamma} \end{bmatrix} \begin{pmatrix} \mathbf{u}_s^\Omega \\ \mathbf{u}_s^\Gamma \end{pmatrix} = \begin{pmatrix} \mathbf{f}_{u,\text{ext}}^\Omega = \mathbf{0} \\ \mathbf{f}_{u,\text{ext}}^\Gamma \end{pmatrix} \quad \Rightarrow \quad \underbrace{\left(\mathbf{K}_u^{\Gamma\Gamma} - \mathbf{K}_u^{\Gamma\Omega} \mathbf{K}_u^{\Omega\Omega\,-1} \mathbf{K}_u^{\Omega\Gamma}\right)}_{=\mathcal{S}} \mathbf{u}_s^\Gamma = \mathbf{f}_{u,\text{ext}}^\Gamma \,. \tag{4.1.6}$$

The Schur complement $\mathcal{S}$ projects the interface state vector $\mathbf{u}_s^\Gamma$ on the domain and evaluates the resulting fluxes $\mathbf{f}_s^\Gamma$. Usually, the inverse statement, i.e. a Neumann problem, has to be computed for the structure, where a structural displacement vector needs to be obtained under prescribed forces. Therefore, it can be written:

$$\mathbf{u}_s^\Gamma = \mathcal{S}^{-1} \mathbf{f}_s^\Gamma \,, \tag{4.1.7}$$

where $\mathcal{S}^{-1}$ implies, that the matrix system of Eq. (4.1.2) has to be solved for the displacements.

4.1.2 Reduction on the coupling interface for the fluid subdomain

Similar to the structural solver operator $\mathcal{S}$, a fluid solver operator can be introduced. For consistency such an operator is written as:

$$\mathbf{f}_f^\Gamma = \mathcal{F}\mathbf{u}_f^\Gamma \,, \tag{4.1.8}$$

where $\mathbf{u}_f^\Gamma$ is the displacement of the interface processed by the fluid solver to obtain the interface forces $\mathbf{f}_f^\Gamma$. Using the CBS scheme, these interface forces are computed from the Cauchy surface stress as:

$$\mathbf{f}_f^\Gamma = \int_{\Gamma_c} \mathbf{N}_v^T \boldsymbol{\Upsilon}^T \boldsymbol{\sigma}_f \, d\Gamma_c = \int_{\Gamma_c} \mathbf{N}_v^T \boldsymbol{\Upsilon}^T \boldsymbol{\tau}_f \, d\Gamma_c - \int_{\Gamma_c} \mathbf{N}_v^T p_f \boldsymbol{n} \, d\Gamma_c \,. \tag{4.1.9}$$

Behind the operator $\mathcal{F}$ several operations need to be performed. Based on the interface displacement $\mathbf{u}_f^\Gamma$, the displacement vector for the whole fluid domain is required to be obtained in a first step. This task is part of the mesh deformation algorithm, which is written in an operational context as:

$$\mathbf{u}_f = \mathcal{G}\mathbf{u}_f^\Gamma \,. \tag{4.1.10}$$

Details on the mesh deformation will be described in a following subsection. Once the fluid domain displacement is obtained, the new position of each node can be calculated easily as:

$$\mathbf{x}_f = \mathbf{u}_f + \mathbf{x}_f^0 , \tag{4.1.11}$$

where $\mathbf{x}_f^0$ is the initial nodal position, i.e. the location of the nodes at $t = 0$. Using Eq. (3.4.19), the mesh velocity can be computed from the new nodal position. From an operational point of view, this second step can be written as:

$$\mathbf{w}_f = \mathcal{W}\mathbf{u}_f . \tag{4.1.12}$$

With this mesh velocity, the actual fluid solver, or in this case the CBS scheme, can be invoked to get the resulting forces on the fluid interface:

$$\mathbf{f}_f^\Gamma = \mathcal{C}\mathbf{w}_f . \tag{4.1.13}$$

Therefore, the fluid solver operator can be replaced as:

$$\mathbf{f}_f^\Gamma = (\mathcal{C} \circ \mathcal{W} \circ \mathcal{G})\,\mathbf{u}_f^\Gamma \quad \Rightarrow \quad \mathcal{F} = \mathcal{C} \circ \mathcal{W} \circ \mathcal{G} . \tag{4.1.14}$$

This operational view also underlies the partitioned solution approach, mentioned in the introduction of this thesis.

4.2 Finite element grid deformation

In the previous section, a grid deformation operator $\mathcal{G}$ as part of the fluid solver operator $\mathcal{F}$ is shown to be necessary for the update of the nodal positions. Since the grid quality has a major influence on the solution accuracy and on the convergence, the grid deformation operator has to fulfill the requirements of avoiding extreme element shapes and of keeping the boundary layer for viscous flow calculations. Several methods exist for such deformation operator $\mathcal{G}$.

In [dBvdSB07], radial basis functions are used for this task, but the mesh quality strongly depends on the type of the basis function and its support radius. Another promising method is based on the concept of Delauny graphs, [LQX06]. But for high deformations, this method requires an incremental application of this Delauny graph. Certainly, the most common method is the spring analogy method, [DF02], where the edges are represented through springs with a certain stiffness.

In this thesis, a variant of this method is used, where the grid is treated as a pseudo structure, i.e. the fluid domain is seen as a solid body, on which the interface displacement field is prescribed as a boundary condition. According to the linear static structural system, given in the left part of Eq. (4.1.6), such grid deformation can be written as:

$$\mathbf{K}_g\mathbf{u}_f = \mathbf{0} \quad \Rightarrow \quad \begin{bmatrix} \mathbf{K}_g^{\Omega\Omega} & \mathbf{K}_g^{\Omega\Gamma} \\ \mathbf{K}_g^{\Gamma\Omega} & \mathbf{K}_g^{\Gamma\Gamma} \end{bmatrix} \begin{pmatrix} \mathbf{u}_f^\Omega \\ \mathbf{u}_f^\Gamma \end{pmatrix} = \begin{pmatrix} \mathbf{0} \\ \mathbf{0} \end{pmatrix} , \tag{4.2.1}$$

where

$$\mathbf{K}_g = \int_{\Omega_f} (\mathcal{D}\mathbf{N}_v)^T \boldsymbol{E}_g \, (\mathcal{D}\mathbf{N}_v)\, d\Omega_f .$$

Eq. (4.2.1) has to be solved for $\mathbf{u}_f^\Omega$ every time the interface displacement field changes. For the stress-strain matrix $\boldsymbol{E}_g$, a linear material behavior is assumed, which is isotropic for each element. Therefore, a locally adapted stress-strain matrix is used, where for each element, the elastic modulus E_g and Poisson's ratio ν_g need to be calculated.

To obtain a higher stiffness for small elements, the Jacobian determinant, which arises during the numerical integration, can be simply neglected, [Hug00, ZTZ05, Bat96]. This is to say for the elastic modulus:

$$E_{g,i} = \frac{1}{\Omega_{e,i}}\,, \tag{4.2.2}$$

where Ω_e is the volume size of the element in question, [JT94, STB03]. The stiffness for each finite element $E_{g,i}$ can also be evaluated as the inverse of the minimal element edge length:

$$E_{g,i} = \frac{1}{\min(l_{e,ij})}; \quad j = 1 \ldots N_{\text{edges}}\,, \tag{4.2.3}$$

where $l_{e,ij}$ is the length of the jth edge for the element i. Thus, smaller elements near the wall have a higher stiffness than greater elements in the farfield. A third possibility is to use the shortest distance from a node to the nearest solid wall, d_w, and thus the element stiffness is expressed as:

$$E_{g,i} = \frac{1}{d_{w,i}}\,. \tag{4.2.4}$$

Further, the element stiffness can be calculated from the characteristic length, which is given in Eq. (3.4.4):

$$E_{g,i} = \frac{1}{\mathsf{h}_i}\,. \tag{4.2.5}$$

All these stiffness evaluation methods can also be combined and in this thesis two combinations are used:

- usage of the wall distance and the characteristic length:

$$E_{g,i} = \frac{1}{d_{w,i}\mathsf{h}_i} \tag{4.2.6}$$

- usage of the wall distance and the Jacobian determinant:

$$E_{g,i} = \frac{1}{d_{w,i}\Omega_{e,i}} \tag{4.2.7}$$

For the second pseudo material parameter - Poisson's ratio - different values are possible, which were investigated in [XA04]. Since the results obtained with the pseudo structural approach have no physical meaning, also negative values for Poisson's ratio can be considered, although such material does not exist. Using positive values, as typical solids have, a stretching in one direction is always accompanied with a compression in the other directions. This might lead to a degradation of the element aspect ratios. Therefore, a negative value for Poisson's ratio $\nu_g = -0.5$ is used, [XA04]. This results in the advantageous behavior, that a grid element, which is compressed in one direction, is also shortened in the other two perpendicular directions. Thus, the initial element aspect ratios can be preserved.

In terms of the computational effort, it should be noted, that it is sufficient to create and to factorize $\mathbf{K}_g$ only once at the beginning of the simulation for most engineering problems. Further, an exact solution of Eq. (4.2.1) in the sense of a structural problem, is usually not necessary, but the resulting mesh should show good convergence behavior and not extensively deformed element shapes. Therefore, also iterative methods, in particular conjugate gradient methods, can be used with a relatively high termination threshold to accelerate the solution.

4.3 Finite element data transfer

Using the two- and three-field approach, the interface problem arises as a weak expression of the displacement's equality at the interface due to the variation of the Lagrange multiplier field.

For the three-field approach, the interface problem could be written from Eq. (2.5.9) as:

$$\int_{\Gamma_{ci}} \delta\boldsymbol{\lambda}_i^T \left(\boldsymbol{u}_c - \boldsymbol{u}_i\right) d\Gamma_{ci} = 0\,. \tag{4.3.1}$$

Using again a shape function interpolation of the interface variables:

$$\boldsymbol{u}_i \approx \mathbf{N}_u^{(i)}\mathbf{u}_i; \qquad \boldsymbol{\lambda}_i \approx \mathbf{N}_\lambda^{(i)}\dot{\boldsymbol{\lambda}}_i; \tag{4.3.2}$$

the three-field interface problem can be rewritten in discretized form as:

$$\mathbf{M}_{\lambda u}^{(ic)}\mathbf{u}_c^\Gamma = \mathbf{M}_{\lambda u}^{(ii)}\mathbf{u}_i^\Gamma\,, \tag{4.3.3}$$

where the interface mass matrices are defined as:

$$\mathbf{M}_{\lambda u}^{(ij)} = \int_{\Gamma_{ci}} \mathbf{N}_\lambda^{(i)T}\mathbf{N}_u^{(j)}\, d\Gamma_{ci}\,. \tag{4.3.4}$$

Clearly, the shape functions $\mathbf{N}_u^{(i)}$ have to be the same as for the field discretization, while the shape functions $\mathbf{N}_\lambda^{(i)}$ can be chosen freely under the requirements of solvability of the above matrix system. This freedom of choice opens a broad range of possibilities for the multipliers, which will be the topic of the next subsections.

At this stage, it should be noted, that a matrix $\mathbf{M}_{\lambda u}^{(ii)}$ is quadratic due to the usage of the same interface grid for the shape function interpolation of $\boldsymbol{\lambda}_i$ and $\boldsymbol{u}_i$, i.e. $\boldsymbol{\lambda}_i$ is localized as discussed in section 2.5.1. On the other hand, the matrix $\mathbf{M}_{\lambda u}^{(ic)}$ is usually a rectangular matrix due to the different interface grid representation of the frame and field. Further, the numerical evaluation of $\mathbf{M}_{\lambda u}^{(ic)}$ is a non-trivial task, which requires some computational effort. The discussion of the evaluation will be expanded in an extra subsection.

For the direct two-field approach, a similar interface problem is obtained from Eq. (2.5.18):

$$\int_{\Gamma_{ij}} \delta\boldsymbol{\lambda}_{ij}^T \left(\boldsymbol{u}_i - \boldsymbol{u}_j\right) d\Gamma_{ij} = 0\,, \tag{4.3.5}$$

which leads with the aid of the shape function interpolation of Eq. (4.3.2) to the following matrix system:

$$\mathbf{M}_{\lambda u}^{(i)}\mathbf{u}_i^\Gamma = \mathbf{M}_{\lambda u}^{(j)}\mathbf{u}_j^\Gamma\,, \tag{4.3.6}$$

with the interface mass matrices:

$$\mathbf{M}_{\lambda u}^{(i)} = \int_{\Gamma_{ij}} \mathbf{N}_\lambda^T\mathbf{N}_u^{(i)}\, d\Gamma_{ij}\,. \tag{4.3.7}$$

Setting now the *i*th subdomain to be the fluid and the *j*th subdomain to be the structure according to Eq. (2.5.19), the interface matrix system can be rewritten as:

$$\mathbf{M}_{\lambda u}^{(f)}\mathbf{u}_f^\Gamma = \mathbf{M}_{\lambda u}^{(s)}\mathbf{u}_s^\Gamma\,. \tag{4.3.8}$$

In general both interface mass matrices are rectangular. But defining the Lagrange multiplier on one involved interface, at least one matrix can be made quadratic. Again, the other matrix then needs to be computed from shape functions defined on two different discrete interface representations. This evaluation of the interface mass matrix is described next.

4.3.1 Data transfer schemes based on the weak interface problem

In the next sections, some popular transfer schemes are introduced, which are often used in FSI problems. For simplicity, only the two-field approach will be considered, but the statements here could be easily adopted for the three-field approach too. The schemes only differ in the choice of the shape functions $\mathbf{N}_\lambda$ for the Lagrange multiplier field. Due to the weak formulation, all schemes share the property that they are conservative *a priori*. Another desired feature is accuracy of the transfer scheme, which is mainly influenced by $\mathbf{N}_\lambda$ and by the evaluation of the interface mass matrices.

Once the shape functions, $\mathbf{N}_\lambda$, have been chosen and the interface transfer matrices calculated, they also need to be used for the load transfer. Basically, the load transfer is provided by the exchange of the Lagrange multiplier represented through the first and second integral in Eq. (2.5.9) or Eq. (2.5.18). The reuse of the interface transfer matrices for the load transfer is also a result of the principle of virtual work, which can be written for discrete nodal values at the interface as:

$$\delta\mathbf{u}_f^{\Gamma T}\mathbf{f}_f^\Gamma = \delta\mathbf{u}_s^{\Gamma T}\mathbf{f}_s^\Gamma \,. \tag{4.3.9}$$

Assuming, that the displacement transfer is accomplished with the aid of a general rectangular coupling matrix $\mathbf{P}$ as:

$$\mathbf{u}_f^\Gamma = \mathbf{P}\mathbf{u}_s^\Gamma \,, \tag{4.3.10}$$

then the transfer of forces is obtained as the transposed scheme:

$$\mathbf{f}_s^\Gamma = \mathbf{P}^T\mathbf{f}_f^\Gamma \tag{4.3.11}$$

to ensure the principle of virtual work at the interface. Therefore, the load transfer is automatically specified by a given displacement transfer. Several types of transfer schemes can be constructed by defining proper shape functions $\mathbf{N}_\lambda$, which will discussed in the following sections.

4.3.2 Conservative interpolation

Taking the Dirac delta function on the fluid interface representation for the Lagrange multipliers, it can be shown, that the integral vanishes and the scheme reduces to the evaluation of the structural shape functions $\mathbf{N}_u^{(s)}$ at the fluid nodes position $\boldsymbol{x}_{f,i}$. The entries for the coupling matrix $\mathbf{P}$ are therefore:

$$\mathsf{P}_{ij} = \mathsf{N}_{u,j}^{(s)}(\boldsymbol{x}_{f,i}) \,. \tag{4.3.12}$$

The scheme is sketched principally in Figure 4.1(a) for a simple 1D problem, where the shape function on the fluid and structural interface are depicted together with the Dirac delta shape function used for the interpolation of the Lagrange multiplier. This transfer procedure is similar to that presented in [FLL98] and often referred to as conservative interpolation or node projection scheme, since the structural nodes on the interface are mapped to the closest fluid interface element and the transposed load transfer conserves the overall interface load from the fluid to the structure.

4.3.3 Galerkin's method

The conservative interpolation could lead to unphysical effects in terms of the load transfer, if two interface mesh sizes are highly different, [CL97]. An improvement is the use of the fluid shape functions for the Lagrange multipliers at the interface, Figure 4.1(b):

$$\mathbf{N}_\lambda = \mathbf{N}_u^{(f)} \,. \tag{4.3.13}$$

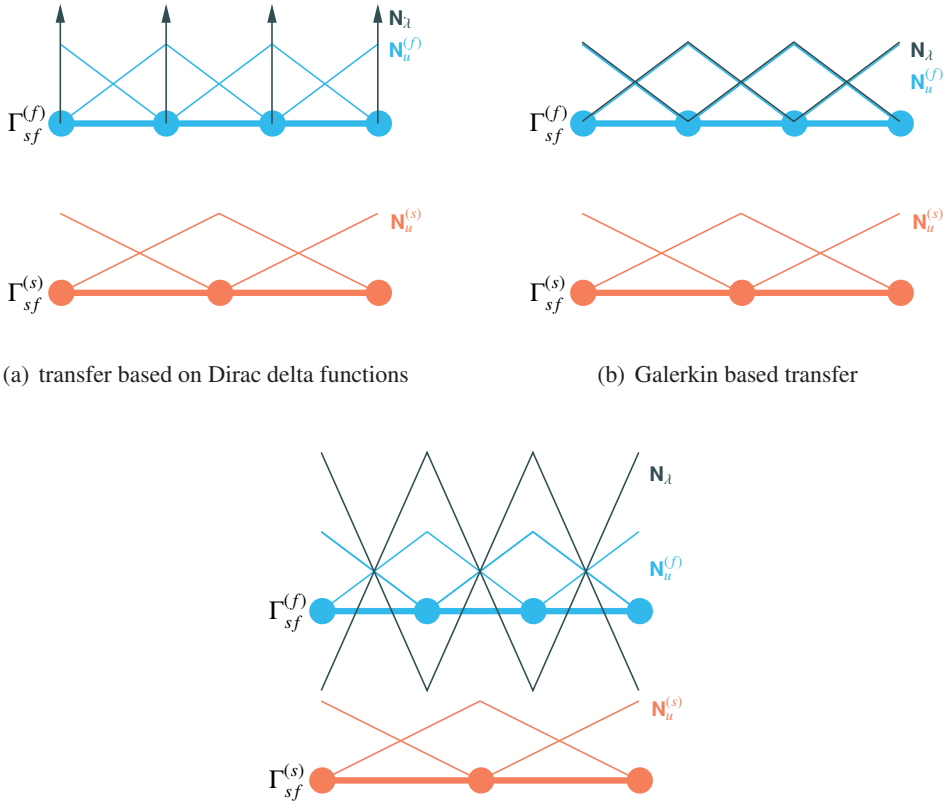

(a) transfer based on Dirac delta functions

(b) Galerkin based transfer

(c) dual-Lagrange based transfer

Figure 4.1: Principle sketches of simplified 1D transfer problems using different transfer schemes - fluid, structural and Lagrange shape functions on the interface grid representations

This choice is advantageous, since the matrix $\mathbf{M}_{\lambda u}^{(f)} = \check{\mathbf{M}}^{(ff)}$ is positive definite and thus regular. The transposed load transfer according to Eq. (4.3.11) is evaluated by:

$$\mathbf{f}_s^\Gamma = \check{\mathbf{M}}^{(sf)}[\check{\mathbf{M}}^{(ff)}]^{-1}\mathbf{f}_f^\Gamma = \check{\mathbf{M}}^{(sf)}\mathbf{t}_f^\Gamma\,, \tag{4.3.14}$$

where $\check{\mathbf{M}}^{(ff)}$ and $\mathbf{t}_f^\Gamma$ denote the mass matrix of the fluid interface and the discrete traction vector at the fluid interface, respectively. This scheme is equivalent to that proposed in [CL97] and also minimizes the L_2-norm of the jump of the traction field across the interface. The main difficulty lies in the computation of the matrix $\mathbf{M}_{\lambda u}^{(s)} = \check{\mathbf{M}}^{(sf)}$, which is done by the aid of N_{gp} quadrature points in each of the N_{ie} elements of an integration grid:

$$\check{\mathbf{M}}^{(sf)} = \int_{\Gamma_{sf}} \mathbf{N}_u^{(s)^T}\mathbf{N}_u^{(f)}\,d\Gamma_{sf} = \sum_{ie=1}^{N_{ie}}\sum_{gp=1}^{N_{gp}} \psi_{gp}\,\mathbf{N}_u^{(s)^T}(\boldsymbol{x}_{gp})\mathbf{N}_u^{(f)}(\boldsymbol{x}_{gp})\,, \tag{4.3.15}$$

where ψ_{gp} is the weight of the quadrature point. This scheme is frequently referred to as quadrature-projection scheme. For integration, either the fluid or the structural representation of the interface or an independent interface grid can be used. For curved interfaces, it is advisable to use an integration grid based on the fluid interface, as only then, an exact load conservation can be ensured [UHH07a].

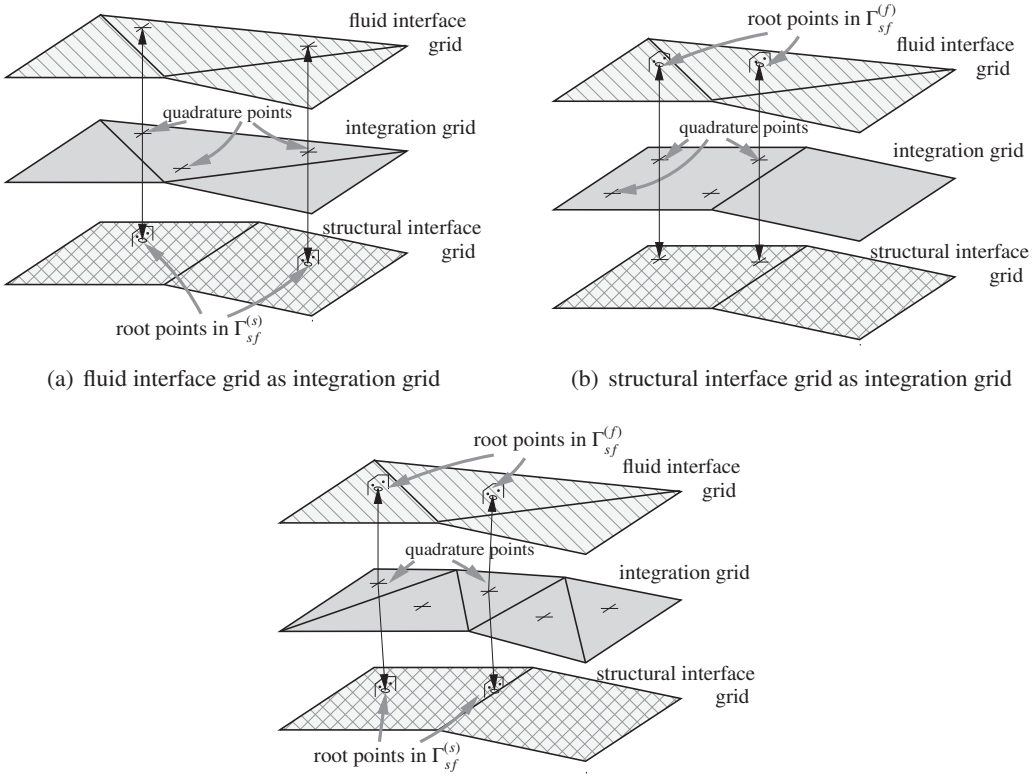

(a) fluid interface grid as integration grid

(b) structural interface grid as integration grid

(c) independent integration grid

Figure 4.2: Possibilities for the integration grids to calculate the transfer mass matrices

4.3.4 Dual-Lagrange multiplier

Although the matrix $\mathbf{M}_{\lambda u}^{(f)} = \check{\mathbf{M}}^{(ff)}$ in the Galerkin based interpolation is sparse and positive definite, the inversion process can be computational expensive in systems with many degrees of freedom. By choosing an appropriate space for the Lagrange multipliers depending on the shape functions of the fluid interface representation, this matrix can be diagonalized making the inversion process trivial. This is the idea of the so-called dual-Lagrange multipliers introduced in [Pus04, FPW05]. For instance, considering an interface discretized by quadrilateral elements with the shape functions being:

$$\mathsf{N}_{u,k}^{(f)} = \mathsf{N}_{u,ij}^{(f)} = \tfrac{1}{4}(1+\xi_1\xi_{1i})(1+\xi_2\xi_{2j}) \quad \text{where} \quad \xi_{1i} = \pm 1;\ \xi_{2j} = \pm 1\,, \tag{4.3.16}$$

where (ξ_1, ξ_2) are the local coordinates within a finite element. The corresponding shape functions for the Lagrange multipliers defined on the same discretization are:

$$\mathsf{N}_{\lambda,k} = \mathsf{N}_{\lambda,ij} = \tfrac{1}{4}(1+3\xi_1\xi_{1i})(1+3\xi_2\xi_{2j})\,. \tag{4.3.17}$$

A one-dimensional example on the dual-Lagrange multipliers is depicted in Figure 4.1(c). Appropriate dual-Lagrange multipliers according to higher order shape functions of the interface can be found likewise. The evaluation of the matrix $\mathbf{M}_{\lambda u}^{(s)} = \check{\mathbf{M}}^{(sf)}$ is accomplished by quadrature points too.

4.3.5 Minimizing the Sobolev-norm

As previously mentioned, the Galerkin based transfer also minimizes the jump of the displacements over the interface in the L_2 norm. An extended transfer can be constructed, which minimizes the Sobolev-norm:

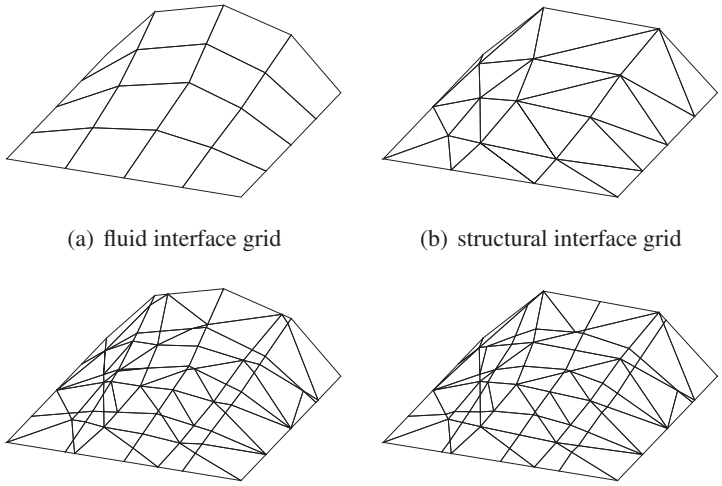

(a) fluid interface grid

(b) structural interface grid

(c) merged grid - fluid reference

(d) merged grid - structural reference

Figure 4.3: Construction of a merged grid as integration grid

$$\frac{\partial}{\partial \mathbf{u}_f^\Gamma}\left(\int_{\Gamma_{sf}} \sum_{n=0}^{q} \left|\varsigma_{SN,n}\mathcal{A}^n(\boldsymbol{u}_f - \boldsymbol{u}_s)\right|^2 \, d\Gamma_{sf}\right)^{\frac{1}{2}} = 0\,, \tag{4.3.18}$$

where $\mathcal{A}^n$ operates on a function to get the nth spatial derivative. With $q = 0$, and using the shape function interpolation, the Galerkin based transfer can be obtained, while with $q = 1$ the discretization process results in [JH04]:

$$\left(\check{\mathbf{M}}^{(ff)} + \varsigma_{SN}\check{\mathbf{K}}^{(ff)}\right)\mathbf{u}_f^\Gamma = \left(\check{\mathbf{M}}^{(fs)} + \varsigma_{SN}\check{\mathbf{K}}^{(fs)}\right)\mathbf{u}_s^\Gamma\,, \tag{4.3.19}$$

where $\check{\mathbf{K}}^{(ij)} = \int_{\Gamma_{sf}} \nabla\mathbf{N}_u^{(i)^T}\nabla\mathbf{N}_u^{(j)}\, d\Gamma_{sf}$ is the interface stiffness matrix and $\varsigma_{SN} = \varsigma_{SN,1}/\varsigma_{SN,0}$ denotes its weight. The transposed scheme is conservative due to the properties of the shape functions, but the system might be algebraically badly conditioned for specific choices of ς_{SN}. This transfer scheme can smooth a transfer value from a coarse to a fine mesh. Unfortunately, experience has shown that the transposed scheme can lead to locally unphysical oscillations.

4.3.6 Automatic generation of the integration grid

As already stated, a quadrature rule is used to compute the transfer mass matrices, where quadrature points defined on an integration grid are mapped perpendicularly to the interface grids, Figure 4.2. As can be seen from this figure, accuracy can be lost due to the violation of regularity, which is assumed by the quadrature rule, i.e. the quadrature points of one integration element are mapped to different elements of the fluid or structural interface.

Using an independent integration grid, the position and optimal number of the quadrature points can be found by computing a merged grid [JH04, JJGL05, HL03], which is constructed appropriately from the fluid and structural interface grids, Figure 4.3. Two characteristic possibilities of such a merged grid exist in a three-dimensional space, which have the same topology but different geometric references, Figure 4.3(c) and 4.3(d). While the structural interface grid of Figure 4.3(b) is mapped onto the fluid interface mesh in Figure 4.3(c), the fluid interface grid is mapped onto the structural interface representation in Figure 4.3(d).

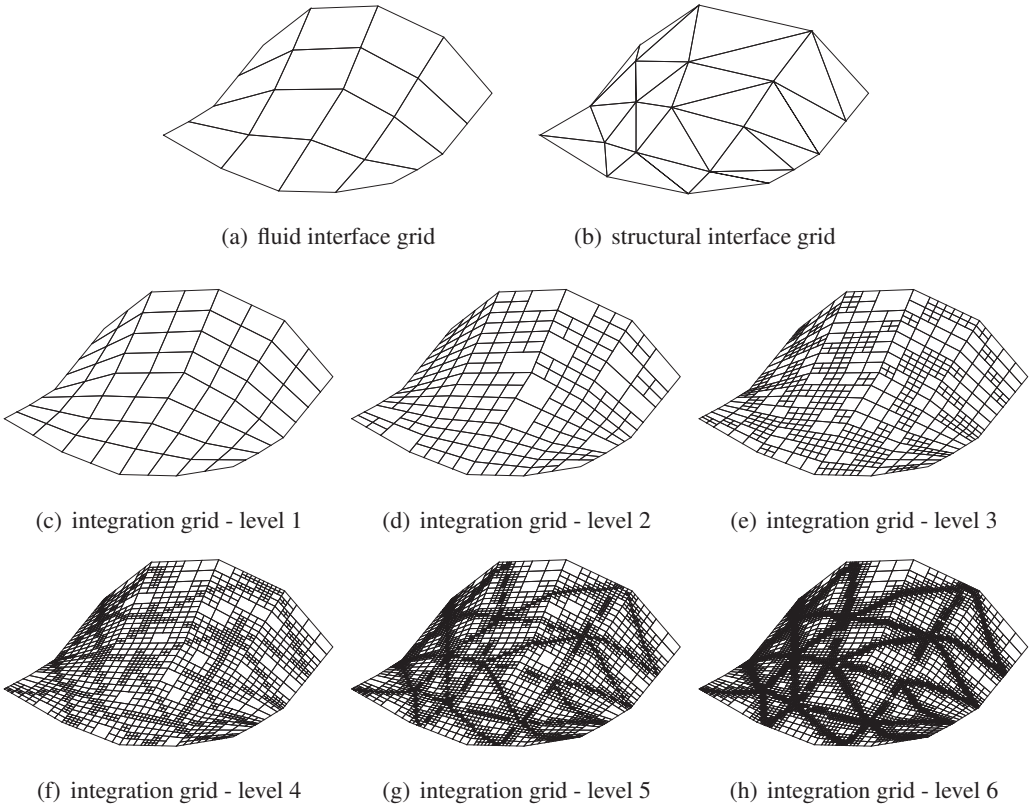

(a) fluid interface grid (b) structural interface grid

(c) integration grid - level 1 (d) integration grid - level 2 (e) integration grid - level 3

(f) integration grid - level 4 (g) integration grid - level 5 (h) integration grid - level 6

Figure 4.4: Adaptive refinement of the integration grid

Using a grid like this, the regularity assumption of the quadrature remains valid, and the accuracy can be improved noticeably. The main loss of accuracy is then due to the so-called faceting error, which occurs due to a point projection on a curved surface. A natural choice and applied here, is the projection of quadrature points carried out perpendicularly to the target surface mesh.

Since the automatic construction of a merged mesh is a non-trivial and error-prone task in three dimensions, it is computationally more robust to use an adaptive quadtree-based h-refinement of the integration mesh. In Figure 4.4, a sequence of refinement levels of the integration grid is depicted, whereby the integration grid is initially set to the fluid interface grid. New elements in the integration elements, and therefore more quadrature points, are introduced in the vicinity of the fluid mesh edges, which is best seen in Figure 4.4(f) to 4.4(h). The refinement is based on a hierarchical balanced quadtree data structure of the integration mesh and the criterion for an element refinement is the adherence of the quadrature regularity rule, i.e. if all quadrature points of one integration element are associated with the same projection element. This criterion might lead to infinitely small integration elements and a termination criterion needs to be evaluated.

4.3.7 Patch-test

With the patch-test, a transfer scheme can be checked in terms of its accuracy. The test has its origin in general finite element procedures for mechanical problems and is a necessary condition for convergence [Bat96, ZTZ05]. For the finite element data transfer schemes, the patch-test is passed, if a constant stress can be transmitted from one to the other interface grid.

In the case of non-curved (flat) or nested surfaces, the interfaces are geometrically coincident and an exact integration is achieved with merged meshes [DB06, HL03]. Therefore, the patch-

test is passed, if the shape functions for the Lagrange multiplier are defined in an appropriate space [EB01]. Using the adaptive refinement of the integration mesh, the integration is performed approximately exact and thus the patch-test can only be passed within a certain tolerance.

On non-coincident (curved) interfaces, the patch-test is *per se* not passed due to the faceting error [Pus04, DB06, HL03]. Utilizing the Galerkin based transfer for the transfer of tractions, Eq. (4.3.14) yields:

$$\mathbf{t}_s^\Gamma = [\check{\mathbf{M}}^{(ss)}]_{\text{struct}}^{-1}\check{\mathbf{M}}^{(sf)}\mathbf{t}_f^\Gamma\,, \tag{4.3.20}$$

where $[\check{\mathbf{M}}^{(ss)}]_{\text{struct}}$ is the structural interface mass matrix usually evaluated on the structural interface mesh indicated by the subscript $[]_{\text{struct}}$. The failure of the patch-test is caused by geometric discrepancy of the coupled surface grids and the evaluation of $[\check{\mathbf{M}}^{(ss)}]_{\text{struct}}$ and $\check{\mathbf{M}}^{(sf)}$ on different surface grids.

Evaluating the structural interface mass matrix in contrast on the integration mesh, i.e. using $[\check{\mathbf{M}}^{(ss)}]_{\text{int}}$ instead of $[\check{\mathbf{M}}^{(ss)}]_{\text{struct}}$, the same surface Jacobian's for both surface mass matrices in Eq. (4.3.20) are used and the patch-test is passed [HL03]. However, the resulting transfer scheme will not be conservative, since on curved interface surfaces usually

$$[\check{\mathbf{M}}^{(ss)}]_{\text{struct}}[\check{\mathbf{M}}^{(ss)}]_{\text{int}}^{-1} \neq \boldsymbol{I} \tag{4.3.21}$$

holds, where $\boldsymbol{I}$ is the identity matrix. Nevertheless, in the case of convergence, i.e. fine interface grids, the interface geometries become coincident and the patch-test will be passed using Eq. (4.3.20).

In summary, a transfer scheme is desired, which is load conservative as well as accurate in terms of passing the patch test. However, on arbitrary curved interface grids only one of these properties can be achieved and in this thesis, a scheme that is unconditional load conservative is preferred.

4.3.8 Evaluation of the coupling matrix using the adaptive refinement of the integration grid

It remains to define a termination criterion for usage of the adaptive refinement of the integration grid. Otherwise and as mentioned above, the adaptive mesh refinement may lead to infinitely small integration elements. Therefore, a maximum level of refinements can be provided or alternatively, further element refinements are not allowed once the element size has reached a certain minimum value.

Further, a termination criterion can be provided through the patch-test. Thus, after each refinement level of the integration mesh, the patch-test is performed. The resulting tractions on the target interface should reach unity, if the interface meshes are flat or nested and the integration is performed exactly. Any discrepancy of the nodal target tractions from unity $(1 + \text{err}_{loc})$ can be used to localize integration elements with a significant integration error, which are labeled for potential refinement. Is the discrepancy within a user-specified tolerance or within the machine accuracy, no further refinement is required. On curved interfaces, the patch-test is only passed within a tolerance due to faceting error and the criterion of tractions equal to unity is replaced with the criterion that the tractions will not change within the tolerance err_{loc} from one refinement level to the next. A global criterion to terminate the refinement procedure is provided by the relative error in the L_2 norm for a load transfer of a constant pressure field:

$$\|\text{err}\|_2 = \sqrt{\frac{\int\limits_{\Gamma_{sf}} (p_f - p_s)^2\, d\Gamma_{sf}}{\int\limits_{\Gamma_{sf}} p_f^2\, d\Gamma_{sf}}} \approx \sqrt{\frac{\sum\limits_{i=1}^{N_{n,s}} (\mathsf{p}_{f,i} - \mathsf{p}_{s,i})^2 \mathsf{A}_{s,i}}{\sum\limits_{i=1}^{N_{n,f}} \mathsf{p}_{f,i}^2 \mathsf{A}_{f,i}}} < \varsigma_T\,, \tag{4.3.22}$$

where $\mathsf{A}_{s,i}$, $\mathsf{A}_{f,i}$ are the areas associated with the node i, $N_{n,s}$ and $N_{n,f}$ denote the number of structural and fluid interface nodes, and ς_T is a user-defined tolerance for the data transfer.

4.4 Solution of the discrete two-field approach

With the given ingredients of the coupled solution described in the previous sections, the discrete two-field approach of Eq. (2.5.19) can be developed to obtain for the interface:

$$\begin{array}{r} \text{Fluid:} \\ \text{Structure:} \\ \text{State Transfer:} \end{array} \begin{bmatrix} \mathcal{F} & 0 & -\mathcal{M}_{ff} \\ 0 & \mathcal{S} & \mathcal{M}_{sf} \\ -\mathcal{M}_{ff} & \mathcal{M}_{fs} & 0 \end{bmatrix} \begin{bmatrix} \mathbf{u}_f^\Gamma \\ \mathbf{u}_s^\Gamma \\ \acute{\boldsymbol{\lambda}} \end{bmatrix} = \begin{bmatrix} \mathbf{0} \\ \mathbf{f}_s^\Gamma \\ \mathbf{0} \end{bmatrix}, \tag{4.4.1}$$

where for consistency a full operational view is used and it is assumed, that external forces are applied on the structural side of the interface only. In the above equation, the $\mathcal{M}$-operators are the interface mass matrices defined in Eq. (4.3.7):

$$\mathcal{M}_{ff} = \mathbf{M}_{\lambda u}^{(f)}; \qquad \mathcal{M}_{fs} = \mathbf{M}_{\lambda u}^{(s)}; \qquad \mathcal{M}_{sf} = \mathbf{M}_{\lambda u}^{(s)^T}.$$

Eq. (4.4.1) represents the classical coupling approach for FSI problems with the unknowns $\mathbf{u}_f^\Gamma$, $\mathbf{u}_s^\Gamma$, and $\acute{\boldsymbol{\lambda}}$ on the interface. With a partitioned coupling approach and taking into account that the fluid is treated as a Dirichlet and the structure as a Neumann problem, the system reduces to:

$$\mathbf{u}_s^\Gamma = \mathcal{S}^{-1} \circ (\mathbf{f}_s^\Gamma - \mathcal{M}_{sf} \circ \underbrace{\mathcal{M}_{ff}^{-1} \circ \mathcal{F} \circ \underbrace{\mathcal{M}_{ff}^{-1} \circ \mathcal{M}_{fs} \circ \mathbf{u}_s^\Gamma}_{=\mathbf{u}_f^\Gamma}}_{=\acute{\boldsymbol{\lambda}}}). \tag{4.4.2}$$

Here, it can be seen, that the operator $\mathcal{M}_{ff}^{-1}$ is used in its inverted form, i.e. a system with the matrix $\mathbf{M}_{\lambda u}^{(f)}$ needs to be solved. This is consistent with defining the Lagrange multiplier on the fluid side of the interface as it is shown for the data transfer schemes discussed above.

Without access to the matrices of each solver $\mathcal{S}$ or $\mathcal{F}$, the classical Richardson iteration can be used to find a solution of the reduced system (4.4.2):

$$\mathbf{u}_{s,k+1}^\Gamma = \varsigma_{RI} \underbrace{\mathcal{S}^{-1} \circ (\mathbf{f}_s^\Gamma - \mathcal{M}_{sf} \circ \mathcal{M}_{ff}^{-1} \circ \mathcal{F} \circ \mathcal{M}_{ff}^{-1} \circ \mathcal{M}_{fs} \circ \mathbf{u}_{s,k}^\Gamma)}_{\check{\mathbf{u}}_{s,k+1}^\Gamma} + (1 - \varsigma_{RI}) \mathbf{u}_{s,k}^\Gamma, \tag{4.4.3}$$

where ς_{RI} is the user defined relaxation parameter for the Richardson iteration, which is usually in the range of 0.5 to 0.9. Here, in each iteration a Dirichlet-Neumann (DN) step, $\mathcal{F}$-$\mathcal{S}^{-1}$ is invoked to get the displacement field of the fluid and structure on the interface, respectively. For weak coupled problems, usually a small number of iterations is needed to find the equilibrium state. For strong coupled problems, the relaxation parameter ς_{RI} needs to be reduced to very small values and the number of iterations increases considerably. In such situations it may be better to use higher class iteration procedures in particular Krylov subspace methods.

To apply such methods, a non-linear vector function needs to be generated, which for the reduced system can be obtained as:

$$\mathbf{R}(\mathbf{u}_s^\Gamma) = \mathcal{S}^{-1}(\mathbf{f}_s^\Gamma - \mathcal{M}_{sf} \circ \mathcal{M}_{ff}^{-1} \circ \mathcal{F} \circ \mathcal{M}_{ff}^{-1} \circ \mathcal{M}_{fs} \circ \mathbf{u}_s^\Gamma) - \mathbf{u}_s^\Gamma = \mathbf{0}. \tag{4.4.4}$$

To find a solution $\mathbf{u}_s^\Gamma$, which satisfies $\mathbf{R} = \mathbf{0}$, the Newton-GMRES method can be applied, see [Kel95] for algorithmic details. Other methods to solve $\mathbf{R} = \mathbf{0}$, like the Bi-CGSTAB iteration,

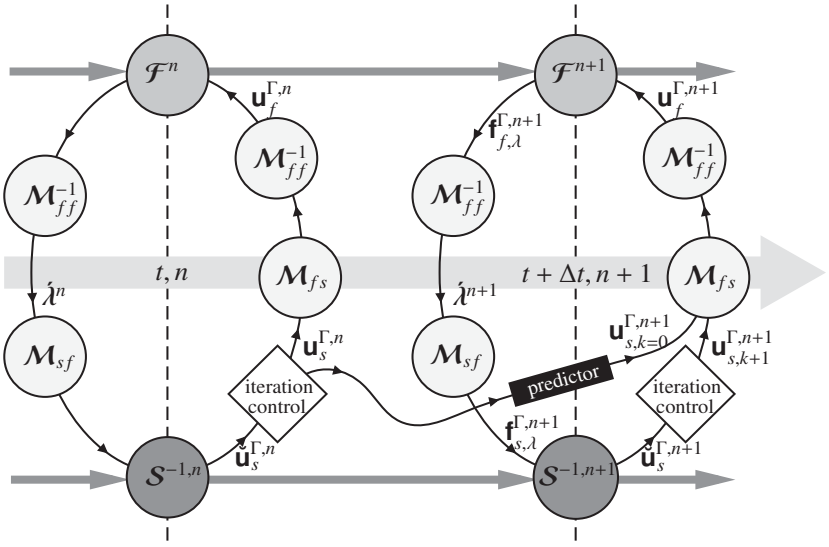

Figure 4.5: Time integration and equilibrium iteration for the two-field problem

were investigated in [Ste02]. Comparison of different iteration methods for a simplified structure-structure coupled problem can be found in [Nie09].

However, all methods share the property, that a full DN step has to be carried out for one iteration. From a computational point of view, the most expensive part is to solve the fluid problem. Therefore, the number of iterations should be reduced whenever possible. Using the Newton-GMRES method for the iteration, at least three DN steps per iteration are needed, which makes this method only applicable for strong coupled problems, where several iterations are needed anyway. For transient problems, where in each time step such iteration is required, reducing the number of DN steps is even more attractive.

The principal sketch of solving a transient coupled problem with the two-field approach is depicted in Figure 4.5. For the time $t + \Delta t$, the fluid interface displacements $\mathbf{u}_f^{\Gamma,n+1}$ are calculated from an initial guess for the structural interface displacements $\mathbf{u}_{s,k=0}^{\Gamma,n+1}$ using finite element data transfer. With these displacements, the fluid part of the coupled problem is advanced from the time t to $t + \Delta t$ involving the grid deformation $\mathcal{G}$, the calculation of the grid velocities $\mathcal{W}$ and the CBS scheme $\mathcal{C}$. With calling the fluid operator $\mathcal{F}$, the fluid interface forces $\mathbf{f}_{f,\lambda}^{\Gamma,n+1}$ are obtained and the discrete Lagrange multiplier field $\dot{\lambda}^{n+1} = \mathcal{M}_{ff}^{-1}\mathbf{f}_{f,\lambda}^{\Gamma,n+1}$ is calculated. This Lagrange multiplier field is transmitted to the structural side of the interface and updated interface displacements $\check{\mathbf{u}}_s^{\Gamma,n+1}$ are obtained by advancing the structural part of the coupled problem from the time t to $t + \Delta t$. Depending on the iteration method used (Richardson iteration, Newton-GMRES, etc.), an iteration control instance updates to the interface displacements $\mathbf{u}_{s,k+1}^{\Gamma,n+1}$ by e.g. relaxation. Further iterations can be run or the iteration procedure breaks and the next time level is considered.

Using the Richardson iteration with $\varsigma_{RI} = 1$ and setting the maximum number of iteration for each time level to one, the simple staggered scheme or loose coupling method is obtained, which is often used for transient weak coupled problems. However, the simple staggered approach is usually only stable for a certain time step Δt.

To improve the accuracy of the simple staggered scheme, an appropriate predictor can be used for the initially estimated structural interface displacements $\mathbf{u}_{s,k=0}^{\Gamma,n+1}$. Several choices are available [Pip97]:

$$\mathbf{u}_{s,k=0}^{\Gamma,n+1} = \mathbf{u}_s^{\Gamma,n} + \Delta t\, \dot{\mathbf{u}}_s^{\Gamma,n} \tag{4.4.5}$$

$$\mathbf{u}_{s,k=0}^{\Gamma,n+1} = \mathbf{u}_s^{\Gamma,n} + \frac{\Delta t}{2}\left(3\dot{\mathbf{u}}_s^{\Gamma,n} - \dot{\mathbf{u}}_s^{\Gamma,n-1}\right) \tag{4.4.6}$$

$$\mathbf{u}_{s,k=0}^{\Gamma,n+1} = \mathbf{u}_s^{\Gamma,n} + \Delta t\, \dot{\mathbf{u}}_s^{\Gamma,n} + \frac{\Delta t^2}{2}\, \ddot{\mathbf{u}}_s^{\Gamma,n} \tag{4.4.7}$$

$$\mathbf{u}_{s,k=0}^{\Gamma,n+1} = \mathcal{S}^{-1,n+1}(\mathbf{f}_s^{\Gamma} - \mathbf{f}_{s,\lambda}^{\Gamma,n})\,. \tag{4.4.8}$$

The predictor of Eq. (4.4.5) is first order time accurate, while the predictor (4.4.6) and (4.4.7) are second order accurate. With the dual-time stepping scheme within the fluid solver presented in section 3.4.6, a second order time accuracy in the time integration scheme of the whole coupled system can be reached with the predictor (4.4.6), [FvdZG06]. The predictor (4.4.8) is basically a pre-computation of the structure with the forces at the interface from the previous time step. Thus, the time accuracy order of this predictor depends on the order of the time integration scheme within the structural solver, which is usually second order. Good experience with the predictor (4.4.8) could be obtained, if the coupled problem involves also rigid body motion of the interface.

4.5 Solution of the discrete three-field approach

Analogous to the two-field problem of Eq. (4.4.1), the discrete three-field approach of Eq. (2.5.9) can be obtained for the interface as:

$$\begin{array}{r} \text{Fluid:} \\ \text{Structure:} \\ \text{Transfer Fluid:} \\ \text{Transfer Structure:} \\ \text{Frame:} \end{array} \begin{bmatrix} \mathcal{F} & 0 & \mathcal{M}_{ff} & 0 & 0 \\ 0 & \mathcal{S} & 0 & \mathcal{M}_{ss} & 0 \\ \mathcal{M}_{ff} & 0 & 0 & 0 & -\mathcal{M}_{fc} \\ 0 & \mathcal{M}_{ss} & 0 & 0 & -\mathcal{M}_{sc} \\ 0 & 0 & -\mathcal{M}_{cf} & -\mathcal{M}_{cs} & 0 \end{bmatrix} \begin{bmatrix} \mathbf{u}_f^{\Gamma} \\ \mathbf{u}_s^{\Gamma} \\ \lambda_f \\ \lambda_s \\ \mathbf{u}_c \end{bmatrix} = \begin{bmatrix} \mathbf{0} \\ \mathbf{f}_s^{\Gamma} \\ \mathbf{0} \\ \mathbf{0} \\ \mathbf{0} \end{bmatrix}, \tag{4.5.1}$$

where the fluid and structural operators $\mathcal{F}$ and $\mathcal{S}$ involve the computations of all fluid and structural subdomains, respectively. The matrix operators are defined similarly to the two-field approach and according to Eq. (4.3.4) as:

$$\mathcal{M}_{ff} = \mathbf{M}_{\lambda u}^{(ff)}; \qquad \mathcal{M}_{ss} = \mathbf{M}_{\lambda u}^{(ss)}; \qquad \mathcal{M}_{fc} = \mathbf{M}_{\lambda u}^{(fc)};$$
$$\mathcal{M}_{sc} = \mathbf{M}_{\lambda u}^{(sc)}; \qquad \mathcal{M}_{cf} = \mathbf{M}_{\lambda u}^{(fc)^T}; \qquad \mathcal{M}_{cs} = \mathbf{M}_{\lambda u}^{(sc)^T}\,.$$

Using the three-field approach, the coupling between the two types of subdomains are performed through the two Lagrange-multiplier fields λ_f and λ_s. It is important to remember here, that each Lagrange multiplier field is defined on their corresponding subdomain, i.e. they are localized [PF00]. This basically means, that each subdomain is only connected to the frame. Further, the frame displacement field can be discretized independently of each subdomain connected to the frame. This provides an additional feature of constructing a smooth transfer by using higher order elements for the frame displacements $\boldsymbol{u}_c$, i.e. using a $C1$-continuity shape function like Hermitian shape functions [Bat96, ZTZ05]. However, a solution of Eq. (4.5.1) in a partitioned way is usually difficult to obtain, especially if a simple staggered scheme is desired.

Without any assumption, the system (4.5.1) can be reduced to obtain:

$$\underbrace{\begin{bmatrix} \mathcal{M}_{ss} \circ \mathcal{S}^{-1} \circ \mathcal{M}_{ss} & \mathcal{M}_{sc} \\ -\mathcal{M}_{cs} & \mathcal{M}_{cf} \circ \mathcal{M}_{ff}^{-1} \circ \mathcal{F} \circ \mathcal{M}_{ff}^{-1} \circ \mathcal{M}_{fc} \end{bmatrix}}_{=\mathcal{B}} \begin{bmatrix} \lambda_s \\ \mathbf{u}_c \end{bmatrix} = \begin{bmatrix} \mathcal{M}_{ss} \circ \mathcal{S}^{-1} \circ \mathbf{f}_s^{\Gamma} \\ \mathbf{0} \end{bmatrix}. \tag{4.5.2}$$

This system can be solved using an iterative method, e.g. Newton-GMRES, by introducing the residual as a vector function $\mathbf{R}(\acute{\boldsymbol{\lambda}}_s, \mathbf{u}_c)$:

$$\mathbf{R}(\acute{\boldsymbol{\lambda}}_s, \mathbf{u}_c) = \mathcal{B}\begin{bmatrix} \acute{\boldsymbol{\lambda}}_s \\ \mathbf{u}_c \end{bmatrix} - \begin{bmatrix} \boldsymbol{\mathcal{M}}_{ss} \circ \boldsymbol{\mathcal{S}}^{-1} \circ \mathbf{f}_s^{\Gamma} \\ \mathbf{0} \end{bmatrix}. \tag{4.5.3}$$

Due to the different physical nature of $\acute{\boldsymbol{\lambda}}_s$ and $\mathbf{u}_c$ the system matrix operator $\mathcal{B}$ might be badly conditioned and a scaling/ preconditioning of $\mathcal{B}$ needs to be used to obtain reasonable results.

A further reduction of Eq. (4.5.2) is possible with the assumption, that the matrix behind $\boldsymbol{\mathcal{M}}_{sc}$ has more rows than columns. i.e.:

$$N_{DOF,c} \leq N_{DOF,s}\,, \tag{4.5.4}$$

where $N_{DOF,c}$ and $N_{DOF,s}$ are the number of degrees of freedom for the frame and structural interface, respectively. Then, the frame displacement field can be computed with the assistance of the Moore-Penrose pseudo-inverse $\boldsymbol{\mathcal{M}}_{cs}^{+}$ as, [LH87]:

$$\mathbf{u}_c = \underbrace{(\boldsymbol{\mathcal{M}}_{cs} \circ \boldsymbol{\mathcal{M}}_{sc})^{-1} \circ \boldsymbol{\mathcal{M}}_{cs}}_{\boldsymbol{\mathcal{M}}_{cs}^{+}} \circ \boldsymbol{\mathcal{M}}_{ss} \circ \mathbf{u}_s^{\Gamma}\,, \tag{4.5.5}$$

which is equivalent to solve a least square problem for the fourth equation of Eq. (4.5.1). With this pseudo inverse, the three-field system further reduces to:

$$\underbrace{\boldsymbol{\mathcal{M}}_{cf} \circ \boldsymbol{\mathcal{M}}_{ff}^{-1} \circ \boldsymbol{\mathcal{F}} \circ \boldsymbol{\mathcal{M}}_{ff}^{-1} \circ \boldsymbol{\mathcal{M}}_{fc} \circ \boldsymbol{\mathcal{M}}_{cs}^{+} \circ \boldsymbol{\mathcal{M}}_{ss} \circ \boldsymbol{\mathcal{S}}^{-1} \circ (\mathbf{f}_s^{\Gamma} - \boldsymbol{\mathcal{M}}_{ss} \circ \acute{\boldsymbol{\lambda}}_s)}_{=\mathbf{f}_c} = \underbrace{\boldsymbol{\mathcal{M}}_{cs} \circ \acute{\boldsymbol{\lambda}}_s}_{=\mathbf{f}_c}\,. \tag{4.5.6}$$

Both sides of this equation represents the force field $\mathbf{f}_c$ on the frame. To use this fact to construct an iterative procedure, it remains to find a way to calculate the vector $\acute{\boldsymbol{\lambda}}_s$ from $\mathbf{f}_c$. Again the principle of virtual work, Eq. (4.3.9), can be utilized to find:

$$\acute{\boldsymbol{\lambda}}_s = \boldsymbol{\mathcal{M}}_{cs}^{+\,T} \circ \mathbf{f}_c = \boldsymbol{\mathcal{M}}_{sc} \circ (\boldsymbol{\mathcal{M}}_{cs} \circ \boldsymbol{\mathcal{M}}_{sc})^{-1} \circ \mathbf{f}_c\,. \tag{4.5.7}$$

Finally, a DN step for the three-field approach can be constructed as:

$$\mathbf{f}_c = \boldsymbol{\mathcal{M}}_{cf} \circ \boldsymbol{\mathcal{M}}_{ff}^{-1} \circ \boldsymbol{\mathcal{F}} \circ \boldsymbol{\mathcal{M}}_{ff}^{-1} \circ \boldsymbol{\mathcal{M}}_{fc} \circ \boldsymbol{\mathcal{M}}_{cs}^{+} \circ \boldsymbol{\mathcal{M}}_{ss} \circ \boldsymbol{\mathcal{S}}^{-1} \circ (\mathbf{f}_s^{\Gamma} - \boldsymbol{\mathcal{M}}_{ss} \circ \boldsymbol{\mathcal{M}}_{cs}^{+\,T} \circ \mathbf{f}_c)\,, \tag{4.5.8}$$

with

$$\boldsymbol{\mathcal{M}}_{cs}^{+\,T} = \boldsymbol{\mathcal{M}}_{sc} \circ (\boldsymbol{\mathcal{M}}_{cs} \circ \boldsymbol{\mathcal{M}}_{sc})^{-1}\,. \tag{4.5.9}$$

Usually, it is advantageous to proceed the DN step for the frame displacement field and a reordering of the above equation thus leads to:

$$\mathbf{u}_c = \boldsymbol{\mathcal{M}}_{cs}^{+} \circ \boldsymbol{\mathcal{M}}_{ss} \circ \boldsymbol{\mathcal{S}}^{-1} \circ (\mathbf{f}_s^{\Gamma} - \boldsymbol{\mathcal{M}}_{ss} \circ \boldsymbol{\mathcal{M}}_{cs}^{+\,T} \circ \boldsymbol{\mathcal{M}}_{cf} \circ \boldsymbol{\mathcal{M}}_{ff}^{-1} \circ \boldsymbol{\mathcal{F}} \circ \boldsymbol{\mathcal{M}}_{ff}^{-1} \circ \boldsymbol{\mathcal{M}}_{fc} \circ \mathbf{u}_c)\,. \tag{4.5.10}$$

To directly compare this DN step with the two-field approach, the operator chain can be accomplished for the structural displacement field as:

$$\mathbf{u}_s^{\Gamma} = \boldsymbol{\mathcal{S}}^{-1} \circ (\mathbf{f}_s^{\Gamma} - \boldsymbol{\mathcal{M}}_{ss} \circ \boldsymbol{\mathcal{M}}_{cs}^{+\,T} \circ \boldsymbol{\mathcal{M}}_{cf} \circ \boldsymbol{\mathcal{M}}_{ff}^{-1} \circ \boldsymbol{\mathcal{F}} \circ \boldsymbol{\mathcal{M}}_{ff}^{-1} \circ \boldsymbol{\mathcal{M}}_{fc} \circ \boldsymbol{\mathcal{M}}_{cs}^{+} \circ \boldsymbol{\mathcal{M}}_{ss} \circ \mathbf{u}_s^{\Gamma})\,. \tag{4.5.11}$$

Comparing this DN step with the one obtained from the two-field approach of Eq. (4.4.2), the three-field matrices can be identified as:

$$\boldsymbol{\mathcal{M}}_{ss} \circ \boldsymbol{\mathcal{M}}_{cs}^{+\,T} \circ \boldsymbol{\mathcal{M}}_{cf} \mathrel{\hat{=}} \boldsymbol{\mathcal{M}}_{sf}; \qquad \boldsymbol{\mathcal{M}}_{fc} \circ \boldsymbol{\mathcal{M}}_{cs}^{+} \circ \boldsymbol{\mathcal{M}}_{ss} \mathrel{\hat{=}} \boldsymbol{\mathcal{M}}_{fs} = \boldsymbol{\mathcal{M}}_{sf}^{T}\,. \tag{4.5.12}$$

Therefore, the same iteration methods can be used for the three-field approach as for the two-field approach. Especially, a simple staggered procedure, which results from the Richardson iteration by setting $\varsigma_{RI} = 1$ and $k_{max} = 1$, can be used here including a predictor $\mathbf{u}_{s,k=0}^{\Gamma,n+1}$. The advantage of the three-field approach lies in the independent discretization of the frame and that each subdomain is connected to frame only.

4.6 Consistent time integration

As already discussed in section 3.4.6, the fluid domain is usually time resolved with a second order time-accurate three-point backward difference scheme. Furthermore and as seen from Eq. (3.4.19), the grid velocities arising due to a grid motion use the same time discretization scheme as the primary fluid variables.

On the other hand, the spatially discretized structural subsystem is usually solved with the aid of the Newmark method, see [Hug00] for an introduction. Using the approximation $\mathbf{d}_s^n$, $\mathbf{v}_s^n$ and $\mathbf{a}_s^n$ for $\mathbf{u}_s(t)$, $\dot{\mathbf{u}}_s(t)$ and $\ddot{\mathbf{u}}_s(t)$, respectively, the structural system to solve is written as:

$$\begin{aligned} & \mathbf{M}_u \mathbf{a}_s^{n+1} + \mathbf{f}_{u,\text{int}}(\mathbf{d}_s^{n+1}) = \mathbf{f}_{u,\text{ext}} \\ \text{with} \quad & \mathbf{d}_s^{n+1} = \mathbf{d}_s^n + \Delta t \mathbf{v}_s^n + \frac{\Delta t^2}{2}([1 - 2\varsigma_\beta]\,\mathbf{a}_s^n + 2\varsigma_\beta\,\mathbf{a}_s^{n+1}) \\ & \mathbf{v}_s^{n+1} = \mathbf{v}_s^n + \Delta t([1 - \varsigma_\gamma]\,\mathbf{a}_s^n + \varsigma_\gamma\,\mathbf{a}_s^{n+1})\,. \end{aligned} \tag{4.6.1}$$

If the Newmark parameters ς_β and ς_γ are set to $\varsigma_\beta = 0.25$ and $\varsigma_\gamma = 0.5$, the scheme is second order time accurate and similar to the trapezoidal rule.

Compared to Eq. (3.4.19), the structural velocities are computed with a different scheme, i.e. $\mathbf{v}_s$ and $\mathbf{w}_f$ are inconsistently approximated, although both subdomains are treated with second order time accurate integration schemes. To circumvent this inconsistency, the structural accelerations as well as the velocities can temporally be discretized with a three-point backward difference scheme:

$$\mathbf{a}_s^{n+1} = \frac{3\mathbf{v}_s^{n+1} - 4\mathbf{v}_s^n + \mathbf{v}_s^{n-1}}{2\Delta t}; \qquad \mathbf{v}_s^{n+1} = \frac{3\mathbf{d}_s^{n+1} - 4\mathbf{d}_s^n + \mathbf{d}_s^{n-1}}{2\Delta t}\,, \tag{4.6.2}$$

which results in solving the structural problem including non-linearities as:

$$\frac{1}{4\Delta t^2}\mathbf{M}_u(9\mathbf{d}_s^{n+1} - 12\mathbf{d}_s^n + 3\mathbf{d}_s^{n-1} - 8\Delta t\mathbf{v}_s^n + 2\Delta t\mathbf{v}_s^{n-1}) + \mathbf{f}_{u,\text{int}}(\mathbf{d}_s^{n+1}) = \mathbf{f}_{u,\text{ext}}\,. \tag{4.6.3}$$

This scheme is second order time accurate and consistent with the time integration scheme of the fluid domain.

4.7 Chapter summary

In this chapter, the numerical scheme based on finite elements for the coupled aeroelastic problem is presented. An operational view is employed for each coupling part, starting with the structural subdomain, where the structural interface operator is intentified as the Schur complement. The fluid grid needs to be adapted due to the structural displacements at the interface. A pseudo-structural approach is used for this fluid grid deformation, where the material parameters can be chosen regardless of any physical correctness.

A further important coupling aspect is the data transfer across non-matching interface grids. From the weak coupling conditions presented in chapter 2, different discrete data transfer schemes are derived, which share the property of load and energy conservation. To improve the accuracy of the transfer, a h-refinement of the integration grid is proposed.

Furthermore, the numerical time integration and the equilibrium iteration are discussed for the two-field approach. For the three-field approach, the same coupling matrices are identified, which alreay appeared within the iteration process of the two-field approach. Thus, no change for the iteration scheme itself is needed when conducting the three-field approach.

Moreover, the fact, that usually both - fluid and structure - are treated with different numerical time integration schemes, is overcome by a proposed consistent time integration approach for the structure, so that both subsystems use the same temporal discretization for the interface velocity.

Part II

Verification and Application

5 Verification of the CBS Scheme

In this chapter, the performance and properties of the CBS scheme are shown for examples of pure fluid motion on fixed grids, i.e. $\boldsymbol{w}_f = \boldsymbol{0}$ and $\boldsymbol{s}_f = \boldsymbol{v}_f$. To solve such flow problems, the CBS scheme is coded in an object-oriented way using the programming language C++ and the multi-processing programming interface OpenMP. Compressible inviscid, laminar viscous and turbulent viscous fluid flows over the NACA0012 airfoil are shown and compared with data provided in literature. Furthermore, unsteady as well as incompressible flow is tested for well-documented flow problems.

5.1 Inviscid flow past the NACA0012 airfoil

First of all, a flow problem, where all viscous effects are neglected, is considered. Thus, the CBS scheme for inviscid flow problems as described in section 3.4.4 is used to solve the example of this section. As a test case, an inviscid steady flow past the NACA0012 airfoil at a subsonic Mach number of $Ma_\infty = 0.5$ and an angle of attack of $\alpha = 3°$ is chosen. A sequence of grids with linear triangular elements is generated for this flow problem ranging from a very coarse to fine grid resolution. A certain number of nodes is distributed on the airfoil, whereas the grid spacing at the leading and trailing edge times this number of nodes is kept constant. Thus, with 100 elements on the surface of the NACA0012 airfoil, the leading and trailing edge spacing are $0.0064 l_c$ (where l_c denotes the chord length) and with 400 surface elements the spacing reduces to $0.0016 l_c$. The farfield for all grids is generated to be 50 times of the chord length around the airfoil. This value is chosen because no significant change in the solution could be observed using a higher distance. Close-up views on the grids around the airfoil are shown in Figure 5.1.

The results obtained with the flow solver for this subsonic flow problem are shown in Figure 5.2 with the Mach number and pressure distribution around the airfoil in Figure 5.2(a) and Figure 5.2(b) on the finest grid level. In Figure 5.2(c), the obtained C_p-distribution on the surface is shown together with the surface pressure distribution obtained from [JM86] and with the well-validated DLR TAU solver [RK08]. The calculated pressure distribution is in good agreement with the given reference surface pressure. From Figure 5.2(d), the same statement can be made for the total surface pressure loss coefficient defined as:

$$C_{p,tot} = \frac{p + \frac{\rho}{2}v^2 - (p_\infty + \frac{\rho_\infty}{2}v_\infty^2)}{\frac{\rho_\infty}{2}v_\infty^2} = C_p + \frac{\rho v^2}{\rho_\infty v_\infty^2} - 1\,. \tag{5.1.1}$$

The lift coefficient obtained in [JM86] is 0.4296 and calculated to 0.4226 for the TAU solver on the present finest grid. With the CBS scheme, a lift of $C_l = 0.4202$ is computed, which is less than 1% in difference to the TAU value on the same fine grid. In Figure 5.3, the convergence of the lift and drag coefficients over different grid levels (elements on the airfoil surface) is depicted. With more elements, the lift converges to the above mentioned lift value. The drag coefficient converges to $5.12 \cdot 10^{-4}$ and to $4.98 \cdot 10^{-4}$ for the CBS scheme and the TAU solver, respectively.

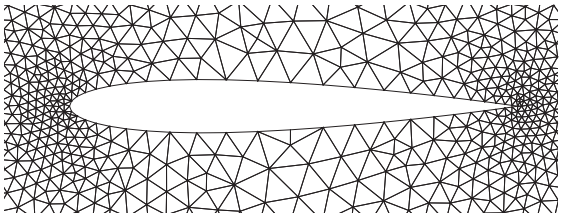

(a) 50 surface elements on the airfoil (full grid: 4171 nodes and 8246 elements)

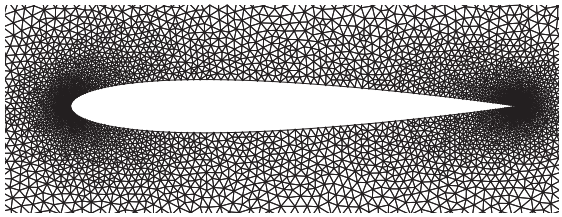

(b) 200 surface elements on the airfoil (full grid: 8212 nodes and 16178 elements)

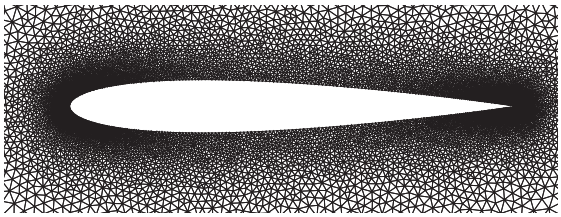

(c) 400 surface elements on the airfoil (full grid: 12374 nodes and 24302 elements)

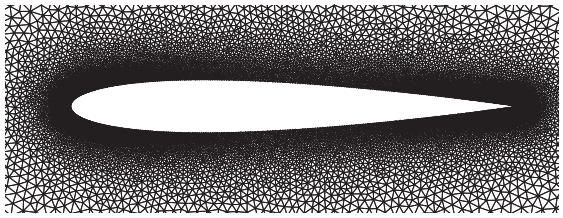

(d) 600 surface elements on the airfoil (full grid: 16281 nodes and 31916 elements)

Figure 5.1: Close-up views on the unstructured grids for calculations of inviscid flow past the NACA0012 airfoil

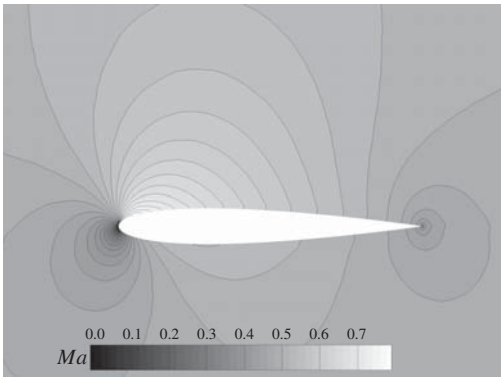

(a) Mach number contours

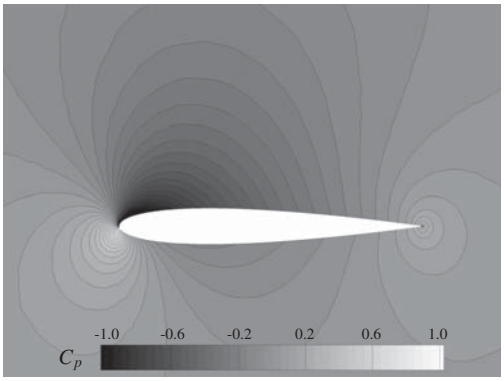

(b) pressure contours

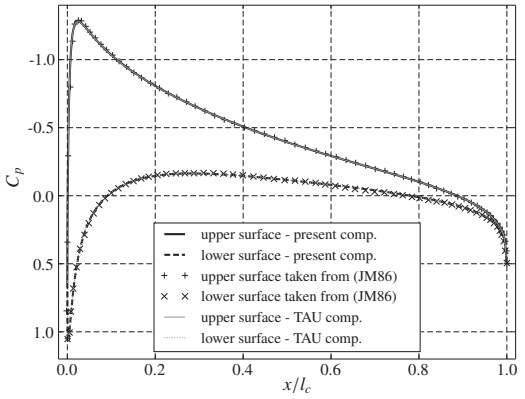

(c) surface pressure distribution

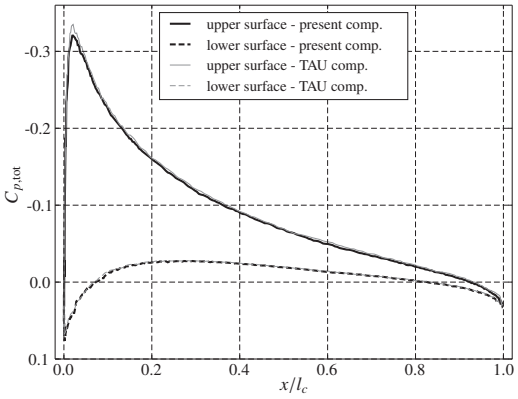

(d) total surface pressure loss

Figure 5.2: Results for the inviscid testcase on the finest grid level - flow at $Ma_\infty = 0.5$ and $\alpha = 3°$ past the NACA0012 airfoil

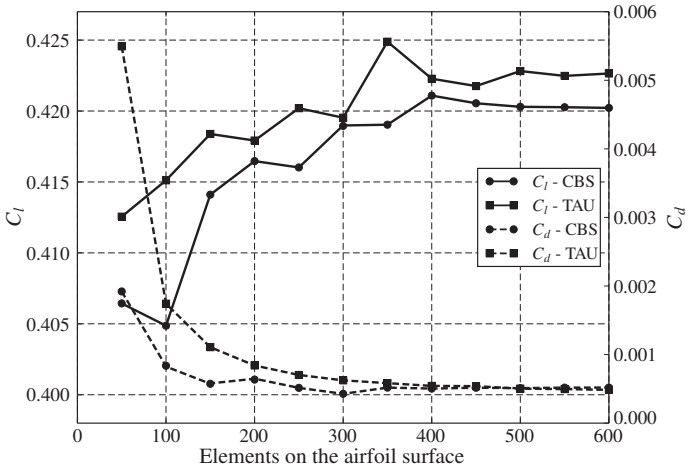

Figure 5.3: Convergence of the lift and drag coefficients using the CBS scheme and the TAU solver - inviscid flow at $Ma_\infty = 0.5$ and $\alpha = 3°$ past the NACA0012 airfoil

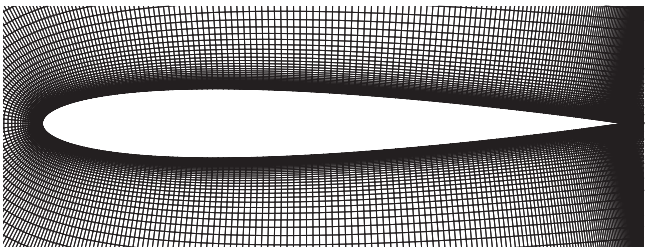

Figure 5.4: Structured grid for calculation of laminar viscous flow past the NACA0012 airfoil - level 0 (561x81 nodes, 44800 elements)

The drag is very low for both solvers, but is not perfectly zero, which would be expected according to d'Alembert's paradox.

Finally, it should be noted, that the same results on the finest grid are obtained with running the CBS scheme in unsteady mode (i.e. with the dual time stepping scheme) with a real time step of $\Delta t^R = (0.01, 0.005, 0.001)$ s. This indicates the correct implementation of the dual time stepping scheme.

5.2 Laminar viscous flow problems

In this section, more complex fluid problems are considered for validation of the CBS scheme on fixed grids. Here, additional diffusive terms, resulting from viscosity and conductivity, should no longer be neglected and the CBS scheme is used as described in section 3.3.2. Again, the fluid flow past a NACA0012 airfoil is investigated here and the solution is compared with results obtained with the TAU solver. Furthermore, an incompressible flow example is investigated, which uses the artificial compressibility concept as described in section 3.4.3.

5.2.1 Laminar viscous flow past the NACA0012 airfoil

The solution of the CBS and the DG-CBS scheme obtained from the simulation of the fluid flow past the NACA0012 airfoil is used again here to verify the fluid solver. As a testcase, a flow with a Mach number of $Ma_\infty = 0.5$, Reynolds number of $Re = 5000$ and an angle of attack of $\alpha = 0°$

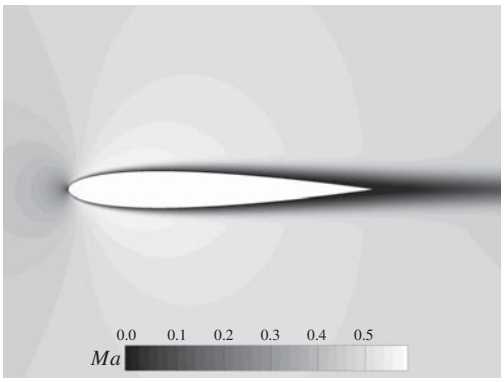

(a) Mach number contours

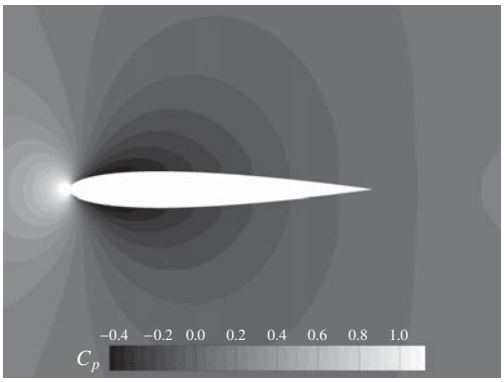

(b) pressure contours

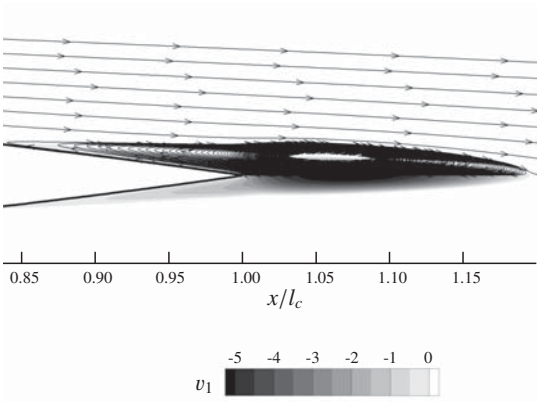

(c) upper trailing edge vortex together with the velocity contours v_1

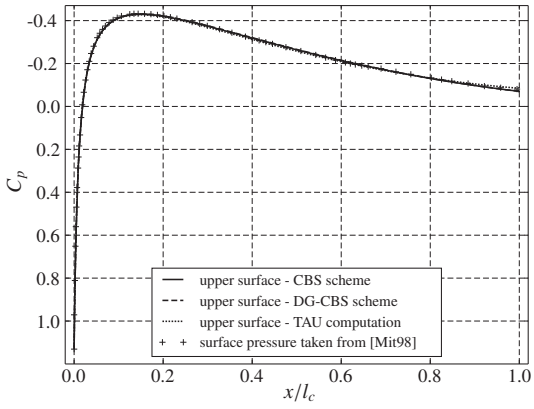

(d) surface pressure distribution

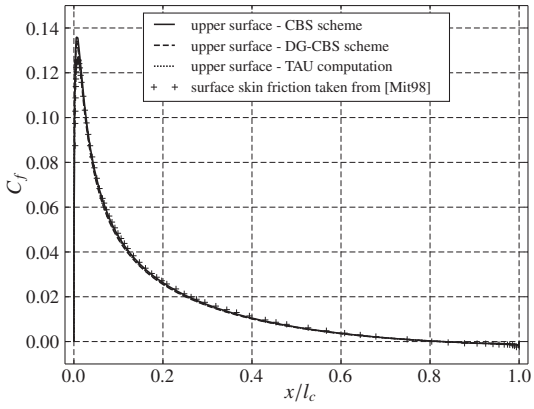

(e) surface skin friction distribution

Figure 5.5: Results for the laminar viscous testcase - flow at $Ma_\infty = 0.5$, $Re = 5000$ and $\alpha = 0°$ past the NACA0012 airfoil on the finest grid level (grid level 0)

is chosen. This testcase is characterized by two – symmetric to the airfoil chord – steady trailing edge vortex, which has to be resolved by the solver.

A structured grid around the airfoil is generated, Figure 5.4, to calculate the fluid flow on different grid levels. The computational grid at level 0 as shown in Figure 5.4 is a C-type grid and consists of 561x81 points. On the airfoil, 401 points are distributed, whereas at the leading and trailing edge a grid spacing of $0.001 l_c$ and $0.0006 l_c$ are chosen, respectively.

In the context of the CBS scheme, the usage of quadrilateral elements are novel compared to [NCZ06, TN05, Liu05, Hic08, Nit03, NMWM04, NL06], where triangles to fill the computational domain are exclusively applied. Although the computational effort is higher using quadrilateral elements, the accuracy is clearly improved. This arises from the fact, that the viscous stress and the heat flux can only be interpolated as constants in each triangular element by using linear shape functions [Bat96, Hug00]. In contrast, using bilinear quadrilateral elements, the viscous stress and heat flux can vary linearly over the elements due to the linear variation of the metric within this kind of elements.

In Figure 5.5, the results of this testcase are depicted for the finest grid level, where in Figure 5.5(a) and Figure 5.5(b) the contour plots of the Mach number and the pressure are shown, respectively. Moreover, the upper trailing edge vortex is shown in Figure 5.5(c) together with the negative flow velocity contours for v_1. This vortex is situated between $0.84 < x/l_c < 1.19$. Although not shown, there is also lower trailing edge vortex, where the fluid flow rotates in an anticlockwise direction.

To verify the results, the pressure and skin friction coefficient are compared with results obtained with the well-validated flow solver TAU, [RK08]. Further, reference values could be found in [Mit98]. It can be observed from Figure 5.5(d), that the surface pressure distribution is in good agreement with results obtained with TAU and with the data given in [Mit98]. Additionally, the surface pressure obtained with the DG version of the CBS scheme is plotted, which is similar to the conventional CBS scheme.

In Figure 5.5(e), the corresponding upper surface friction distribution are shown for the CBS and DG-CBS scheme as well as for the TAU simulation and the data obtained from [Mit98]. Good agreement of the present CBS and DG-CBS scheme compared to the TAU simulation on the same fine grid can be found. Small discrepancies to the results of [Mit98] are observed. Especially the maximum value of C_f is higher on the current grid than that of this reference. Furthermore, the x-position where the surface friction changes its algebraic sign is 0.84 for both version of the CBS scheme and TAU, which again indicates the start of reverse flow.

Finally, the relative error in the L_2-norm of the surface pressure for different grid levels is depicted in Figure 5.6. The reference surface pressure is chosen to the one, which is obtained with TAU on the finest grid level (level 0). For both versions of the CBS scheme, the error is less than 0.14% on level 0 and only small difference can be noticed between the CBS and the DG-CBS scheme in terms of this error. Further, it is remarkable, that the relative surface pressure error for both variants of the CBS scheme is less than that for TAU on the coarser grid levels $(1, 2, 3)$, whereas with the DG-CBS scheme a slightly lower error value compared to the standard CBS is obtained on each grid level. This improvement is caused due the local flux conservation property of the DG-CBS scheme. However, the main advantage of the DG-CBS scheme is the fact, that no global system of linear equations is needed to be solved in each time step. This might be useful in situations, when matrix lumping is unavailable.

5.2.2 Unsteady laminar viscous flow past a cylinder

To test the dual time stepping scheme adapted in section 3.4.6, the two-dimensional flow over a cylinder in a channel is investigated. In literature, often an incompressible flow is studied. Here,

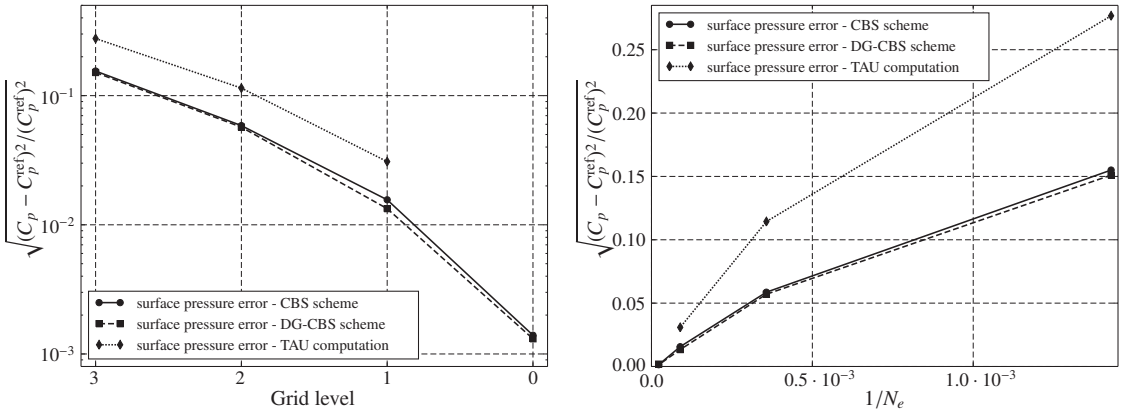

(a) rel. error vs. grid levels (b) rel. error vs. $1/N_e$

Figure 5.6: Relative error in the L_2-norm of the surface pressure for different grid levels and algorithms - laminar viscous flow at $Ma_\infty = 0.5$, $Re = 5000$ and $\alpha = 0°$ past the NACA0012 airfoil (reference is the surface pressure on the finest grid level obtained with the TAU code)

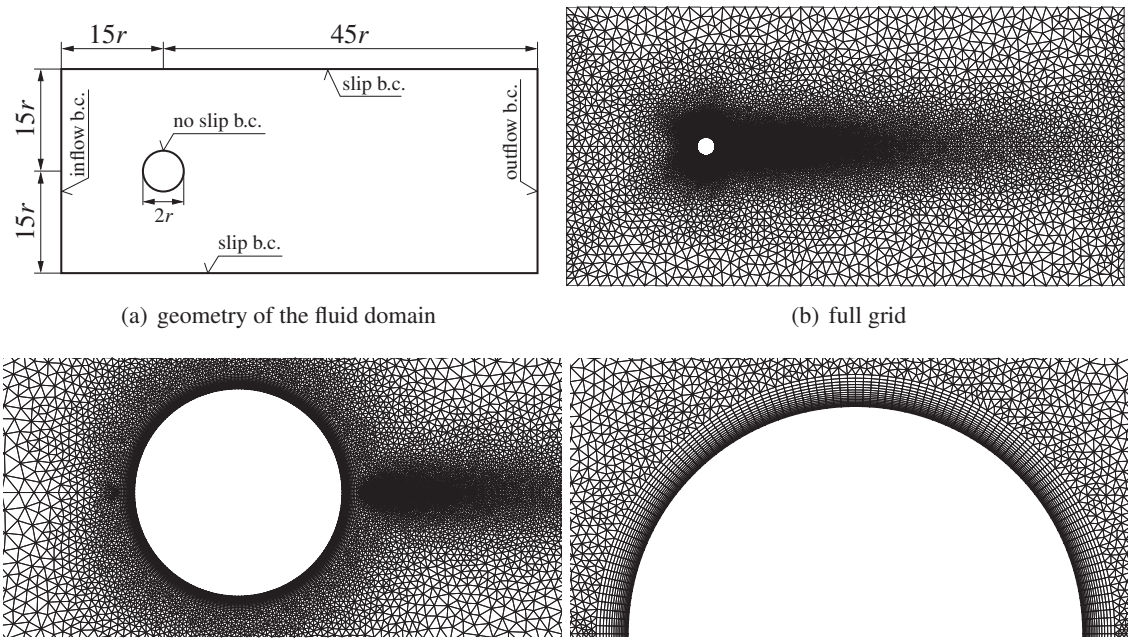

(a) geometry of the fluid domain (b) full grid

(c) close-up view on the cylinder (d) close-up view on the upper cylinder surface

Figure 5.7: Domain geometry and hybrid grid for the calculations of laminar viscous flow over a cylinder

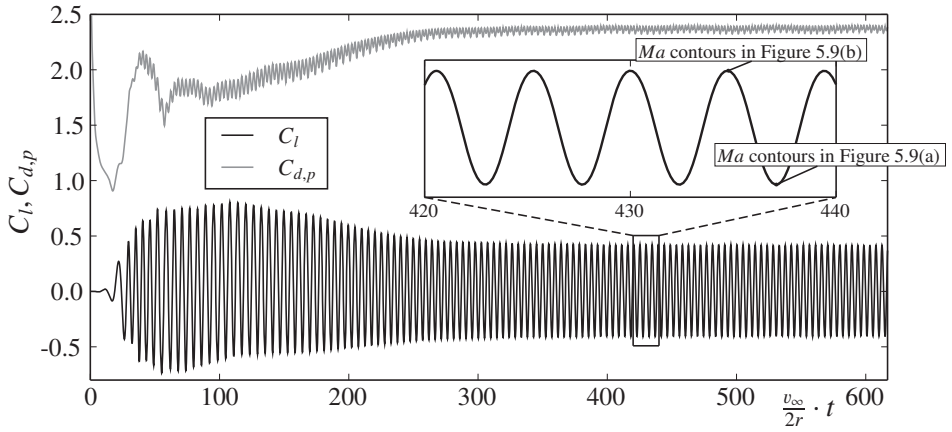

Figure 5.8: Time histories of the lift and drag coefficients for a viscous fluid flow past a cylinder at $Ma_{\text{inlet}} = 0.7$ and $Re = 2000$, real time step size $\Delta t^R = 4.0 \cdot 10^{-4}$ s

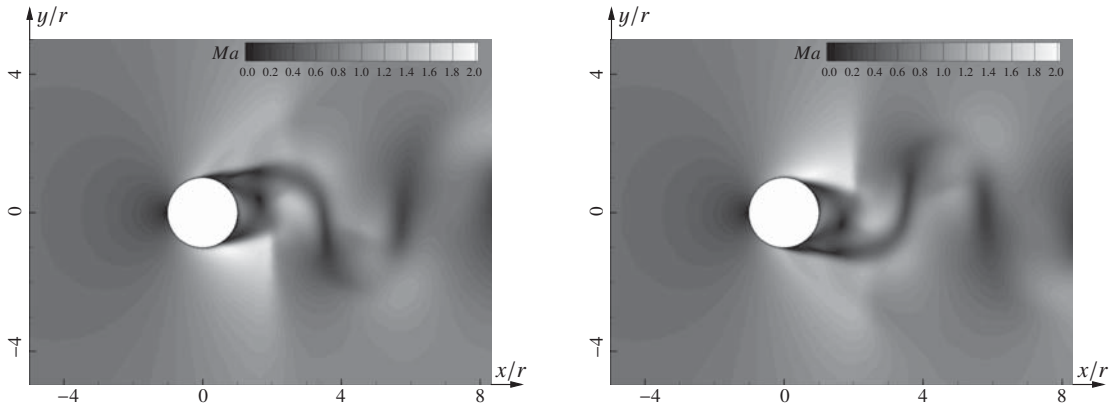

(a) Mach number contours minimal lift

(b) Mach number contours maximal lift

Figure 5.9: Mach number contours at the minimal and maximal lift for an unsteady viscous fluid flow past a cylinder at $Ma_{\text{inlet}} = 0.7$ and $Re = 2000$

a compressible case with a relatively high Mach number is chosen as a testcase, which involves a shock-boundary layer interaction.

The grid and the dimension of this problem are shown in Figure 5.7. Again, a hybrid grid is employed, which consists of 31444 triangles and 3200 quadrilaterals connected with the aid of 19110 nodes. On the boundary of the cylinder, 200 nodes are placed with constant space to each other. 51 points are located on the upper and lower channel wall, respectively, which are equally spaced, too. The structured mesh around the cylinder is created by 16 layers. The dimensions of the domain are depicted in Figure 5.7(a) together with the prescribed boundary conditions. The no-slip boundary condition for the velocity is applied on the cylinder surface. Further, the cylinder surface is assumed to be adiabatic regarding the energy equation. The slip boundary condition for the velocity is applied to the channel walls.

The flow at the inlet has a Mach number of $Ma_{\text{inlet}} = 0.7$ and a Reynolds number of $Re = 2000$ based on the diameter of the cylinder. At the inlet the corresponding values for the density as well as the velocity and at the outlet only the free stream pressure are prescribed. Initially, the free stream values of the density, velocity and energy are used for the whole domain at $t^R = 0$. A real time step size of $\Delta t^R = 4.0 \cdot 10^{-4}$ s is used throughout the simulation.

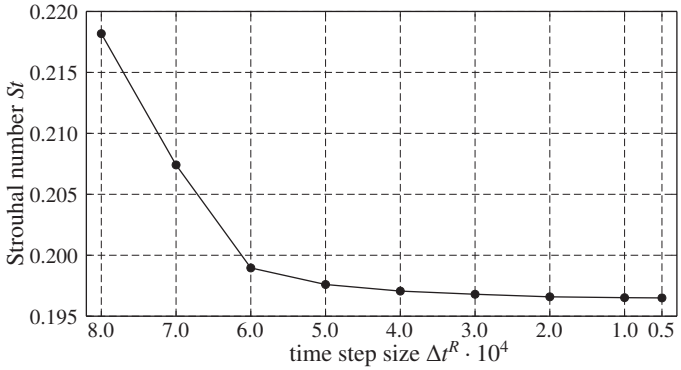

Figure 5.10: Convergence of the Strouhal number over different time step sizes for a viscous fluid flow past a cylinder at $Ma_{\text{inlet}} = 0.7$ and $Re = 2000$

Obviously, such a flow is highly unsteady and forms the well-known von Kármán vortex sheet behind the cylinder after an initial phase. In Figure 5.8, the time histories of the lift and drag are plotted, where the periodic character of the von Kármán vortex sheet can be observed. From the detailed view of the lift evolution, a Strouhal number of:

$$St = \frac{l\,f}{v_\infty} = \frac{2r\,f}{v_\infty} = 0.197 \tag{5.2.1}$$

can be determined, which is close to the usually assumed Strouhal number of 0.2. In the above equation, l is the characteristic length, which is equal to the diameter of the cylinder and f is the frequency of the vortex shedding. In Figure 5.9, the Mach number contours at time instants of minimal and maximal lift are shown and the periodic structure of the vortex sheet is seen here, too.

Finally, the convergence of the Strouhal number for different time step sizes is depicted in Figure 5.10. For very coarse time steps, the Strouhal number is high and then rapidly converges to a limit value for very fine time step sizes. For a time step size of $\Delta t^R = 4.0 \cdot 10^{-4}$ s, a reasonable value for St is obtained.

5.2.3 Incompressible laminar flow past a backward facing step

In this section, the capability of the CBS scheme to solve incompressible flow problems is demonstrated. Here, the classical testcase of a laminar incompressible flow at a Reynolds number of $Re = 229$ past a backward facing step is chosen and compared with experimental data provided in [DP74]. The setup of this problem is shown in Figure 5.11(a). The channel entrance is placed at a distance of four step heights upstream, while the total length of the channel is 40 step heights. The diameter at the entrance is two step heights. The experimentally obtained velocity profile is prescribed at the entrance, which is approximated as [Tho06]:

$$\begin{aligned}\frac{v_1}{v_\infty} = {} & 0.6624\left(\frac{x_2}{h_s}\right)^6 - 7.5547\left(\frac{x_2}{h_s}\right)^5 + 33.9\left(\frac{x_2}{h_s}\right)^4 - 75.283\left(\frac{x_2}{h_s}\right)^3 \\ & + 83.368\left(\frac{x_2}{h_s}\right)^2 - 37.793\left(\frac{x_2}{h_s}\right) + 2.6959\,.\end{aligned} \tag{5.2.2}$$

At the channel exit, the pressure is set to the ambient pressure. The no slip condition for the velocities is applied at all solid walls. Further, the Reynolds number of $Re = 229$ is based on the step height.

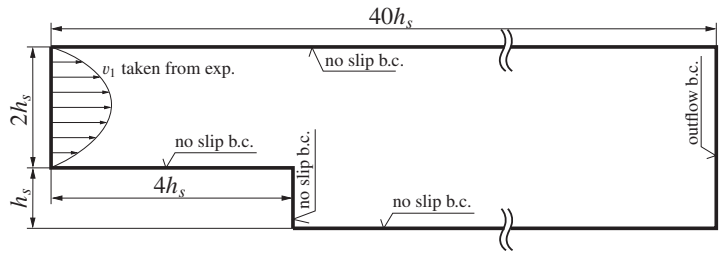

(a) geometry of the fluid domain

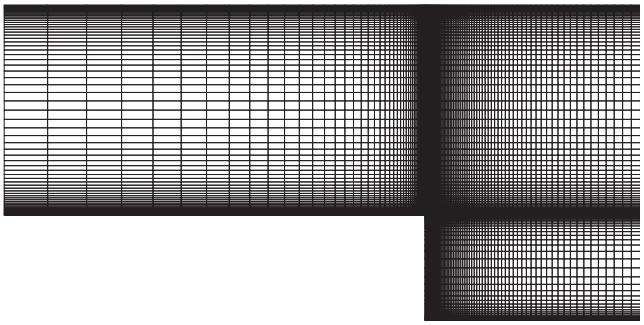

(b) close-up view on the backward facing step

Figure 5.11: Domain geometry and structured grid for the calculations of incompressible laminar flow past a backward facing step

The grid used for the computation is a structured mesh partly shown in Figure 5.11(b) and consists of 17136 quadrilateral elements and 17421 nodes.

In Figure 5.12(a), the horizontal velocity contours are shown. As seen, the step leads to a flow separation downstream the corner and a reattachment at the lower channel wall, which is caused due to an adverse pressure gradient. The resulting vortex is depicted in Figure 5.12(b). Further, the reattachment length is obtained as $x_R/h_s = 9.54$, which is in good agreement with experimental reported length of 9.77 published in [DP74]. To validate the computational results, several velocity profiles at distinguished horizontal locations are compared with the experimentally obtained data also published in [DP74]. The comparison is shown in Figure 5.12(c) and as seen the velocity profiles computed with the flow solver are in good agreement with the experimental data. Thus, the capability of the CBS scheme to solve incompressible flows is satisfied with only minor modifications to the compressible version of the CBS scheme.

5.3 Turbulent flow problems

In this section, the CBS scheme for turbulent flow problems is investigated. In this thesis, the method of one point closure is used, where the governing conservation equations are averaged in time or space leading to the Reynolds-averaged Navier-Stokes (RANS) equations. Using this averaging, additional transport equations - turbulence models - need to be additionally considered. Such turbulence models are quite standard in CFD and can handle a broad range of fluid problems with adequate computational costs. In appendix A.2, the turbulence modeling with the CBS scheme in the ALE frame of reference is described in detail, where a Favre and Reynolds averaging is applied to the governing fluid equations and two models to determine the eddy viscosity are introduced. The first model is the well-known Spalart-Allmaras turbulence model as a representative of a one-equation turbulence model. This model is used to calculate turbulent

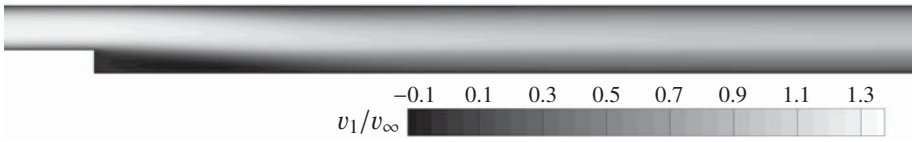

(a) horizontal velocity contours

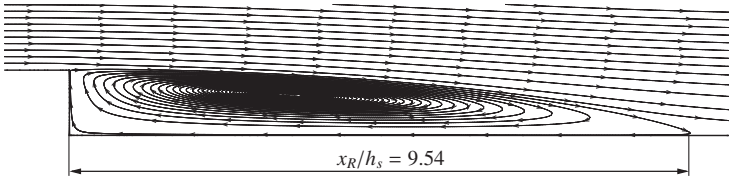

(b) vortex in lee of the step

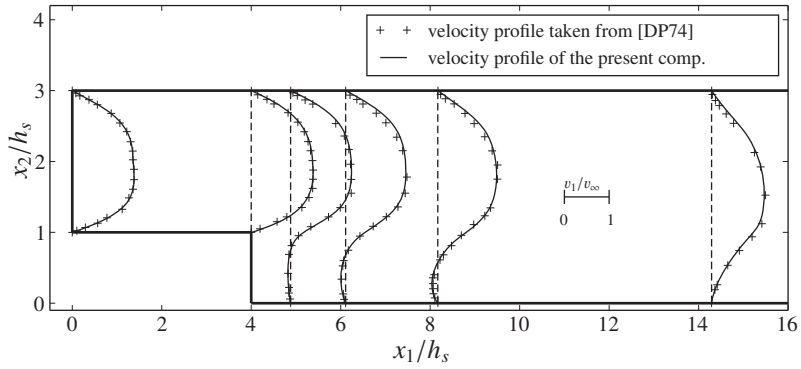

(c) comparison of velocity profiles with experimental data from [DP74]

Figure 5.12: Results for the incompressible testcase - laminar viscous flow at $Re = 229$ past a backward facing step

flows past the NACA0012 airfoil in the subsequent section. Nevertheless, in section A.2.4.2 the discretization of the k-ω baseline (BSL) and shear stress transport (SST) model of Menter using the CBS scheme are additionally shown. These models are two-equation turbulence models and like the Spalart-Allmaras model often used for aeronautical applications.

5.3.1 Turbulent flow past the NACA0012 airfoil

The NACA0012 airfoil is again used, but now a turbulent flow at a low Reynolds number is studied. As noted in [RS09], turbulence models like the Spalart-Allmaras model are not designed to predict transition from laminar to turbulence when run in conjunction with a full RANS solver, i.e. such one point closure models have not any transition modeling capability *per se*. Nevertheless, the characteristic behavior of the turbulent viscosity for a low-Reynolds number fluid flow can be shown. In [RS09], some data are given, which are compared with results obtained with the turbulent CBS scheme. Additionally, the TAU solver is again used to verify the CBS scheme.

In Figure 5.13 the hybrid grid used for the turbulent calculations is shown. The grid consists of 36700 nodes connected by 25354 triangular and 23800 quadrilateral elements. At the leading and trailing edge of the airfoil, a grid spacing of $0.002 l_c$ is set. A normal grid spacing at the wall of $5 \cdot 10^{-5} l_c$ yields a minimal y^+ of less than 0.5. The airfoil wall itself is discretized with 400 elements.

A freestream Mach number of $Ma_\infty = 0.2$, a Reynolds number of $Re = 100000$ and an angle of attack of $\alpha = 5°$ are used as initial conditions. In Figure 5.14(a), the non-dimensional

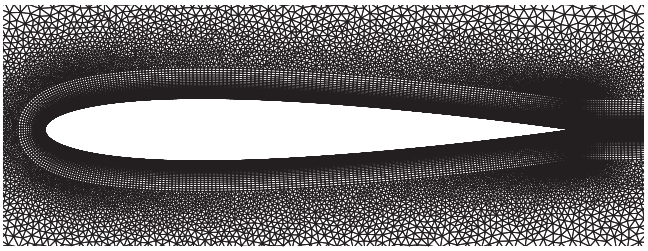

Figure 5.13: Hybrid grid for calculations of the turbulent flow past the NACA0012 airfoil - close-up view on the airfoil

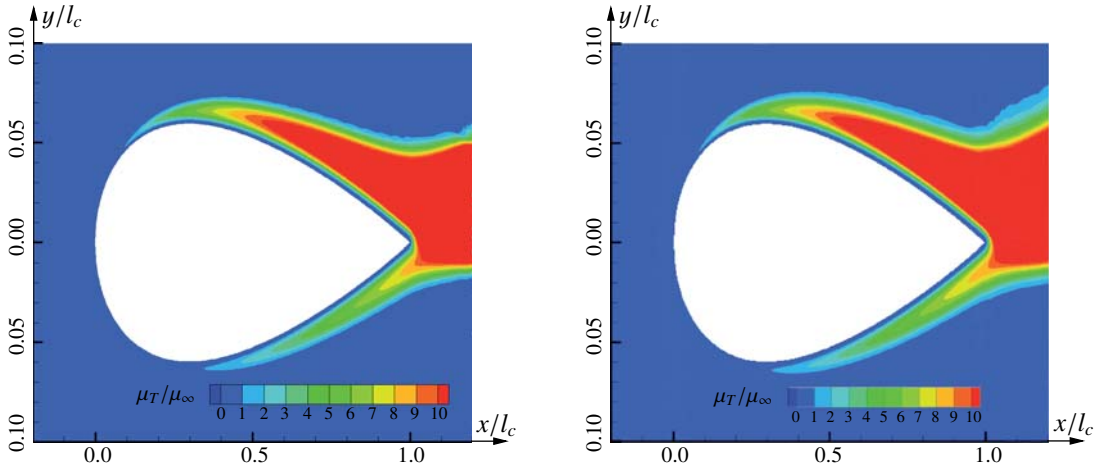

(a) CBS scheme (b) solution from [RS09]

Figure 5.14: Turbulent dynamic eddy viscosity contours - turbulent flow at $Ma_\infty = 0.2$, $Re = 100000$ and $\alpha = 5°$ past the NACA0012 airfoil

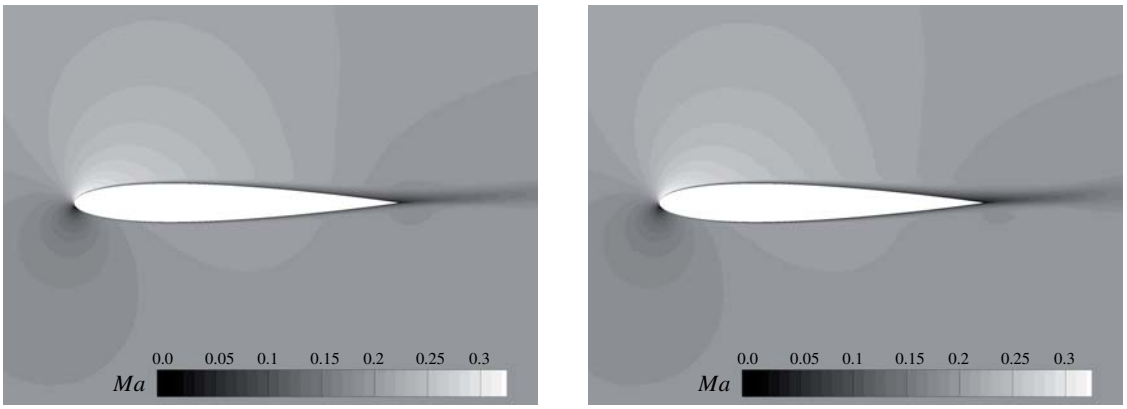

(a) CBS scheme (b) TAU solution

Figure 5.15: Mach number contours - turbulent flow at $Ma_\infty = 0.2$, $Re = 100000$ and $\alpha = 5°$ past the NACA0012 airfoil

	CBS		Ref. [RS09]	
	upper	lower	upper	lower
$Ma_\infty = 0.20$	0.091	0.325	0.081	0.314
$Ma_\infty = 0.55$	0.098	0.351	~ 0.12	~ 0.32

Table 5.1: Upper and lower NACA0012 airfoil location, where the values of μ_T/μ_∞ first exceed unity - variation of the farfield Mach number, whereas $Re = 100000$, $\alpha = 5°$

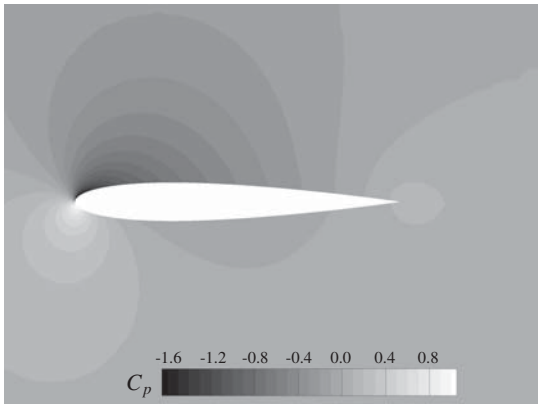

(a) pressure contours - CBS scheme

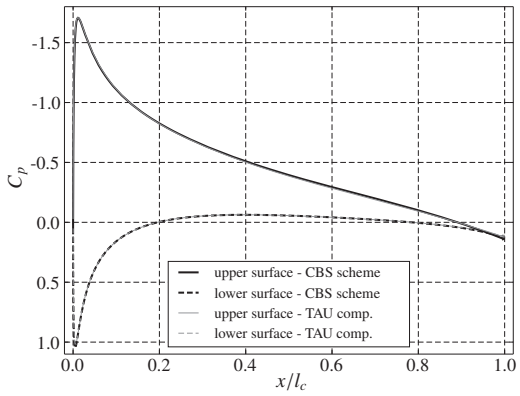

(b) surface pressure - comparison of TAU and the CBS scheme

Figure 5.16: Pressure contours and surface pressure distribution - turbulent flow at $Ma_\infty = 0.2$, $Re = 100000$ and $\alpha = 5°$ past the NACA0012 airfoil

dynamic eddy viscosity contours using the present CBS scheme are shown. For comparison, the results for the same configuration reported in [RS09] are replotted in Figure 5.14(b). Both contour plots are in very good agreement. However, the y-range of the $\mu_T > \mu_\infty$ values at the trailing edge is smaller than that found in [RS09]. The minimal x-position on the upper side of the airfoil, where the non-dimensional eddy viscosity becomes 1, is computed with the CBS scheme to $x^u_{min}/l_c(\mu_T > \mu_\infty) = 0.091$, whereas in [RS09] a value of 0.081 was reported. For the lower side of the airfoil, this value is $x^l_{min}/l_c(\mu_T > \mu_\infty) = 0.325$, which agrees well with the location of 0.314 obtained in the reference. These values together with locations obtained at one additional Mach number are summarized in Table 5.1. From this table, it can be seen, that the source of turbulence moves only slightly further downstream, i.e. the upper and lower airfoil location, where the values of μ_t/μ_∞ first exceed unity, increase a bit with higher Mach numbers. The values for the location at $Ma_\infty = 0.55$ taken from the reference are estimated from a plot in [RS09]. Further, a dependency of these locations on the grid density is reported in the reference and thus the values obtained here with the CBS scheme are satisfactory.

The Mach number contours of the case with $Ma_\infty = 0.2$ are shown in Figure 5.15 for the solution with the CBS scheme and the TAU solver. It can be seen, that the CBS scheme provides a slightly smoother soultion compared with the results obtained with TAU. Finally, the pressure contours of CBS solution are shown in Figure 5.16(a) and the according surface pressure distribution is plotted and compared with TAU in Figure 5.16(b). It can be conclude, that the surface pressure obtained with the CBS scheme is in good agreement with the TAU computed on the same grid.

5.4 Chapter summary

In this chapter, the implementation of the presented CBS scheme is verified by the aid of several fluid flow problems ranging from inviscid to laminar and turbulent viscous fluid flow. For the steady inviscid fluid flow past the NACA0012 airfoil, good agreement with available published data and another flow solver are shown. Convergence of the lift and drag coefficients are observed varying the resolution of the unstructured mesh. Steady laminar fluid flow cases are conducted for compressible flows past the NACA0012 airfoil and for incompressible flows past a backward facing step within a channel. The results of simulations with both flow models show a good agreement with data published in literature. Again, results are compared with data obtained with the well-validated fluid solver TAU and spatial convergence is shown for the CBS as well as for the DG-CBS scheme on a serie of structured grids. Thus, it is shown, that the CBS scheme is widely applicable for general fluid dynamics, which is an important property for a CFD algorithm. Unsteady flow problems are verified by the flow past a cylinder, where the well-known von Kármán vortex sheet is observed.

Further, results of turbulent flow past the NACA0012 airfoil are compared, with data found in literature and thus the Spalart-Allmaras turbulence model is verified in conjunction with the CBS scheme for compressible fluids.

Finally, it should be noted, that many more example applications of the CBS scheme can be found in literature, e.g. [NMWM04, ZBN05, NCZ06, NL06, TNB08, BNvL$^+$10, BBH10, SNRA10]. This chapter is restricted to summarize the results solely obtained with the CBS scheme. However some new aspects are employed, e.g. the usage of quadrilateral elements in the boundary layer yields more accurate results than that obtained in [Hic08]. To the author's knowledge, so far only pure triangular elements are used in the literature. Furthermore, turbulent flows are calculated here, which is satisfactorily done so far only for incompressible fluid flow problems, e.g. [NL06].

6 Assessment of the Coupling Environment

In this chapter, the coupling environment is computationally investigated in terms of the grid deformation, the data transfer as well as the time integration and equilibrium iteration. In the first section, the finite grid deformation for different grid types will be analyzed using several pseudo stiffness evaluation methods. The data transfer algorithm - especially the adaptive h-refinement of the integration grid - will be demonstrated for a simple model problem and a more complex three-dimensional wing structure in the second section. Further, the advantage of the novel three-field approach in conjunction with a higher order discretization of the interface frame will be shown, which leads to a smooth data transfer.

A simple FSI problem of a thin and flexible panel excited under an inviscid isentropic fluid is used to verify the equilibrium iteration scheme for the two- and three-field approach. Finally, a more complex aeroelastic problem is chosen to validate the coupling environment with experimental data. A simple staggered iteration procedure is applied to simulate a flapping and flexible airfoil in a low-Reynolds number flow regime.

6.1 Finite element grid deformation

6.1.1 Unstructured grid with high deformation

In this section, a simple test problem adapted from [STB03, XA04] with high grid deformations is investigated, which uses the unstructured grid shown in Figure 6.1. This grid consists of 1189 nodes connected to 2198 triangular elements. The interface, which is subject to deformation, is

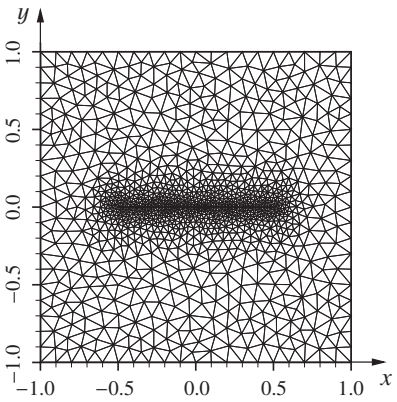

Figure 6.1: Initial grid for investigation of the finite element grid deformation

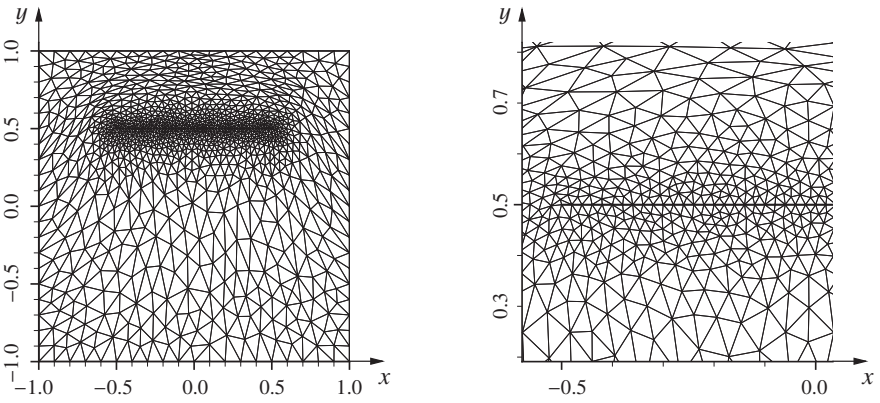

(a) full grid (b) close-up view on the interface

Figure 6.2: Deformed grid due to interface translation

located at $y = 0$ in the interval of $-0.5 \leq x \leq 0.5$. At this interface 100 nodes are equally distributed. The quality of the grid is measured in terms of the aspect ratio, which is defined as the ratio of the circumradius of the triangle to twice its inradius. Thus, the aspect ratio of an equilateral triangle is exactly one. The mean aspect ratio of the present grid is 1.075, which is obtained by integration of all elemental aspect ratios over the domain and dividing the value by the whole area. The highest aspect ratio of a triangle is 1.609.

Using the six possibilities of the elemental stiffness evaluation, Eq. (4.2.2) to (4.2.7), three deformation types of the grid are investigated: a vertical translation of the interface to $y = 0.5$, an interface rotation of 45° around the origin and a bending of the interface to a circular arc with an angle of 180°, whereas the length of the interface is kept constant.

6.1.1.1 Translation of the interface

In a first test campaign, the desired interface translation to $y = 0.5$ is computed in three equal steps, where in each step the stiffness matrix is newly calculated and the previously deformed grid is used as a new basis. This translational movement is important because it divides the computational domain into two parts: a region with compressed elements and a region with stretched elements.

In Figure 6.2, the resulting deformed grid using the stiffness evaluation strategy of Eq. (4.2.2) is depicted because this strategy leads to the smallest maximum aspect ratio. However, all stiffness evaluation possibilities behave similar. Due to the large interface displacements, the average and maximum aspect ratio grow non-linearly with the interface translation, Figure 6.3. The usage of the combined stiffness evaluation methods of Eq. (4.2.6) and (4.2.7) results in the worst meshes, whereas the length scale based methods of Eq. (4.2.3) and (4.2.5) give the best meshes in terms of the average aspect ratio. For the maximum aspect ratio, these two methods are also the best until a translation of $y = 0.33$ (second step). However, for the final, third step, the stiffness method of Eq. (4.2.2) results in the smallest maximum aspect ratio.

In Figure 6.4, the aspect ratios of the deformed grids are plotted against the number of steps used for the interface translation to $y = 0.5$. For the combined stiffness evaluation methods of Eq. (4.2.6) and (4.2.7), no usable grid could be obtained with only one step. Further, it can be seen from Figure 6.4(a), that with two steps onward the average aspect ratio remains constant, whereas the stiffness methods of Eq. (4.2.3) and (4.2.5) perform best. Considering the maximum aspect ratio of a triangle in the deformed mesh, the only suitable grid after one step of deformation could be obtained with the method of Eq. (4.2.2), Figure 6.4(b). With more steps used for the interface translation, also the methods of Eq. (4.2.3) and (4.2.5) give good meshes.

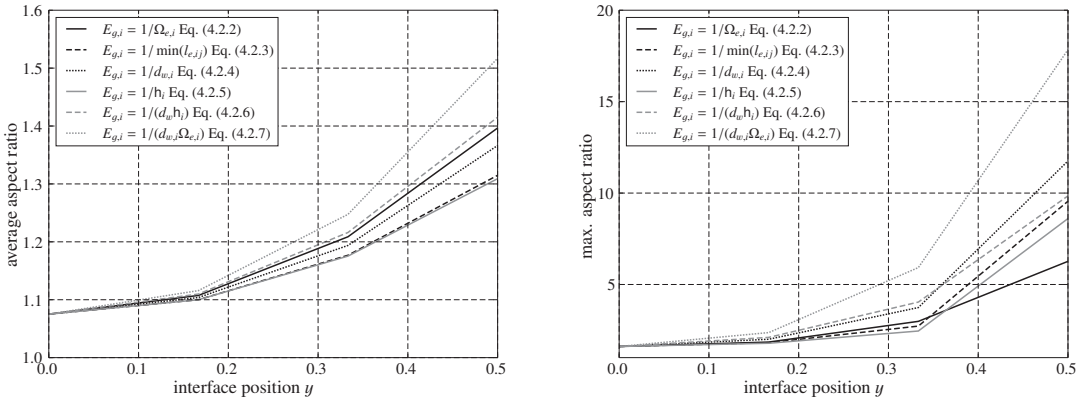

(a) average aspect ratio (b) maximum aspect ratio

Figure 6.3: Grid quality for interface translation to $y = 0.5$ - translation done in three steps

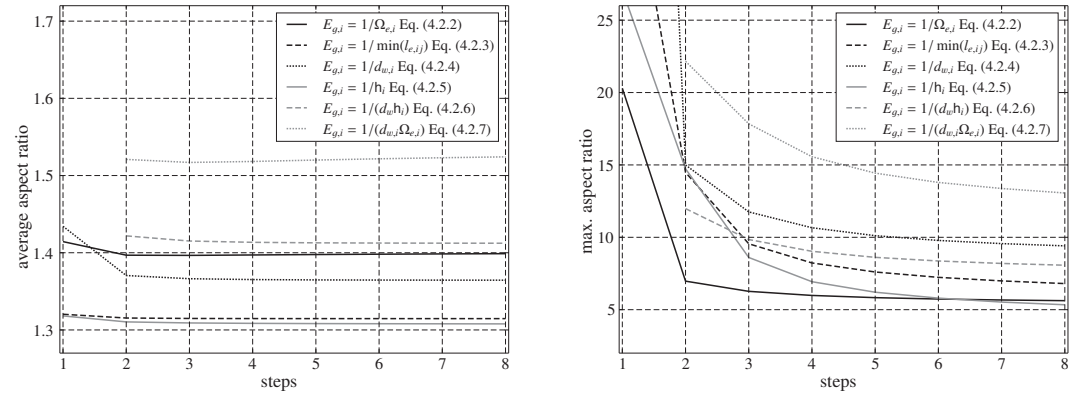

(a) average aspect ratio (b) maximum aspect ratio

Figure 6.4: Grid quality for interface translation to $y = 0.5$ - influence of the step number

6.1.1.2 Rotation of the interface

For this testcase, the interface is rotated with an angle of 45° around the point $(0, 0)$. A successful deformation of the grid in three steps can be seen in Figure 6.5, where the combination of wall distance and characteristic length for the stiffness evaluation, i.e. Eq. (4.2.6), is used due to its best performance in terms of the maximum aspect ratio, Figure 6.6(b). Another method, which also gives a good deformed grid, is the one which uses only the wall distance as the stiffness criterion, i.e. Eq. (4.2.4). This method also gives a good average aspect ratio, Figure 6.6(a). The procedures, that have been performed very well for the vertical translation of the interface (Eq. (4.2.3) and (4.2.5)), now give the poorest meshes with unacceptable high maximum aspect ratios (method of Eq. (4.2.5)) or even degenerated meshes after the second step (method of Eq. (4.2.3)).

Moreover, using Eq. (4.2.3) as the stiffness evaluation method, a valid grid could be obtained only in 4 and more steps to the desired rotation, Figure 6.7(a). However, the obtained grid shows elements with very high aspect ratios, Figure 6.7(b). Further, as already observed for the vertical interface translation, the average aspect ratio remains almost constant for each stiffness strategy, Figure 6.7(a). In summary, for the rotation testcase, the methods which use Eq. (4.2.4) and (4.2.6),

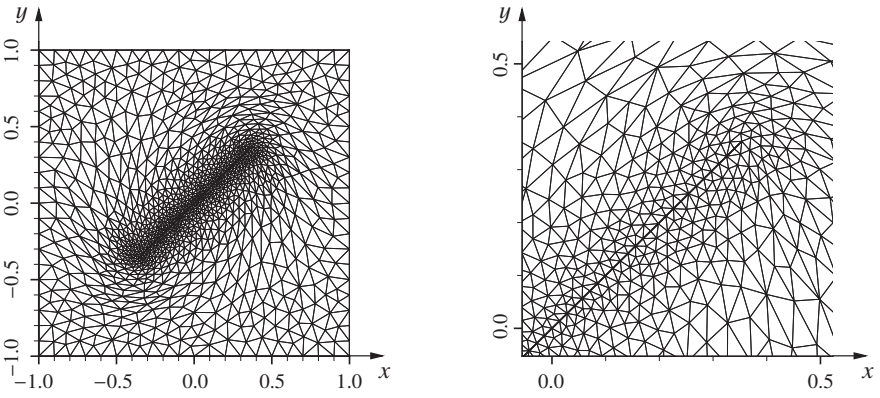

(a) full grid (b) close-up view on the interface

Figure 6.5: Deformed grid due interface rotation

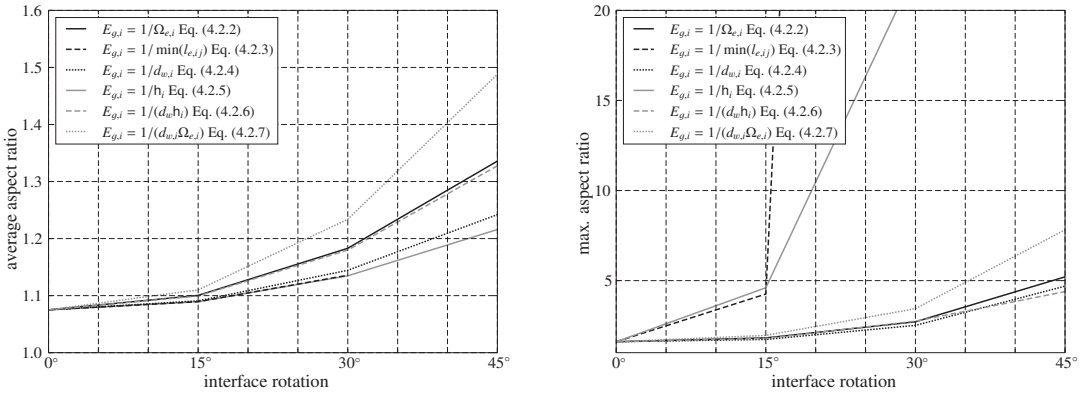

(a) average aspect ratio (b) maximum aspect ratio

Figure 6.6: Grid quality for interface rotation to 45° - rotation done in three steps

gives the best grids and also with only one step these strategies give reasonably good meshes, Figure 6.7(b).

6.1.1.3 Bending of the interface

As the last and most demanding testcase, the bending of the interface to a circular arc is investigated, whereas the length of the interface is kept constant. For the parameter studies, a central angle of 180° is used for the circular arc. In Figure 6.8, a successful deformation of the interface in three steps is depicted, which uses again Eq. (4.2.6) as stiffness evaluation. Together with the strategy of Eq. (4.2.4), this method provides the best results in terms of the maximum aspect ratio, Figure 6.9(b). In addition, the stiffness methods based on a length scale, i.e. Eq. (4.2.3) and (4.2.5), again perform very poorly regarding the maximum aspect ratio, although the average aspect ratio shows good values, Figure 6.9(a).

Using a different number of steps to reach the desired bending of 180°, the same statements as for the rotation testcase of the previous subsection can be expressed here. However, the solely acceptable grid deformed with only one step, is obtained with the stiffness strategy of Eq. (4.2.6), Figure 6.10(b). Further, it should be noted, that with the method of Eq. (4.2.3) the highest aspect ratio remains high, even with 8 steps. Therefore, this method is not plotted in Figure 6.10(b).

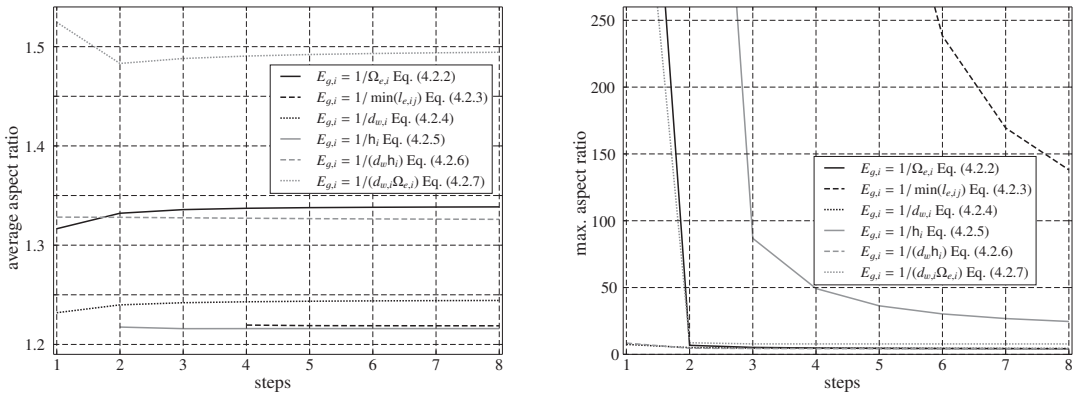

(a) average aspect ratio (b) maximum aspect ratio

Figure 6.7: Grid quality for interface rotation to 45° - influence of the step number

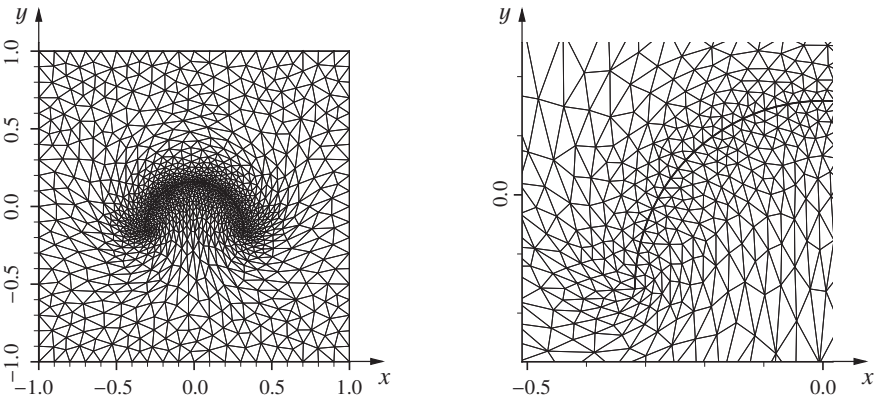

(a) full grid (b) close-up view on the interface

Figure 6.8: Deformed grid due interface bending

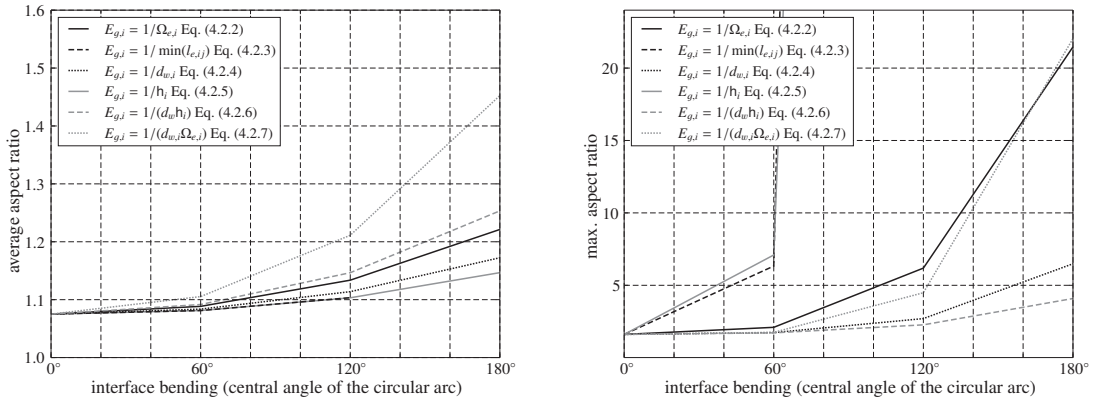

(a) average aspect ratio (b) maximum aspect ratio

Figure 6.9: Grid quality for interface bending to a circular arc with a central angle of 180° - bending done in three steps

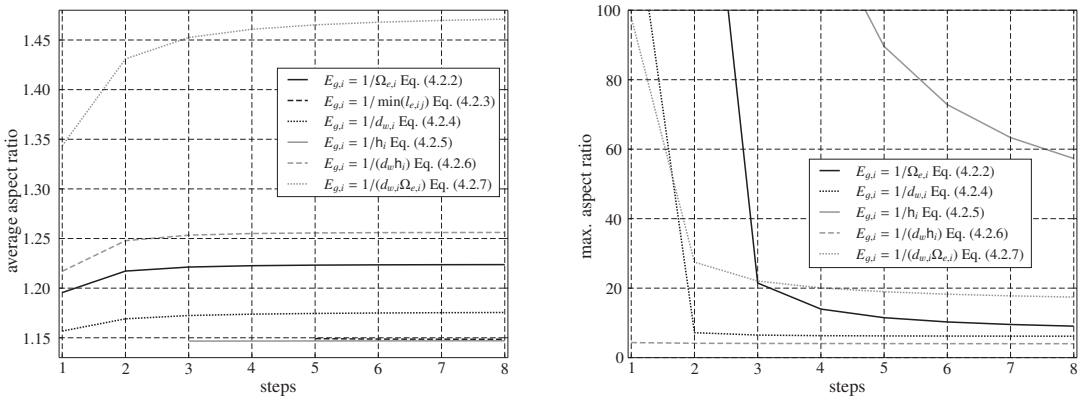

(a) average aspect ratio

(b) maximum aspect ratio

Figure 6.10: Grid quality for interface bending to a circular arc with a central angle of 180° - influence of the step number

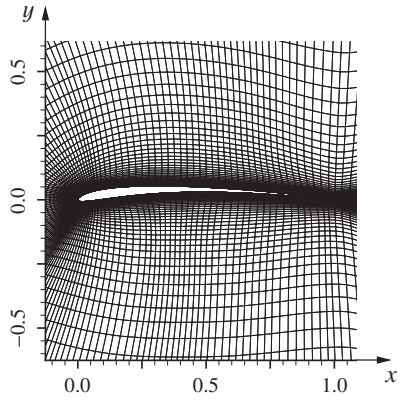

Figure 6.11: Structured grid for flow simulation past the flapping SG04 airfoil

In summary, for the rotation and bending testcase, the best results could be obtained with the stiffness strategy based on a combination of the wall distance and the characteristic length, i.e. Eq. (4.2.6). Good results could be obtained with this method for the vertical translation testcase, although other methods perform better for this interface movement.

6.1.2 Structured grid with high deformation and rigid body motion

In this section, a further grid deformation testcase is investigated. For a flapping and flexible airfoil simulation, a robust mesh update algorithm is needed, which prevents the structured grid from containing distorted elements. In Figure 6.11 a structured grid around a thin airfoil is shown, which contains 216x80 quadrilateral elements.

For testing of the grid deformation, a pure plunging motion with a sinusoidal vertical translation and an amplitude of double the airfoil chord length is assumed. The farfield of the grid is kept fixed in space and therefore the translation results in a mesh deformation rather than only a rigid body motion of the whole grid. A typical beam-like deformation is incorporated to this motion with a deflection amplititude at the trailing edge to be a quarter of the cord length. This deformation is also assumed to have a temporal sine characteristic, i.e. at the top and bottom dead

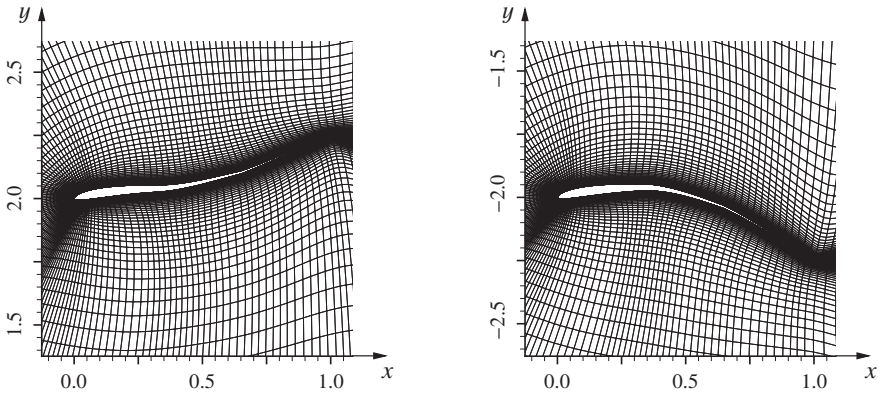

(a) top dead center (b) bottom dead center

Figure 6.12: Deformed structured grid due to rigid vertical translation and airfoil deformation

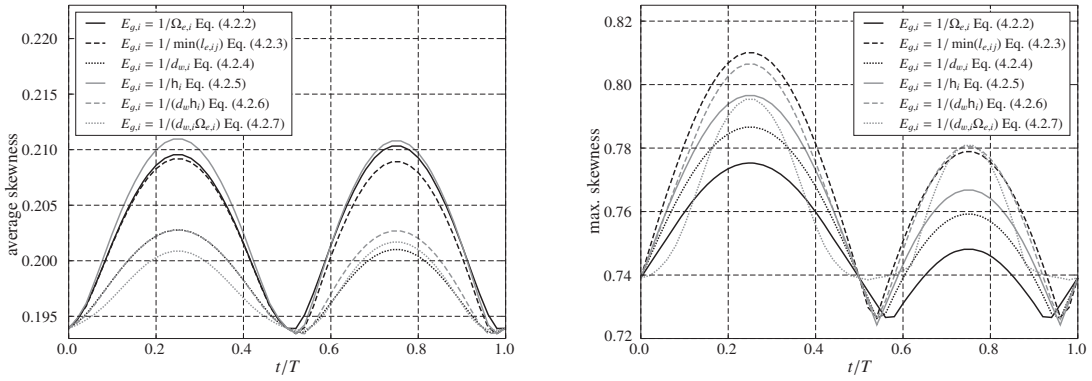

(a) average skewness (b) maximum skewness

Figure 6.13: Grid quality for structured grid deformation during a flapping cycle

center the deformation is positive and negative, respectively. For this testcase, the stiffness matrix for each method is evaluated only once for the initial grid and is then used throughout the flapping motion. To assess the quality of the resulting mesh, the average and maximum skewness of the elements are considered. The skewness of a quadrilateral element is defined as the maximum, relative and absolute difference of the inner angles to be orthogonal, i.e. a skewness of 0.0 would be the optimal shape of a rectangle. The average skewness of the initial grid is 0.194, while the maximum skewness is 0.739.

In Figure 6.12, the deformed grids at the top and bottom dead center are shown, where the stiffness is evaluated according to Eq. (4.2.2) due to its best performance in terms of the maximum skewness, Figure 6.13(b) and Table 6.1. In Figure 6.13, the average and maximum skewness using the different stiffness evaluation strategies over one period are depicted. It can be observed, that each method is able to produce valid meshes for this strong flapping motion, although the deformation for each time step is done only in one step. Regarding the average skewness in Figure 6.13(a), its value increases while the airfoil moves to the top dead center ($t/T = 0.25$) and decreases then again to the mid of the downstroke ($t/T = 0.5$). Shortly after the mid-downstroke, the average skewness increases to the bottom dead center ($t/T = 0.75$) and decreases then during the upstroke to its initial value. Integrating the skewness evolutions over one period, it can be noticed, that the stiffness methods based on the wall distance give the best results in terms of the average skewness.

	mean skewness	
	average	maximum
$E_{g,i} = 1/\Omega_{e,i}$; Eq. (4.2.2):	0.2029	0.7497
$E_{g,i} = 1/\min(l_{e,ij})$; Eq. (4.2.3):	0.2023	0.7703
$E_{g,i} = 1/d_{w,i}$; Eq. (4.2.4):	0.1982	0.7570
$E_{g,i} = 1/\mathsf{h}_i$; Eq. (4.2.5):	0.2034	0.7621
$E_{g,i} = 1/(d_w \mathsf{h}_i)$; Eq. (4.2.6):	0.1986	0.7678
$E_{g,i} = 1/(d_{w,i}\Omega_{e,i})$; Eq. (4.2.7):	0.1976	0.7603

Table 6.1: Mean values of the average and maximum skewness over one flapping period for several stiffness evaluation methods

For the maximum skewness, the same behavior during a flapping period can be observed, Figure 6.13(b), except the maximum skewness at the bottom dead center is lower than its value at the top dead center for all methods. Although other methods provide temporarily smaller maximum skewness values, the methods based on the element area and the wall distance give the best results at the top and bottom dead center. Thus, these both schemes also results in the lowest integrated mean values of the maximum skewness, Table 6.1. In summary, all methods give reasonably good deformed grid. However, the stiffness evaluation scheme based on the wall distance has shown the property, that this method gives meshes, which have a good average as well as maximum skewness values.

6.2 Interface data transfer

In this section, the developed adaptive quadtree-based h-refinement of the integration mesh proposed in section 4.3.6 is investigated. Further, a smooth transfer scheme is proposed, which uses the three-field coupling approach. All the examples presented in this part employ the Galerkin based transfer. The performance of the different transfer schemes, which has been described in section 4.3.2 to 4.3.5, will be analyzed in the context of the panel flutter problem in an own chapter.

6.2.1 Simple model problem

In a first testcase, a simple data transfer between two non-matching grids is investigated. Here, the level of adaptive refinement of the integration mesh and the curvature of the involved grids are examined in terms of the error in a constant flux transfer, i.e. the patch test is used. In Figure 6.14, the fluid and structural interface grids are shown. A load transfer is assumed, i.e. a data transfer from the fluid to the structural representation of the interface is applied. To ensure load conservation, the integration is performed on a grid based on the fluid interface grid. This integration is subjected to the adaptive quadtree-based h-refinement to improve the accuracy of the transfer.

To investigate the influence of the grid's curvature on the transfer error, the interface meshes are projected on a sphere with a certain curvature. The curvature is defined as the inverse of the

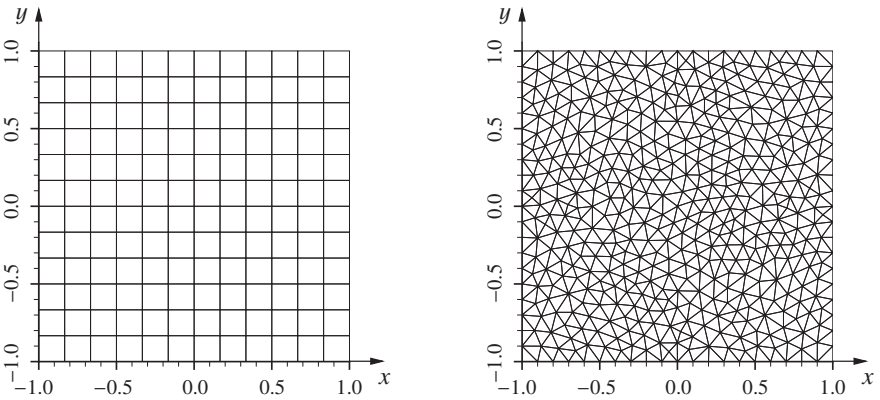

(a) fluid interface grid (b) structural interface grid

Figure 6.14: Interface grids used for the model problem - without curvature

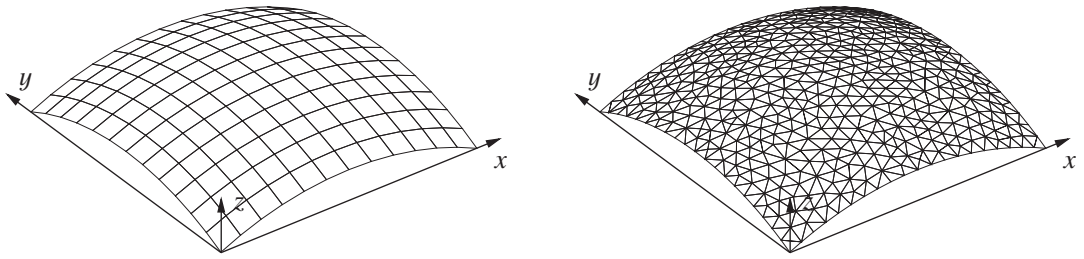

(a) fluid interface grid (b) structural interface grid

Figure 6.15: Interface grids used used for the model problem - curvature of 0.4

sphere's radius. An example of the three-dimensional interface grids with a curvature of 0.4 is shown in Figure 6.15.

The results of the data transfer are depicted in Figure 6.16, where the relative error in the L_2-norm of the obtained structural flux to the constant fluid flux is computed according to Eq. (4.3.22). In Figure 6.16(a), this error is plotted over the levels of the integration mesh refinement. As seen from this figure, a transfer without adaptive refinement (level 0) yields an error, which is identical for different curvature of the interface grids. Using the flat interface grids (curvature is 0.0), the error can be considerably reduced with more levels of integration mesh refinement. This improvement is caused by the more accurate integration for the transfer matrices using the Galerkin based transfer. However, increasing the curvature the error can only be asymptotically decreased to a certain value. For a curvature of 0.7, a level higher than 3 is ineffective in terms of the error and its value remains at approximately 10^{-3}. Therefore, the transfer accuracy is not only influenced by the quality of the integration, but also by the curvature of the interface grids. Due to the curvature, the so-called faceting error becomes the dominant factor for the data transfer accuracy of highly curved interfaces. Using a high integration accuracy with six refinement levels, the error increases with higher curvature as seen in Figure 6.16(b). From this figure also the independence of the curvature, when using non-refined integration grids, can be seen. In this case the integration error is a dominant factor for the accuracy of the data transfer.

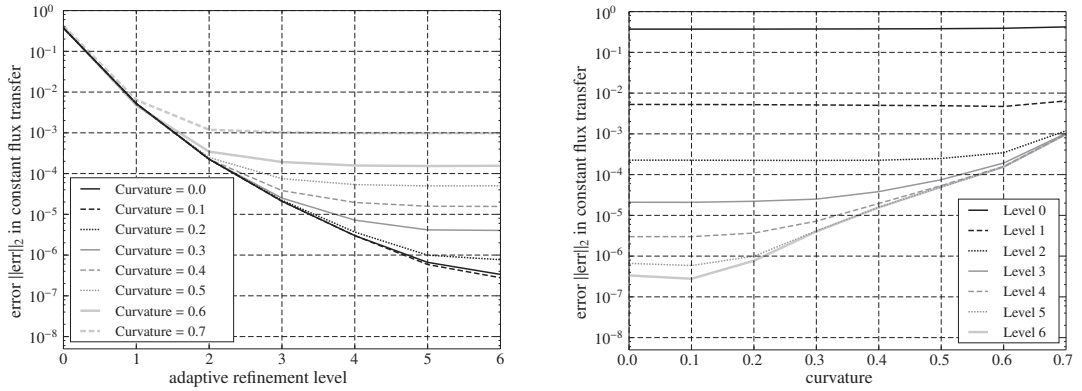

(a) error over levels of refinement for different curvature

(b) error over curvature for different levels of refinement

Figure 6.16: Error in constant flux transfer at different curvature of the interface grids and using different levels of adaptive refinement for the integration grid

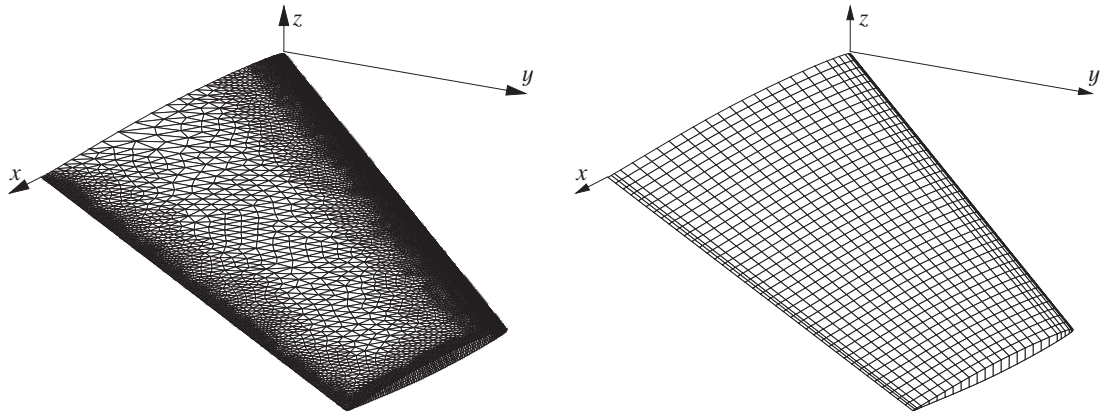

(a) fluid interface grid

(b) structural interface grid

Figure 6.17: Interface grids of the AGARD wing 445.6

6.2.2 Data transfer for the AGARD wing 445.6

In a more realistic testcase, the data transfer over the interface meshes of the AGARD wing 445.6 is investigated. The numerical aeroelastic analysis is widely used as a benchmark problem, see e.g. [Gup96, GM00, FL00, CZY06, LB93]. The flutter behavior of this wing is experimentally analyzed in an AGARD report by [YLF63]. In this thesis, only the data transfer properties are highlighted rather than to conduct a full aeroelastic analysis.

For the wing, the 2.5 ft weakened model number 3 is used, which has a 45° quarter-chord sweep angle, a panel aspect ratio of 1.65, a taper ratio of 0.66, and the cross sections given by the NACA65A004 airfoil. The fluid interface mesh is shown in Figure 6.17(a) and the structure is modeled using 27x40 solid elements, whose interface is depicted in Figure 6.17(b). The fluid interface holds 30666 elements and 15380 nodes.

In Figure 6.18, the relative error in the L_2-norm of a constant flux transfer is depicted, where the fluid and structural interface discretization have served as the integration mesh and a constant flux distribution is applied on the fluid interface mesh. If the integration mesh is set to the structural interface mesh, the error remains high and by increasing the level of adaptive refinements,

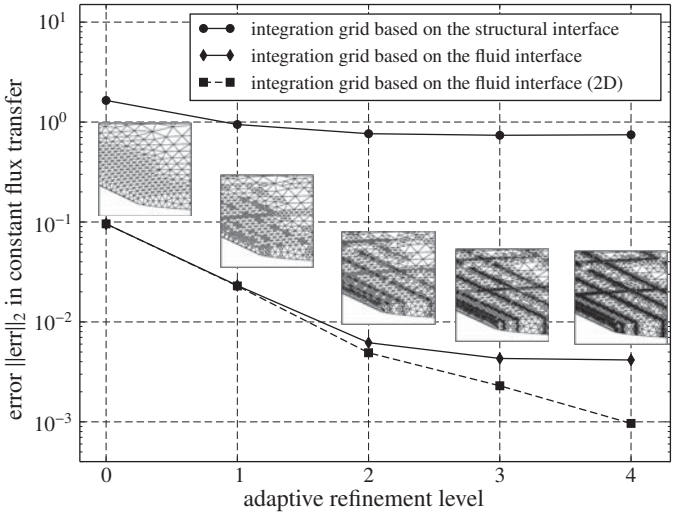

Figure 6.18: Error in constant flux transfer at different using different levels of adaptive refinement for the integration grid

no improvement of the transfer can be observed. Utilizing the fluid interface as the integration mesh, a considerable transfer improvement can be noticed up to the second refinement level. Additional refinements, i.e. more quadrature points, are ineffective in terms of the error due to the predominance of the faceting error in three dimensions. The dashed line in Figure 6.18 represents the transfer of the same configuration as above except that flat interface meshes are used, i.e. the z-coordinate of the interface discretization is set to zero to circumvent the faceting error. Without the presence of the faceting error, a further improvement of the data transfer can be observed with increasing level of refinements.

6.2.3 A smooth transfer using the three-field approach

In section 4.5 and with Eq. (4.5.12), the adaptation of the data transfer problems in the context of the three-field approach to the utilization with the numerical algorithms used for the two-field approach could be developed. Thus, the data transfer properties of the three-field approach can be studied separated from a real physical problem.

It was already mentioned, that the discretization of the frame can be done independently from a grid connected to the frame. The advantage of such transfer is the smoothness of the data transmitted to the target grid, if the connectivity frame is discretized with higher order interpolation functions. For instance, C^1 continuous shape functions can be used to discretize the displacement field of the frame, whereas the shape function of the two grids linked to the frame are interpolated with C^0 continuous shape functions. In Figure 6.19, the three interface representations are shown, which use different discretizations. The fine fluid and the coarse structural interfaces hold 65x34 and 10x5 quadrilateral C^0 continuous elements, respectively. The connectivity frame is discretized with only 6x3 C^1 continuous elements, which use Hermitian rectangle shape functions derived from standard Hermitian Euler beam shape functions, see section 11.14 of [ZT05]. Thus, each node of the connectivity frame has four degrees of freedom, corresponding to the values of:

$$u_3, \quad \frac{\partial u_3}{\partial x}, \quad \frac{\partial u_3}{\partial y}, \quad \frac{\partial^2 u_3}{\partial x \partial y},$$

whereas the fluid and structural interfaces have only the displacement u_3 as the degree of freedom.

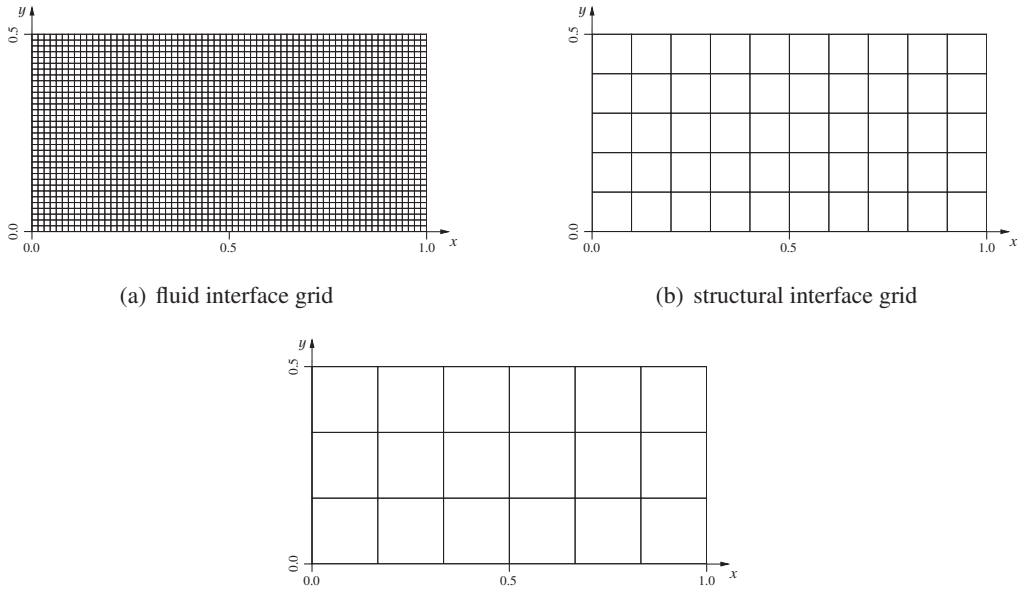

(a) fluid interface grid

(b) structural interface grid

(c) connectivity frame grid

Figure 6.19: Structured interface grids used displacement field transfer

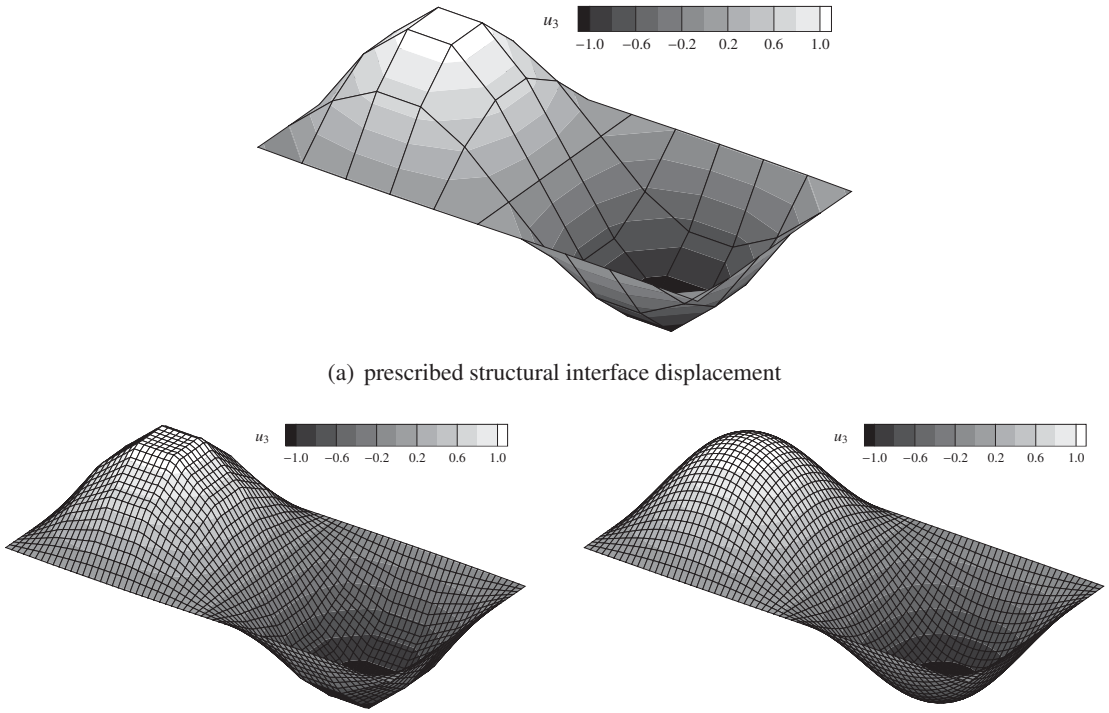

(a) prescribed structural interface displacement

(b) obtained fluid interface displacement - two-field approach

(c) obtained fluid interface displacement - three-field approach

Figure 6.20: Interface displacement fields at the interface

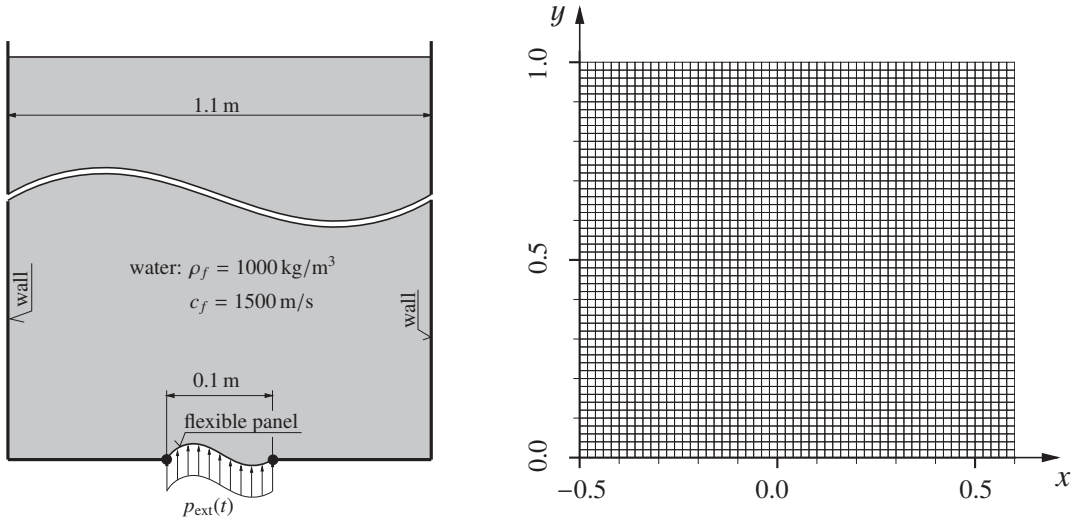

(a) physical setup

(b) grid for the acoustic fluid

Figure 6.21: Problem setup and fluid grid of elastic-acoustic coupled problem

This combination of interface discretization is now used for the displacement transfer using the two- and three-field approach. A structural displacement field is prescribed as shown in Figure 6.20(a), which is analytically described by:

$$u_3 = \sin(2\pi x) \cdot \sin(2\pi y)\,.$$

The resulting displacement field using the two-field approach in connection with the Galerkin based transfer is shown in Figure 6.20(b). Here, an exact integration of the coupling matrices could be easily reached by using the merge mesh approach of section 4.3.6. As can be seen from this figure, the obtained fluid displacements follow exactly the linear behavior of the coarse structural elements, i.e. the edges of the structural interface loom at the resulting fluid displacements. This transfer behavior might lead to unphysical CFD solutions, especially when dealing with transonic or supersonic flows.

Finally, the obtained fluid interface displacement field using the three-field approach is shown in Figure 6.20(c), where again an exact integration together with the Galerkin based transfer is applied. As seen, the nodal fluid displacements are much smoother than the field obtained with the two-field approach. Such a smooth transfer is more favorable in terms of a solution of the fluid domain with the CBS scheme or other CFD algorithms. However, the transfer based on the three-field approach is initially more expensive due to its computation of more coupling matrices, but the smooth interface displacements might reduce the inner iteration of the CFD scheme. It should be noted here, that the transposed load transfer remains conservative and thus this approach is advantageous.

6.3 Iterative solution of an elastic-acoustic problem

In this section, a simple FSI model is simulated to verify the staggered iteration procedure, which is described in section 4.4 and 4.5. The testcase consists of a flexible panel, which is coupled to an inviscid isentropic fluid (acoustic fluid). The panel is excited with an external force and due to its oscillating movement, acoustic waves travel through the fluid domain to an open end. A similar

	two-field approach		three-field approach	
	Richardson	NGMRES	Richardson	NGMRES
DN cycles:	20512	14999	18934	12996
mean DN cycles per time step:	20.51	15.00	18.93	13.00

Table 6.2: Number of Dirichlet-Neumann cycles needed for the elastic-acoustic coupled problem using different iteration schemes

testcase is described in [FKW06], but here a modified setup of the testcase is used to design a strongly coupled problem, where the high density fluid is coupled with a flexible structure.

The physical setup of the elastic-acoustic problem is shown in Figure 6.21(a). A density of $\rho_f = 1000\,\mathrm{kg/m^3}$ and a speed of sound of $c_f = 1000\,\mathrm{m/s}$ for the water is assumed. On the lower edge of the fluid domain, a thin and flexible aluminum panel is mounted, which has a length of $l_s = 0.1\,\mathrm{m}$ and a height of $h_s = 1\,\mathrm{mm}$.

The fluid domain is discretized with 55x50 equispaced quadratic 8-node finite elements shown in Figure 6.21(b). The primary unknown is a velocity potential from which the pressure is calculated as the secondary variable, see section 7.3.4 of [Bat96] for details of this formulation. At the top edge, an open boundary condition is applied and at all other edges, wall boundary conditions are set. The thin structure is modeled as a two-dimensional von Kármán plate (von Kármán beam) with 25 elements, see [Hur01] for implementation details. An external time-dependent pressure force acts on the panel with:

$$p_{\mathrm{ext}}(t) = 5 \cdot 10^4\,\mathrm{N/m^2}\,\sin(2\pi f t)$$

with a frequency of $f = 1000\,\mathrm{Hz}$. Further, it should be noted, that the fluid and structural interface grids are non-matched making it necessary to use a data transfer scheme. Thus, the Galerkin based transfer is applied, where the integration of the coupling matrices is exactly accomplished by the merge mesh approach described in section 4.3.6. For the three-field approach, the connectivity frame is discretized with only 4 elements using C^1 continuous Hermitian shape functions.

In Figure 6.22(a), the panel midpoint deflection is plotted over the time using different iteration schemes, where for all schemes a constant time step of $\Delta t = 50\,\mu\mathrm{s}$ is set. For the two-field approach, Eq. (4.4.3) and (4.4.4) are utilized to accomplish the Richardson and the Newton-GMRES iteration, respectively. For the three-field approach, Eq. (4.5.2) is used to run the Newton-GMRES algorithm, whereas Eq. (4.5.12) is applied to set up the Richardson iteration. As one can see, all schemes result in the same deformation behavior. In Figure 6.22(b), the panel deflection within the time interval of $0.040\,\mathrm{s} \leq t \leq 0.043\,\mathrm{s}$ is depicted. During this time span the panel exhibits three oscillations and this deformation has a higher mode. For two time points ($t = 0.04225\,\mathrm{s}$ and $t = 0.04275\,\mathrm{s}$), the pressure distribution within the fluid field is shown in Figure 6.22(c) and 6.22(d). These pressure distributions are similar for all iteration schemes.

To assess the iteration schemes in terms of their computational costs, the number of Dirichlet-Neumann cycles is logged. In Table 6.2, the numbers of DN cycles for each scheme required to run the simulation are listed. The iterations in each time step are terminated, when a residual of 10^{-6} is reached. Since the problem is strongly coupled, the relaxation parameter ς_{RI} for the Richardson iteration is needed to set to a very low number of $\varsigma_{RI} = 0.1$. Therefore, the number of cycles is higher than that needed for the Newton-GMRES iteration. Further, the number of cycles for the three-field approach is less than that for two-field scheme, which is caused by the

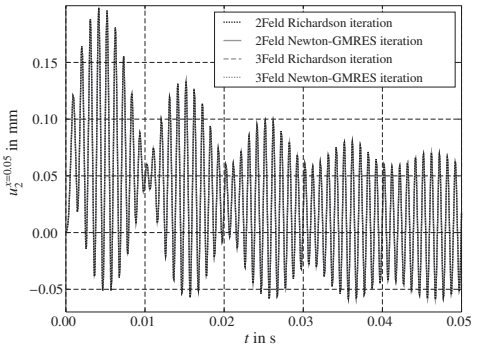

(a) panel midpoint deflection using different iteration schemes

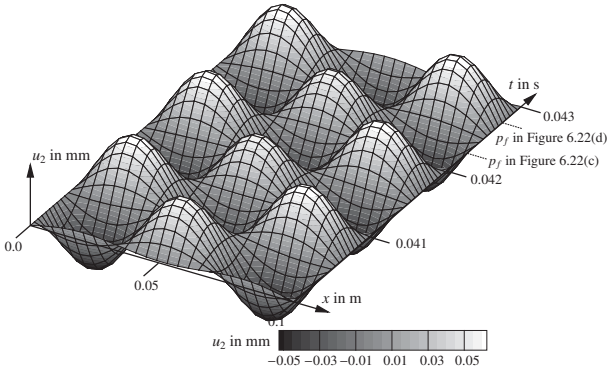

(b) typical panel deflection over three periods

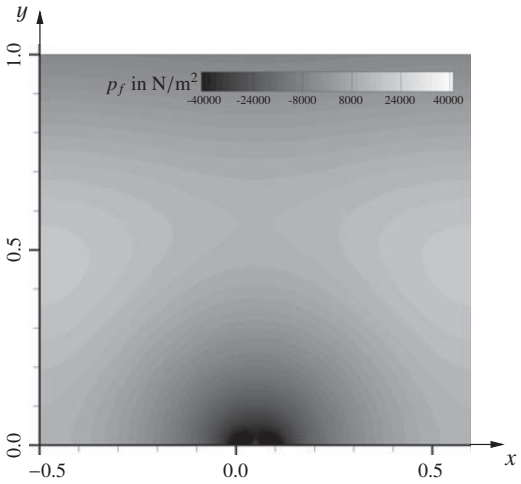

(c) pressure distribution at $t = 0.04225$

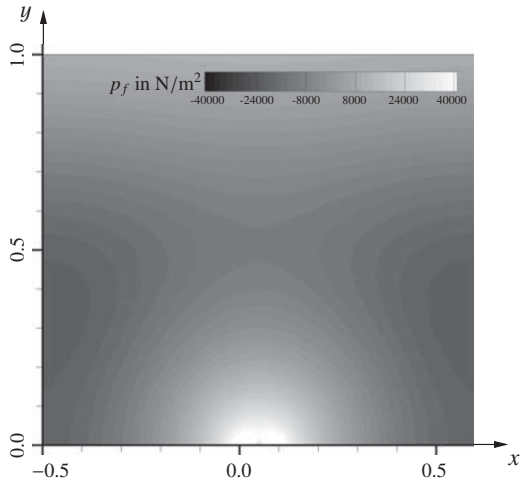

(d) pressure distribution at $t = 0.04275$

Figure 6.22: Results for the elastic-acoustic coupled problem

smooth transfer property by using C^1 continuous Hermitian frame elements. Thus, for the present elastic-acoustic coupled problem, the three-field approach gives also promising results in terms of the computational costs.

6.4 Simple staggered solution of a complex coupled problem - flapping airfoil simulation

In this section, a more complex FSI problem is investigated and validated. The numerical simulation of an oscillating and flexible airfoil for flapping wing propulsion is chosen, due to the availability of experimental data. These data have been produced within the project "Analysis of the flapping flight with flexible airfoils" of the DFG priority program SPP1207. Inspired by the flapping flight of birds, such an airfoil can be used for future micro air vehicles to improve thrust efficiency. The size of such moving vehicles and the low flight speed range cause a low-Reynolds-number flow regime with a typical Reynolds number of about $Re = 10^6$. The accurate prediction of the flow behavior using CFD is still challenging due to the occurrence of laminar-turbulent transition [LS07, YKW$^+$07, RWS07, OMH$^+$05]. The transition takes place along a laminar separation bubble, which is caused by a strong adverse pressure gradient within the laminar boundary

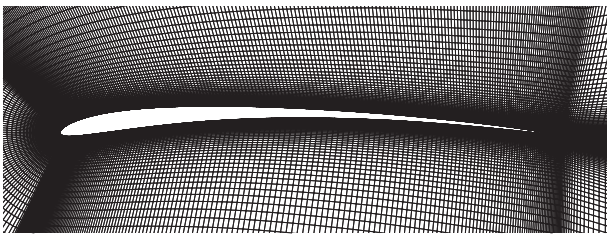

Figure 6.23: close-up view on the structured grid for flow calculation over the SG04 airfoil

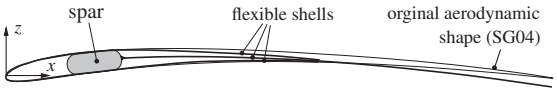

Figure 6.24: Principle design of the flexible airfoil

layer and along the smooth aerodynamic surface. Therefore, instead of the CBS scheme, the well-validated finite volume code FLOWer, which solves the unsteady Reynolds-averaged Navier-Stokes equation, is used in conjunction with an e^N method for the transition prediction to take this instability phenomenon into account [RWS07, WR08].

A coupled problem involving the CBS scheme will be the topic of the next chapter. In this section, the coupling environment, with a conservative transfer scheme, the grid deformation and simple staggered time integration scheme with a predictor is validated. More precisely the following numerical components are used for the computation:

1. FLOWer together with an e^N method for transition prediction for the fluid domain
2. the commercially available finite element solution package ANSYS® for the structural domain, [ANS06]
3. the conservative interpolation as described in section 4.3.2 for the data transfer
4. the stiffness evaluation based on the wall distance, i.e. Eq. (4.2.4), for the finite element grid deformation due to its performance evaluated in section 6.1.2
5. the simple staggered two-field approach for the time integration of the coupled problem with the predictor of Eq. (4.4.8)

6.4.1 Simulation setup

For the fluid part of the coupled computation, a structured grid around the SG04 airfoil is generated with 585x129 nodes, Figure 6.23. The SG04 airfoil was designed based upon a handfoil of a seagull with a camber of 4% and its aerodynamic behavior was published in [UKH+07, BRU+10]. The use of the wall distance based stiffness evaluation method for the fluid grid deformation is motivated due to the results obtained in section 6.1.2.

For the structural part of the simulation environment, a non-linear finite element model of the airfoil is designed. This numerical model is based on a design using carbon reinforced plastic with a stiff forebody and an overlapping three-shell concept, Figure 6.24. Further, the finite element model contains layered shell elements for the carbon reinforced plastic plates and contact elements to model the area, where the upper and lower shell are in contact with the central shell. This model is structurally validated with a manufactured wind tunnel model in terms of the first eigenfrequency, eigenform and mass, see [UHHW08, BRU+10] for details. The structural airfoil has a camber, which is higher than that for the original SG04 airfoil. This higher camber is designed in a way, that at a gliding flight with a Reynolds number of $Re = 10^5$ and angle of attack $\alpha = 3°$ the aerodynamic shape is obtained.

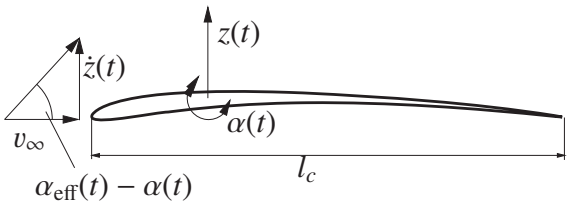

Figure 6.25: Definition of the effective angle of attack

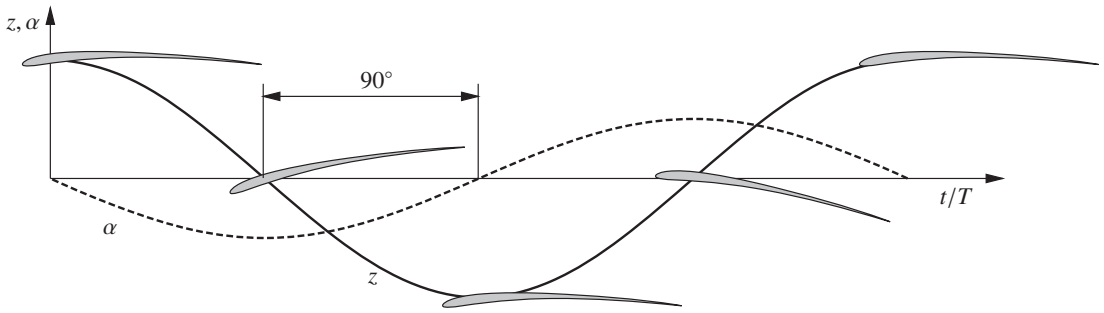

Figure 6.26: Combined pitch-plunge motion witch 90° phase shift

6.4.2 Flapping flight motion parameters

A harmonic pitching-plunging motion of the airfoil is investigated for the flapping flight simulation, i.e. the motion is prescribed through the structural model. The plunging part of the motion can be expressed as:

$$z(t) = \hat{z}\sin(2\pi f t)\,, \tag{6.4.1}$$

with $z(t)$ being the position of the quarter-chord line. The effective angle of attack due to the pitching motion is then, see also Figure 6.25:

$$\begin{aligned}\alpha_{\text{eff}}(t) &= \alpha(t) + \arctan\left(\frac{\dot{z}(t)}{v_\infty}\right) = \alpha_0 - \hat{\alpha}\cos(2\pi f t) + \arctan\left(\frac{2K\hat{z}}{l_c}\cos(2\pi f t)\right) \\ &\approx \alpha_0 + \left(\frac{2K\hat{z}}{l_c} - \hat{\alpha}\right)\cdot\cos(2\pi f t)\,,\end{aligned} \tag{6.4.2}$$

where $K = \pi f l_c / v_\infty$ is the reduced frequency and a phase angle of 90° between the plunging and pitching motion is assumed. The following parameters of the flapping flight simulation are used:

- reduced frequency of $K = 0.2$
- plunging amplitude of $\hat{z} = 0.5 l_c$
- angle of attack of $\alpha_0 = 4°$
- effective angle of attack amplitude of $\hat{\alpha}_{\text{eff}} = \frac{2K\hat{z}}{l_c} - \hat{\alpha} = 4°$
- Reynolds number of $Re = 10^5$
- time step size of $\Delta t = \frac{1}{500 f}$
- critical N-factor of $N_{\text{crit}} = 8$ (corresponds to a turbulence level of 0.1%).

A sketch of this combined pitching-plunging motion is depicted in Figure 6.26.

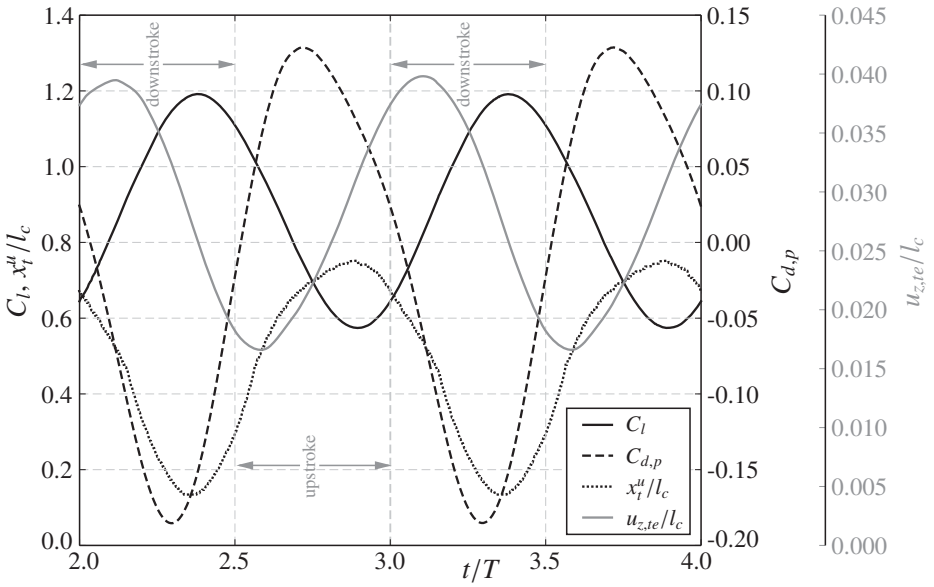

Figure 6.27: Lift and pressure induced drag coefficients as well as transition location and trailing edge deformation of the flapping flexible airfoil over two periods of motion

6.4.3 Validation of a reference testcase

The resulting time history of the lift and pressure induced drag coefficient as well as the evolution of the transition location of the upper airfoil side and the trailing edge deformation are shown in Figure 6.27 for two periods of the motion. It can be seen, that due to the unsteady fluid flow, the always positive lift has its maximum during the downstroke shortly after the mid-downstroke, although the highest effective angle of attack is reached at $t/T = 0.25 + i$ (i being the period number). The mean lift over one period is $\overline{C}_l = 0.8802$. The highest negative drag, i.e. thrust, is also reached during the downstroke shortly after the mid-downstroke, but before the maximum lift is obtained. On the other hand, the highest positive drag is obtained shortly before the mid-upstroke. Integrating the drag over one period gives the mean drag, which is computed as $\overline{C}_{d,p} =$

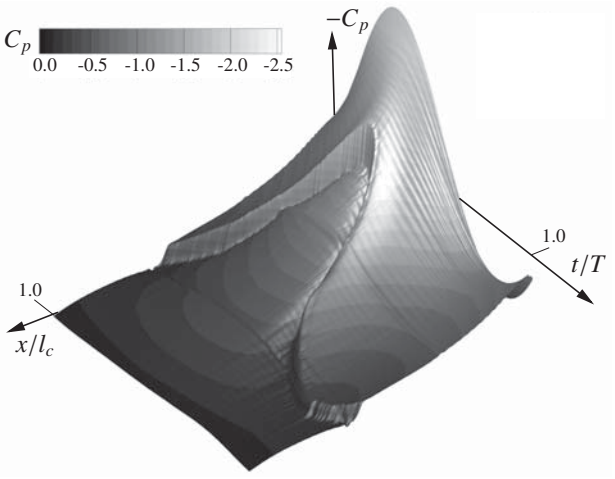

Figure 6.28: Pressure distribution of the upper airfoil over one period

−0.0128, i.e. thrust is generated during one flapping period. From the time history plot of the transition location, it can be observed, that the laminar separation bubble moves from the trailing edge towards the leading edge during the downstroke and moves back during the upstroke, whereas it never reaches the last 30% of the rear part. Thus, the laminar separation bubble is present at all times for the flapping flexible airfoil.

The trailing edge deformation evolution is depicted without the rigid body motion part, i.e. the evolution in Figure 6.27 shows the pure deformation in the local airfoil coordinate system. The highest deformation is numerically obtained shortly after the top dead center at $t/T = 0.1 + i$. The deformation decreases, i.e. the camber increases, while the airfoil moves to the bottom dead center. The lowest deformation is computed shortly after the bottom dead center and during the upstroke the camber is then decreased. The phase shift between the lift and the trailing edge deformation is $\Delta t/T = 0.275 = 100°$.

The lowest reached transition location is obtained at $t/T = 0.35 + i$ with a value of $x_t^u/l_c = 0.134$. The effect of this laminar separation bubble to the pressure distribution of the upper side of the airfoil is shown in Figure 6.28, where the C_p-value is plotted over the $x/l_c - t/T$-plane for one period. A jump in the C_p distribution is induced due to laminar-turbulent transition. This jump moves together with transition location from the trailing to the leading edge and back during one period of motion, where the height of the jump increases with lower values of x_t^u/l_c. Interesting is the correlation between the lift and transition location. At the time, when the lowest transition location is reached, the lift has its maximum value and *vice versa*.

The turbulent shear stress distribution, which is an adequate indicator for the transition from laminar to turbulent flow, is shown in Figure 6.29 for four discrete time points together with the turbulent shear stress obtained in wind tunnel test campaigns, published in [BRU+10]. These experimental data were obtained with the aid of stereoscopic PIV measurements at the flapping airfoil, where the flow velocity was captured at several window locations around the airfoil and at multiple time instances. These sets of velocity vector images are ensemble averaged to get the desired turbulent stress. It can be observed from the comparison, that at the top dead center the computed transition location is more upstream than that found in the experiment, Figure 6.29(a). This situation changes during the downstroke and at the mid-downstroke the calculated transition location lies behind the experimental found location, Figure 6.29(b). This indicates, that the change of x_t^u is insufficiently resolved by the numerical scheme. During the upstroke the experimentally found transition location is again more downstream than numerically predicted, Figure 6.29(c) and 6.29(d). This disagreement was already noticed for the rigid version of the airfoil and is likely caused by the turbulence assumption of the URANS solver, [BRU+10, Ban11].

6.5 Chapter summary

In this chapter, parts of the coupling environment are numerically verified and validated. Furthermore, several options for the fluid grid deformation and data transfer schemes are assessed. For the fluid grid deformation it is found, that the stiffness evaluation methods introduced in section 4.2 perform similarly. However, the stiffness strategy based on the wall distance and the characteristic length is recommended to use for the simple testcases with the unstructured grid. For the structured grid in conjunction with the flapping-bending grid deformation, the best grids are obtained with the stiffness evaluation methods based on the wall distance. Thus, for general fluid grid deformations, the method which uses (4.2.6) is recommended.

Regarding the interface data transfer it is shown, that for low-curved interface grids an adaptive refinement of the integration grids leads to a reduction of the transfer error. For highly curved

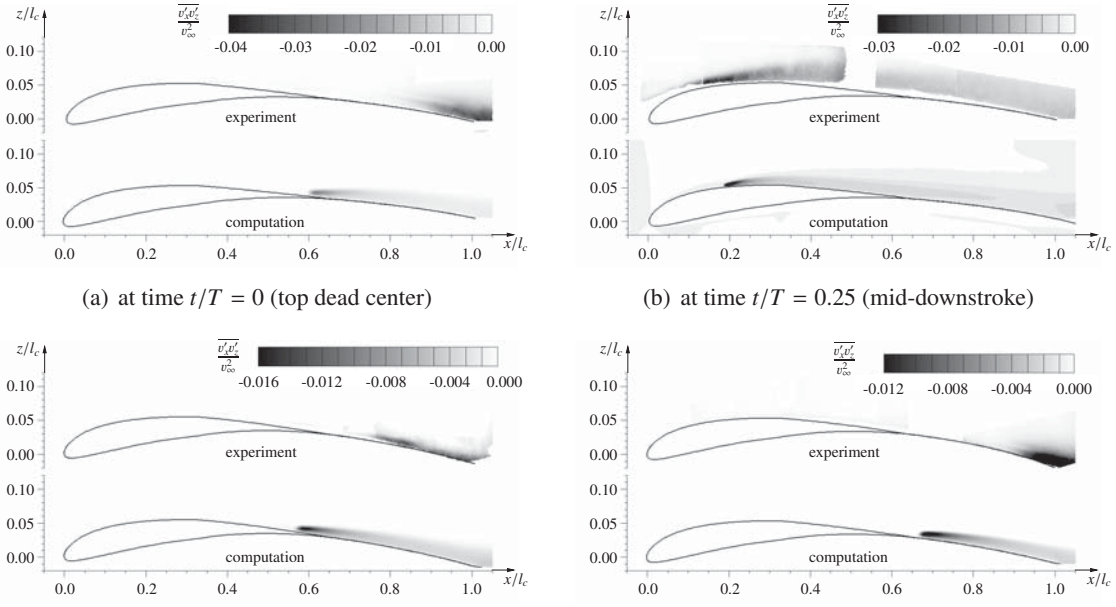

(a) at time $t/T = 0$ (top dead center)

(b) at time $t/T = 0.25$ (mid-downstroke)

(c) at time $t/T = 0.625$ (upstroke)

(d) at time $t/T = 0.75$ (mid-upstroke)

Figure 6.29: Comparison of computational and experimental results in terms of the turbulent shear stress distribution around the airfoil at several time instances - experimental data from [BRU+10]

interfaces, another error - the faceting error - becomes present and the transfer error cannot be more reduced. This faceting error is also identified by the data transfer for a realistic wing configuration.

Further, a smooth transfer scheme is proposed in this chapter, which uses the three-field coupling approach with a higher spatial order discretization of the connectivity frame. This transfer scheme remains also load conservative, which is an important property for computational aeroelasticity.

The three-field approach is further investigated in the context of an elastic-acoustic FSI problem, where two equilibrium iteration schemes - Richardson iteration and Newton-GMRES - are studied in terms of the number of DN cycles. For this strongly coupled problem, it is shown, that with the usage of the Newton-GMRES iteration scheme the number of DN cycles are reduced for both, the two- and three-field approach. Further, the smooth transfer of the three-field leads to the best computational effort for this problem.

In the last section of this chapter, the simulation of the flapping airfoil at a low Reynolds-number flow is validated with experimental data. Since transition prediction is needed for such flow problems, FLOWer with an e^N method is used. Here, a simple staggered two-field coupling procedure is utilized together with the conservative interpolation and the finite element fluid grid deformation. Thus, the validated structural finite element model is coupled to the fluid grid and the simulation is compared to experimental data in terms of the turbulent shear stress distribution. It could be shown that the experimental data are principally captured by the numerical simulation, although the change in the transition location in reality is faster than numerically predicted.

7 Finite Element Fluid-Structure Interaction - Panel Flutter Problem

In this chapter, the typical non-linear and dynamic aeroelastic phenomenon of the panel flutter is intensively investigated with the aid of schemes presented in chapter 3 and 4. This classical aeroelastic problem exhibits a limit cycle oscillation (LCO), i.e. the flutter amplitude is restricted due to the non-linear nature of the thin structure.

7.1 Problem description

The panel flutter problem is a classical phenomenon in aeroelasticity and consists of a clamped or simply supported plate over which a fluid flows. Usually, this plate or panel is very thin and has therefore to be modeled as a non-linearly behaving structure. Due the fluid flow, the panel can exhibit a self-exciting oscillation. Another aeroelastic behavior, which can be observed, is a steady deflection of the panel known as divergence. Which of these aeroelastic phenomena exhibit, depends on the combination of parameters in particular the panel thickness, the flow Mach number or the flow pressure at infinity. Further, the panel flutter problem is often used as an aeroelastic model problem, since the phenomena observed here are also present in aircraft wings.

In Figure 7.1, the setup of the panel flutter problem is depicted. The fluid flows tangentially over the panel, which has a height h_s and a length l_s. Underneath the panel a constant pressure of $p_{f,\infty}$ is applied. The pressure induced by the flow deforms the panel, which in turns influences the flow field.

7.1.1 Structural model of the panel

To take the large structural deformation into account, the panel itself is modeled with the von Kármán plate model, where the non-linearity comes from an in-plane restoring force, whose value depends on the panel deflection, [Dow77, CD04]. Therefore, the amplitude of a panel oscillation is limited due to the restoring force and this kind of flutter phenomenon is called limit cycle oscillation (LCO).

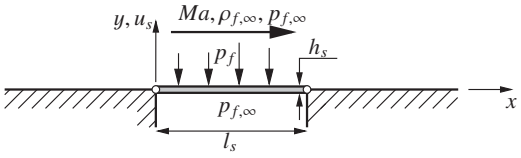

Figure 7.1: Description of the panel flutter problem

The structural displacement-based action functional I_s for a thin one-dimensional von Kármán plate, i.e. a constant plate behavior in spanwise direction, can be expressed as:

$$\begin{aligned} I_s(u_s) = \int_{t_1}^{t_2} \Bigg\{ \int_0^{l_s} \frac{1}{2} \left[D \left(\frac{\partial \theta_s}{\partial x} \right)^2 + \tfrac{5}{6} G \left(\frac{\partial u_s}{\partial x} - \theta_s \right)^2 + \frac{B_0 + B_x}{2} \left(\frac{\partial u_s}{\partial x} \right)^2 \right] dx \\ - \int_0^{l_s} \frac{1}{2} \left[\rho_s h_s \left(\frac{\partial u_s}{\partial t} \right)^2 + \frac{\rho_s h_s^3}{12} \left(\frac{\partial \theta_s}{\partial t} \right)^2 \right] dx - \int_0^{l_s} u_s \hat{p}_s \, dx \Bigg\} dt \,, \end{aligned} \tag{7.1.1}$$

where u_s is defined as the deflection of the panel, i.e. as the deformation in y-direction. The first integral represents the potential and the second denotes the kinetic energy. The angle θ_s is the rotation of the plate section. The values D and G denote the plate stiffness and shear module of the panel with:

$$D = \frac{E h_s^3}{12(1 - \nu_s^2)}; \qquad G = \frac{E}{2(1 + \nu_s)}; \tag{7.1.2}$$

with E and ν_s being the stiffness module and Poisson's ratio of the panel, respectively. The non-linearity occurs due to the force $B_x = B_x(\partial u_s / \partial x)$:

$$B_x = \frac{E h_s}{2 l_s} \int_0^{l_s} \left(\frac{\partial u_s}{\partial x} \right)^2 dx \,. \tag{7.1.3}$$

The structural system is spatially discretized by Timoshenko beam elements, which are free of shear locking, resulting in the following matrix system, [Hur01, FK93]:

$$\left[(\rho_s h_s) \mathbf{M}_u + \frac{\rho_s h_s^3}{12} \mathbf{M}_\theta \right] \ddot{\mathbf{u}}_s + \left[D \mathbf{K}_u + \tfrac{5}{6} G h_s \mathbf{K}_\theta + \tfrac{1}{2} E h_s (\mathbf{u}_s^T \mathbf{K}_R \mathbf{u}_s) \mathbf{K}_R \right] \mathbf{u}_s = \mathbf{f}_{u,\text{ext}} \,, \tag{7.1.4}$$

where it is assumed, that the panel is not pre-stressed, i.e. $B_0 = 0$. Clearly, the non-linearity is given by the third part of the stiffness term. For a definition of the matrices $\mathbf{M}_u$, $\mathbf{M}_\theta$, $\mathbf{K}_u$, $\mathbf{K}_\theta$ and $\mathbf{K}_R$ consult [FK93, Hur01].

7.1.2 Aeroelastic parameters of the panel flutter problem

All the structural parameters like panel length, thickness, stiffness and the fluid parameters like density, pressure and velocity of the flowing air at infinity can be expressed through three aeroelastic parameters. The first parameter is the non-dimensional mass ratio, here defined as r_m, which can be written as:

$$r_m = \frac{\rho_{f,\infty} l_s}{\rho_s h_s} = \frac{\rho_{f,\infty}}{\rho_s \frac{h_s}{l_s}} \,. \tag{7.1.5}$$

A second parameter is the non-dimensional dynamic pressure r_p, which is:

$$r_p = \frac{\rho_{f,\infty} v_{f,\infty}^2 l_s^3}{D} = \frac{\rho_{f,\infty} v_{f,\infty}^2 12(1 - \nu_s^2)}{E \left(\frac{h_s}{l_s} \right)^3} \,. \tag{7.1.6}$$

The key aeroelastic parameter is the reduced frequency K, which is defined as:

$$K = \frac{\pi f l_s}{v_{f,\infty}} \,. \tag{7.1.7}$$

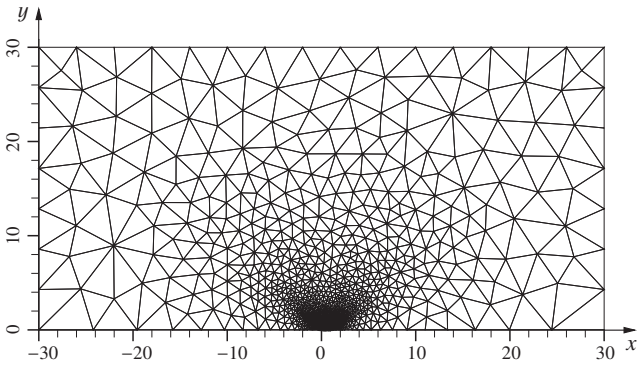

Figure 7.2: Unstructured grid for calculations of inviscid panel flutter problem

Here, the reduced frequency is the result of the computation for the panel flutter problem. Therefore, the Mach number Ma_∞ is used as third input parameter. The aeroelastic problem of the panel flutter is thus defined by the three input parameters (r_m, r_p, Ma_∞). Given a panel with the material density ρ_s, Young's modulus E and Poisson's ratio ν_s as well as the geometric parameters h_s and l_s, the fluid density and the velocity at infinity are obtained from Eq. (7.1.5) and (7.1.6), respectively. From the definition of the Mach number Eq. (3.2.11), the temperature or the pressure at infinity can be obtained. Usually, the mass ratio r_m is fixed and the response of the system due to the Mach number and the non-dimensional dynamic pressure r_p is studied to obtain a stability chart.

7.2 Transonic panel flutter - methodology assessment

Initially, the panel flutter problem is investigated at a transonic Mach number of $Ma_\infty = 1.0$. The panel is made by aluminum with a density of $\rho_s = 2700\,\mathrm{kg/m^3}$. Young's modulus and Poisson's ratio are $E = 7.1 \cdot 10^{10}\,\mathrm{N/m^2}$ and $\nu_s = 0.34$, respectively. The geometry of the panel is set to a thickness of $h_s = 4.537\,\mathrm{mm}$ and a length of $l_s = 1.0\,\mathrm{m}$. The panel is simply supported at $x/l_s = 0.0$ and $x/l_s = 1.0$.

In [Mas02], a bifurcation of the panel's aeroelastic behavior with a constant mass ratio of $r_m = 0.1$ was reported when increasing the non-dimensional dynamic pressure r_p from 160 to 180. At a pressure of $r_p = 180$ a LCO can be observed and for $r_p = 160$ a divergence of the panel is predicted. For a pressure of $r_p = 170$, flutter should be obtained and therefore this case is chosen to study the influence of the different transfer schemes, the performance of the structural predictors in conjunction with a simple staggered time integration scheme. Further, the proposed consistent time integration scheme is investigated as well as the performance of the DG-CBS compared to standard CBS scheme.

For this testcase, an inviscid fluid is assumed and therefore the Euler equations of the fluid motion are solved. In Figure 7.2, the used triangular mesh for the fluid domain is depicted. This grid consists of 7516 nodes connected to 14521 elements. Small elements are placed in the vicinity of the panel ($0.0 \leq x \leq 1.0$). The fluid interface is discretized with 400 elements.

7.2.1 Influence of the transfer scheme

First, the influence of the different transfer schemes presented in section 4.3 on the flutter behavior of the panel is studied. Additionally, the non-conservative load transfer often used in aeroelas-

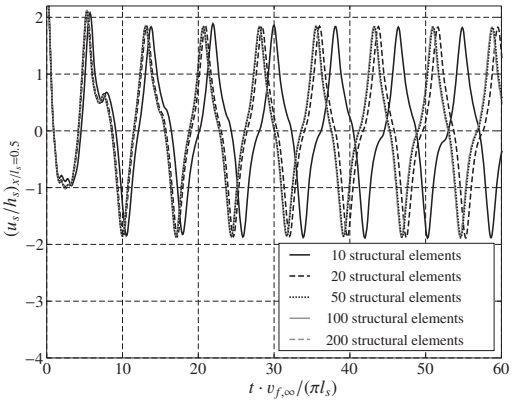

(a) Galerkin based transfer

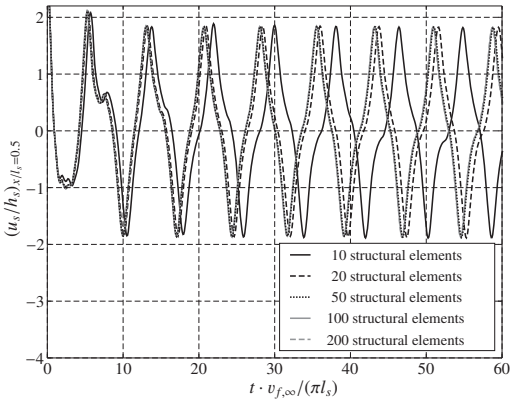

(b) dual-Lagrange based transfer

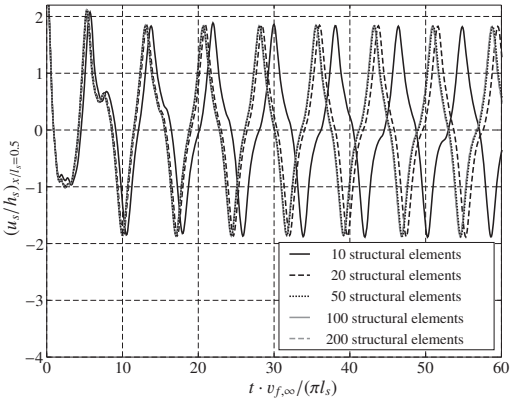

(c) conservative Interpolation

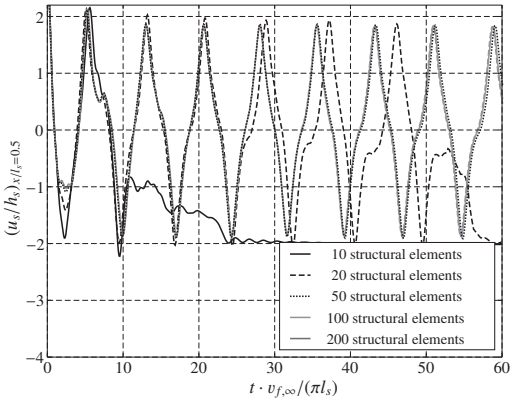

(d) non-conservative Interpolation

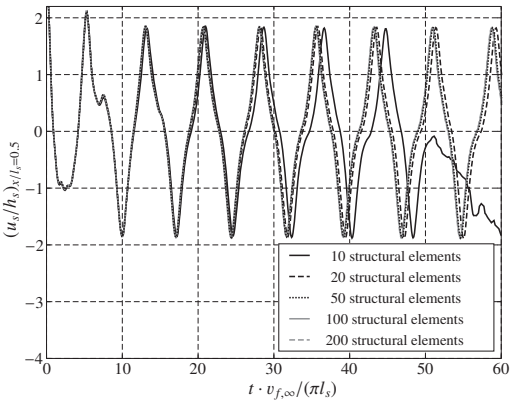

(e) Sobolov norm based transfer

Figure 7.3: Midpoint deflection of the panel using different transfer schemes and number of elements

tic computations is included in this study. For the non-conservative load transfer, the structural pressure load at the nodes are calculated from the fluid pressure with the aid of the fluid shape functions, i.e. the structural nodes need to be mapped on a proper fluid element and the pressure is calculated from the adjoined fluid nodes.

A constant time step of $\Delta t = 10^{-3}$ s is used for all calculations presented in this section. Further, in terms of the CBS scheme, the explicit scheme with $\theta_1 = 0.75$ and $\theta_2 = 0.0$ is applied

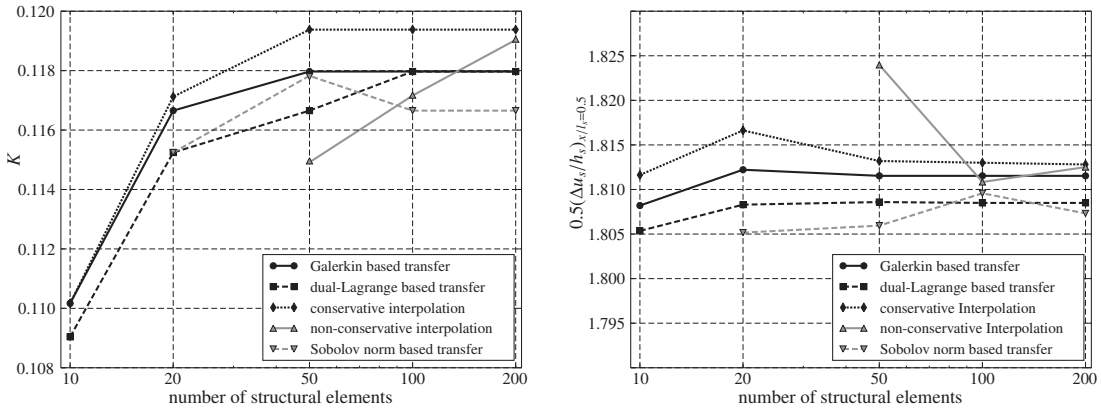

(a) reduced frequency

(b) panel midpoint amplitude

Figure 7.4: Reduced frequency and midpoint amplitude of the LCO using different transfer schemes and number of elements

as well as the lumped mass matrix option to obtain a matrix free solution procedure. The iterative equilibrium iteration depicted in Figure 4.5 is used to suppress possible errors due to a simple staggered time integration scheme, i.e. the Richardson equilibrium iteration is applied.

In Figure 7.3, the midpoint deflections of the panel using different transfer schemes are shown for various numbers of structural elements. The time history plots are non-dimensionalized with $\pi l_s / v_{f,\infty}$ so that the reduced period time, $1/K$, can be directly identified.

In Figure 7.3(a), the panel's midpoint deflection using the Galerkin based transfer is depicted, where the coupling matrix $\check{\mathbf{M}}^{(sf)}$ is computed based on a merged mesh, which can be simply obtained from the fluid and structural interface grids. Even for a very coarse structural mesh, a flutter behavior of the panel is obtained and the results fit well with those reported in [Mas02]. For 50 and more structural elements, identical results are obtained and no differences in terms of flutter amplitude and frequency can be seen. The convergence of the reduced frequency and the amplitude regarding the number of structural elements is shown in Figure 7.4. For the Galerkin based transfer, a reduced frequency of $K = 0.118$ and a midpoint amplitude of $0.5(\Delta u_s/h_s)_{x/l_s=0.5} = 1.812$ are obtained for 50 and more elements. In [Mas02], a reduced frequency of 0.110 and a non-dimensional amplitude of 1.79 could be reconstructed, but a structured grid with 80 elements on the fluid interface was used for these computations.

The deflection of the panel discretized with 50 elements over one period of the limit cycle oscillation is shown in Figure 7.5(a), where the panel deformation is also colored. The panel is fully deflected in positive y-direction at a non-dimensional time $t \cdot v_{f,\infty}/(\pi l_s) = 74.7$. The structure then rapidly deflects to the opposite direction. From the bottom dead center, the panel is now deformed to the top dead center, while the deflection shows a wavelike behavior, where the first 50% of the panel reaches a positive deflection at $t \cdot v_{f,\infty}/(\pi l_s) \approx 79.2$ before the remaining panel part follows upward. This main deformation behavior of the panel is accompanied by higher modes, which are also excited by the fluid flow. The corresponding pressure coefficient on the structural discretization is shown in Figure 7.5(b), where a weak shock occurs on the panel, which is mostly present while the panel deforms from bottom to the top dead center. This shock moves from the middle to the end of the panel and the Galerkin based transfer is able to resolve this shock on the coarse structure, while the pressure distribution is transmitted from a fine fluid interface grid. Finally, the Mach number contours at four discrete time points are shown in Figure 7.6. In Figure 7.6(a) and 7.6(d), the moving weak shock is again visible.

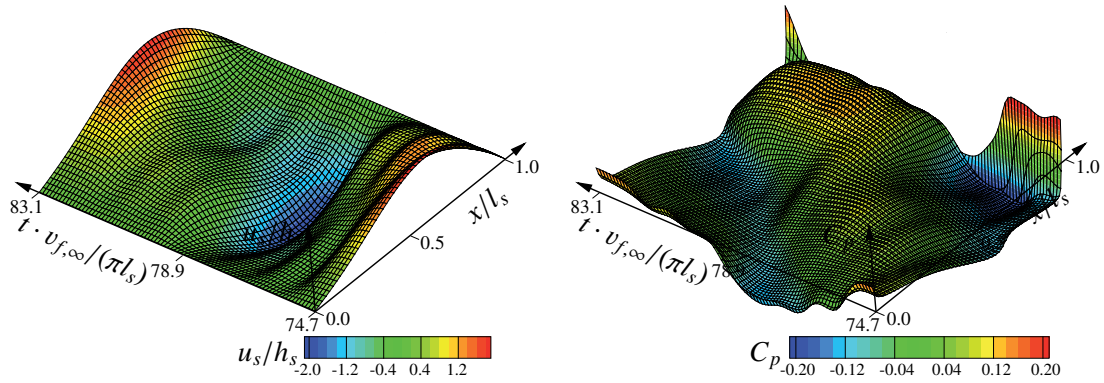

(a) panel deformation

(b) pressure coefficient

Figure 7.5: Deformation of the panel during one cycle of oscillation and the according pressure load on the panel using the Galerkin based transfer with 50 structural elements

The time history of the midpoint deflection using dual-Lagrange multipliers for the data transfer shows nearly the same behavior as the Galerkin based transfer scheme, Figure 7.3(b). With 100 and more structural elements, the same LCO frequency is obtained, Figure 7.4(a), and only a slightly lower midpoint amplitude compared to the Galerkin based transfer is computed, Figure 7.4(b). The advantage of the dual-Lagrange multipliers lies in the computational costs of inverting the matrix $\mathbf{M}^{(f)}_{\lambda u} = \check{\mathbf{M}}^{(ff)}$. Therefore, this is a favorable transfer scheme for FSI problems involving many degrees of freedom.

The conservative interpolation shows a similar midpoint panel deflection behavior as the Galerkin or the dual-Lagrange based transfer, see Figure 7.3(c). The reduced frequency and the midpoint deflection of this scheme converge to a slightly higher value than that for the Glaerkin based transfer, Figure 7.4(a) and Figure 7.4(b). But it should keep in mind that this identical behavior is due to the fine fluid interface grid compared to the structural interface representation. As soon as, the structural interface grid becomes much finer as the fluid interface grid, unphysical oscillation in the transmitted pressure will be present [UHH07a]. This unphysical oscillation is caused by the property of this scheme, that some structural nodes will not receive any forces from the fluid interface due to the different discretization of the interface, [CL97].

Using the non-conservative interpolation as described above, no flutter is observed, when the structure is discretized with 10 or 20 finite elements, Figure 7.3(d). Only with 50 and more elements a LCO of the panel is identified and with 100 structural elements similar flutter frequencies and amplitudes are obtained, Figure 7.4(a) and Figure 7.4(b). The main reason for this behavior is the artificial energy loss during the data transfer, i.e. the load computed by the CBS scheme is not conserved, when transmitted to the structure. Therefore, this scheme cannot be recommended for aeroelastic computations.

In Figure 7.3(e), the midpoint deflection of the panel is shown using the Sobolev-norm based transfer scheme with $\varsigma_{SN} = 0.3$, whereby the integration is performed on a merged mesh. For 50 and more structural elements, almost an identical time history as for the transfer using the Galerkin based can be identified. However, the panel losses stability after a few cycles for 10 elements ($t \cdot v_{f,\infty}/(\pi l_s) > 50$) and no flutter is observed. The reduced frequency converges to lower value than that for the Galerkin based transfer, Figure 7.4(a), whereas no definite convergence is observed for the amplitude with 200 structural elements. The main difficulty of the Sobolev-norm based transfer is to estimate an optimal parameter ς_{SN}. In [JH04], a suggestion for the evaluation of the weight ς_{SN} is given, which is of local character and only applicable for structured grids. Therefore, this scheme cannot be recommended for general aeroelastic application yet.

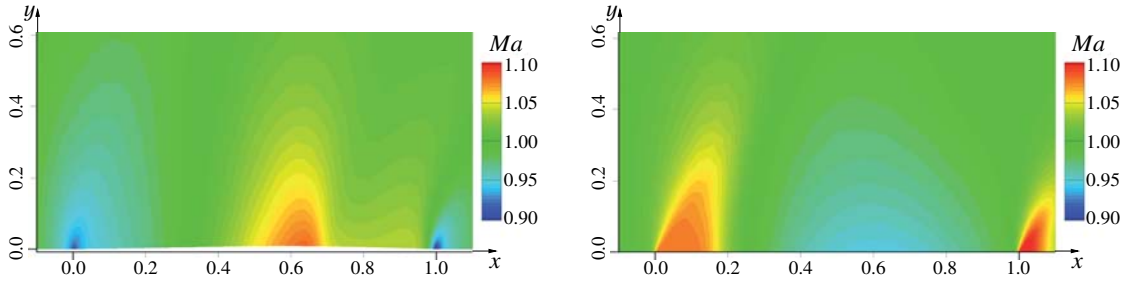

(a) Mach number contours at $t \cdot v_{f,\infty}/(\pi l_s) = 74.7$

(b) Mach number contours at $t \cdot v_{f,\infty}/(\pi l_s) = 76.8$

(c) Mach number contours at $t \cdot v_{f,\infty}/(\pi l_s) = 78.9$

(d) Mach number contours at $t \cdot v_{f,\infty}/(\pi l_s) = 81.0$

Figure 7.6: Mach number contours of the fluid passing the panel at four time points using the Galerkin based transfer with 50 structural elements

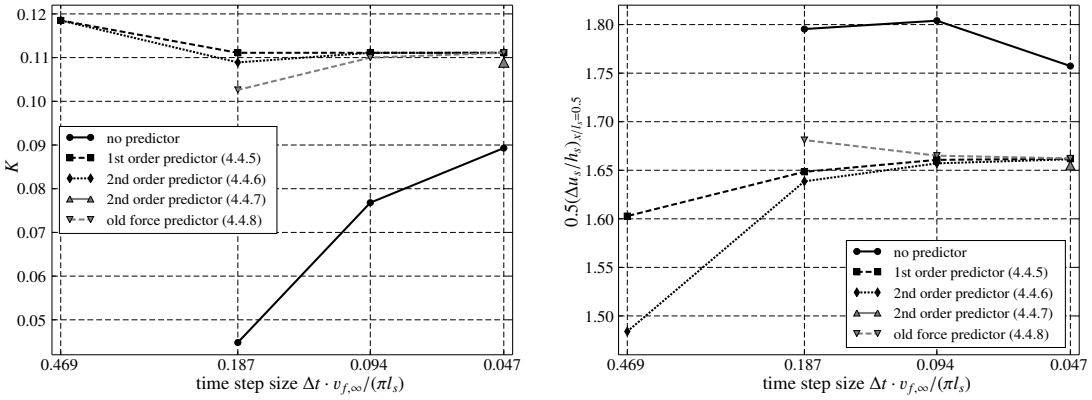

(a) reduced frequency

(b) panel midpoint amplitude

Figure 7.7: Reduced frequency and midpoint amplitude of the LCO using different predictors at several time step sizes

In summary, the Galerkin and the dual-Lagrange based transfer as well as the conservative interpolation give similar results for the transonic panel flutter problem. The dual-Lagrange based transfer is recommended here, since this scheme is load conservative and combines the general applicability for different interface discretization with the efficiency of a matrix-free transfer scheme like the conservative interpolation.

7.2.2 Influence of the time integration scheme

In a next investigative campaign, the panel flutter problem is studied with a simple staggered time integration scheme, i.e. the data transmission from the fluid to the structure and vice versa is only accomplished once in a time step to reduce the computational effort. Thus, the first and second

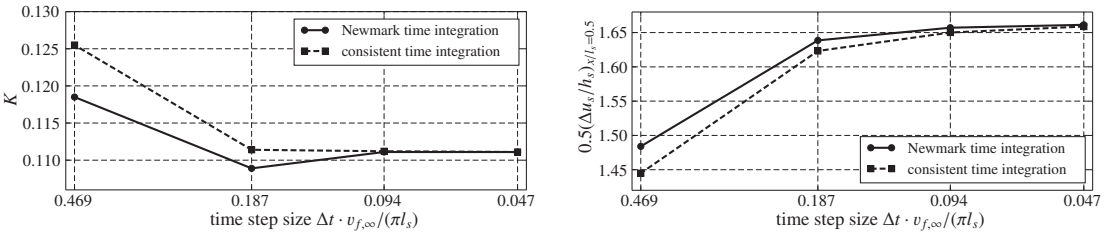

(a) reduced frequency

(b) panel midpoint amplitude

Figure 7.8: Reduced frequency and midpoint amplitude of the LCO using time integration schemes at several time step sizes

order structural predictors Eq. (4.4.5) to (4.4.8) are tested at several time step sizes with a structural discretization of 100 elements and with the application of the dual-Lagrange based transfer due to its performance observed in the previous section. The remaining parameters are kept unchanged.

First, an inconsistent time integration of the coupled system is used, i.e. for the structural subsystem, the Newmark scheme of Eq. (4.6.1) is utilized. Using a small time step size of $\Delta t = 0.5 \cdot 10^{-3}$ s, which corresponds to a non-dimensional time step of $\Delta t \cdot v_{f,\infty}/(\pi l_s) = 0.047$, all schemes except the one without predictor result in a similar flutter frequency and amplitude, Figure 7.7. Without any predictor, a considerably lower reduced frequency and higher amplitude are obtained. Moreover, with the second order predictor from Eq. (4.4.7), a slightly lower frequency and amplitude as for the other predictors are computed. The reduced frequency for the schemes with predictor is a bit smaller as the frequency obtained with Richardson equilibrium iteration from the previous section. Further, the amplitude of the LCO is decreased when a simple staggered scheme is used.

Increasing the time step size to $\Delta t = 1.0 \cdot 10^{-3}$ s or $\Delta t \cdot v_{f,\infty}/(\pi l_s) = 0.094$, the predictor of Eq. (4.4.7) fails to predict flutter for the testcase, Figure 7.7. For very coarse time steps ($\Delta t \cdot v_{f,\infty}/(\pi l_s) = 0.468$), only the first and second order predictor from Eq. (4.4.5) and Eq. (4.4.6) predict flutter.

Finally, it should noted, that Figure 7.7 represents the temporal convergence of the presented coupling scheme and regarding the panel flutter problem, and the second order predictor (4.4.6) gives the best results even for very coarse time steps.

Switching the structural time integration scheme to the three-point difference backward scheme, the resulting coupling scheme is consistent in terms of the time integration. In Figure 7.8, the Newmark and the consistent three-point difference backward time integration scheme for the structural subsystem are compared for several time steps in terms of the reduced frequency and the midpoint panel flutter amplitude. Here, the second order predictor (4.4.6) for both integration methods is applied. For small time steps, both time integration methods results in an identical flutter frequency and amplitude. For very coarse time step sizes, the differences in both values become noticeable. Especially from the reduced frequency convergence plot, it can be seen, that the consistent time integration scheme yields a better convergence behavior than the classical Newmark integration scheme.

To summarize, with a simple staggered time integration scheme of the coupled problem in conjunction with the usage of the structural predictor, the computational time can be reduced due to the omission of the equilibrium iteration within a time step. Nevertheless, the results obtained with such a scheme are reliable in terms of both the flutter frequency and amplitude. Further, similar results are observed when the Newmark or the consistent three-point backward difference scheme for the structural time integration is used.

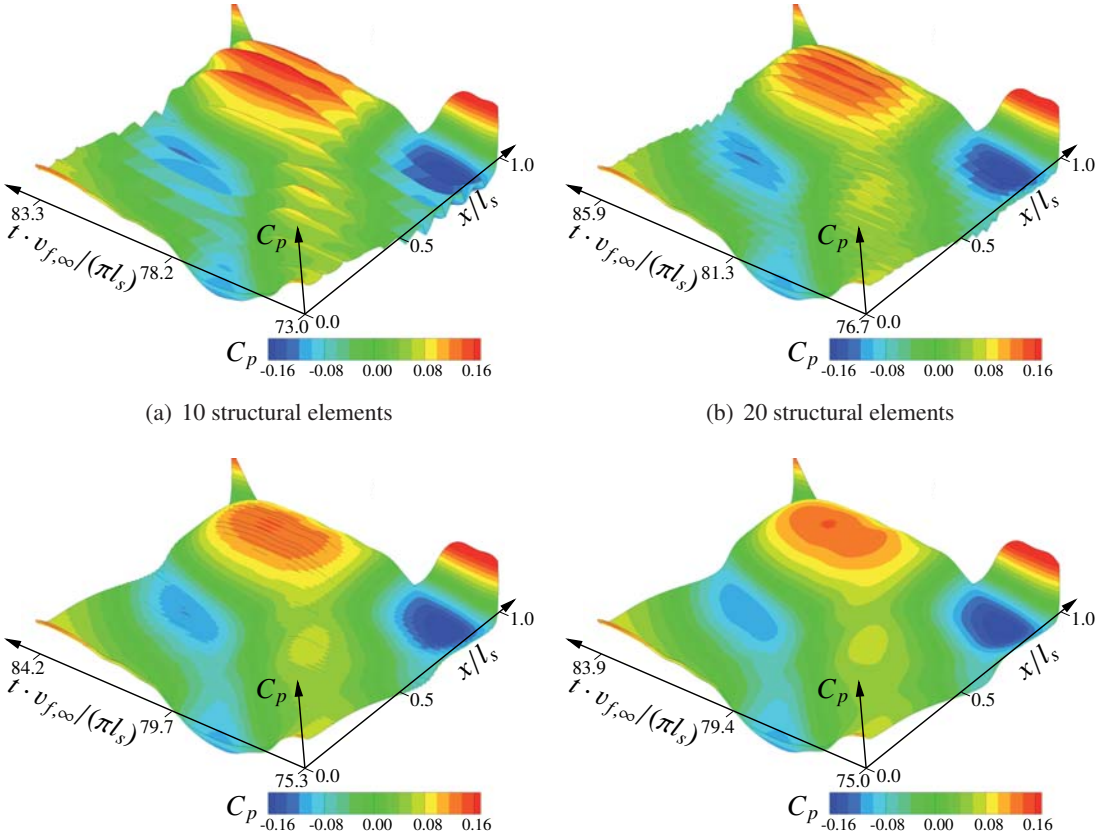

(a) 10 structural elements

(b) 20 structural elements

(c) 50 structural elements

(d) 100 structural elements

Figure 7.9: Fluid interface pressure during one cycle of oscillation using the two-field approach (dual-Lagrange based transfer) for several structural discretization

7.2.3 Comparison of the two- and three-field coupling approach

In terms of the two-field approach, the structural displacements are directly transmitted to the fluid grid, which in turns influences the fluid pressure distribution. In Figure 7.9, the fluid interface pressure is depicted over the time for one limit cycle period using the two field coupling approach. This pressure is again warped in the third direction for visualization. Different structural discretizations are used and a constant time step size of $\Delta t \cdot v_{f,\infty}/(\pi l_s) = 0.094$ as well as the simple staggered time integration with the three-point backward time discretization for the structure are applied. For the data transmission, the dual-Lagrange based transfer is utilized. As seen from Figure 7.9(a), equidistant unphysical oscillation in the pressure distribution can be noticed. Such oscillations, which result in small and very local shocks, are caused by the transfer of the displacement field from a coarse structural to a finer discretized fluid interface. More precisely, after the displacement field transfer, the fluid interface becomes chiseled, which is responsible for local pressure changes. This kind of chiseled fluid interface was already observed in Figure 6.20(b).

To overcome this transfer behavior, more elements for the panel discretization can be used. In Figure 7.9(d), the fluid interface pressure is depicted, where the structural panel consists of 100 finite elements, while the fluid interface still contains 400 elements. The local pressure disturbances are less visible as in the case, where the structure has only 10 elements. Clearly, an optimal solution would be obtained with matched fluid and structural interface grids, but often such demand is far away from being possible.

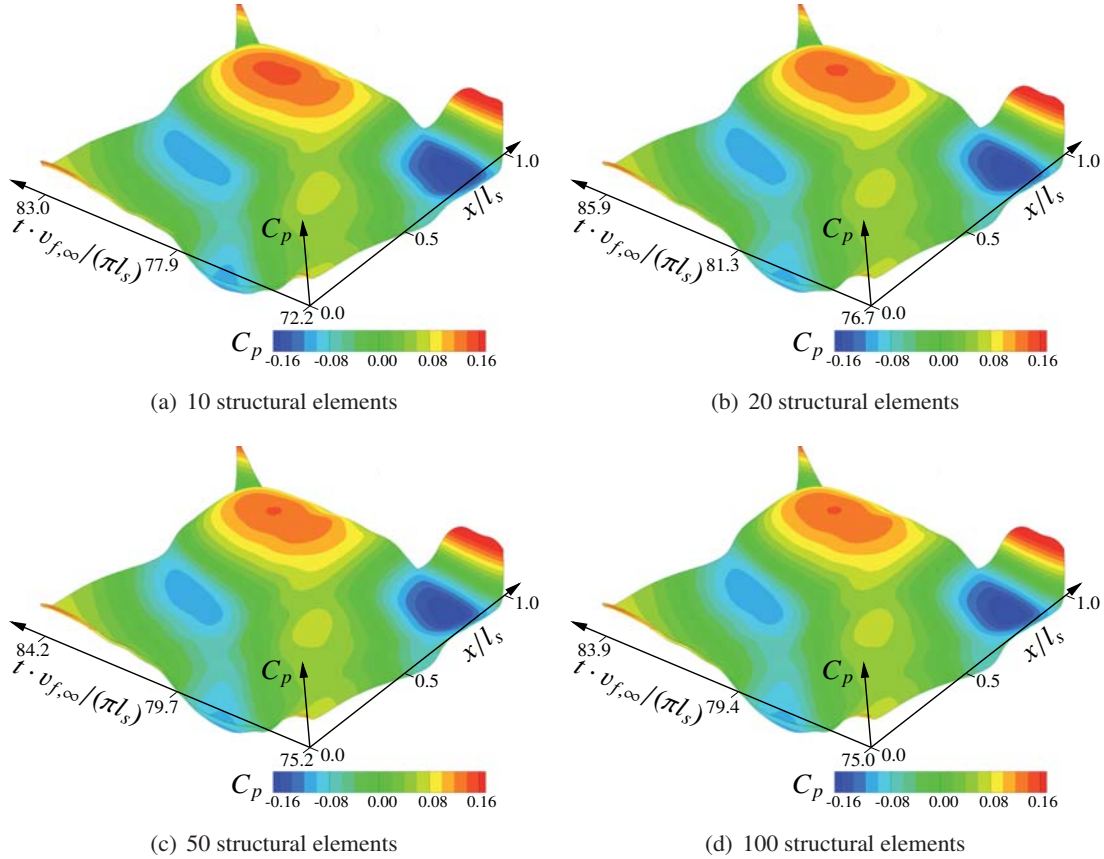

(a) 10 structural elements

(b) 20 structural elements

(c) 50 structural elements

(d) 100 structural elements

Figure 7.10: Fluid interface pressure during one cycle of oscillation using the three-field approach (Galerkin based transfer) for several structural discretization

Another solution of this coarse-to-fine data transfer over non-matched interface grids is the application of the three-field approach in conjunction with an independent frame discretization with C^1 continuous elements as proposed in section 6.2.3. Here, the frame is automatically created, so that the requirement of Eq. (4.5.4) is barely satisfied. For the coupling matrices, the Galerkin scheme is utilized and the remaining parameters are kept unchanged. In Figure 7.10 the obtained pressure on the fluid interface is shown. Using the three-field approach, the pressure distribution is much smoother and the local pressure oscillations are no longer apparent for all structural discretizations. Thus, the three-field approach, which is used here to employ an accurate displacement field transfer scheme, is a favorable method to simulate a coupling problem involving a compressible fluid.

Comparing the reduced frequency as well as the amplitude of the two-field approach with those of the three-field approach, similar results are obtained, Figure 7.11. Only for a very coarse structural grid, small differences are noticeable. This basically indicates that both coupling approaches are conservative in terms of the load transfer and in terms of the energy transfer over the interface. Due to the more accurate results for the fluid domain when using the three-field approach, this approach is the preferred coupling scheme.

7.2.4 Comparison of the CBS and the DG-CBS scheme

The temporal as well as the spatial structural convergence have been employed in the previous sections and it remains to clarify, the spatial convergence in terms if the fluid grid resolution.

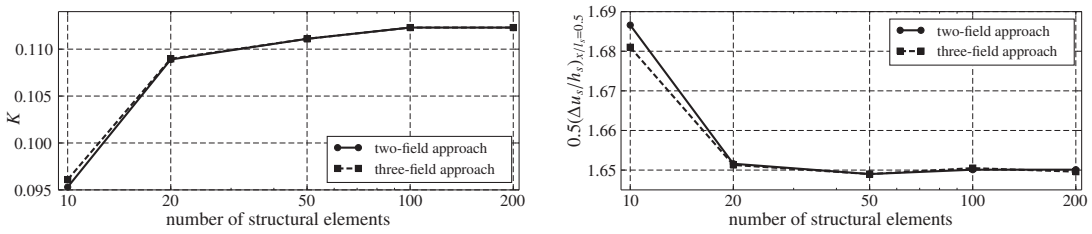

(a) reduced frequency (b) panel midpoint amplitude

Figure 7.11: Reduced frequency and midpoint amplitude of the LCO using different coupling approaches and number of elements

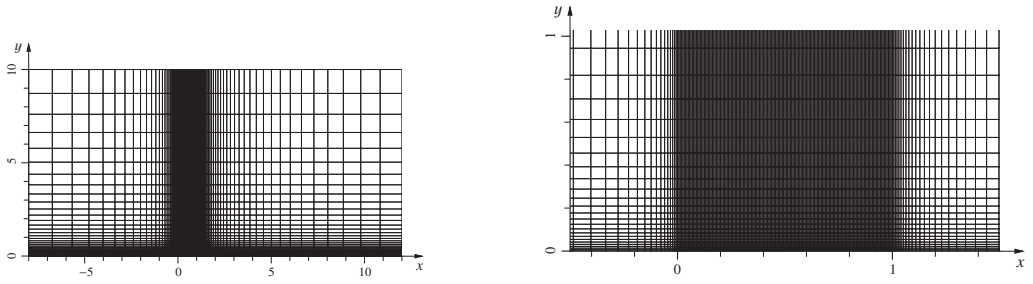

(a) full grid (b) close-up view on the panel

Figure 7.12: Example of a structured grid for calculations of inviscid panel flutter problem - 160 elements distributed on the panel

According to section 5.2.1, a structured grid is now used for the panel flutter problem, due to its simple creation of similar grids with bilinear or biquadratic finite elements at different resolution levels. In Figure 7.12, an example of a structured grid is shown, which is characterized by the existence of 160 elements distributed on the panel. Other fluid grids created for the computations use 80, 120, 160, 240 or 320 elements on the panel interface. Again the panel flutter phenomenon is computed with the same parameter set as described above ($Ma_\infty = 1.0$, $r_m = 0.1$, $r_p = 170$) and with the aid of the three-field coupling approach.

In Figure 7.13, the midpoint deflection together with the midpoint velocity is shown for different discretizations and for different spatial order of finite elements. Using a coarse grid with bilinear elements and with 80 elements on the interface, a high flutter frequency of 0.167 and 0.164 for the CBS and DG-CBS scheme are obtained. Comparing these results with a finer grid, e.g. 320 elements at the interface, Figure 7.13(b), this high frequency is caused by a non-satisfying midpoint velocity time history. While the panel moves to the top dead center, the velocity shows a higher mode, where the midpoint velocity almost reaches zero.

Using grids with biquadratic elements, similar expressions can be made. Although slightly better results are obtained when using 80 elements at the fluid interface, the velocity time history of the midpoint deflection is still insufficient, Figure 7.13(c). With 120 quadratic elements at the interface, the midpoint velocity shows a behavior similar to the case, where 320 linear elements at the interface are used, and a reasonable flutter frequency is therefore obtained.

Finally, the relative error of the obtained flutter frequencies over the number of elements used to discretize the fluid interface is plotted in Figure 7.14 for the CBS as well as the DG-CBS scheme. Since a structured grid is used in [Mas02], the frequency reported there is chosen as reference. Using linear elements, the differences between the curve for the CBS and the DG-CBS

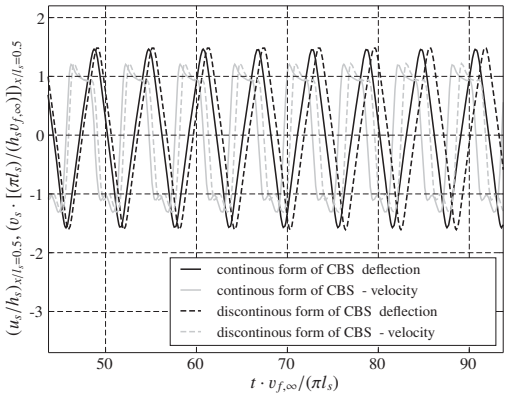

(a) 80 linear elements on the fluid interface

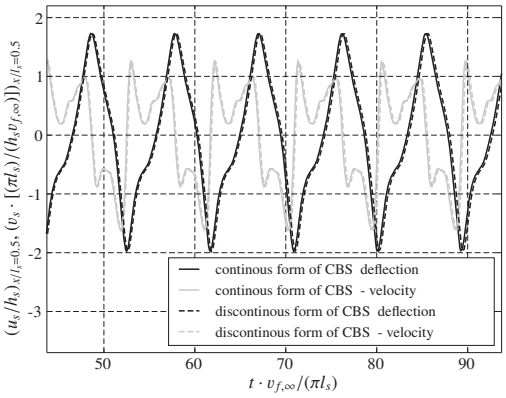

(b) 320 linear elements on the fluid interface

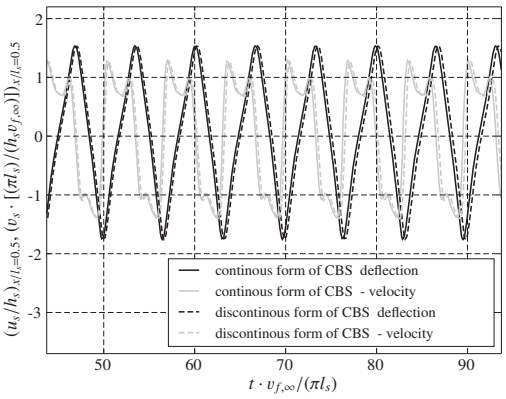

(c) 80 quadratic elements on the fluid interface

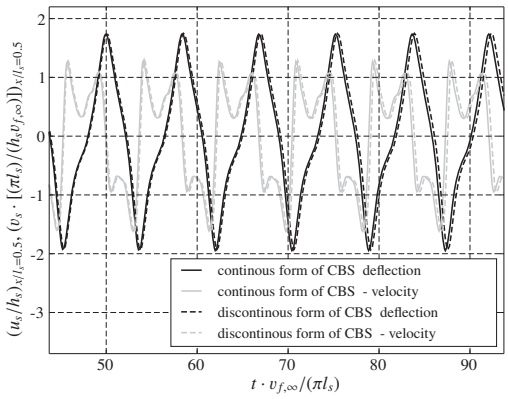

(d) 120 quadratic elements on the fluid interface

Figure 7.13: Midpoint deflection of the panel using different version of CBS scheme and number of elements at the fluid interface

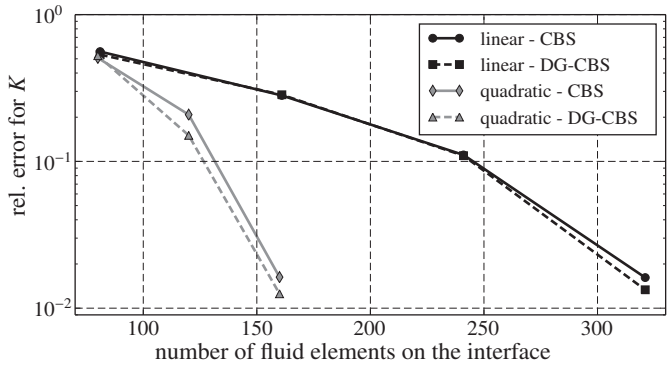

Figure 7.14: Relative error of the reduced frequency using different versions of the CBS scheme and number of elements on the interface

scheme are marginal. Only with 320 fluid interface elements, relative error is lower as for the DG version. Using a biquadratic grid with 160 elements on the fluid interface, the error becomes similar small as the value for 320 linear elements. Moreover, it should be noted, that the difference between the CBS and the DG-CBS scheme is noticeable for the case with biquadratic elements. Therefore, it can be conclude here, that application of the DG-CBS scheme for the solely reason of improving the accuracy is only attractive, when quadratic elements are used for the fluid grid.

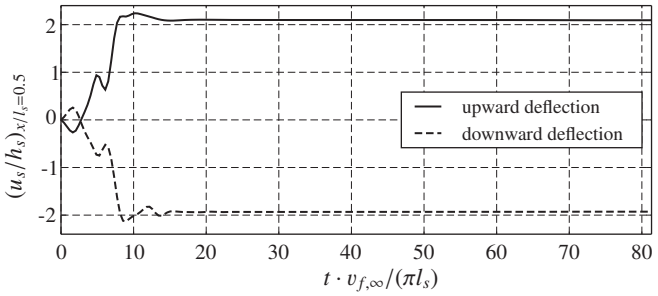

Figure 7.15: Midpoint deflection of the panel at $Ma_\infty = 0.9$, $r_m = 0.1$, $r_p = 200$ - upward and downward deflection

7.2.5 Choice of schemes for upcoming simulations

Due to the experience obtained in the previous subsections, the following schemes and parameters are used for all upcoming calculations:

- the simple staggered solution strategy, i.e. $\varsigma_{RI} = 1.0$ and setting the maximum number of iteration for each time level to one to save computational effort
- the second order structural predictor of Eq. (4.4.6) due to its accuracy and stability
- a time step size of $\Delta t = 0.001$ s to guarantee accurate flutter calculations over a wide range of non-dimensional pressure
- the consistent time integration, i.e. the time integration of Eq. (4.6.3) is used for the structure due to its better stability at higher time step sizes
- 100 linear structural elements for the panel
- the usage of the unstructured grid from Figure 7.2
- the application of the three-field approach together with the Galerkin based transfer due to its smooth data transfer property
- a lumped mass matrix and $\theta_1 = 0.75$ and $\theta_2 = 0$ within the CBS scheme to save computational effort with this matrix free form
- the continuous Galerkin version of the CBS scheme

The last point needs some further explanation. Although with the DG-CBS scheme, a local conservative procedure can be designed, the effect on the panel flutter results is marginal as shown in the previous section. Thus, the continuous Galerkin version of the CBS scheme is chosen here.

7.3 Panel behavior at subsonic flow

With the given parameters and settings, which behave best for the transonic panel flutter at $Ma_\infty = 1.0$, several simulations can be conducted of the panel interacting with fluid flow. Initially, the panel behavior is investigated at subsonic Mach numbers varying the non-dimensional dynamic pressure r_p and mass ratio r_m. At a Mach number of $Ma_\infty = 0.9$, the panel shows no flutter. Instead, it deflects in the upward or downward direction depending on r_p and the initial value for the panel velocity as for example shown in Figure 7.15. An initial velocity is necessary to trigger the panel deflection, when an inviscid fluid model is used. Here, the initial velocity distribution has the same form as the panel deflection assuming a constant pressure. This distribution is scaled with a maximum value of $|0.1|$ m/s at the panel midpoint. For the subsonic case, a positive or negative

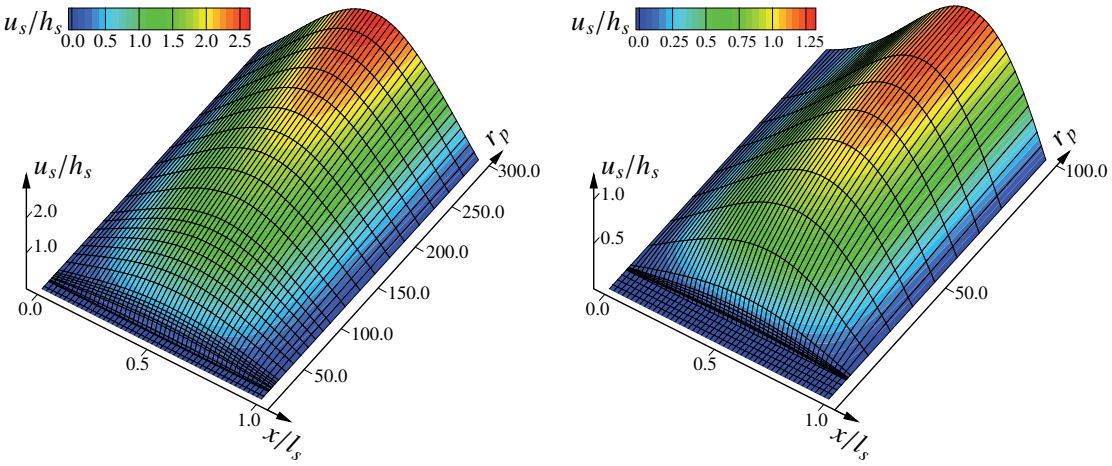

(a) $Ma_\infty = 0.9$ (b) $Ma_\infty = 0.98$

Figure 7.16: Upward panel deflection for different non-dimensional dynamic pressure values and two Mach numbers at $r_m = 0.1$

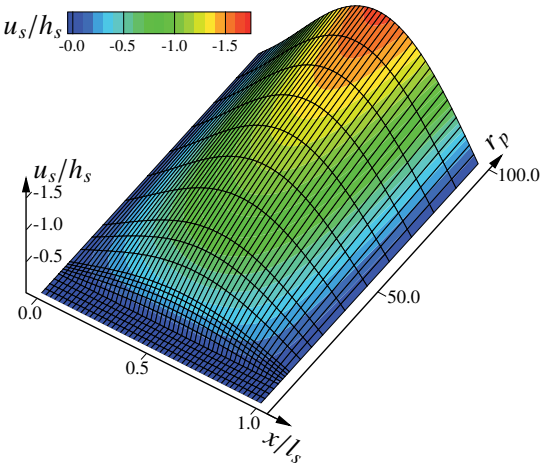

Figure 7.17: Downward panel deflection for different non-dimensional dynamic pressure values at $Ma_\infty = 0.98$, $r_m = 0.1$

velocity distribution is applied depending on the desired deflection direction. Thereby, it is not mandatory, that a positive initial velocity leads to an upward panel deflection, see Figure 7.15. Indeed, in some cases, the panel deforms always in one direction independently of a positive or negative initial velocity distribution.

In Figure 7.16(a), the upward panel deflection for different values of r_p is shown, where a Mach number of $Ma_\infty = 0.9$ and a non-dimensional mass ratio of $r_m = 0.1$ are set. It can be observed from this figure, that the highest deformation is nearly at the panel midpoint for all r_p. This situation changes by increasing the Mach number to $Ma_\infty = 0.98$, where now the highest deformation can be found at $x/l_s = 0.63$ independently of r_p, Figure 7.16(b). Such downstream shift of the highest deformation location cannot be found, if the panel deflects downward, Figure 7.17. For the downward deformed panel at $Ma_\infty = 0.98$, the highest deformation is found to be at $x/l_s = 0.53$. This behavior is caused by the occurrence of a shock situated near the downstream end of the upward deflected panel, which is absent in the case of the downward deflected

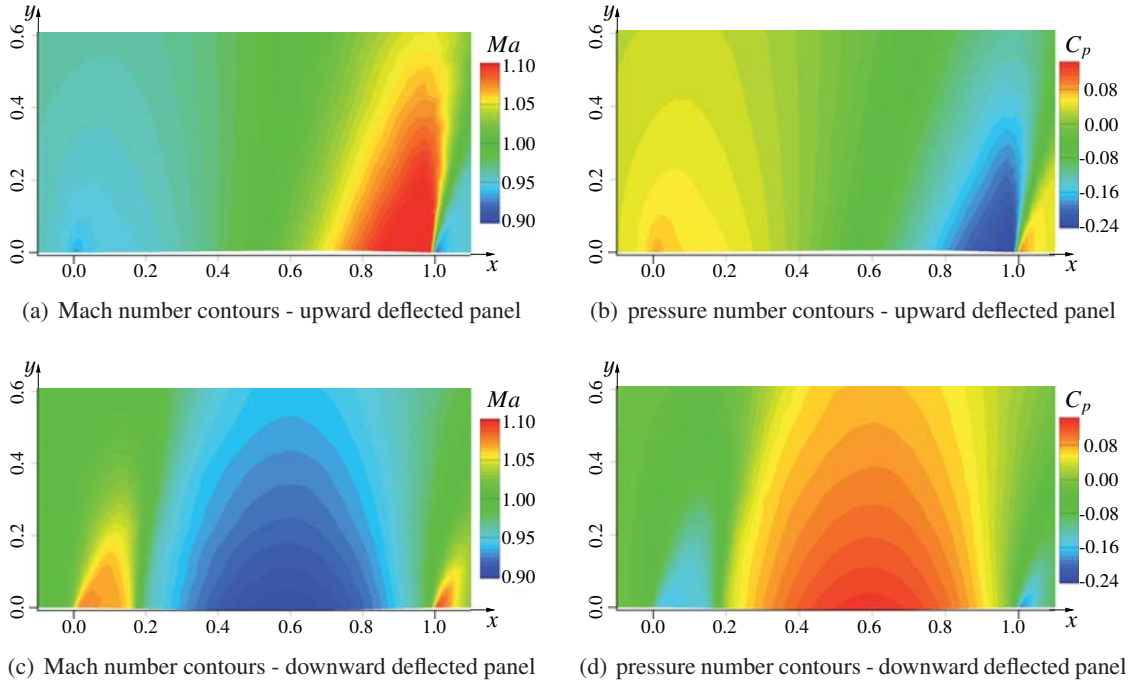

(a) Mach number contours - upward deflected panel

(b) pressure number contours - upward deflected panel

(c) Mach number contours - downward deflected panel

(d) pressure number contours - downward deflected panel

Figure 7.18: Mach number and pressure contours of the fluid passing the panel at $Ma_\infty = 0.98$, $r_p = 100$, $r_m = 0.1$ - upward and downward deflected panel

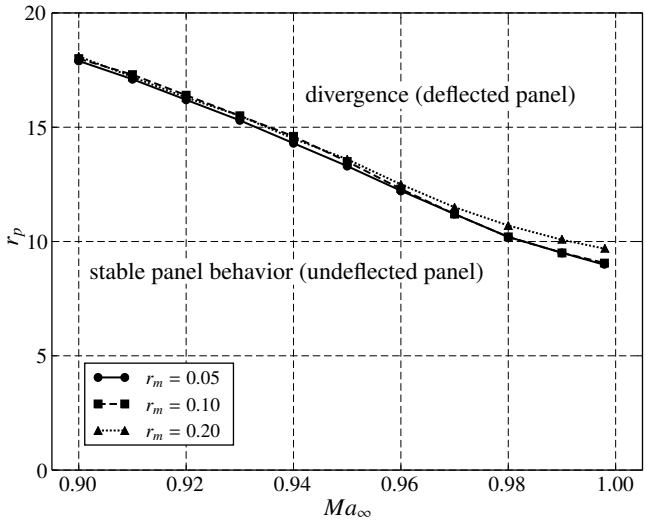

Figure 7.19: Critical non-dimensional dynamic pressure vs. the farfield Mach number for different r_m - subsonic stability chart

structure, Figure 7.18. In Figure 7.18, the Mach number and the pressure contours of the fluid passing the panel are shown, where $Ma_\infty = 0.98$, $r_p = 100$, $r_m = 0.1$ are used as parameters. Such shock with its transonic effects leads to a shift of the maximum deflection location, whereas the solution without a shock remains more symmetric about the panel midpoint. Comparing the up- and downward deformation form, it is remarkable, that the absolute deformation of Figure 7.16(b) is lower than that in Figure 7.17.

Furthermore, it can be observed from the two plots of Figure 7.16, that there exists a certain value for r_p depending on the Mach number, where the deflection of the panel is activated. This critical pressure is equal to $r_{p,\text{crit}} = 18.0$ and $r_{p,\text{crit}} = 10.2$ for a Mach number of $Ma_\infty = 0.9$ and $Ma_\infty = 0.98$, respectively. In Figure 7.19, the critical r_p is plotted over the Mach number for different mass ratios r_m and it can be seen, that the influence of r_m is marginal. An explanation for this observation is the absence of inertia loads in the case of a static deflection. Only for Mach numbers close to $Ma_\infty = 1.0$, slightly higher critical pressures for higher r_m can be noticed. Nevertheless, with higher Mach numbers Ma_∞ the critical pressure decreases in an almost linear way. A stable panel behavior is observed below these curves, i.e. an initially deformed plate will fall back to an undeformed structure. Above these curves, the panel deflects up- or downward to a certain equilibrium.

Finally, the up- and downward midpoint deflection of the structure over the dynamic pressure is depicted in Figure 7.20 for several farfield Mach numbers and mass ratios. First of all, it should be noted, that the influence of the mass ratio r_m is again insignificant in the subsonic range. For the downward deflected plate, the panel deforms as soon as the stability boundary of Figure 7.19 is passed and the midpoint deformation increases with increasing the r_p. Due to the use of the von Kármán plate model, this deformation behavior is non-linear. A similar behavior can be noticed for the upward deflected case, except that here a deformed structure for values of r_p up to 2500 is obtained only at $Ma_\infty = 0.9$. With a Mach number of $Ma = 0.98$, an upward deformed plate is only achieved for $r_p \leq 100$ and otherwise, only a downward deflected panel behavior is observed. For $Ma = 0.94$, this characteristic value is $r_p \approx 320$.

7.4 Panel behavior at supersonic flow

The principal aeroelastic behavior changes with supersonic flow conditions. Depending on the non-dimensional dynamic pressure r_p, the panel exhibits a limit cycle oscillation. Characteristic values of such LCO are the reduced frequency and the amplitude of the oscillation. Moreover, it is observed, that the temporal mean of a point on the panel is shifted downwards. Thus, the deformations of the structure at the top and bottom dead center as well as the mean value are further characteristic values.

First of all, the non-dimensional dynamic pressure r_p is varied for three inflow Mach numbers, $Ma_\infty = (1.04, 1.08, 1.12)$, at a non-dimensional mass ratio of $r_m = 0.1$. The panel deflection of the LCO at the top and bottom dead center for different values of r_p can be viewed in Figure 7.21. It can be noticed from Figure 7.21(a), that the location of the maximum deformation of the deflected panel at the top dead center is shifted downstream and situated between $0.58 \leq x/l_s \leq 0.64$, whereas the location increases with higher r_p. The same observation can be made for the deflected plate at the bottom dead center, Figure 7.21(b). Increasing the Mach number to $Ma_\infty = 1.08$, the maximum panel deformation at the top dead center also increases, whereas the location of the maximum remains nearly unchanged, Figure 7.21(c). The deflection at the bottom dead center shows a similar behavior, but the increase turns out to be considerably smaller, Figure 7.21(d). With a Mach number of $Ma_\infty = 1.12$, the panel shows even higher deformations at the top and bottom dead center, Figure 7.21(e) and Figure 7.21(f). The location of the upper maximum deflection is for this case $0.58 \leq x/l_s \leq 0.62$, whereas the highest values are obtained at $r_p = 500$. From the series of figures, it can be observed, that the panel deformation form at the top dead center changes with the Mach number, especially for higher r_p, whereas the shape at the bottom dead center remains unchanged.

Similar to the behavior at subsonic Mach numbers, a LCO of the panel is activated at a certain r_p, which further can be noticed from Figure 7.21. For a Mach number of $Ma_\infty = 1.04$ and a mass ratio of $r_m = 0.1$, this value is $r_p = 24.1$. Below this value, an initially deflected plate will fall back

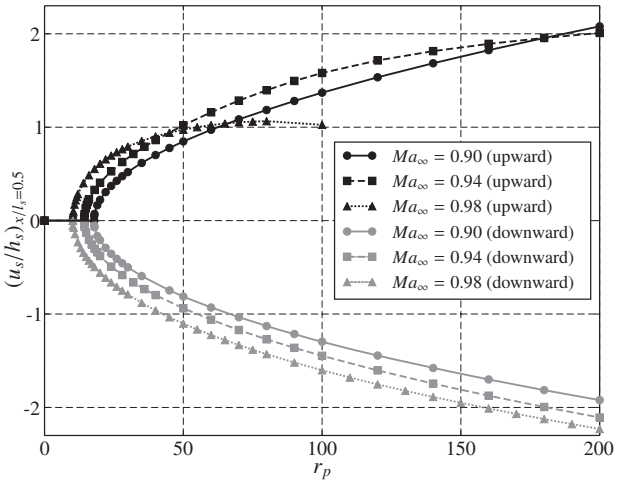

(a) $r_m = 0.05$

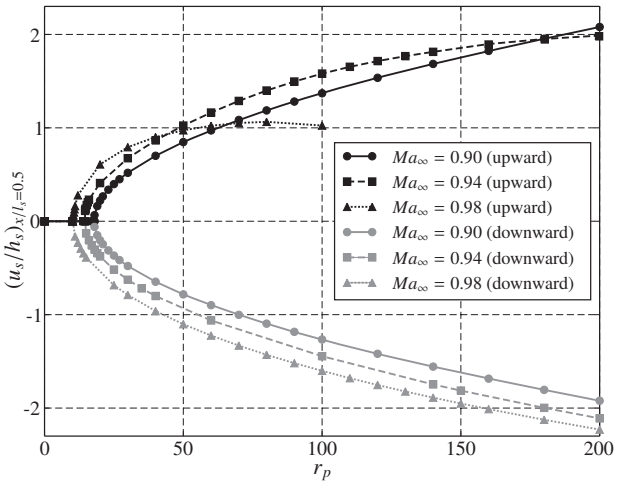

(b) $r_m = 0.10$

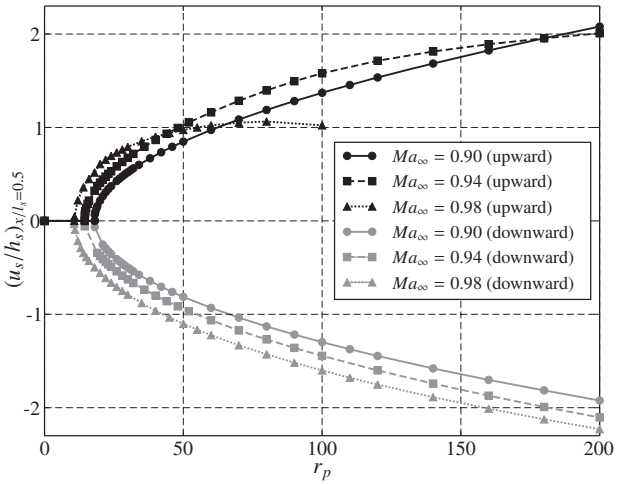

(c) $r_m = 0.20$

Figure 7.20: Up- and downward midpoint deflection of the panel over the non-dimensional dynamic pressure for different Mach numbers Ma_∞ and mass ratios r_m

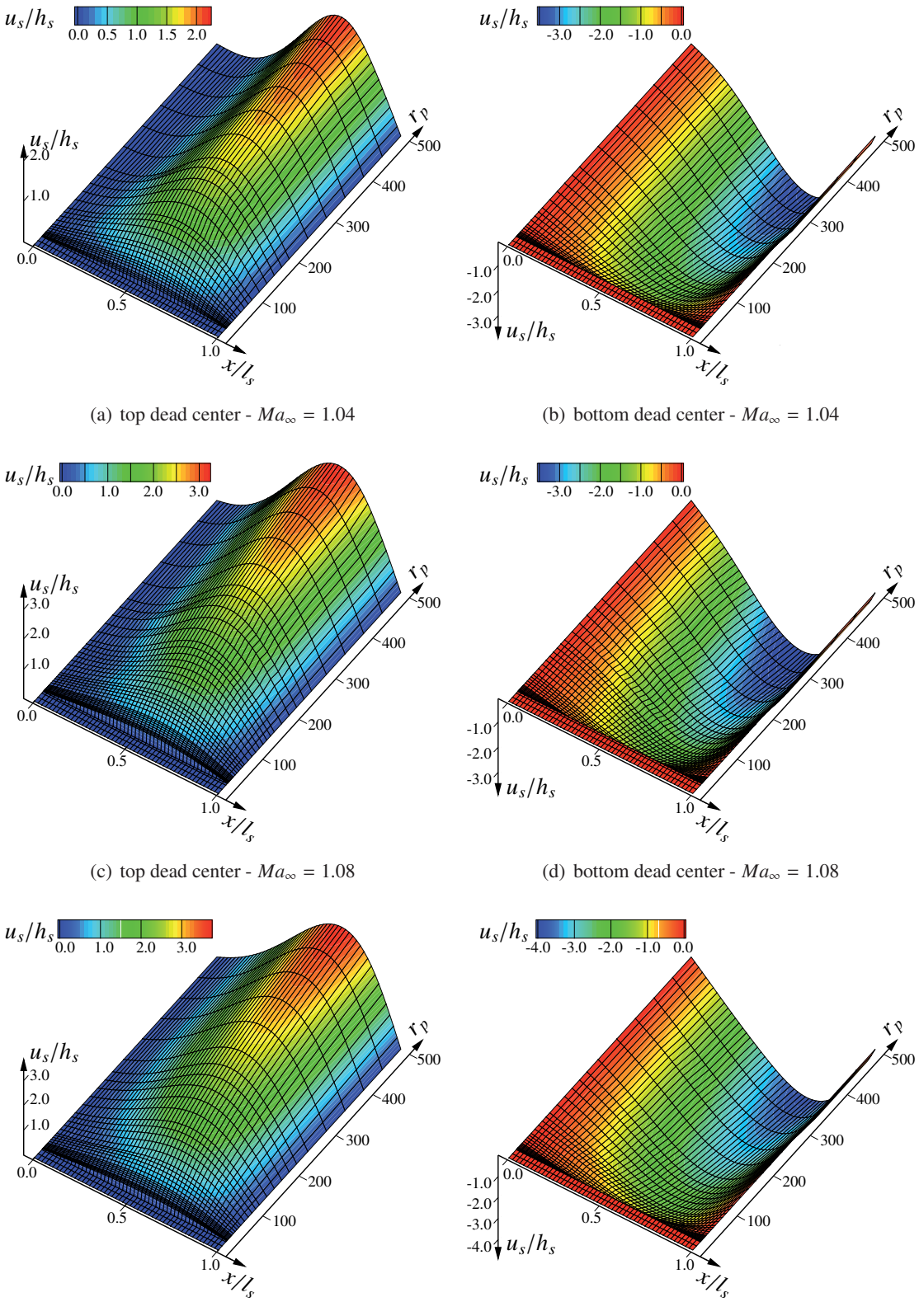

(a) top dead center - $Ma_\infty = 1.04$

(b) bottom dead center - $Ma_\infty = 1.04$

(c) top dead center - $Ma_\infty = 1.08$

(d) bottom dead center - $Ma_\infty = 1.08$

(e) top dead center - $Ma_\infty = 1.12$

(f) bottom dead center - $Ma_\infty = 1.12$

Figure 7.21: Panel deflection at the top and bottom dead center for different non-dimensional dynamic pressure values and three Mach numbers at $r_m = 0.1$

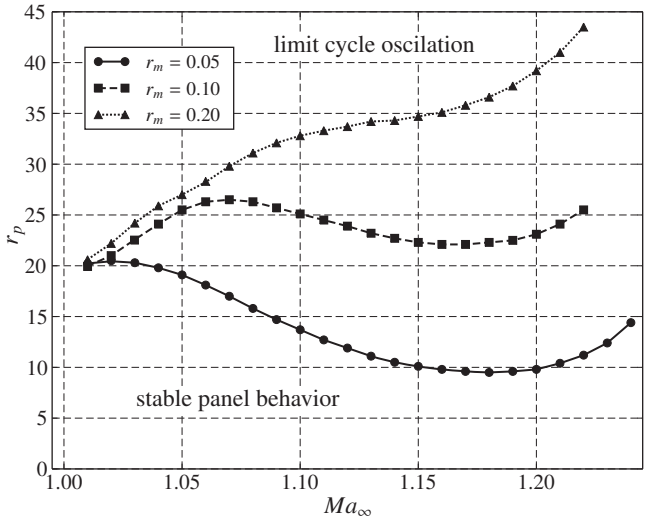

Figure 7.22: Critical non-dimensional dynamic pressure vs. the farfield Mach number for different r_m - supersonic stability chart

to its undeflected state and the behavior is thus stable. On the other hand, the panel shows a LCO above this value for this specific set of parameters. In Figure 7.22, the critical r_p are plotted over the Mach number for three mass ratios. Contrary to the subsonic stability chart, Figure 7.19, the mass ratio r_m has a significant influence on the stability boundary. To the author's knowledge, this effect was not investigated in literature before. For low supersonic Mach numbers, the difference in the critical r_p is small, but increases considerably with higher Mach numbers. Moreover, a supersonic dip in the stability boundary with its local minimum at $Ma_\infty = 1.17$ is found for $r_m = 0.1$. Decreasing the mass ratio to $r_m = 0.05$, the range of the dip is expanded at lower critical r_p-values, whereas an increase to $r_m = 0.2$ leads to a cancellation of the local minimum at a higher stability boundary.

The reduced frequency over r_p is shown in Figure 7.23. In this figure, the Mach number as well as the non-dimensional mass ratio are varied. For a Mach number of $Ma_\infty = 1.08$ and a mass ratio of $r_m = 0.1$, Figure 7.23(b), it can be observed, that the frequency of the LCO increases non-linearly with higher dynamic pressures and converges to a value of $K = 0.312$ for high values of r_p. Increasing the Mach number to $Ma_\infty = 1.12$, the same principal relationship is noticed, but the curve is shifted to higher frequencies. Decreasing the Mach number to $Ma_\infty = 1.04$, the frequency is reduced and a limit value of K for the considered range of r_p cannot be noticed.

Doubling the mass ratio r_m, the development of the flutter frequency is nearly identical for $r_p < 80$, Figure 7.23(c). With higher dynamic pressures, the panel shows higher frequencies of the LCO as with $r_m = 0.1$. For $Ma_\infty = 1.12$, the flutter frequency converges to $K = 0.408$. For $r_m = 0.05$ and $Ma_\infty = 1.04$, Figure 7.23(a) the development of the $K - r_p$-curve is again nearly identical as for the case with $r_m = 0.1$. However, increasing the Mach number to 1.08 or 1.12 the curves show a plateau at $35 < r_p < 90$ and local minima of the curves can be noticed at $r_p = 20$. A second local minimum at $r_p = 400$ can be seen for $Ma_\infty = 1.12$.

In Figure 7.24, the midpoint deflections of the panel at the top and bottom dead center are shown. Similar to the subsonic pure deflection panel behavior, the deformation increases non-linearly with higher r_p as soon as the critical r_p is exceeded. For $r_m = 0.1$, the deformation increases with higher Mach numbers, whereas the rate of change for the top dead center deformation is slightly higher as for the bottom dead center, Figure 7.24(b). Furthermore, the LCO is asymmetric, i.e. the midpoint deformation at the bottom dead center is greater than the deflection

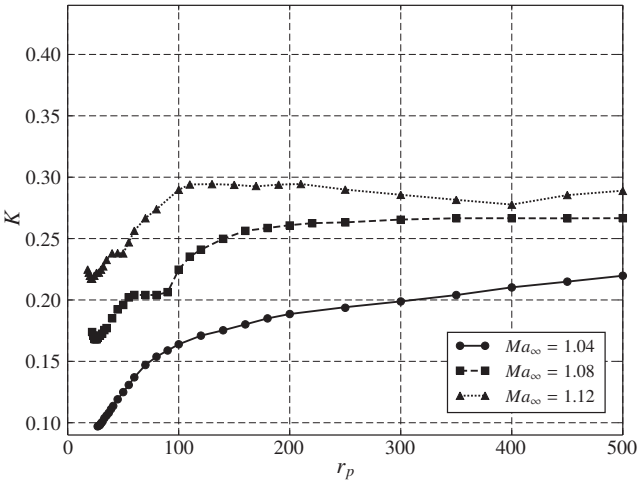

(a) reduced frequency at $r_m = 0.05$

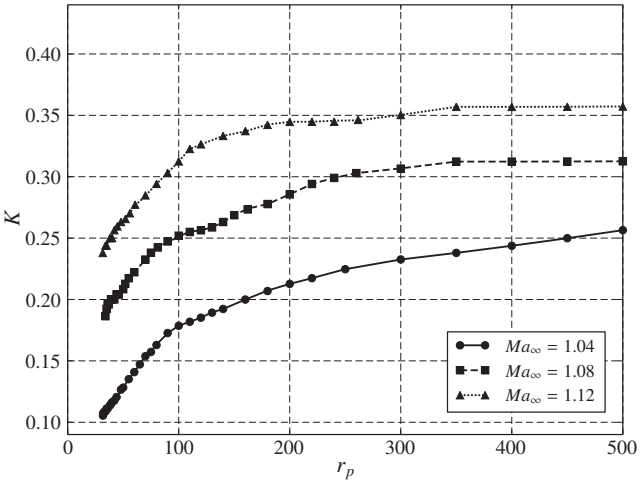

(b) reduced frequency $r_m = 0.10$

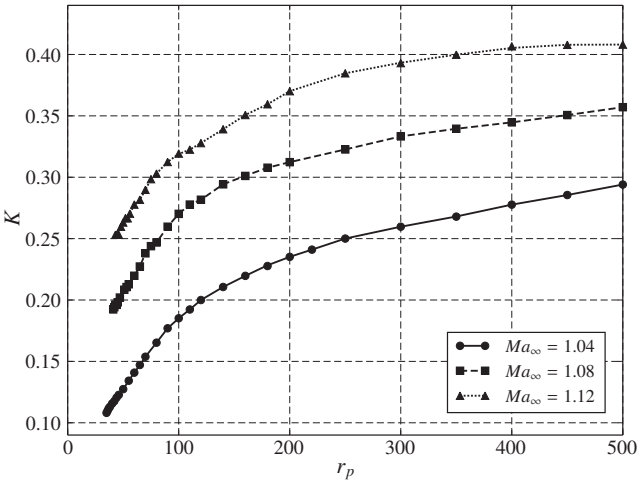

(c) reduced frequency $r_m = 0.20$

Figure 7.23: Reduced frequency of the panel's oscillation over the non-dimensional dynamic pressure for different Mach numbers Ma_∞ and mass ratios r_m

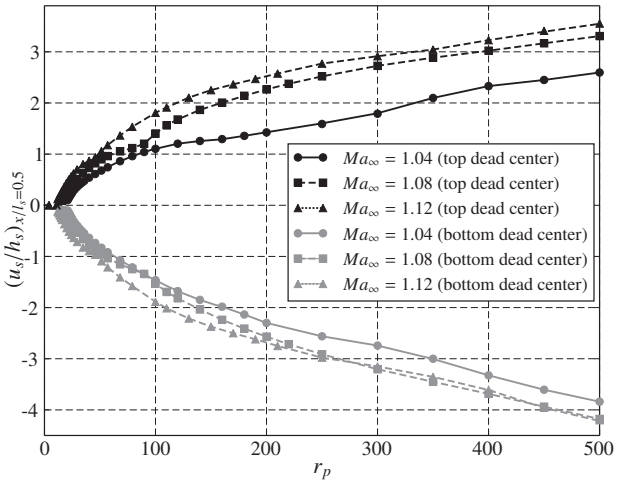

(a) $r_m = 0.05$

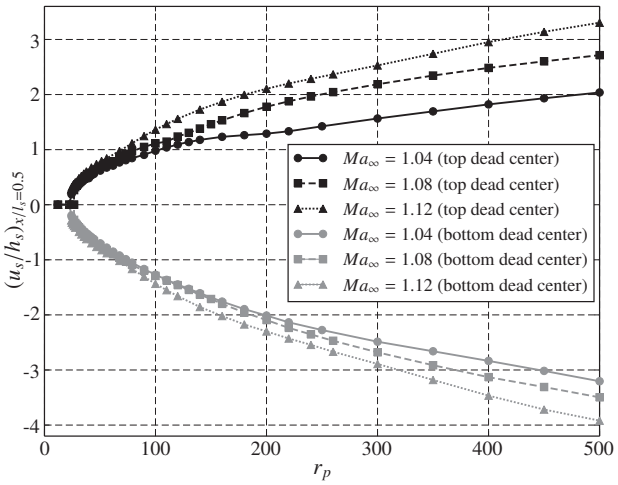

(b) $r_m = 0.10$

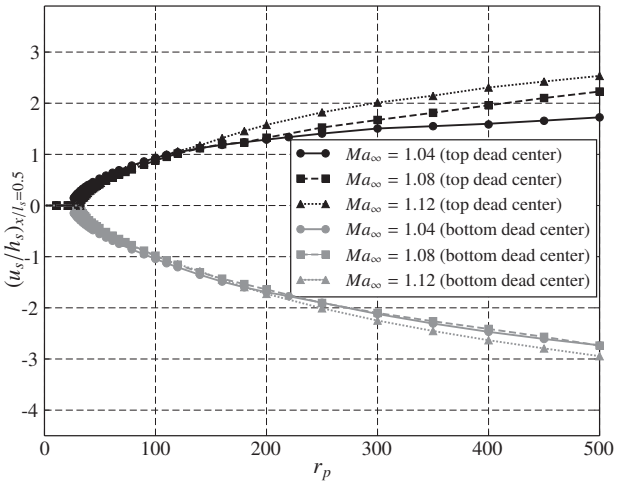

(c) $r_m = 0.20$

Figure 7.24: Panel midpoint deformation at the top and bottom dead center over the non-dimensional dynamic pressure for different Mach numbers Ma_∞ and mass ratios r_m

at the top dead center. This fact also can be seen from the figures in the appendix, Figure A.1 to Figure A.9, where the frequencies and periods as well as the amplitudes and means of the deformation are depicted for each considered combination of Mach number and mass ratio. For example in Figure A.4, the development of the panel's mean deformation is plotted. With higher values of r_p, this LCO's deformation mean is decreased to negative values.

Increasing r_m to 0.2, the deformation range of the structure is reduced, Figure 7.24(c). Interestingly, the bottom dead center deformations for a Mach number of 1.04 and 1.08 show almost identical results. For $r_m = 0.05$, the highest considered midpoint deformation can be observed, although the differences to the deflection at $r_p = 500$ and $r_m = 0.1$ is small, Figure 7.24(a).

Finally, the correlation of the frequency and the amplitude of the LCO is illustrated in Figure 7.25. Considering first the curve with $r_m = 0.1$ and $Ma_\infty = 1.04$ from Figure 7.25(b), it can be seen, that the relationship is nearly linear. This situation changes with higher Mach numbers due to the non-linearity of the structure. The same observation at lower amplitudes can be made for a mass ratio of $r_m = 0.2$. For $r_m = 0.05$, a non-linear relationship is noticed for all Mach numbers. Moreover, the relationship becomes non-injective for a Mach number of 1.08 and 1.12, e.g. for $Ma_\infty = 1.12$ and $K = 0.27$, two amplitude of the LCO are possible depending on r_p.

7.5 Panel flutter stability chart

With the given analyses of the panel at sub- and supersonic flow conditions, the complete stability boundary chart can be assembled. The stability boundary chart of the panel is depicted in Figure 7.26 for the three considered values of the mass ratio. It can be seen, that with a Mach number of $Ma_\infty < 1.0$ the stability boundary divides the $Ma - r_p$-plane into an area with divergence and an area with stable deflection behavior. For a Mach number $Ma_\infty > 1.0$, the $Ma - r_p$-plane is divided into areas with a stable and with an unstable flutter behavior. This result agrees with that obtained in [DB93]. As already discussed above, a supersonic dip occurs with its minimum value of the stable boundary pressure at $Ma_\infty = 1.17$ for $r_m = 0.1$ and at $Ma_\infty = 1.18$ for $r_m = 0.05$. For $r_m = 0.2$, such dip is not present. Further, it should be pointed out again, that the mass ratio has only a minor influence on the static subsonic stability, whereas for the supersonic flutter stability, r_m is responsible for an increase of the stability boundary. This is due to the higher fluid mass, which has to be moved by the dynamic oscillation of the structure, i.e. the inertia load is increased with higher r_m.

It remains to analyze the panel behavior at $Ma_\infty = 1.0$. In Figure 7.27, the up- or downward deflection as well as the top and bottom dead center deformation of the panel at its midpoint is plotted over the dynamic pressure r_p at different mass ratios.

First, the case with $r_m = 0.1$ is considered, Figure 7.27(b). With a value of $r_p = 4.5$, the deflection behavior of the panel is activated and depending on the initial conditions, the plate deflects up- or downwards. For values $53 < r_p < 165$, a downward deflected panel is obtained as the sole solution. With $r_p \geq 170$, the panel starts to oscillate and a LCO is obtained. Therefore, this case ($r_m = 0.1$, $Ma_\infty = 1.0$ and $r_p = 170$) is attractive and was thus chosen to study the various numerical schemes presented in this thesis.

A similar behavior can be noticed, when the mass ratio is varied. For $r_m = 0.05$, the range where the panel behavior changes from static deflection to a LCO is shifted to higher values of r_p, i.e. the first flutter case is at $r_p = 190$. On the other hand, the panel starts already at $r_p \geq 160$ to oscillate for $r_m = 0.20$. Moreover, the flutter amplitudes at certain dynamic pressures increase with higher r_m, whereas the midpoint deflection behavior remains nearly unchanged.

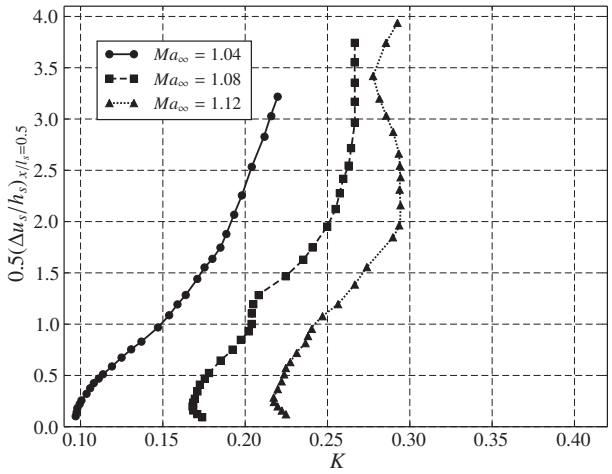

(a) $r_m = 0.05$

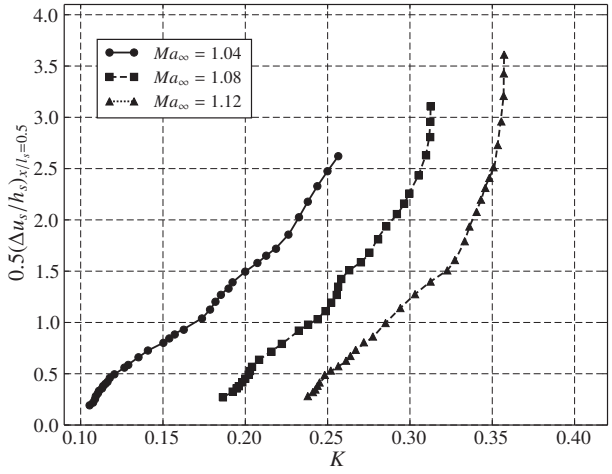

(b) $r_m = 0.10$

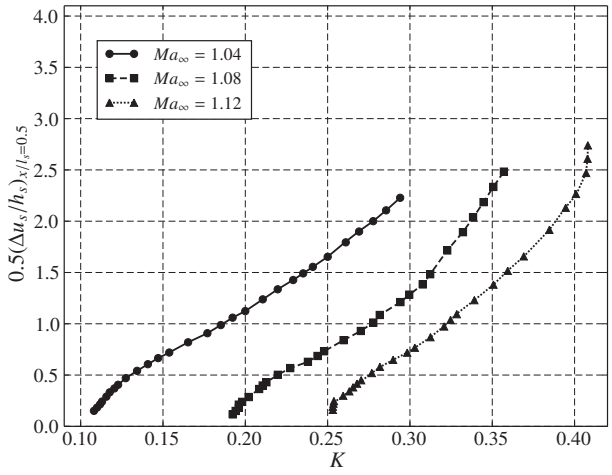

(c) $r_m = 0.20$

Figure 7.25: Midpoint deflection of the panel at the top and bottom dead center over the reduced frequency for different Mach numbers Ma_∞ and mass ratios r_m

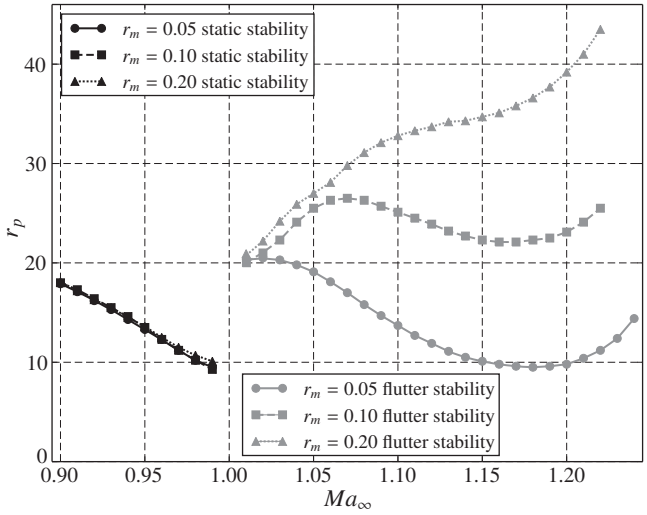

Figure 7.26: Stability boundary chart

7.6 Influence of turbulence

To investigate the influence of the Reynolds number on the panel flutter behavior, a hybrid grid is generated, which contains 300 elements at the panel interface, Figure 7.28. To keep the boundary layer thickness small over the panel, the grid's left inflow boundary is situated at $x = -l_s$, i.e. the grid starts a panel length before the panel itself. Further, the grid is designed to allow simulations with a broad range of Reynolds numbers.

First, a flutter case with $Ma_\infty = 1.1$, $r_m = 0.1$ and $r_p = 250$ is analyzed. In Figure 7.29, the midpoint deflections of the panel at different Reynolds numbers are depicted. In Table 7.1, specific values of the LCO at further Reynolds numbers are summarized. In that table, the midpoint deformation values of the top and bottom dead center, $((u_s/h_s)^{\text{top}}$, $(u_s/h_s)^{\text{bottom}})$, the amplitude and the mean, $(0.5(\Delta u_s/h_s)$ and $(\overline{u_s}/h_s))$, as well as the reduced frequency K are listed. It can be observed, that the main influence of the Reynolds number is given on the amplitude of the LCO rather than on the frequency, which remains nearly unchanged. At a very low Reynolds number of $Re = 10^5$, the flutter amplitude is lower compared to the amplitude of the LCO at $Re = 10^6$. Comparing the curves for $Re = 10^6$ and 10^7 the amplitude decrease slightly with increasing Re. Furthermore, the panel midpoint oscillates around a mean value which is lower than zero. This mean offset is decreased with increasing the Reynolds number from $Re = 1 \cdot 10^5$ to $3 \cdot 10^6$. This panel flutter behavior is mainly driven by the damping influence of a boundary layer as noted in [GV02].

Running the panel flutter simulation in the same point of the parameter space but in the inviscid mode of the CBS scheme with according boundary conditions, a significantly higher flutter amplitude and frequency is obtained, Table 7.1. This further underlines the damping influence of the boundary layer.

To further examine this influence, the parameters are changed to a stable flutter case, i.e. simulations are now accomplished with a non-dimensional dynamic pressure of $r_p = 100$, whereas the remaining parameters are kept unchanged. In Figure 7.30(a), the panel midpoint deflections are depicted for this stable flutter case for different Reynolds numbers. From this plot, it can be observed, that the panel oscillations are strongly damped. For very low and high Reynolds numbers, this damping is very distinctive, whereas for $Re = (3 \cdot 10^5, 1 \cdot 10^6)$ the damping becomes smaller. A reason for this behavior is given by the factor $(\mu + \mu_T)/Re$ in the diffusion term of the

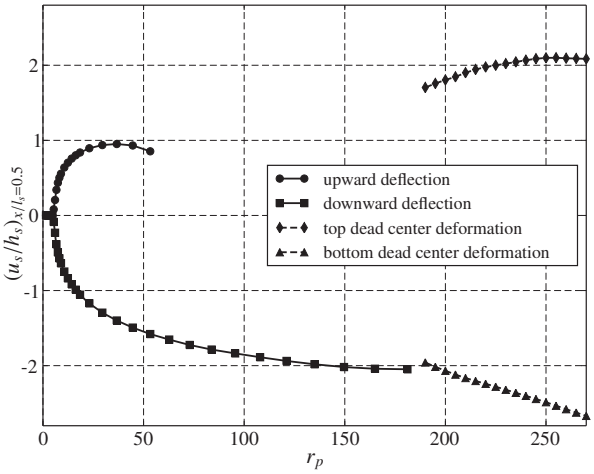

(a) $r_m = 0.05$

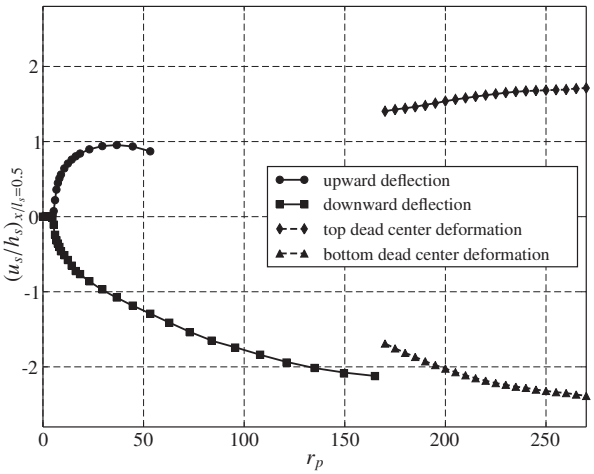

(b) $r_m = 0.10$

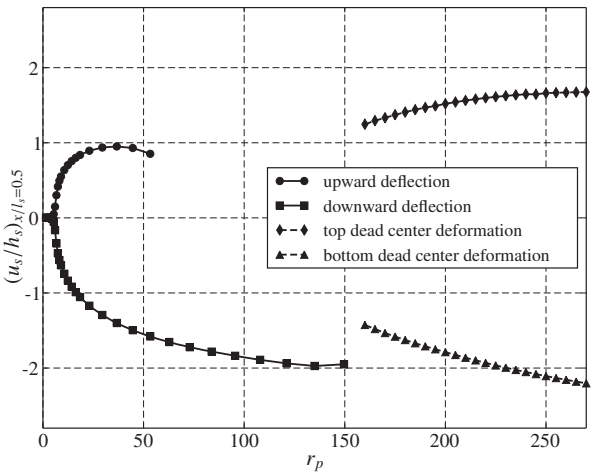

(c) $r_m = 0.20$

Figure 7.27: Panel up- and downward midpoint deflection as well as the amplitude at the top and bottom dead center for different dynamic pressures and mass ratios at $Ma_\infty = 1.0$

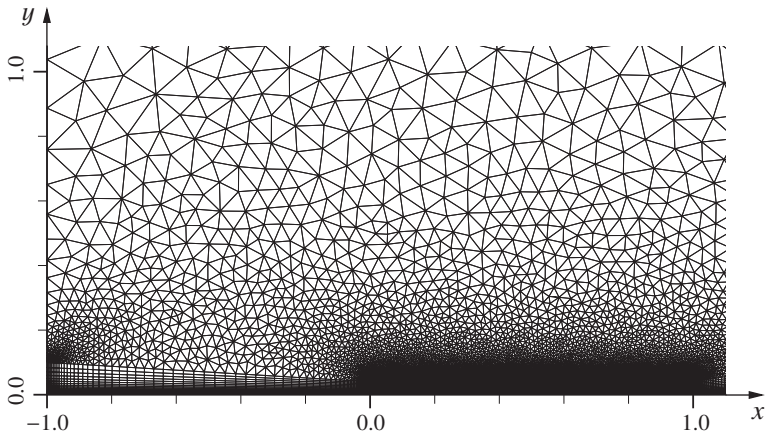

Figure 7.28: Close-up view on the hybrid grid for calculations of the turbulent panel flutter problem (number of nodes: 19832; number of quadrilateral elements: 12900; number of triangular elements: 13307)

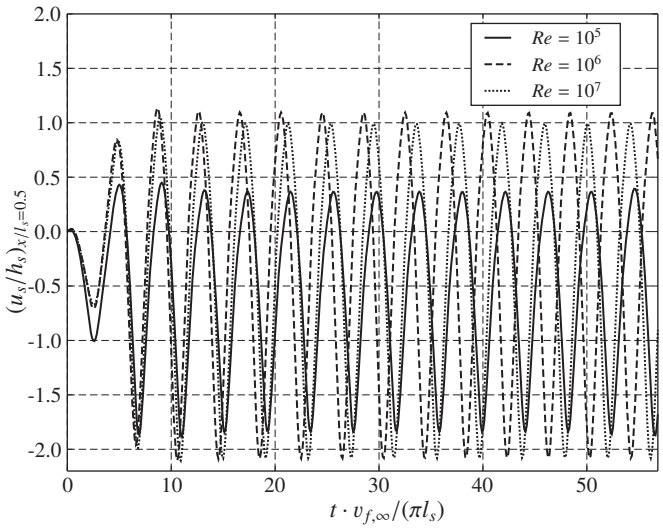

Figure 7.29: Midpoint deflection of the panel for different Reynolds numbers at $Ma = 1.1$, $r_m = 0.1$ and $r_p = 250$ - time step size $\Delta t = 0.001$ s $\Rightarrow \Delta t \cdot v_{f,\infty}/(\pi l_s) = 0.114$

non-dimensional RANS equations (see section A.2), which becomes higher for lower Reynolds numbers and for higher μ_T. The dynamic eddy viscosity μ_T in turns increases with increasing Re. These two contrary influences lead to a minimum value for the factor $(\mu + \mu_T)/Re$.

To quantify the influence, the logarithmic decrement ϑ and the damping ratio ζ:

$$\zeta = \frac{\vartheta}{\sqrt{(2\pi)^2 + \vartheta^2}}; \qquad \vartheta = \frac{1}{N_o} \ln \frac{u_s^{\text{top},3}}{u_s^{\text{top},3+N_o}}; \tag{7.6.1}$$

can be calculated from the time history plots. In the equations above, N_o denotes the number of peaks considered for the logarithmic decrement and $u_s^{\text{top},3}$ is the third peak in the midpoint deflection. For the calculation of the damping ratio, N_o is set to 6. In Figure 7.30(b), the logarithmic decrement and the damping ratio are plotted over the Reynolds number. For $Re = 1 \cdot 10^5$, a high

	$(u_s/h_s)^{\text{top}}$	$(u_s/h_s)^{\text{bottom}}$	$0.5(\Delta u_s/h_s)$	$(\overline{u_s}/h_s)$	K
$Re = 1 \cdot 10^5$:	0.366	-1.839	1.102	-0.737	0.244
$Re = 3 \cdot 10^5$:	1.134	-2.162	1.648	-0.514	0.259
$Re = 6 \cdot 10^5$:	1.170	-2.166	1.668	-0.498	0.260
$Re = 1 \cdot 10^6$:	1.084	-2.082	1.583	-0.499	0.259
$Re = 3 \cdot 10^6$:	1.120	-2.110	1.615	-0.495	0.251
$Re = 6 \cdot 10^6$:	1.056	-2.089	1.572	-0.516	0.244
$Re = 1 \cdot 10^7$:	0.994	-2.081	1.537	-0.544	0.246
inviscid calc.:	2.171	-2.434	2.303	-0.132	0.314

Table 7.1: Midpoint deflection at the top and bottom dead center, amplitudes, mean values as well as reduced frequency of the LCO at different Reynolds numbers - $Ma_\infty = 1.1$, $r_m = 0.1$ and $r_p = 250$

damping ratio of 15.6% is obtained. Increasing the Reynolds number, the influence of the damping decreases and reaches its lowest value at $Re = 6 \cdot 10^5$ with 7.5%. The damping then increases with higher Re and a strong damping of 21.2% can be obtained at $Re = 1 \cdot 10^7$.

Due to this damping, the stability boundary of the panel flutter problem is influenced by the Reynolds number. In Figure 7.31, the stability boundary chart of the panel in the transonic Mach number range is depicted for inviscid and turbulent flows at $r_m = 0.1$. Compared to the boundary of an inviscid inflow, the critical dynamic pressures for the turbulent flow are shifted to higher values. This means, that the flutter behavior is stabilized due to the presence of a boundary layer. This shift is between $110 \leq \Delta r_p \leq 120$, depending on the Mach and Reynolds number. Such high shift in the low-supersonic flow regime was also found in [HAN09] for a Mach number of

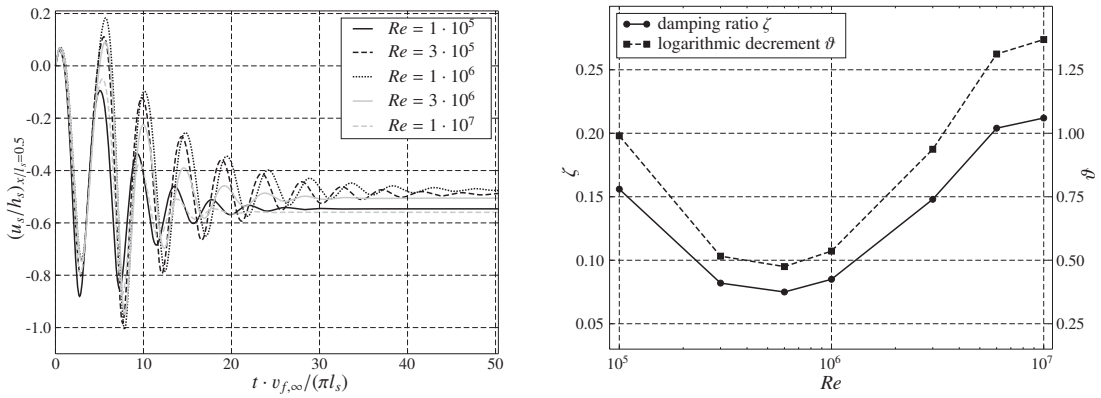

(a) midpoint deflection

(b) damping ratio and logarithmic decrement over Re

Figure 7.30: Midpoint deflection of the panel for different Reynolds numbers as well as the according damping ratio and logarithmic decrement for $Ma = 1.1$, $r_m = 0.1$, $r_p = 100$ and $\Delta t = 0.001\,\text{s} \Rightarrow \Delta t \cdot v_{f,\infty}/(\pi l_s) = 0.072$

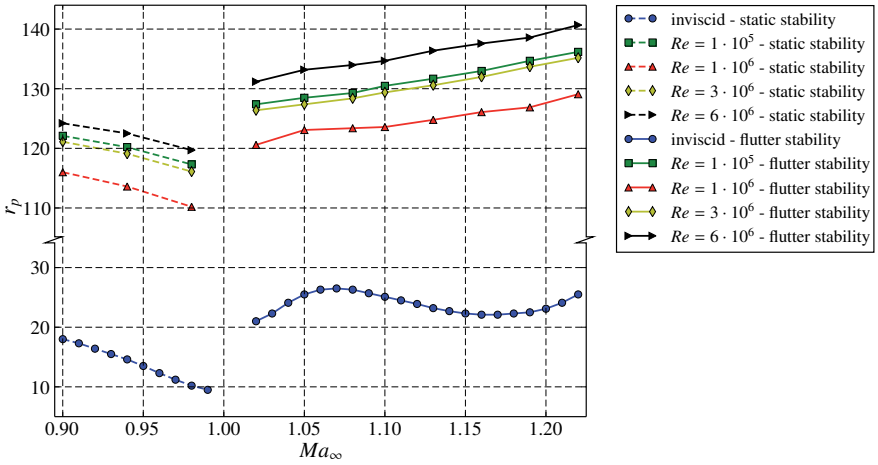

Figure 7.31: Stability boundary chart at different Reynolds numbers at $r_m = 0.1$

$1.1 \leq Ma_\infty \leq 1.3$. Moreover, the supersonic dip observed for the inviscid flow is absent for turbulent viscous fluid.

7.7 Chapter summary

In this chapter, the panel flutter problem is investigated with the finite element approach proposed in this thesis. On the structural side, this panel is modeled with the non-linear von Kármán plate theory. With the identified input parameter set (Ma_∞, r_p, r_m) for a given aluminum plate, the panel flutter problem serves as a benchmark problem to assess the numerical schemes. Due to the change in the aeroelastic behavior, when increasing the dynamic pressure from 160 to 180 at $Ma_\infty = 1.0$ and $r_m = 0.1$, several coupled computations are conducted at $r_p = 170$ with different numerical schemes. A LCO should be observed at this point in the parameter space.

Investigating the different data transfer schemes, the Galerkin and the dual-Lagrange based transfer as well as the conservative interpolation give similar results in terms of the frequency and amplitude of the LCO. With its local accuracy together with a global load conservation property and due to the efficiency of a matrix-free transfer scheme, the dual-Lagrange based transfer is an attractive approach for the data transmission of the coupled system.

To reduce the computational effort by omitting the equilibrium, the simple staggered time integration in conjunction with a structural predictor is analyzed for the panel flutter problem. Not all predictors are capable to capture a reasonable LCO and only the first and the second order predictor, (4.4.5) and (4.4.6), give reliable results for very coarse time steps. Furthermore, similar results are obtained, when the Newmark or the consistent three-point backward difference scheme for the structural time integration is used.

The comparison of the two- and three-field approach has shown, that both the frequency and the amplitude of the LCO are only marginally affected by the type of the coupling approach. However, the fluid field solution shows artificial shocks, when using a small number of structural elements and the two-field coupling. A smooth data transfer can be designed with the three-field approach and such shocks are omitted, which leads to a clean fluid solution.

This DG-CBS scheme with its advantage of a local flux conservation crossing two adjacent elements is compared to the continuous CBS scheme. Only with the usage of biquadratic or very fine bilinear elements, more accurate results in terms of the flutter frequency are obtained with DG-CBS scheme.

Consequently, the panel flutter behavior is systematically investigated at sub- and supersonic flow conditions using a simple staggered time integration scheme with the consistent time integration in the fluid and structural field and with the proposed three-field approach. At subsonic flow conditions, the panel shows a static deflection behavior in up- or downward direction depending on the structural initial conditions and the dynamic pressure r_p. Furthermore, the stability boundary is computed at different non-dimensional mass ratios. The critical $r_p(Ma_\infty)$, where the panel first deflect, is mainly independent of the non-dimensional mass ratio r_m.

In the supersonic flow regime, the panel shows a LCO and the stability chart indicates a strong dependency on the mass ratio. For low values of r_m, a supersonic dip in the stability boundary is observed. The frequency of the LCO increases with increasing the Mach number, dynamic pressure and mass ratio. Moreover, a linear dependency between the frequency and the amplitude of the LCO for high mass ratios and low supersonic Mach numbers has been found.

Considering a turbulent flow, the boundary layer leads to an additional damping behavior. Thereby, the frequency of the LCO remains unaffected by varying the Reynolds number. However, the amplitude and the mean deformation of the oscillation strongly depends on Re. Furthermore, the damping influence of the Reynolds number is quantified and a minimum value of the damping ratio and logarithmic decrement is identified for a certain point in the parameter space. Finally, due to the additional damping, the stability boundary is shifted to higher values of r_p.

8 Summary and Conclusion

In this thesis, a coupled multiphysical system is considered, whereas the focus is upon aeroelastic problems. For a consistent formulation of such coupled systems, an energy based variational formulation is chosen to describe initially the structural and fluid subsystem by Hamilton's principle. Both basic fluid model equations - inviscid and viscous fluid models - are employed by this weak variational energy principle. This procedure allows to describe the coupled problem by the classical direct two-field approach as well as by a novel indirect three-field approach.

To discretize the entire system consistently with finite elements, the CBS scheme is employed for the fluid domain described by the Navier-Stokes equation in ALE frame of reference. This allows the fluid domain to be temporally deformable, which is essential for aeroelastic computations. The CBS scheme is verified for a wide range of typical fluid problems ranging from inviscid, viscous, incompressible and turbulent flows. A good agreement with data published in literature and with the further solver TAU are found, which underlines the applicability of the CBS scheme for different fluid flow models.

The DG-CBS scheme as a novel and attractive approach has been derived from the continuous version. One important advantage of the DG version is the design of the element edge flux to be locally conservative. For the example of the laminar flow over the NACA0012 airfoil as well as for the panel flutter problem, a comparison of the CBS and DG-CBS scheme is made on structured fluid grids including grid convergence studies. With biquadratic, more accurate results in terms of the flutter frequency are obtained with DG-CBS scheme. Moreover, no global system of linear equations needs to be solved at the computational expense of addidtional element edge flux calculations with the DG version. This might be attractive for fluid grids with a high number of degrees of freedom.

Consequently, the whole coupled system is further discretized with finite elements including the structural subdomain, the deformation of the fluid grid and the transfer scheme. For the fluid grid deformation, it is found, that all of the presented stiffness evaluation methods perform similarly. The stiffness strategy based on the wall distance and the characteristic length is recommended to be used for the simple testcases with the unstructured grid. For a structured grid around an airfoil, the best grids are obtained with the stiffness methods based on the wall distance. Thus, for general fluid grid deformations, the method, which use a combination of the wall distance and the characteristic length, can be recommended and is hence applied for the panel flutter problem.

Based on the unified weak variational coupling schemes, several data transfer schemes are introduced, which share the property of load and energy conservation. With a h-refinement of the integration grid, a significant reduction of the transfer error is observed for low-curved interface meshes. The decrease of the transfer error is limited by the facetting error, which is identified for highly curved interface meshes and for a realistic wing configuration. For the panel flutter problem at $Ma_\infty = 1.0$ and $r_p = 170$, the Galerkin and the dual-Lagrange based transfer as well as the conservative interpolation gives similar results in terms of the frequency and amplitude of the LCO. With its local accuracy together with a global load conservation property and due to the efficiency of a matrix-free transfer scheme, the dual-Lagrange based transfer is an attractive approach for the data transmission of the coupled system.

A smooth transfer scheme is proposed, which uses the novel three-field coupling approach with a higher spatial order discretization of the connectivity frame. Regarding the time integration and equilibrium iteration, the three-field approach is assessed for a strongly coupled problem. With the use of the Newton-GMRES iteration scheme, the number of DN cycles is reduced for the three-field approach. Moreover, the same coupling matrices are identified for the three-field approach, which alreay appeared within the iteration process of two-field approach. This allows the application of a simple staggered time integration scheme for the panel flutter problem. The comparison of the two- and three-field approach shows that both, the frequency and the amplitude of the LCO, are only marginally affected. However, the smooth data transfer leads to a clean fluid solution without artificial shocks, which has been observed with the two-field approach and a small number structural elements at the interface.

Furthermore, a consistent time integration approach for the structure is proposed, so that both subsystems use the same temporal discretization. Here, similar results in terms of the LCO's frequency and amplitude are obtained, when the Newmark or the consistent three-point backward difference scheme for the structural time integration of the panel is applied.

Thus, the panel flutter problem using a simple staggered time integration scheme with the consistent time integration for the fluid and structural subsystem and with the proposed three-field approach could be analyzed in detail running numerous simulations. At subsonic flow conditions, the panel shows a static deflection behavior in up- or downward direction depending on Ma_∞ and r_p, but indepentent of r_m. On the other hand, the panel exhibits a LCO and the critical values of the dynamic pressure strongly depend on the mass ratio. For low values of r_m, a supersonic dip in the stability boundary is observed. It is shown, that the frequency of the LCO increases with increasing Mach number, dynamic pressure and mass ratio. Moreover, a linear dependency between the frequency and the amplitude of the LCO for high mass ratios and low Mach numbers is found.

Turbulence modeling with the aid of the CBS scheme in the context of an aeroelastic problem is employed in this thesis. The Spalart-Allmaras turbulence model in conjunction with the CBS scheme is primarily verified with data found in literature and with the flowsolver TAU for pure compressible fluid flow over an airfoil. For the panel flutter problem, the turbulent boundary layer leads to an additional damping behavior. The frequency of the LCO is unaffected by the Reynolds number, but a dependency regarding Re is noticed for the amplitude and the mean deformation. Finally, a strong shift of the critical dynamic pressure to higher values could be observed for the stability chart, which is caused by the damping influence.

Subsequent work regarding this thesis certainly involves the investigation of the panel flutter phenomenon in three dimensions. This is motivated by the good performance of the CBS scheme in 3D found in literature. Another topic, which should be considered further, is the application of the three-field coupling approach for more than two subdomains, e.g. fluid-fluid-structure or fluid-structure-structure interaction. In this context, the performance of the presented coupling scheme in conjunction with an incompressible fluid could be a subject for research. Herein, the avoidance of the added mass effect due to an artificial compressibility within the CBS scheme is an interesting aspect. Moreover, attempts to improve the standard finite element methodology by a NURBS based isogeometric analysis can be observed in literature, see [CHB09] and the references therein. A NURBS based coupling scheme is a straightforward enhancement to the present methodology. Further, an adaptive refinement - mesh, polynomial, or a combination of both - is surely an attractive approach to improve the accuracy of the methodology. Finally, from the CFD point of view, more precise numerical methods were established and thus, the CBS scheme could be enhanced with a transition prediction scheme as well as with a large or detached eddy simulation (LES/DES) methodology to capture more complex fluid flow phenomena.

Bibliography

[ACD09] G. Altay and M. Cengiz Dokmeci. Fluid-fluid and -solid interaction problems: Variational principles revisited. *International Journal of Engineering Science*, 47(1):83–102, 2009.

[ACM99] K. Abdel-Motaglay, R. Chen, and C. Mei. Nonlinear flutter of composite panels under yawed supersonic flow using finite elements. *AIAA Journal*, 37(9):1025–1032, 1999.

[ANS06] ANSYS Inc. ANSYS 11.0 documentation. http://www.ansys.com, 2006.

[Ban11] S.E. Bansmer. *Stroemungsanalyse an einem zwei- und dreidimensional schlagenden Fluegelsegment*. PhD thesis, TU Braunschweig, Braunschweig, 2011.

[Bat96] K. J. Bathe. *Finite element procedures*. Prentice Hall, New Jersey, 1996.

[BBH10] Y. Bao, D. Boffi, and C. Huang. Numerical simulation of flow over three circular cylinders in equilateral arrangements at low Reynolds number by a second-order characteristic-based split finite element method. *Computers & Fluids*, 39(5):882–899, 2010.

[BC10] A. T. Barker and X.-C. Cai. Scalable parallel methods for monolithic coupling in fluid-structure interaction with application to blood flow modeling. *Journal of Computational Physics*, 229(3):642–659, 2010.

[BCRS05] F. Bassi, A. Crivellini, S. Rebay, and M. Savini. Discontinuous galerkin solution of the Reynolds-averaged Navier-Stokes and k-[omega] turbulence model equations. *Computers & Fluids*, 34(4-5):507–540, 2005.

[Ben04] O. O. Bendiksen. Modern developments in computational aeroelasticity. *Proceedings of the Institution of Mechanical Engineers, Part G: Journal of Aerospace Engineering*, 218(3):157–177, 2004.

[BG04] D. Boffi and L. Gastaldi. Stability and geometric conservation laws for ALE formulations. *Computer Methods in Applied Mechanics and Engineering*, 193(42-44):4717–4739, 2004.

[BH82] A. N. Brooks and T. J. R. Hughes. Streamline upwind/Petrov-Galerkin formulations for convection dominated flows with particular emphasis on the incompressible Navier-Stokes equations. *Computer Methods in Applied Mechanics and Engineering*, 32(1-3):199–259, 1982.

[Bla06] J. Blazek. *Computational fluid dynamics: principles and applications*. Elsevier Science Ltd, 2 edition, 2006.

[Blo98] F. J. Blom. A monolithical fluid-structure interaction algorithm applied to the piston problem. *Computer Methods in Applied Mechanics and Engineering*, 167(3-4):369–391, 1998.

[BNvL+10] R. L. T. Bevan, P. Nithiarasu, R. van Loon, I. Sazonov, H. Luckraz, and A. Garnham. Application of a locally conservative galerkin (LCG) method for modelling blood flow through a patient-specific carotid bifurcation. *International Journal for Numerical Methods in Fluids*, 0(0):n/a, 2010.

[BO99] C. E. Baumann and J. T. Oden. A discontinuous hp finite element method for the euler and Navier-Stokes equations. *International Journal for Numerical Methods in Fluids*, 31(1):79–95, 1999.

[BRU+10] S. Bansmer, R. Radespiel, R. Unger, M. Haupt, and P. Horst. Experimental and numerical fluid-structure analysis of rigid and flexible flapping airfoils. *AIAA Journal*, 48(9):1959–1974, 2010.

[BS06] H.-J. Bungartz and M. Schaefer. *Fluid-structure interaction: modelling, simulation, optimisation*. Springer, Berlin, 2006.

[BS08] O. O. Bendiksen and G. Seber. Fluid-structure interactions with both structural and fluid nonlinearities. *Journal of Sound and Vibration*, 315(3):664–684, 2008.

[CC76] T. J. Chung and J. N. Chiou. Analysis of unsteady compressible boundary layer flow via finite elements. *Computers and Fluids*, 4:1–12, 1976.

[CD04] R. Clark and E. H. Dowell. *A modern course in aeroelasticity*. Kluwer Academic Publishing, 2004.

[CGN05] P. Causin, J. F. Gerbeau, and F. Nobile. Added-mass effect in the design of partitioned algorithms for fluid-structure problems. *Computer Methods in Applied Mechanics and Engineering*, 194(42-44):4506–4527, 2005.

[CHB09] J. A. Cottrell, T. J. R. Hughes, and Y. Bazilevs. *Isogeometric analysis: toward integration of CAD and FEA*. John Wiley and Sons, 2009.

[Chu02] T. J. Chung. *Computational fluid dynamics*. Cambridge University Press, 2002.

[CL97] J. R. Cebral and R. Loehner. Conservative load projection and tracking for fluid-structure problems. *AIAA Journal*, 35(4):687–692, 1997.

[Coc03] B. Cockburn. Discontinuous Galerkin methods. *ZAMM*, 83(11):731–754, 2003.

[CZY06] X. Chen, G. Zha, and M. Yang. Numerical simulation of 3-D wing flutter with fully coupled fluid- structure interaction approach. *AIAA-Paper 2006-0697*, 2006.

[DB93] G. Davis and O. O. Bendiksen. Transonic panel flutter. *AIAA-Paper 93-1476*, 1993.

[DB06] D. Dureisseix and H. Bavestrello. Information transfer between incompatible finite element meshes: Application to coupled thermo-viscoelasticity. *Computer Methods in Applied Mechanics and Engineering*, 195(44-47):6523–6541, 2006.

[dB08] A. de Boer. *Computational fluid-structure interaction - Spatial coupling, shell and mesh deformation*. PhD thesis, Technische Universiteit Delft, Department of Aerodynamics and Wind Energy, Delft, 2008.

[dBvdSB07] A. de Boer, M. S. van der Schoot, and H. Bijl. Mesh deformation based on radial basis function interpolation. *Computers & Structures*, 85(11-14):784–795, 2007.

[dBvZB08] A. de Boer, A. H. van Zuijlen, and H. Bijl. Comparison of conservative and consistent approaches for the coupling of non-matching meshes. *Computer Methods in Applied Mechanics and Engineering*, 197(49-50):4284–4297, 2008.

[DF02] C. Degand and C. Farhat. A three-dimensional torsional spring analogy method for unstructured dynamic meshes. *Computers & Structures*, 80(3-4):305–316, 2002.

[DGH82] J. Donea, S. Giuliani, and J. P. Halleux. An arbitrary Lagrangian-Eulerian finite element method for transient dynamic fluid-structure interactions. *Computer Methods in Applied Mechanics and Engineering*, 33(1-3):689–723, 1982.

[DGP94] D. Drikakis, P. A. Govatsos, and D. E. Papantonis. A characteristic-based method for incompressible flows. *International Journal for Numerical Methods in Fluids*, 19(8):667–685, 1994.

[DH03] J. Donea and A. Huerta. *Finite element methods for flow problems*. John Wiley & Sons, 2003.

[DLR09] DLR. Technical documentation of the DLR TAU-Code release 2009.2.0. Technical report, DLR, Institute of Aerodynamic and Flow Technology, Braunschweig, 2009.

[Dow70] E. H. Dowell. Panel flutter: a review of the aeroelastic stability of plates and shells. *AIAA Journal*, 8:385–399, 1970.

[Dow73] E. H. Dowell. Aerodynamic boundary layer effects on flutter and damping of plates. *Journal of Aircraft*, 10(12):734–738, 1973.

[Dow77] E. H. Dowell. *Aeroelasticity of plates and shells*. Noordhoff International Publishing, Leyden, 1977.

[DP74] M. K. Denham and M. A. Patrick. Laminar flow over a downstream-facing step in a two-dimensional flow channel. *Transactions of the Institution of Chemical Engineers*, 52:361–367, 1974.

[DP06] W. Dettmer and D. Peric. A computational framework for fluid-rigid body interaction: Finite element formulation and applications. *Computer Methods in Applied Mechanics and Engineering*, 195(13-16):1633–1666, 2006.

[DSVP+10] J. Degroote, A. Souto-Iglesias, W. Van Paepegem, S. Annerel, P. Bruggeman, and J. Vierendeels. Partitioned simulation of the interaction between an elastic structure and free surface flow. *Computer Methods in Applied Mechanics and Engineering*, 199(33-36):2085–2098, 2010.

[EB01] N. El-Abbasi and K. J. Bathe. Stability and patch test performance of contact discretizations and a new solution algorithm. *Computers & Structures*, 79(16):1473–1486, 2001.

[EGP09] S. Etienne, A. Garon, and D. Pelletier. Perspective on the geometric conservation law and finite element methods for ALE simulations of incompressible flow. *Journal of Computational Physics*, 228(7):2313–2333, 2009.

[Far04] C. Farhat. CFD-Based nonlinear computational aeroelasticity. In E. Stein, R. de Borst, and T. J. R. Hughes, editors, *Encyclopedia of Computational Mechanics*. John Wiley & Sons, Ltd, Chichester, 2004.

[FGG01] C. Farhat, P. Geuzaine, and C. Grandmont. The discrete geometric conservation law and the nonlinear stability of ALE schemes for the solution of flow problems on moving grids. *Journal of Computational Physics*, 174(2):669–694, 2001.

[FK93] Z. Friedman and J. B. Kosmatka. An improved two-node Timoshenko beam finite element. *Computers & Structures*, 47(3):473–481, 1993.

[FKW06] B. Flemisch, M. Kaltenbacher, and B. I. Wohlmuth. Elasto-acoustic and acoustic-acoustic coupling on non-matching grids. *International Journal for Numerical Methods in Engineering*, 67(13):1791–1810, 2006.

[FL00] C. Farhat and M. Lesoinne. Two efficient staggered algorithms for the serial and parallel solution of three-dimensional nonlinear transient aeroelastic problems. *Computer Methods In Applied Mechanics And Engineering*, 182:499–515, 2000.

[FLL98] C. Farhat, M. Lesoinne, and P. LeTallec. Load and motion transfer algorithms for fluid/structure interaction problems with non-matching discrete interfaces: Momentum and energy conservation, optimal discretization and applications. *Computer Methods in Applied Mechanics and Engineering*, 157(1-2):95–114, 1998.

[FLM95] C. Farhat, M. Lesoinne, and N. Maman. Mixed explicit/implicit time integration of coupled aeroelastic problems: Three-field formulation, geometric conservation and distributed solution. *International Journal for Numerical Methods in Fluids*, 21(10):807–835, 1995.

[Foe74] H. W. Foersching. *Grundlagen der Aeroelastik*. Springer, Berlin, 1974.

[Foe07] C. Foerster. *Robust methods for fluid-structure interaction with stabilised finite elements*. PhD thesis, Universitaet Stuttgart, Institut fuer Baustatik und Baudynamik, 2007.

[FP01] J. H. Ferziger and M. Peric. *Computational Methods for Fluid Dynamics*. Springer, Berlin, 3rd edition, 2001.

[FPW05] B. Flemisch, M. A. Puso, and B. I. Wohlmuth. A new dual mortar method for curved interfaces: 2D elasticity. *International Journal for Numerical Methods in Engineering*, 63(6):813–832, 2005.

[FRWB10] C. Farhat, A. Rallu, K. Wang, and T. Belytschko. Robust and provably second-order explicit-explicit and implicit-explicit staggered time-integrators for highly non-linear compressible fluid-structure interaction problems. *International Journal for Numerical Methods in Engineering*, 84(1):73–107, 2010.

[FvdZG06] C. Farhat, K. G. van der Zee, and P. Geuzaine. Provably second-order time-accurate loosely-coupled solution algorithms for transient nonlinear computational aeroelasticity. *Computer Methods In Applied Mechanics And Engineering*, 195:1973–2001, 2006.

[FVJ+06] C. A. Figueroa, I. E. Vignon-Clementel, K. E. Jansen, T. J. R. Hughes, and C. A. Taylor. A coupled momentum method for modeling blood flow in three-dimensional deformable arteries. *Computer Methods in Applied Mechanics and Engineering*, 195(41-43):5685–5706, 2006.

[FWR07] C. Foerster, W. A. Wall, and E. Ramm. Artificial added mass instabilities in sequential staggered coupling of nonlinear structures and incompressible viscous flows. *Computer Methods in Applied Mechanics and Engineering*, 196(7):1278–1293, 2007.

[Gal15] B. G. Galerkin. Series solution of some problems in elastic equilibrium of rods and plates. *Vestnik Inzhenerov i Tekhikov*, 19:897–908, 1915.

[GBD+03] M. Glueck, M. Breuer, F. Durst, A. Halfmann, and E. Rank. Computation of wind-induced vibrations of flexible shells and membranous structures. *Journal of Fluids and Structures*, 17(5):739–765, 2003.

[GM00] R. E. Gordnier and R. B. Melville. Transonic flutter simulations using an implicit aeroelastic solver. *Journal of Aircraft*, 37(5):872–879, 2000.

[GSE98] P. M. Gresho, R. L. Sani, and M. S. Engelman. *Incompressible flow and the finite element method: advection-diffusion and isothermal laminar flow*. John Wiley & Sons, 1998.

[Gup96] K. K. Gupta. Development of a finite element aeroelastic analysis capability. *Journal of Aircraft*, 33(5):995–1002, 1996.

[GV02] R. E. Gordnier and M. R. Visbal. Development of a three-dimensional viscous aeroelastic solver for nonlinear panel flutter. *Journal of Fluids and Structures*, 16(4):497–527, 2002.

[HAC74] C. W. Hirt, A. A. Amsden, and H. K. Cook. An arbitrary Lagrangian-Eulerian method for all flow speeds. *Journal of Computational Physics*, 14:227–253, 1974.

[Ham34] W. R. Hamilton. On a general method in dynamics. *Philosophical Transactions of the Royal Society (part II)*, pages 247–308, 1834.

[HAN09] A. Hashimoto, T. Aoyama, and Y. Nakamura. Effects of turbulent boundary layer on panel flutter. *AIAA Journal*, 47(12):2785–2791, 2009.

[Har06] R. Hartmann. Adaptive discontinuous Galerkin methods with shock-capturing for the compressible Navier-Stokes equations. *International Journal for Numerical Methods in Fluids*, 51(9-10):1131–1156, 2006.

[Hei04] M. Heil. An efficient solver for the fully coupled solution of large-displacement fluid-structure interaction problems. *Computer Methods in Applied Mechanics and Engineering*, 193(1-2):1–23, 2004.

[Hel14] E. Hellinger. Die allgemeine Ansaetze der Mechanik der Kontinua. *Encyklopaedie der mathematischen Wissenschaften IV*, 4:654–655, 1914.

[HFH89] T. J. R. Hughes, L. P. Franca, and G. M. Hulbert. A new finite element formulation for computational fluid dynamics: VIII. the Galerkin/least-squares method for advective-diffusive equations. *Computer Methods in Applied Mechanics and Engineering*, 73(2):173–189, 1989.

[HHLP10] R. Hartmann, J. Held, T. Leicht, and F. Prill. Discontinuous Galerkin methods for computational aerodynamics – 3D adaptive flow simulation with the DLR PADGE code. *Aerospace Science and Technology*, 14(7):512–519, 2010.

[Hic08] R. Hickey. *The characteristic based split (CBS) scheme for turbulent compressible flows*. PhD thesis, University of Wales, School of Engineering, 2008.

[HL88] A. Huerta and W. K. Liu. Viscous flow with large free surface motion. *Computer Methods in Applied Mechanics and Engineering*, 69(3):277–324, 1988.

[HL03] M. W. Heinstein and T. A. Laursen. A three dimensional surface-to-surface projection algorithm for non-coincident domains. *Communications in Numerical Methods in Engineering*, 19(6):421–432, 2003.

[HLZ81] T. J. R. Hughes, W. K. Liu, and T. K. Zimmermann. Lagrangian-Eulerian finite element formulation for incompressible viscous flows. *Computer Methods in Applied Mechanics and Engineering*, 29(3):329–349, 1981.

[HSBB06] T. J. R. Hughes, G. Scovazzi, P. B. Bochev, and A. Buffa. A multiscale discontinuous Galerkin method with the computational structure of a continuous Galerkin method. *Computer Methods in Applied Mechanics and Engineering*, 195(19-22):2761–2787, 2006.

[Hug00] T. J. R. Hughes. *The finite element method: linear static and dynamic finite element analysis*. Dover Publications, 2000.

[Hur01] J. Hurka. *Numerische Untersuchung zur Aerolastik duenner Platten*. PhD thesis, RWTH Aachen, 2001.

[Ian06] J. Iannelli. *Characteristics finite element methods in computational fluid dynamics*. Springer, 2006.

[Jam91] A. Jameson. Time dependent calculations using multigrid with application to unsteady flows past airfoils and wings. *AIAA-Paper 91-0596*, 1991.

[JH04] X. M. Jiao and M. T. Heath. Common-refinement-based data transfer between non-matching meshes in multiphysics simulations. *International Journal For Numerical Methods In Engineering*, 61(14):2402–2427, 2004.

[JJGL05] R. K. Jaiman, X. Jiao, P. H. Geubelle, and E. Loth. Assessment of conservative load transfer for fluid-solid interface with non-matching meshes. *International Journal for Numerical Methods in Engineering*, 64(15):2014–2038, 2005.

[JL72] W. P. Jones and B. E. Launder. The prediction of laminarization with a two-equation model of turbulence. *International Journal of Heat and Mass Transfer*, 15(2):301–314, 1972.

[JM86] A. Jameson and D. Mavriplis. Finite volume solution of the two-dimensional Euler equations on a regular triangular mesh. *AIAA Journal*, 24:611–618, 1986.

[JT94] A. A. Johnson and T. E. Tezduyar. Mesh update strategies in parallel finite element computations of flow problems with moving boundaries and interfaces. *Computer Methods in Applied Mechanics and Engineering*, 119(1-2):73–94, 1994.

[Kel95] C. T. Kelley. *Iterative methods for linear and nonlinear equations*. SIAM, 1995.

[Kim10] H.-G. Kim. A new coupling strategy for fluid-solid interaction problems by using the interface element method. *International Journal for Numerical Methods in Engineering*, 81(4):403–428, 2010.

[LB93] E. M. Lee-Rausch and J. T. Batina. Calculation of AGARD wing 445.6 flutter using Navier-Stokes aerodynamics. *AIAA-Paper 93-3476*, 1993.

[LBL08] H. Luo, J. D. Baum, and R. Loehner. Fast p-multigrid discontinuous Galerkin method for compressible flows at all speeds. *AIAA Journal*, 46(3):635–652, 2008.

[Lee77] C. M. Leech. Hamilton's principle applied to fluid mechanics. *The Quarterly Journal of Mechanics & Applied Mathematics*, 30(1):107–130, 1977.

[LF96] M. Lesoinne and C. Farhat. Geometric conservation laws for flow problems with moving boundaries and deformable meshes, and their impact on aeroelastic computations. *Computer Methods in Applied Mechanics and Engineering*, 134(1-2):71–90, 1996.

[LH87] C. L. Lawson and R. J. Hanson. *Solving least squares problems*. Society for Industrial Mathematics, 1987.

[Li06] B. Q. Li. *Discontinuous finite elements in fluid dynamics and heat transfer*. Springer, 2006.

[Liu05] C.-B. Liu. *The characteristic based split (CBS) scheme for laminar and turbulent incompressible flow simulations*. PhD thesis, University of Wales, School of Engineering, 2005.

[LM99] P. LeTallec and S. Mani. Conservation laws for fluid structure interactions. In T. Kvamsdal, editor, *International Symposium on Computational Methods for Fluid Structure Interactions*, pages 61–78. Trondheim, 1999.

[LMZ84] R. Loehner, K. Morgan, and O. C. Zienkiewicz. The solution of non-linear hyperbolic equation systems by the finite element method. *International Journal for Numerical Methods in Fluids*, 4(11):1043–1063, 1984.

[Loe08] R. Loehner. *Applied computational fluid dynamics techniques: An introduction based on finite element methods*. John Wiley & Sons, 2 edition, 2008.

[LPZ87] J. H. W. Lee, J. Peraire, and O. C. Zienkiewicz. The characteristic-Galerkin method for advection-dominated problems - an assessment. *Computer Methods in Applied Mechanics and Engineering*, 61(3):359–369, 1987.

[LQX06] X. Liu, N. Qin, and H. Xia. Fast dynamic grid deformation based on Delaunay graph mapping. *Journal of Computational Physics*, 211(2):405–423, 2006.

[LS07] Y. Lian and W. Shyy. Laminar-turbulent transition of a low Reynolds number rigid or flexible airfoil. *AIAA Journal*, 45(7):1501–1513, 2007.

[Lyn02] P. Lynch. Hamiltonian methods for geophysical fluid dynamics: an introduction. Technical Report IMA Preprints Series, 3742, 2002.

[Mas02] R. Massjung. *Numerical schemes and well posedness in nonlinear aeroelasticity*. PhD thesis, RWTH Aachen, 2002.

[Men93] F. R. Menter. Zonal two equation k-omega turbulence models for aerodynamic flows. *AIAA-Paper 93-2906*, 1993.

[Mit98] S. Mittal. Finite element computation of unsteady viscous compressible flows. *Computer Methods in Applied Mechanics and Engineering*, 157(1-2):151–175, 1998.

[MLN02] A. G. Malan, R. W. Lewis, and P. Nithiarasu. An improved unsteady, unstructured, artificial compressibility, finite volume scheme for viscous incompressible flows: Part I. theory and implementation. *International Journal for Numerical Methods in Engineering*, 54(5):695–714, 2002.

[Mor06] P. J. Morrison. Hamiltonian fluid dynamics. In *Encyclopedia of Mathematical Physics*, volume 2, pages 593–600. 2006.

[MS03] H. G. Matthies and J. Steindorf. Partitioned strong coupling algorithms for fluid-structure interaction. *Computers & Structures*, 81(8-11):805–812, 2003.

[Mue98] P. Mueller. A canonical view of fluid dynamics. In A. K. Richter, editor, *Understanding Physics*, pages 15–29. Copernicus, 1998.

[NCZ06] P. Nithiarasu, R. Codina, and O. C. Zienkiewicz. The characteristic-based split (CBS) scheme - a unified approach to fluid dynamics. *International Journal for Numerical Methods in Engineering*, 66(10):1514–1546, 2006.

[NHM+08] P. Nithiarasu, O. Hassan, K. Morgan, N. P. Weatherill, C. Fielder, H. Whittet, P. Ebden, and K. R. Lewis. Steady flow through a realistic human upper airway geometry. *International Journal for Numerical Methods in Fluids*, 57(5):631–651, 2008.

[Nie09] R. Niesner. *Gekoppelte Simulation thermisch-mechanischer Fluid-Struktur-Interaktionen fuer Hyperschall-Anwendungen*. ZLR-Forschungsbericht / Zentrum fuer Luft- und Raumfahrttechnik, Technische Universitaet Braunschweig, ISSN 0945-2214. Shaker, Aachen, 2009.

[Nit03] P. Nithiarasu. An efficient artificial compressibility (AC) scheme based on the characteristic based split (CBS) method for incompressible flows. *International Journal for Numerical Methods in Engineering*, 56(13):1815–1845, 2003.

[NL06] P. Nithiarasu and C.-B. Liu. An artificial compressibility based characteristic based split (CBS) scheme for steady and unsteady turbulent incompressible flows. *Computer Methods in Applied Mechanics and Engineering*, 195(23-24):2961–2982, 2006.

[NMWM04] P. Nithiarasu, J. S. Mathur, N. P. Weatherill, and K. Morgan. Three-dimensional incompressible flow calculations using the characteristic based split (CBS) scheme. *International Journal for Numerical Methods in Fluids*, 44(11):1207–1229, 2004.

[Noh64] W. F. Noh. A time-dependent, two-space-dimensional, coupled Eulerian-Lagrange code. *Methods in Computational Physics*, 3:117–179, 1964.

[Ode72] J. T. Oden. *Finite elements of nonlinear continua*. McGraw-Hill, 1972.

[OMH+05] M. Ol, B. McCauliffe, E. Hanff, U. Scholz, and C. J. Kaehler. Comparison of laminar separation bubble measurements on a low Reynolds number airfoil in three facilities. *AIAA-Paper 2005-5149*, 2005.

[Pal06] A. F. Palacios. *The Hamilton-type principle in fluid dynamics: fundamentals and applications to magnetohydrodynamics, thermodynamics and astrophysics*. Springer, 2006.

[PF00] K. C. Park and C. A. Felippa. A variational principle for the formulation of partitioned structural systems. *International Journal for Numerical Methods in Engineering*, 47(1-3):395–418, 2000.

[Pip97] S. Piperno. Explicit/implicit fluid/structure staggered procedures with a structural predictor and fluid subcycling for 2D inviscid aeroelastic simulations. *International Journal For Numerical Methods In Fluids*, 25(10):1207–1226, 1997.

[Pus04] M. A. Puso. A 3D mortar method for solid mechanics. *International Journal for Numerical Methods in Engineering*, 59(3):315–336, 2004.

[Ray77] Lord Rayleigh. *The theory of sound*. Macmillan, London, 1877.

[Red02] J. N. Reddy. *Energy principles and variational methods in applied mechanics*. John Wiley & Sons, 2002.

[Rei50] E. Reissner. On a variational theorem in elasticity. *Journal of Mathematics and Physics*, 29(2):90–95, 1950.

[RFPS08] M. R. Ross, C. A. Felippa, K. C. Park, and M. A. Sprague. Treatment of acoustic fluid-structure interaction by localized Lagrange multipliers: Formulation. *Computer Methods in Applied Mechanics and Engineering*, 197(33-40):3057–3079, 2008.

[Rit08] W. Ritz. Ueber eine neue Methode zur Loesung gewisser Variationsprobleme der mathematischen Physik. *Journal fuer die Reine und Angewandte Mathematik*, 135:1–61, 1908.

[RK08] C.-C. Rossow and N. Kroll. High performance computing serves aerospace engineering: Opportunities for next generation product development. *AIAA-Paper 2008-0712*, 2008.

[RS09] C. L. Rumsey and P. R. Spalart. Turbulence model behavior in low Reynolds number regions of aerodynamic flowfields. *AIAA Journal*, 47(4):982–993, 2009.

[RSFP09] M. R. Ross, M. A. Sprague, C. A. Felippa, and K. C. Park. Treatment of acoustic fluid-structure interaction by localized Lagrange multipliers and comparison to alternative interface-coupling methods. *Computer Methods in Applied Mechanics and Engineering*, 198(9-12):986–1005, 2009.

[RWS07] R. Radespiel, J. Windte, and U. Scholz. Numerical and experimental flow analysis of moving airfoils with laminar separation bubbles. *AIAA Journal*, 45(6):1346–1356, 2007.

[Sal88] R. Salmon. Hamiltonian fluid mechanics. *Annual Review of Fluid Mechanics*, 20(1):225–256, 1988.

[Sal98] R. Salmon. *Lectures on geophysical fluid dynamics*. Oxford University Press US, 1998.

[SCH00] M. J. Smith, C. E. S. Cesnik, and D. H. Hodges. Evaluation of some data transfer algorithms for noncontiguous meshes. *Journal of Aerospace Engineering*, 13(2):52–58, 2000.

[SF07] C. M. Scotti and E. A. Finol. Compliant biomechanics of abdominal aortic aneurysms: A fluid-structure interaction study. *Computers & Structures*, 85(11-14):1097–1113, 2007.

[Sha89] F. Shakib. *Finite element analysis of the compressible Euler and Navier-Stokes equations*. PhD thesis, Stanford University, Department of Mechanical Engineering, 1989.

[SMU+10] F. Schaefer, S. Mueller, T. Uffinger, S. Becker, J. Grabinger, and M. Kaltenbacher. Fluid-structure-acoustics interaction of the flow past a thin flexible structure. *AIAA Journal*, 48:738–748, 2010.

[SNRA10] H. Shokouhmand and S. M. A. Noori Rahim Abadi. Finite element analysis of natural heat transfer from an isothermal array of cylinders in presence of vertical oscillations. *Heat and Mass Transfer*, 2010.

[SR07] P. R. Spalart and C. L. Rumsey. Effective inflow conditions for turbulence models in aerodynamic calculations. *AIAA Journal*, 45(10):2544–2553, 2007.

[STB03] K. Stein, T. Tezduyar, and R. Benney. Mesh moving techniques for fluid-structure interactions with large displacements. *Journal of Applied Mechanics*, 70(1):58, 2003.

[Ste02] J. Steindorf. *Partitionierte Verfahren fuer Probleme der Fluid-Struktur Wechselwirkung*. Braunschweiger Schriften zur Mechanik. Inst. f. Angew. Mechanik, Technische Universitaet Braunschweig, Braunschweig, 2002.

[SW68] R. L. Seliger and G. B. Whitham. Variational principles in continuum mechanics. *Proceedings of the Royal Society of London. Series A. Mathematical and Physical Sciences*, 305(1480):1–25, 1968.

[Swa00] G. E. Swaters. *Introduction to Hamiltonian fluid dynamics and stability theory*. CRC Press, 2000.

[TBU00] P. Thevenaz, T. Blu, and M. Unser. Interpolation revisited. *IEEE Transaction on Medical Imaging*, 19(7):739—758, 2000.

[Tho06] C. G. Thomas. *A locally conservative Galerkin (LCG) finite element method for convection-diffusion Navier-Stokes equation*. PhD thesis, University of Wales, School of Engineering, 2006.

[TL79] P. D. Thomas and C. K. Lombard. Geometric conservation law and its application to flow computations on moving grids. *AIAA Journal*, 17(10):1030–1037, 1979.

[TN05] C. G. Thomas and P. Nithiarasu. Influences of element size and variable smoothing on inviscid compressible flow solution. *International Journal of Numerical Methods for Heat & Fluid Flow*, 15(5):420 – 428, 2005.

[TNB08] C. G. Thomas, P. Nithiarasu, and R. L. T. Bevan. The locally conservative galerkin (LCG) method for solving the incompressible Navier-Stokes equations. *International Journal for Numerical Methods in Fluids*, 57(12):1771–1792, 2008.

[UHH07a] R. Unger, M. C. Haupt, and P. Horst. Application of Lagrange multipliers for coupled problems in fluid and structural interactions. *Computers & Structures*, 85(11-14):796–809, 2007.

[UHH07b] R. Unger, M. C. Haupt, and P. Horst. Comparison of iterative solution procedures for fluid and structural interaction problems using two- and three-field approaches. In *Proceedings of the 2nd Conference on Coupled Problems*, Ibiza, Spain, 2007.

[UHHW08] R. Unger, M. C. Haupt, P. Horst, and J. Windte. Structural design and aeroelastic analysis of an oscillating airfoil for flapping wing propulsion. *AIAA-Paper 2008-306*, 2008.

[UKH+07] R. Unger, J. Kleinert, M. C. Haupt, P. Horst, J. Windte, S. Bansmer, C. J. Kaehler, and R. Radespiel. Design and analysis of an aeroelastic validation experiment for moving flexible airfoils. In *Proceedings of the First CEAS European Air and Space Conference*, Berlin, 2007.

[vB09] E. H. van Brummelen. Added mass effects of compressible and incompressible flows in fluid-structure interaction. *Journal of Applied Mechanics*, 76(2):021206–7, 2009.

[VLDV07] J. Vierendeels, L. Lanoye, J. Degroote, and P. Verdonck. Implicit coupling of partitioned fluid-structure interaction problems with reduced order models. *Computers & Structures*, 85(11-14):970–976, 2007.

[vZB05] A. H. van Zuijlen and H. Bijl. Implicit and explicit higher order time integration schemes for structural dynamics and fluid-structure interaction computations. *Computers & Structures*, 83(2-3):93–105, 2005.

[Was75] K. Washizu. *Variational methods in elasticity and plasticity*. International series of monographs on aeronautical sciences and spaceflight . 1. Division, Solid and structural mechanics. Pergamon Press, Oxford [u.a.], 2. ed edition, 1975.

[WC07] J. R. Wright and J. E. Cooper. *Introduction to aircraft aeroelasticity and loads*. John Wiley & Sons, 2007.

[Wil98] D. C. Wilcox. *Turbulence modeling for CFD*. Dcw Industries, Incorporated, 2nd edition, 1998.

[WR08] J. Windte and R. Radespiel. Propulsive efficiency of a moving airfoil at transitional low Reynolds numbers. *AIAA Journal*, 46(9):2165–2177, 2008.

[XA04] Z. Xu and M. Accorsi. Finite element mesh update methods for fluid-structure interaction simulations. *Finite Elements in Analysis and Design*, 40(9-10):1259–1269, 2004.

[YKW+07] W. Yuan, M. Khalid, J. Windte, U. Scholz, and R. Radespiel. Computational and experimental investigations of low-Reynolds-number flows past an aerofoil. *The Aeronautical Journal*, 111(1115):17–30, 2007.

[YLF63] E. C. Yates, N. S. Land, and J. T. Foughner. Measured and calculated subsonic and transonic flutter characteristics of a 45deg sweptback wing platform in air and freon-12 in the langley transonic dynamics tunnel. Technical Report D-1616, AGARD, 1963.

[ZBN05] O. C. Zienkiewicz, R. L. T. Bevan, and P. Nithiarasu. *The finite element method for fluid dynamics*. Elsevier Butterworth-Heinemann, Amsterdam, 6th ed. edition, 2005.

[ZC65] O. C. Zienkiewicz and Y. K. Cheung. Finite elements in the solution of field problems. *The Engineer*, 220:507–510, 1965.

[ZC95] O. C. Zienkiewicz and R. Codina. A general algorithm for compressible and incompressible flow - part I. the split, characteristic-based scheme. *International Journal for Numerical Methods in Fluids*, 20(8-9):869–885, 1995.

[ZMS+95] O. C. Zienkiewicz, K. Morgan, B. V. K. S. Sai, R. Codina, and M. Vasquez. A general algorithm for compressible and incompressible flow - part II. tests on the explicit form. *International Journal for Numerical Methods in Fluids*, 20(8-9):887–913, 1995.

[ZT05] O. C. Zienkiewicz and R. L. Taylor. *The finite element method for solid and structural mechanics*. Elsevier Butterworth-Heinemann, Amsterdam, 6th ed. edition, 2005.

[ZTSP03] O. C. Zienkiewicz, R. L. Taylor, S. J. Sherwin, and J. Peiro. On discontinuous Galerkin methods. *International Journal for Numerical Methods in Engineering*, 58(8):1119–1148, 2003.

[ZTZ05] O. C. Zienkiewicz, R. L. Taylor, and J. Z. Zhu. *The finite element method: Its basis and fundamentals*. Elsevier Butterworth-Heinemann, Amsterdam, 6th ed. edition, 2005.

A Appendix

A.1 Mathematical expressions

- scalar product of two vectors:

$$a = \boldsymbol{a}^T \boldsymbol{b} \tag{A.1.1}$$

- dyadic product of two vectors:

$$\boldsymbol{A} = \boldsymbol{a}\boldsymbol{b}^T \tag{A.1.2}$$

- gradient of a scalar value:

$$\boldsymbol{a} = \nabla a \tag{A.1.3}$$

- gradient of a vectorial value:

$$\boldsymbol{A} = \nabla \boldsymbol{a}^T \tag{A.1.4}$$

- divergence of a vectorial field:

$$a = \nabla^T \boldsymbol{a} \tag{A.1.5}$$

- divergence of a tensorial field:

$$\boldsymbol{a}^T = \nabla^T \boldsymbol{A} \tag{A.1.6}$$

- product rule with two scalars:

$$(ab)' = ab' + a'b \tag{A.1.7}$$

- product rule with a scalar and a vector using the nabla operator (gradient type):

$$\nabla(a\boldsymbol{b}^T) = a\nabla\boldsymbol{b}^T + (\nabla a)\boldsymbol{b}^T \tag{A.1.8}$$

- product rule with a scalar and a vector using the nabla operator (divergence type):

$$\nabla^T(a\boldsymbol{b}) = \boldsymbol{b}^T\nabla a + a\nabla^T\boldsymbol{b} \tag{A.1.9}$$

- product rule with two vectors using the nabla operator (gradient type):

$$\nabla(\boldsymbol{a}^T\boldsymbol{b}) = (\nabla\boldsymbol{b}^T)\boldsymbol{a} + (\nabla\boldsymbol{a}^T)\boldsymbol{b} \tag{A.1.10}$$

- product rule with two vectors using the nabla operator (divergence type):

$$\nabla^T(\boldsymbol{a}\boldsymbol{b}^T) = \boldsymbol{a}^T(\nabla\boldsymbol{b}^T) + \boldsymbol{b}^T(\nabla^T\boldsymbol{a}) \tag{A.1.11}$$

- Laplace operator:

$$(\nabla^T\nabla)a = \nabla^T(\nabla a) \tag{A.1.12}$$

A.2 Turbulence modeling with the CBS scheme in the ALE frame of reference

In chapter 3, the solution of laminar flow using the CBS scheme is discussed, i.e. a flow without vorticities, cross flows, or mixing between the flow layers. Laminar flows are characterized by a small Reynolds number *Re*. Turbulent flows, on the other hand, are unsteady, three-dimensional, contain vorticities, are dissipative due to mixing of flow layers with different momentum, fluctuate on broad range of length and time scales and are characterized by a high Reynolds number, [FP01]. To simulate such flows, the method of *one point closure* is used in this thesis, where the governing conservation equations are averaged in time or space leading to the Reynolds-averaged Navier-Stokes (RANS) equations. Using this approach, additional transport equations - turbulence models - need to be introduced and additionally computed. Such turbulence models are quite standard in computational fluid dynamics and can handle a broad range of fluid problems with adequate computational costs. Here, two turbulence models are investigated: first, the one-equation *Spalart-Allmaras (SA)* and secondly, two-equation *Menter's Baseline (Menter-BSL)* turbulence model. The transport equations of both models are again discretized using the CBS scheme. While the SA model is already in use in the context of the CBS scheme in [NL06, Liu05, Hic08] for steady and unsteady flow problems on fixed grids, to the author's knowledge the Menter-BSL model has been never used before in the context of the CBS scheme. Therefore, the principle ideas for turbulence modeling with the aid of the RANS equation using the ALE form are discussed in the next subsections.

A.2.1 Favre and Reynolds averaging of the governing equations

For a compressible flow, a pure time averaging (which is used here as Reynolds averaging)[1] would lead to more additional terms rather than a mixed form of time (Reynolds) and mass (Favre) averaging, [Bla06, Wil98]. Using the time averaging, a fluid quantity may be expressed as:

$$f = \overline{f} + f' \quad \text{with} \quad \overline{f} = \lim_{\Delta t_T \to \infty} \frac{1}{\Delta t_T} \int_t^{t+\Delta t_T} f \, dt \,, \tag{A.2.1}$$

where $\overline{f}$ is the mean quantity, f' is the turbulent fluctuation and Δt_T denotes a characteristic time interval. The mass averaging is defined as:

$$f = \tilde{f} + f'' \quad \text{with} \quad \tilde{f} = \frac{1}{\overline{\rho}_f} \lim_{\Delta t_T \to \infty} \frac{1}{\Delta t_T} \int_t^{t+\Delta t_T} \rho_f f \, dt = \frac{\overline{\rho_f f}}{\overline{\rho}_f} \,, \tag{A.2.2}$$

where $\tilde{f}$ is the mean and f'' denotes the turbulent fluctuation. The density and pressure are now Reynolds-averaged and the remaining flow variables are Favre-averaged, which results in the following Favre- and Reynolds averaged governing conservation equation of fluid flow in ALE frame of reference, see [Bla06, Wil98] for details:

[1] Indeed, three different forms of Reynolds averaging exist: 1. time averaging, 2. spatial averaging and 3. ensemble averaging [Bla06]

$$\frac{\partial \overline{\rho}_f}{\partial t} + \nabla^T(\overline{\rho}_f \tilde{\boldsymbol{v}}_f) - \tilde{\boldsymbol{w}}_f^T \nabla \overline{\rho}_f = 0 \tag{A.2.3}$$

$$\frac{\partial(\overline{\rho}_f \tilde{\boldsymbol{v}}_f)}{\partial t} + [\nabla^T(\overline{\rho}_f \tilde{\boldsymbol{v}}_f \tilde{\boldsymbol{v}}_f^T)]^T - [\tilde{\boldsymbol{w}}_f^T \nabla(\overline{\rho}_f \tilde{\boldsymbol{v}}_f^T)]^T = -\nabla \overline{p}_f + \mathcal{D}^T(\tilde{\boldsymbol{\tau}}_f + \boldsymbol{\tau}^F) + \overline{\rho}_f \hat{\boldsymbol{b}}_f \tag{A.2.4}$$

$$\begin{aligned}\frac{\partial(\overline{\rho}_f \overset{\circ}{e}_f)}{\partial t} + \nabla^T(\overline{\rho}_f \overset{\circ}{e}_f \tilde{\boldsymbol{v}}_f) - \tilde{\boldsymbol{w}}_f^T \nabla(\overline{\rho}_f \overset{\circ}{e}_f) = &-\nabla^T(\overline{p}_f \tilde{\boldsymbol{v}}_f) + \nabla^T[\tilde{\boldsymbol{Q}}_f^T(\tilde{\boldsymbol{\tau}}_f + \boldsymbol{\tau}^F)] \\ &+ \nabla^T(\kappa_f \nabla \tilde{T}_f - \boldsymbol{q}^F) + \overline{\rho}_f \hat{\boldsymbol{b}}_f^T \tilde{\boldsymbol{v}}_f + \nabla^T \boldsymbol{R}^F \,.\end{aligned} \tag{A.2.5}$$

Compared to the original governing conservative equations, these equations are extended by the Favre-averaged Reynolds stress vector $\boldsymbol{\tau}^F$, by the turbulent heat flux vector $\boldsymbol{q}^F$ and by a third order fluctuating term $\boldsymbol{R}^F$. The quantity $\overset{\circ}{e}_f$ is now the specific total energy including the turbulent kinetic energy k_f:

$$\begin{aligned}\overset{\circ}{e}_f &= \tilde{e}_f + k_f \\ &= \tilde{\epsilon}_f + \tfrac{1}{2}\tilde{\boldsymbol{v}}_f^T \tilde{\boldsymbol{v}}_f + k_f \,,\end{aligned} \tag{A.2.6}$$

where the turbulent kinetic energy is given as:

$$k_f = \frac{1}{2}\widetilde{\boldsymbol{v}_f''^T \boldsymbol{v}_f''} \,. \tag{A.2.7}$$

The term $\boldsymbol{R}^F$ consists of the molecular diffusion and the turbulent transport of the turbulent kinetic energy k_f [Bla06]. These both parts are neglected here, which is a valid approximation for flows with a Mach number up to supersonic range [Wil98]. To model the six components of $\boldsymbol{\tau}^F$ and three components of $\boldsymbol{q}^F$, different approaches exist and the eddy-viscosity hypothesis is here applied, which is described is the next subsection.

A.2.2 Eddy-viscosity hypothesis

The Favre-averaged Reynolds stress vector $\boldsymbol{\tau}^F$ in the above conservation equations arises due to fluctuation term $-(\overline{\rho}\widetilde{v_i'' v_j''})_f$, which is modeled by the Boussinesq eddy-viscosity hypothesis. This eddy-viscosity hypothesis assumes, that the Reynolds stress is related to the strain rate. Thus, the eddy-viscosity hypothesis reads:

$$\boldsymbol{\tau}^F = \mu_T \left(\boldsymbol{I}_0 - \tfrac{2}{3}\boldsymbol{m}\boldsymbol{m}^T\right)\mathcal{D}\tilde{\boldsymbol{v}}_f - \tfrac{2}{3}\boldsymbol{m}\overline{\rho}_f k_f \,, \tag{A.2.8}$$

where μ_T denotes the dynamic eddy viscosity, which has no primary physical meaning but is a function of the local flow properties and is therefore the main subject for turbulence modeling.

Accordingly, the turbulent heat flux vector $\boldsymbol{q}^F$ is modeled as:

$$\boldsymbol{q}^F = -\kappa_T \nabla \tilde{T}_f = -\mu_T \frac{c_p}{Pr_T} \nabla \tilde{T}_f \,, \tag{A.2.9}$$

where $\kappa_T = \mu_T c_p / Pr_T$ is the turbulent thermal conductivity and Pr_T denotes the turbulent Prandtl number, which is usually constant over the flow field ($Pr_T = 0.9$ for air). Therefore, using the eddy-viscosity hypothesis, the turbulence modeling reduces to the determination of one quantity (one point closure), namely μ_T. From the code-implementation point of view, only a few modifications to the laminar version of the code are needed. The non-dimensional conservation equations, where the mean quantity accents and the superscript $(\cdot)^\star$ are omitted for clarity, can be written as:

$$\frac{\partial \rho_f}{\partial t} + \nabla^T \boldsymbol{V}_f - \boldsymbol{w}_f^T \nabla \rho_f = 0 \tag{A.2.10}$$

$$\frac{\partial \boldsymbol{V}_f}{\partial t} + [\nabla^T (\boldsymbol{v}_f \boldsymbol{V}_f^T)]^T - [\boldsymbol{w}_f^T \nabla \boldsymbol{V}_f^T]^T = -\nabla p_f + \frac{\mu_f + \mu_T}{\mu_f Re} \mathcal{D}^T \boldsymbol{\tau}_f - \tfrac{2}{3} \nabla K_f + \rho_f \hat{\boldsymbol{b}}_f \tag{A.2.11}$$

$$\begin{aligned} \frac{\partial E_f}{\partial t} + \nabla^T (\boldsymbol{v}_f E_f) - \boldsymbol{w}_f^T \nabla E_f = -\nabla^T (p_f \boldsymbol{v}_f) + \frac{\mu_f + \mu_T}{\mu_f Re} \nabla^T (\boldsymbol{Q}_f^T \boldsymbol{\tau}_f) - \tfrac{2}{3} \nabla^T (K_f \boldsymbol{v}_f) \\ + \frac{1}{Re} \nabla^T \left[\left(\frac{\kappa_f}{Pr} + \frac{\mu_T}{Pr_T} \right) \nabla T_f \right] + \rho_f \hat{\boldsymbol{b}}_f^T \boldsymbol{v}_f \,. \end{aligned} \tag{A.2.12}$$

Here, the (non-dimensional) conservative turbulent kinetic energy $K_f = \rho_f k_f$ is introduced. Before the two turbulence models are discussed, the change in the original CBS scheme due to the averaging should be highlighted.

A.2.3 Turbulent CBS scheme

To consider the Favre and Reynolds averaging, the calculation of the intermediate momentum, Eq. (3.3.15), as well as the computation of the energy, Eq. (3.3.22), need to be modified, whereas the density/pressure equation, (3.3.17) and (3.3.18), as well as the momentum correction, (3.3.20), remains unchanged. With the procedure given in section 3.3, one can obtained for the calculation of the intermediate momentum:

$$\Delta \check{\mathbf{V}}_f = \mathbf{M}_v^{-1} \Delta t \left\{ \left[-\mathbf{C}_{sV} \mathbf{V}_f - \mathbf{K}_{\tau 2} \mathbf{v}_f - \tfrac{2}{3} \mathbf{G}^T \mathbf{K}_f + \mathbf{f}_{\tau 2} \right] + \Delta t \left[-\mathbf{K}_{sV} \mathbf{V}_f + \mathbf{K}_{pV} (\mathbf{p}_f - \tfrac{2}{3} \mathbf{K}_f) \right] \right\}^n \tag{A.2.13}$$

and for the computation of the energy:

$$\begin{aligned} \Delta \mathbf{E}_f = \mathbf{M}^{-1} \Delta t \Big\{ \Big[-\mathbf{C}_{sE} \mathbf{E}_f - \mathbf{C}_{vE} (\mathbf{p}_f - \tfrac{2}{3} \mathbf{K}_f) - \mathbf{K}_{\tau E2} \mathbf{v}_f - \mathbf{K}_{T2} \mathbf{T}_f + \mathbf{f}_{E2} \Big] \\ + \Delta t \Big[-\mathbf{K}_{sE} \mathbf{E}_f - \mathbf{K}_{vE} (\mathbf{p}_f - \tfrac{2}{3} \mathbf{K}_f) \Big] \Big\}^n \,, \end{aligned} \tag{A.2.14}$$

where $\mathbf{K}_f$ is the vector of the K_f values at the nodes of the mesh, The modified matrices are:

$$\mathbf{K}_{\tau 2} = \int_{\Omega_f} \mathbf{B}_\tau \frac{\mu_f + \mu_T}{Re} \left(\boldsymbol{I}_0 - \tfrac{2}{3} \boldsymbol{m} \boldsymbol{m}^T \right) \mathbf{B}_\tau \, d\Omega_f; \quad \mathbf{K}_{T2} = \int_{\Omega_f} (\nabla \mathbf{N})^T \frac{1}{Re} \left(\frac{\kappa_f}{Pr} + \frac{\mu_T}{Pr_T} \right) (\nabla \mathbf{N}) \, d\Omega_f;$$

$$\mathbf{f}_{\tau 2} = \int_{\Gamma_f} \mathbf{N}_v^T \boldsymbol{\Upsilon}^T \left[\frac{\mu_f + \mu_T}{Re} \left(\boldsymbol{I}_0 - \tfrac{2}{3} \boldsymbol{m} \boldsymbol{m}^T \right) \mathbf{B}_\tau \mathbf{v}_f \right] d\Gamma_f;$$

$$\mathbf{K}_{\tau E2} = \int_{\Omega_f} (\nabla \mathbf{N})^T \boldsymbol{Q}_f^T \frac{\mu_f + \mu_T}{Re} \left(\boldsymbol{I}_0 - \tfrac{2}{3} \boldsymbol{m} \boldsymbol{m}^T \right) \mathbf{B}_\tau \, d\Omega_f;$$

$$\mathbf{f}_{E2} = \int_{\Gamma_f} \mathbf{N}^T \frac{1}{Re} \left(\boldsymbol{Q}^T \left[(\mu_f + \mu_T) \left(\boldsymbol{I}_0 - \tfrac{2}{3} \boldsymbol{m} \boldsymbol{m}^T \right) \mathbf{B}_\tau \mathbf{v}_f \right] + \left(\frac{\kappa_f}{Pr} + \frac{\mu_T}{Pr_T} \right) (\nabla \mathbf{N}) \mathbf{T}_f \right)^T \boldsymbol{n} \, d\Gamma_f \,.$$

Further, using the turbulent CBS scheme for incompressible flows, an appropriate modification to the calculation of the artificial compressibility parameter β is needed, i.e. Eq. (3.4.3) transforms to:

$$\beta = \max(\varsigma_c, \, v_f^{\text{conv}}, \, v_f^{\text{diff}}) = \max \left(\varsigma_c, \, \sqrt{\boldsymbol{v}_f^T \boldsymbol{v}_f}, \, \frac{2(\nu_f + \nu_T)}{h \, Re} \right) , \tag{A.2.15}$$

where $\nu_T = \mu_T/\rho_f$ denotes the kinematic eddy viscosity. Thus, the diffusive velocity v_f^{diff} takes the modified kinematic viscosity into account. Accordingly, using the local time stepping scheme, the diffusive time step size Δt^{diff} from Eq. (3.4.10) is modified as:

$$\Delta t^{\text{diff}} = \frac{h^2 Re}{2(\nu_f + \nu_T)} \tag{A.2.16}$$

to take the modified local viscosity into account. Further and similar to section 3.5, a DG version of the turbulent CBS scheme can be designed likewise.

A.2.4 Determination of the eddy viscosity

The only additional quantities, which have to be calculated, are the eddy viscosity μ_T or ν_T and the turbulent kinetic energy k_f or K_f. While the latter one is sometimes simply omitted (e.g. when using the Spalart-Allmaras model) or results as a by-product of the turbulence model (e.g. in conjunction with almost all two-equation turbulence models), the calculation of the eddy viscosity (and adding it to laminar viscosity) is the only additional task using the turbulent CBS scheme. Different model levels for the turbulence exist: algebraic, one-equation, and two-equation turbulence models. The Spalart-Allmaras model is a representative of an one-equation while Menter's baseline model is a representative of a two-equation model. Both models use additional transport equations, which are then temporally discretized by the CBS scheme followed by a spatial discretization with the aid of finite elements.

A.2.4.1 Spalart-Allmaras model

The Spalart-Allmaras (SA) turbulence model is widely used for aerospace application and incompressible flows. The SA model uses directly a transport equation for a modified eddy viscosity. Thus, the turbulent kinetic energy in the discretized momentum and energy equation, (A.2.13) and (A.2.14) is omitted, i.e. $\mathbf{K}_f = \mathbf{0}$. Adapted from [DLR09, SR07], the transport equation for the modified eddy viscosity $\breve{\nu}$ with variable density and for the ALE frame of reference can be written as:

$$\begin{aligned}\frac{\partial(\rho_f\breve{\nu})}{\partial t} + \nabla^T(\rho_f\breve{\nu}\boldsymbol{v}_f) - \boldsymbol{w}_f^T\nabla(\rho_f\breve{\nu}) = C_{b1}(1-f_{t2})\breve{S}\rho_f\breve{\nu} - \left(C_{w1}f_w - \frac{C_{b1}}{C_\kappa^2}f_{t2}\right)\rho_f\left(\frac{\breve{\nu}}{d_w}\right)^2 \\ + \frac{1}{C_\sigma^\nu}\Big[\nabla^T(\mu_f + \rho_f\breve{\nu})\nabla\breve{\nu} + C_{b2}\rho_f(\nabla\breve{\nu})^T(\nabla\breve{\nu})\Big],\end{aligned} \tag{A.2.17}$$

where:

$$\begin{gathered}\breve{S} = |\nabla\times\boldsymbol{v}_f| + \frac{\breve{\nu}}{C_\kappa^2 d_w^2}f_{v2}; \quad f_{v2} = 1 - \frac{\varpi}{1+\varpi f_{v1}}; \quad f_{v1} = \frac{\varpi^3}{\varpi^3 + C_{v1}^3}; \quad \varpi = \frac{\breve{\nu}}{\nu_f}; \\ f_w = g\left(\frac{1+C_{w3}^6}{g^6+C_{w3}^6}\right)^{1/6}; \quad g = r + C_{w2}(r^6 - r); \quad r = \min\left(\frac{\breve{\nu}}{\breve{S}C_\kappa^2 d_w^2}, 10\right); \\ f_{t2} = C_{t3}\exp(-C_{t4}\varpi^2)\,.\end{gathered} \tag{A.2.18}$$

In the above set of parameters, d_w denotes the shortest distance from a node to the nearest solid wall, $\nabla\times\boldsymbol{v}_f$ is the vorticity and $\breve{S}$ is a modified vorticity. The constants used for this model are:

$$\begin{gathered}C_{b1} = 0.1355; \quad C_{b2} = 0.622; \quad C_\sigma^\nu = \tfrac{2}{3}; \quad C_\kappa = 0.41; \quad C_{v1} = 7.1; \\ C_{w1} = \frac{C_{b1}}{C_\kappa^2} + \frac{1+C_{b2}}{C_\sigma^\nu}; \quad C_{w2} = 0.3; \quad C_{w3} = 2; \quad C_{t3} = 1.3; \quad C_{t4} = 0.5;\end{gathered} \tag{A.2.19}$$

and the turbulent kinematic and dynamic eddy viscosity are finally calculated as:

$$\nu_T = \breve{\nu} f_{v1}; \qquad \mu_T = \rho_f \nu_T = \rho_f \breve{\nu} f_{v1} = \breve{\mu} f_{v1} \,. \tag{A.2.20}$$

Boundary conditions for SA model can be applied at the inlet or farfield with a value of 10% of the prescribed value for the laminar viscosity, which in turn can be evaluated from Sutherland's law (2.4.52):

$$\breve{\nu} = \hat{\breve{\nu}} = 0.1 \nu_f(T_f) \quad \text{on} \quad \Gamma_f^{D,far} \,. \tag{A.2.21}$$

This value is also given as initial conditions:

$$\breve{\nu}(\boldsymbol{x}_f, t = 0) = \hat{\breve{\nu}}^0(\boldsymbol{x}_f) = 0.1 \nu_f(\boldsymbol{x}_f, T_f) \,. \tag{A.2.22}$$

On solid walls the modified eddy viscosity is set to zero:

$$\breve{\nu} = \hat{\breve{\nu}} = 0 \quad \text{on} \quad \Gamma_f^{D,wall} \,. \tag{A.2.23}$$

Non-dimensionalization according to Table 3.1 and application of Eq. (3.1.3), the Galerkin form of Eq. (A.2.17) is obtained as:

$$\begin{aligned}
\int_{\Omega_f} \mathbf{N}^T \Delta\breve{\mu} \, d\Omega_f = -\Delta t \Bigg\{ & \int_{\Omega_f} \mathbf{N}^T \nabla^T (\boldsymbol{v}_f \breve{\mu}) \, d\Omega_f - \int_{\Omega_f} \mathbf{N}^T \boldsymbol{w}_f^T \nabla\breve{\mu} \, d\Omega_f \\
& + \int_{\Omega_f} (\nabla \mathbf{N})^T \left(\frac{\mu_f + \breve{\mu}}{C_\sigma^\nu Re} \right) \nabla\breve{\nu} \, d\Omega_f - \int_{\Omega_f} \mathbf{N}^T \frac{C_{b2}\rho_f}{C_\sigma^\nu Re} (\nabla\breve{\nu})^T (\nabla\breve{\nu}) \, d\Omega_f \\
& - \int_{\Omega_f} \mathbf{N}^T \left[C_{b1}(1 - f_{t2}) \breve{S} - \left(C_{w1} f_w - \frac{C_{b1}}{C_\kappa^2} f_{t2} \right) \frac{\breve{\nu}}{d_w^2 Re} \right] \breve{\mu} \, d\Omega_f \\
& - \int_{\Gamma_f} \mathbf{N}^T \left(\frac{\mu_f + \breve{\mu}}{C_\sigma^\nu Re} \right) (\nabla\breve{\nu})^T \boldsymbol{n} \, d\Gamma_f \Bigg\}^n \\
+ \frac{\Delta t^2}{2} \Bigg\{ & - \int_{\Omega_f} (\boldsymbol{s}_f^T \nabla) \mathbf{N}^T \nabla^T (\boldsymbol{v}_f \breve{\mu}) \, d\Omega_f + \int_{\Omega_f} (\boldsymbol{s}_f^T \nabla) \mathbf{N}^T (\boldsymbol{w}_f^T \nabla\breve{\mu}) \, d\Omega_f \\
& - \int_{\Omega_f} \mathbf{N}^T (\boldsymbol{s}_f^T \nabla) \left[C_{b1}(1 - f_{t2}) \breve{S} - \left(C_{w1} f_w - \frac{C_{b1}}{C_\kappa^2} f_{t2} \right) \frac{\breve{\nu}}{d_w^2 Re} \right] \breve{\mu} \, d\Omega_f \Bigg\}^n ,
\end{aligned} \tag{A.2.24}$$

where integration by parts on second-order term is used and the $1/Re$ coefficients result from the non-dimensionalization procedure. Consistent with the equation of momentum and energy conservation, $\breve{\mu} = \rho_f \breve{\nu}$ is introduced as the primary variable. Further, it should be noted at this point, that due to non-dimensionalization the following quantities need a modified calculation:

$$\breve{S} = |\nabla \times \boldsymbol{v}_f| + \frac{\breve{\nu}}{Re C_\kappa^2 d_w^2} f_{v2}; \quad r = \min\left(\frac{\breve{\nu}}{Re \breve{S} C_\kappa^2 d_w^2}, 10 \right) . \tag{A.2.25}$$

By replacing the continuous fields with the approximations of Eq. (3.3.11) and with $\breve{\mu} = \mathbf{N}\boldsymbol{\breve{\mu}}$, the final matrix form of Eq. (A.2.24) can be written as:

$$\Delta\boldsymbol{\breve{\mu}} = \mathbf{M}^{-1} \Delta t \Big[(-\mathbf{C}_{s\breve{\mu}} \boldsymbol{\breve{\mu}} - \mathbf{K}_{\breve{\mu}} \boldsymbol{\breve{\nu}} + \mathbf{M}_{\breve{\mu}} \boldsymbol{\breve{\mu}} + \mathbf{f}_{\breve{\nu}\Omega} + \mathbf{f}_{\breve{\nu}\Gamma}) + \Delta t (-\mathbf{K}_{s\breve{\mu}} \boldsymbol{\breve{\mu}} - \mathbf{C}_{s\breve{\mu}2} \boldsymbol{\breve{\mu}}) \Big]^n , \tag{A.2.26}$$

with the matrices and vectors:

$$\mathbf{C}_{s\breve{\mu}} = \mathbf{C}_{sE} \quad \mathbf{K}_{\breve{\mu}} = \int_{\Omega_f} (\nabla \mathbf{N})^T \left(\frac{\mu_f + \breve{\mu}}{C_\sigma^\nu Re} \right) (\nabla \mathbf{N})\, d\Omega_f; \quad \mathbf{f}_{\breve{\nu}\Omega} = \int_{\Omega_f} \mathbf{N}^T \frac{C_{b2}\rho_f}{C_\sigma^\nu Re} (\nabla \breve{\nu})^T (\nabla \breve{\nu})\, d\Omega_f;$$

$$\mathbf{K}_{s\breve{\mu}} = \mathbf{K}_{sE} \quad \mathbf{M}_{\breve{\mu}} = \int_{\Omega_f} \mathbf{N}^T \left[C_{b1}(1 - f_{t2})\breve{S} - \left(C_{w1} f_w - \frac{C_{b1}}{C_\kappa^2} f_{t2} \right) \frac{\breve{\nu}}{d_w^2 Re} \right] \mathbf{N}\, d\Omega_f;$$

$$\mathbf{f}_{\breve{\nu}\Gamma} = \int_{\Gamma_f} \mathbf{N}^T \left(\frac{\mu_f + \breve{\mu}}{C_\sigma^\nu Re} (\nabla \mathbf{N}) \breve{\boldsymbol{\nu}} \right)^T \boldsymbol{n}\, d\Gamma_f;$$

$$\mathbf{C}_{s\breve{\mu}2} = \frac{1}{2} \int_{\Omega_f} \mathbf{N}^T \left[C_{b1}(1 - f_{t2})\breve{S} - \left(C_{w1} f_w - \frac{C_{b1}}{C_\kappa^2} f_{t2} \right) \frac{\breve{\nu}}{d_w^2 Re} \right] \mathbf{L}_s\, d\Omega_f\,.$$

This equation is additionally solved in each step of the iteration after the energy equation. Further, a matrix free scheme can be obtained by inverting the lumped mass matrix $\mathbf{M}_L$ instead of $\mathbf{M}$. Also, the residual smoothing procedure and the local time stepping can be applied. For unsteady flow problems, a real time term added to Eq. (A.2.26) resulting in:

$$\Delta\breve{\boldsymbol{\mu}} = \mathbf{M}^{-1}\Delta t \Big[(-\mathbf{C}_{s\breve{\mu}}\breve{\boldsymbol{\mu}} - \mathbf{K}_{\breve{\mu}}\breve{\boldsymbol{\nu}} + \mathbf{M}_{\breve{\mu}}\breve{\boldsymbol{\mu}} + \mathbf{f}_{\breve{\nu}\Omega} + \mathbf{f}_{\breve{\nu}\Gamma}) + \Delta t(-\mathbf{K}_{s\breve{\mu}}\breve{\boldsymbol{\mu}} - \mathbf{C}_{s\breve{\mu}2}\breve{\boldsymbol{\mu}}) \Big]^n - \frac{\Delta t}{\Delta t^R} \Delta\breve{\boldsymbol{\mu}}^R\,, \quad \text{(A.2.27)}$$

where $\Delta\breve{\boldsymbol{\mu}}^R$ is again approximated with a second order backward difference as:

$$\Delta\breve{\boldsymbol{\mu}}^R = \frac{3}{2}\breve{\boldsymbol{\mu}}^n - 2\breve{\boldsymbol{\mu}}^m + \frac{1}{2}\breve{\boldsymbol{\mu}}^{m-1}\,. \quad \text{(A.2.28)}$$

The DG version of this matrix system is again obtained by an additional integration by parts applied on the convective term, which allows breaking the standard finite element assembly. This integration by parts introduces an extra element edge flux, which ensures the element-by-element linking. Thus, according to section 3.5, the DG-CBS version of the Spalart-Allmaras turbulence reads:

$$\Delta\breve{\boldsymbol{\mu}} = \mathbf{M}^{e,-1}\Delta t \Big[(\mathbf{C}^e_{s\breve{\mu}}\breve{\boldsymbol{\mu}} - \mathbf{K}^e_{\breve{\mu}}\breve{\boldsymbol{\nu}} + \mathbf{M}^e_{\breve{\mu}}\breve{\boldsymbol{\mu}} - \mathbf{f}^e_{s\breve{\mu}} + \mathbf{f}^e_{\breve{\nu}\Omega} + \mathbf{f}^e_{\breve{\nu}\Gamma}) + \Delta t(-\mathbf{K}^e_{s\breve{\mu}}\breve{\boldsymbol{\mu}} - \mathbf{C}^e_{s\breve{\mu}2}\breve{\boldsymbol{\mu}}) \Big]^n\,, \quad \text{(A.2.29)}$$

where the matrices and vectors are:

$$\mathbf{C}^e_{s\breve{\mu}} = \mathbf{C}^e_{sE} \quad \mathbf{K}^e_{\breve{\mu}} = \int_{\Omega^e_f} (\nabla \mathbf{N})^T \left(\frac{\mu_f + \breve{\mu}}{C_\sigma^\nu Re} \right) (\nabla \mathbf{N})\, d\Omega^e_f; \quad \mathbf{f}_{\breve{\nu}\Omega} = \int_{\Omega^e_f} \mathbf{N}^T \frac{C_{b2}\rho_f}{C_\sigma^\nu Re} (\nabla \breve{\nu})^T (\nabla \breve{\nu})\, d\Omega^e_f;$$

$$\mathbf{K}^e_{s\breve{\mu}} = \mathbf{K}^e_{sE} \quad \mathbf{M}^e_{\breve{\mu}} = \int_{\Omega^e_f} \mathbf{N}^T \left[C_{b1}(1 - f_{t2})\breve{S} - \left(C_{w1} f_w - \frac{C_{b1}}{C_\kappa^2} f_{t2} \right) \frac{\breve{\nu}}{d_w^2 Re} \right] \mathbf{N}\, d\Omega^e_f;$$

$$\mathbf{f}^e_{s\breve{\mu}} = \int_{\Omega^e_f} \mathbf{N}^T (\boldsymbol{s}_f^T \boldsymbol{n}) \mathbf{N}\breve{\boldsymbol{\mu}}\, d\Gamma^e_f; \quad \mathbf{f}^e_{\breve{\nu}\Gamma} = \int_{\Gamma^e_f} \mathbf{N}^T \frac{\mu_f + \breve{\mu}}{C_\sigma^\nu Re} \boldsymbol{n}^T \mathbf{N}_v \breve{\boldsymbol{\nu}}_{\boldsymbol{x}}\, d\Gamma^e_f;$$

$$\mathbf{C}^e_{s\breve{\mu}2} = \frac{1}{2} \int_{\Omega^e_f} \mathbf{N}^T \left[C_{b1}(1 - f_{t2})\breve{S} - \left(C_{w1} f_w - \frac{C_{b1}}{C_\kappa^2} f_{t2} \right) \frac{\breve{\nu}}{d_w^2 Re} \right] \mathbf{L}_s\, d\Omega^e_f\,.$$

Again, this matrix system is solved on element level, i.e. such system is computed for each element. The additional element edge flux $\mathbf{f}^e_{s\breve{\mu}}$ ensures the element-by-element linking and $\mathbf{f}^e_{\breve{\nu}\Gamma}$ is modified to design a local conservative scheme, where, according to section 3.5.2, the nodal derivative $\breve{\boldsymbol{\nu}}_{\boldsymbol{x}}$ needs to be calculated in an extra post-processing step.

A.2.4.2 k-ω baseline (BSL) and shear stress transport (SST) model of Menter

As a representative of a two-equation turbulence model, Menter's baseline model is chosen here. Due to its similarity, the shear stress transport model of Menter can also be incorporated with minor modifications and is therefore also introduced.

Both models are a combination of the classical k-ω model of Wilcox, [Wil98], and the k-ε model, [JL72]. While the k-ω model is used for the inner part of the boundary layer, the k-ε model transformed to a k-ω representation is used for the outer part of the boundary layer. The transition from one to the other model is done by a blending function, which weights the coefficients of each model. Adapted from [Men93, DLR09, Bla06], the transport equation for the turbulent kinetic energy k_f and the specific turbulent dissipation ω_f with variable density and for the ALE frame of reference can be written as:

$$\begin{aligned}\frac{\partial(\rho_f k_f)}{\partial t} + \nabla^T(\rho_f k_f \boldsymbol{v}_f) - \boldsymbol{w}_f^T \nabla(\rho_f k_f) = \nabla^T(\mu_f + \acute{C}_\sigma^k \mu_T)\nabla k_f + (\mathcal{D}\boldsymbol{v}_f)^T \boldsymbol{\tau}^F \\ - C_\beta^k \rho_f \omega_f k_f\end{aligned} \tag{A.2.30}$$

$$\begin{aligned}\frac{\partial(\rho_f \omega_f)}{\partial t} + \nabla^T(\rho_f \omega_f \boldsymbol{v}_f) - \boldsymbol{w}_f^T \nabla(\rho_f \omega_f) = \nabla^T(\mu_f + \acute{C}_\sigma^\omega \mu_T)\nabla \omega_f \\ + \frac{\acute{C}_\gamma}{\nu_T}(\mathcal{D}\boldsymbol{v}_f)^T \boldsymbol{\tau}^F - \acute{C}_\beta^\omega \rho_f \omega_f^2 \\ + 2\rho_f(1-F_1)\, C_{\sigma 2}^\omega\, \omega_f^{-1} (\nabla k_f)^T (\nabla \omega_f)\,,\end{aligned} \tag{A.2.31}$$

where all coefficients with a $\acute{(\cdot)}$ are subject to weight with a blending function F_1:

$$\acute{f} = F_1 f_1 + (1 - F_1) f_2\,. \tag{A.2.32}$$

For the inner part of the boundary layer, set 1 is used with:

$$C_{\sigma 1}^k = 0.5; \quad C_{\sigma 1}^\omega = 0.5; \quad C_{\beta 1}^\omega = 0.075; \quad C_{\gamma 1} = C_{\beta 1}^\omega / C_\beta^k - C_{\sigma 1}^\omega C_\kappa^2 / \sqrt{C_\beta^k}; \tag{A.2.33}$$

whereas for the outer part of the boundary layer, set 2 is used with:

$$C_{\sigma 2}^k = 1.0; \quad C_{\sigma 2}^\omega = 0.856; \quad C_{\beta 2}^\omega = 0.0828; \quad C_{\gamma 2} = C_{\beta 2}^\omega / C_\beta^k - C_{\sigma 2}^\omega C_\kappa^2 / \sqrt{C_\beta^k}; \tag{A.2.34}$$

where the constant coefficients are:

$$C_\beta^k = 0.09; \quad C_\kappa = 0.41\,. \tag{A.2.35}$$

The blending function is calculated as:

$$\begin{aligned}F_1 = \tanh(arg_1^4); \quad arg_1 = \min\left[\max\left(\frac{\sqrt{k_f}}{C_\beta^k \omega_f d_w}; \frac{500\nu_f}{\omega_f d_w^2}\right); \frac{4\rho_f C_{\sigma 2}^\omega k_f}{CD_{k\omega}\, d_w^2}\right]; \\ CD = \max\left(2\rho_f\, C_{\sigma 2}^\omega\, \omega_f^{-1} (\nabla k_f)^T (\nabla \omega_f); 10^{-20}\right);\end{aligned} \tag{A.2.36}$$

Finally, the turbulent eddy viscosity is computed as:

$$\nu_T = \frac{k_f}{\omega_f}; \quad \mu_T = \rho_f \nu_t = \frac{\rho_f k_f}{\omega_f}\,. \tag{A.2.37}$$

A further improvement of the baseline model is the SST model, [Men93]. The difference to the baseline model is the parameter $C_{\sigma 1}^k$, which changes to $C_{\sigma 1}^k = 0.85$. Furthermore, a shear stress correction is introduced, which results in modified calculation of the turbulent eddy viscosity:

$$\nu_T = \min\left(\frac{k_f}{\omega_f}; \frac{0.31\rho_f k_f}{F_2\,|\nabla \times \boldsymbol{v}_f|}\right), \tag{A.2.38}$$

where

$$F_2 = \tanh(arg_2^2); \quad arg_2 = \max\left(2\frac{\sqrt{k_f}}{C_\beta^k \omega_f d_w}; \frac{500\nu_f}{\omega_f d_w^2}\right). \tag{A.2.39}$$

The boundary conditions for the turbulent kinetic energy and the specific dissipation on the solid walls are:

$$k_f = \hat{k}_f = 0; \quad \omega_f = \hat{\omega}_f = 10\frac{6\mu_f}{\rho_f C_{\beta 1}^\omega d_1^2}; \quad \text{on} \quad \Gamma_f^{D,wall}, \tag{A.2.40}$$

where d_1 is the distance from the first node from the wall. On the farfield boundary the conditions are:

$$\begin{gathered}\omega_f = \hat{\omega}_f = C_\infty^\omega \frac{v_\infty}{l_\Omega} = \omega_\infty; \quad \nu_T = \hat{\nu}_T = 10^{-3}\nu_\infty = \nu_{T,\infty}; \\ k_f = \hat{k}_f = \nu_{T,\infty}\omega_\infty = k_\infty; \quad \text{on} \quad \Gamma_f^{D,far},\end{gathered} \tag{A.2.41}$$

where C_∞^ω is a constant, which lies in the range from 1 to 10 and l_Ω denotes the length of the computational domain. The values for the farfield boundary are also used as initial conditions.

Non-dimensionalization according to Table 3.1 and application of Eq. (3.1.3), the Galerkin form from Eq. (A.2.30) is obtained as:

$$\begin{aligned}\int_{\Omega_f} \mathbf{N}^T \Delta K_f \, d\Omega_f = -\Delta t \Bigg\{ & \int_{\Omega_f} \mathbf{N}^T \nabla^T (\boldsymbol{v}_f K_f) \, d\Omega_f - \int_{\Omega_f} \mathbf{N}^T \boldsymbol{w}_f^T \nabla K_f \, d\Omega_f \\ & + \int_{\Omega_f} (\nabla \mathbf{N})^T \left(\frac{\mu_f + \acute{C}_\sigma^k \mu_T}{Re}\right) \nabla k_f \, d\Omega_f - \int_{\Omega_f} \mathbf{N}^T (\mathcal{D}\boldsymbol{v}_f)^T \boldsymbol{\tau}^F \, d\Omega_f \\ & + \int_{\Omega_f} \mathbf{N}^T C_\beta^k \omega_f K_f \, d\Omega_f - \int_{\Gamma_f} \mathbf{N}^T \left(\frac{\mu_f + \acute{C}_\sigma^k \mu_T}{Re}\right) (\nabla k_f)^T \boldsymbol{n} \, d\Gamma_f \Bigg\}^n \\ + \frac{\Delta t^2}{2} \Bigg\{ & - \int_{\Omega_f} (\boldsymbol{s}_f^T \nabla) \mathbf{N}^T \nabla^T (\boldsymbol{v}_f K_f) \, d\Omega_f + \int_{\Omega_f} (\boldsymbol{s}_f^T \nabla) \mathbf{N}^T (\boldsymbol{w}_f^T \nabla K_f) \, d\Omega_f \\ & - \int_{\Omega_f} \mathbf{N}^T (s_f^T \nabla) C_\beta^k \omega_f K_f \, d\Omega_f \Bigg\}^n,\end{aligned} \tag{A.2.42}$$

Similar, the Galerkin form of Eq. (A.2.31) is:

$$\begin{aligned}\int_{\Omega_f} \mathbf{N}^T \Delta\breve{\omega}_f \, d\Omega_f = -\Delta t \Bigg\{ & \int_{\Omega_f} \mathbf{N}^T \nabla^T (\boldsymbol{v}_f \breve{\omega}_f) \, d\Omega_f - \int_{\Omega_f} \mathbf{N}^T \boldsymbol{w}_f^T \nabla \breve{\omega}_f \, d\Omega_f \\ & + \int_{\Omega_f} (\nabla \mathbf{N})^T \left(\frac{\mu_f + \acute{C}_\sigma^\omega \mu_T}{Re} \right) \nabla \omega_f \, d\Omega_f - \int_{\Omega_f} \mathbf{N}^T \frac{\acute{C}_\gamma}{\nu_T} (\mathcal{D}\boldsymbol{v}_f)^T \boldsymbol{\tau}^F \, d\Omega_f \\ & + \int_{\Omega_f} \mathbf{N}^T C_\beta^\omega \, \omega_f \breve{\omega}_f \, d\Omega_f - \int_{\Gamma_f} \mathbf{N}^T \left(\frac{\mu_f + \acute{C}_\sigma^\omega \mu_T}{Re} \right) (\nabla \omega_f)^T \boldsymbol{n} \, d\Gamma_f \\ & - \int_{\Omega_f} \mathbf{N}^T 2\rho_f (1 - F_1) \, C_{\sigma 2}^\omega \, \omega_f^{-1} (\nabla k_f)^T (\nabla \omega_f) \, d\Omega_f \Bigg\}^n \\ + \frac{\Delta t^2}{2} \Bigg\{ & - \int_{\Omega_f} (\boldsymbol{s}_f^T \nabla) \mathbf{N}^T \nabla^T (\boldsymbol{v}_f \breve{\omega}_f) \, d\Omega_f + \int_{\Omega_f} (\boldsymbol{s}_f^T \nabla) \mathbf{N}^T (\boldsymbol{w}_f^T \nabla \breve{\omega}_f) \, d\Omega_f \\ & - \int_{\Omega_f} \mathbf{N}^T (s_f^T \nabla) C_\beta^\omega \, \omega_f \breve{\omega}_f \, d\Omega_f \Bigg\}^n . \end{aligned} \tag{A.2.43}$$

Again, integration by parts on second order terms is carried out and $K_f = \rho_f k_f$ and $\breve{\omega}_f = \rho_f \omega_f$ is introduced as primary variables. The final matrix form of Eq. (A.2.42) can then be written as:

$$\Delta \mathbf{K}_f = \mathbf{M}^{-1} \Delta t \Big[(-\mathbf{C}_{sK} \mathbf{K}_f - \mathbf{K}_K \mathbf{k}_f - \mathbf{M}_K \mathbf{K}_f + \mathbf{f}_{K\Omega} + \mathbf{f}_{k\Gamma}) + \Delta t (-\mathbf{K}_{sK} \mathbf{K}_f - \mathbf{C}_{sK2} \mathbf{K}_f) \Big]^n , \tag{A.2.44}$$

and of Eq. (A.2.43) as:

$$\Delta \breve{\boldsymbol{\omega}}_f = \mathbf{M}^{-1} \Delta t \Big[(-\mathbf{C}_{s\breve{\omega}} \breve{\boldsymbol{\omega}}_f - \mathbf{K}_{\breve{\omega}} \boldsymbol{\omega}_f - \mathbf{M}_{\breve{\omega}} \breve{\boldsymbol{\omega}}_f + \mathbf{f}_{\breve{\omega}\Omega} + \mathbf{f}_{\omega\Gamma} + \mathbf{f}_{K\breve{\omega}}) + \Delta t (-\mathbf{K}_{s\breve{\omega}} \breve{\boldsymbol{\omega}}_f - \mathbf{C}_{s\breve{\omega}2} \breve{\boldsymbol{\omega}}_f) \Big]^n , \tag{A.2.45}$$

where the matrices and vectors are:

$$\mathbf{K}_K = \int_{\Omega_f} (\nabla \mathbf{N})^T \left(\frac{\mu_f + \acute{C}_\sigma^k \mu_T}{Re} \right) (\nabla \mathbf{N}) \, d\Omega_f ; \quad \mathbf{K}_{\breve{\omega}} = \int_{\Omega_f} (\nabla \mathbf{N})^T \left(\frac{\mu_f + \acute{C}_\sigma^\omega \mu_T}{Re} \right) (\nabla \mathbf{N}) \, d\Omega_f ;$$

$$\mathbf{K}_{sK} = \mathbf{K}_{s\breve{\omega}} = \mathbf{K}_{sE} \quad \mathbf{M}_K = \int_{\Omega_f} \mathbf{N}^T (C_\beta^k \omega_f) \mathbf{N} \, d\Omega_f ; \quad \mathbf{M}_{\breve{\omega}} = \int_{\Omega_f} \mathbf{N}^T (C_\beta^\omega \omega_f) \mathbf{N} \, d\Omega_f ;$$

$$\mathbf{f}_{k\Gamma} = \int_{\Gamma_f} \mathbf{N}^T \left(\frac{\mu_f + \acute{C}_\sigma^k \mu_T}{Re} (\nabla \mathbf{N}) \mathbf{k}_f \right)^T \boldsymbol{n} \, d\Gamma_f ; \quad \mathbf{f}_{\omega\Gamma} = \int_{\Gamma_f} \mathbf{N}^T \left(\frac{\mu_f + \acute{C}_\sigma^\omega \mu_T}{Re} (\nabla \mathbf{N}) \boldsymbol{\omega}_f \right)^T \boldsymbol{n} \, d\Gamma_f ;$$

$$\mathbf{C}_{sK} = \mathbf{C}_{s\breve{\omega}} = \mathbf{C}_{sE} ; \quad \mathbf{f}_{K\Omega} = \int_{\Omega_f} \mathbf{N}^T (\mathcal{D}\boldsymbol{v}_f)^T \boldsymbol{\tau}^F \, d\Omega_f ; \quad \mathbf{f}_{\breve{\omega}\Omega} = \int_{\Omega_f} \mathbf{N}^T \frac{\acute{C}_\gamma}{\nu_T} (\mathcal{D}\boldsymbol{v}_f)^T \boldsymbol{\tau}^F \, d\Omega_f ;$$

$$\mathbf{C}_{sK2} = \int_{\Omega_f} \mathbf{N}^T C_\beta^k \, \omega_f \mathbf{L}_s \, d\Omega_f ; \quad \mathbf{C}_{s\breve{\omega}2} = \int_{\Omega_f} \mathbf{N}^T C_\beta^\omega \, \omega_f \mathbf{L}_s \, d\Omega_f ;$$

$$\mathbf{f}_{K\breve{\omega}} = \int_{\Omega_f} \mathbf{N}^T 2\rho_f (1 - F_1) \, C_{\sigma 2}^\omega \, \omega_f^{-1} (\nabla k_f)^T (\nabla \omega_f) \, d\Omega_f .$$

These both equations are solved in each time step after the energy equation. For unsteady problems, the real time terms according to section 3.4.6 are added to the above matrix equations. Local time stepping, residual smoothing and mass matrix diagonalization can also be used here. Furthermore, a discontinuous version of this matrix system is obtained by an additional integration by parts on the convective terms to remove the standard finite element assembly.

A.3 Additional panel flutter results

Additionally to results presented in section 7.4, panel flutter results in for the nine combinations of $Ma_\infty = (1.04, 1.08, 1.12)$ and $r_m = (0.05, 0.1, 0.2)$ are depicted in the following figures. In each of the figures, the reduced frequency K, the reduced period $1/K$ as well as the value of the upper and lower panel midpoint deflection and the resulting amplitude and mean are plotted over the non-dimensional pressure.

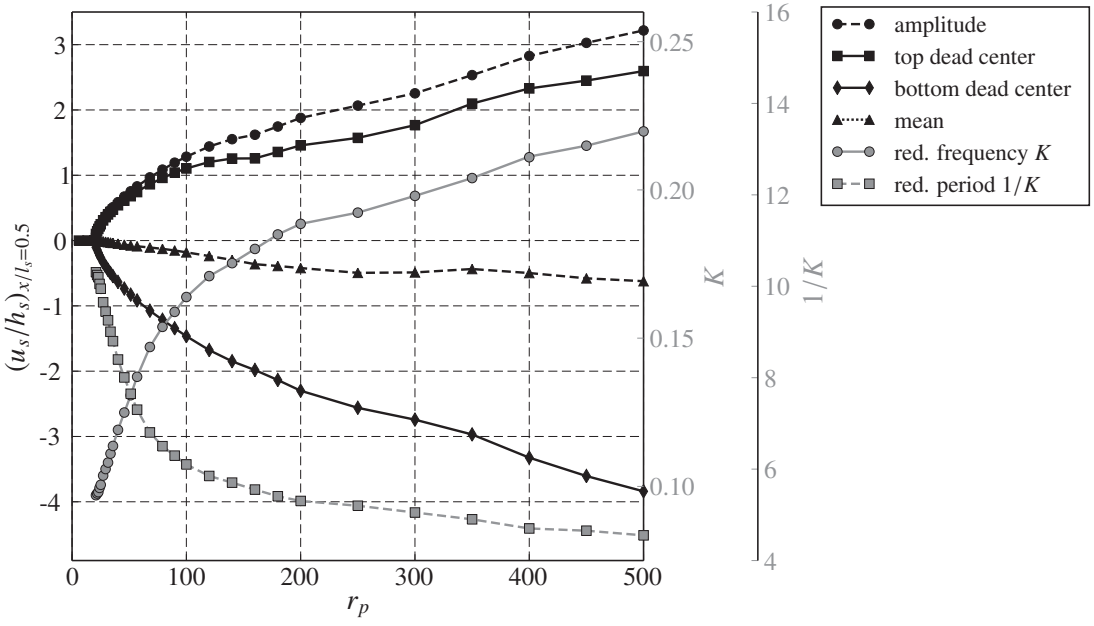

Figure A.1: LCO of the panel at $Ma_\infty = 1.04$, $r_m = 0.05$

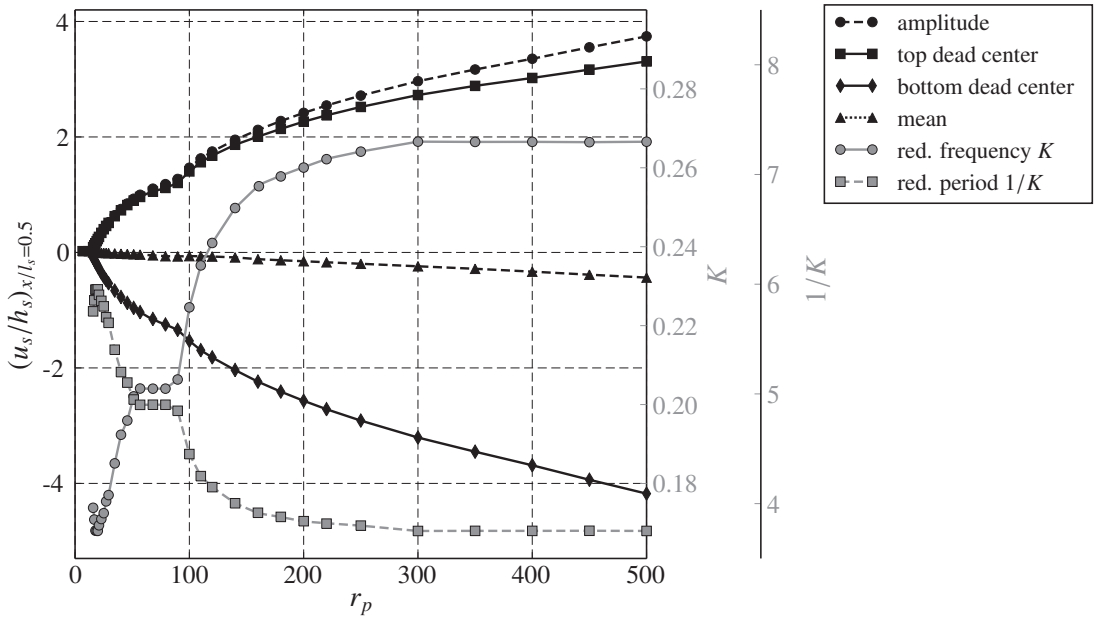

Figure A.2: LCO of the panel at $Ma_\infty = 1.08$, $r_m = 0.05$

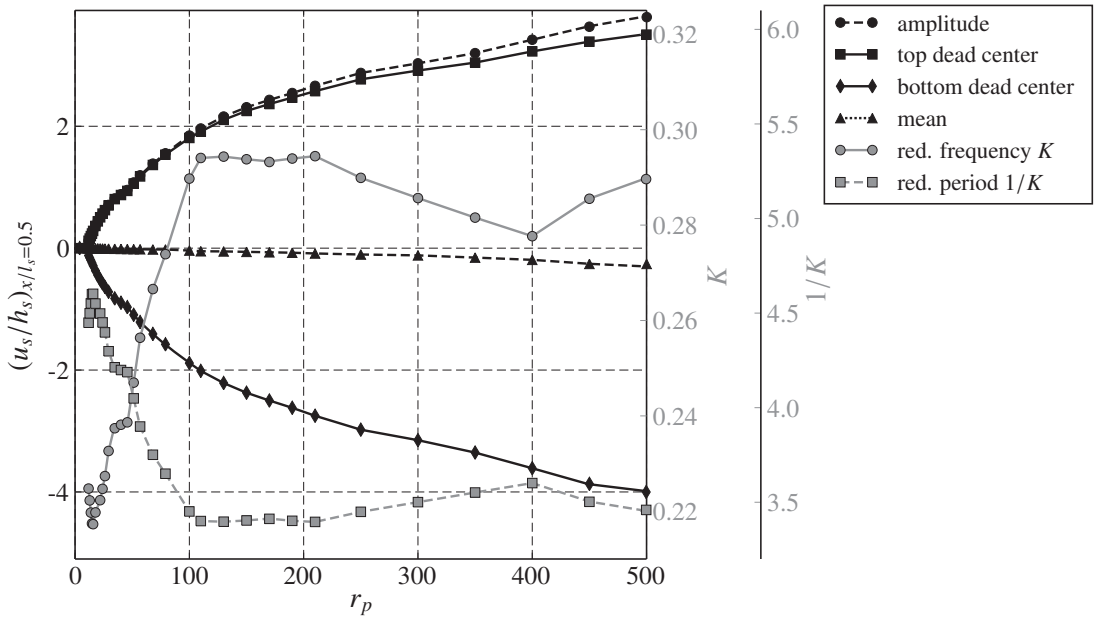

Figure A.3: LCO of the panel at $Ma_\infty = 1.12$, $r_m = 0.05$

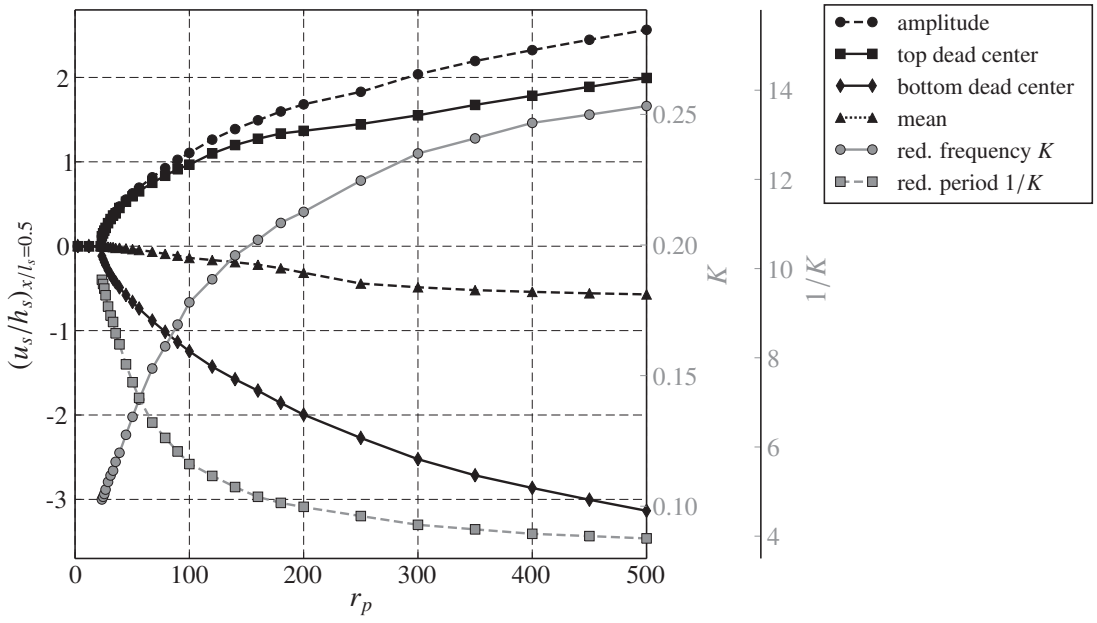

Figure A.4: LCO of the panel at $Ma_\infty = 1.04$, $r_m = 0.1$

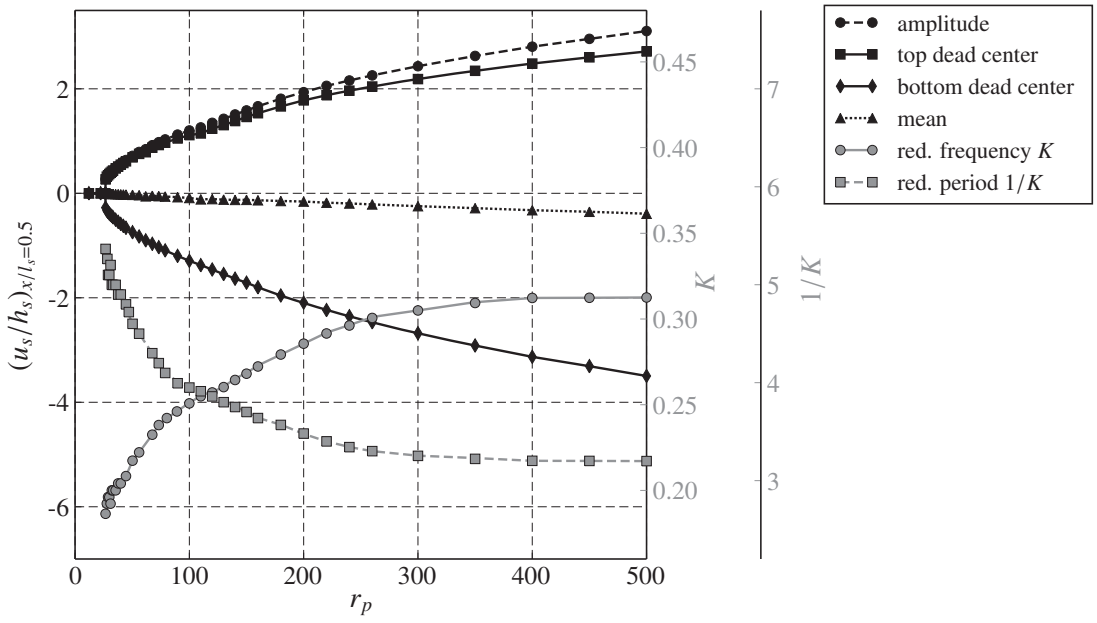

Figure A.5: LCO of the panel at $Ma_\infty = 1.08$, $r_m = 0.1$

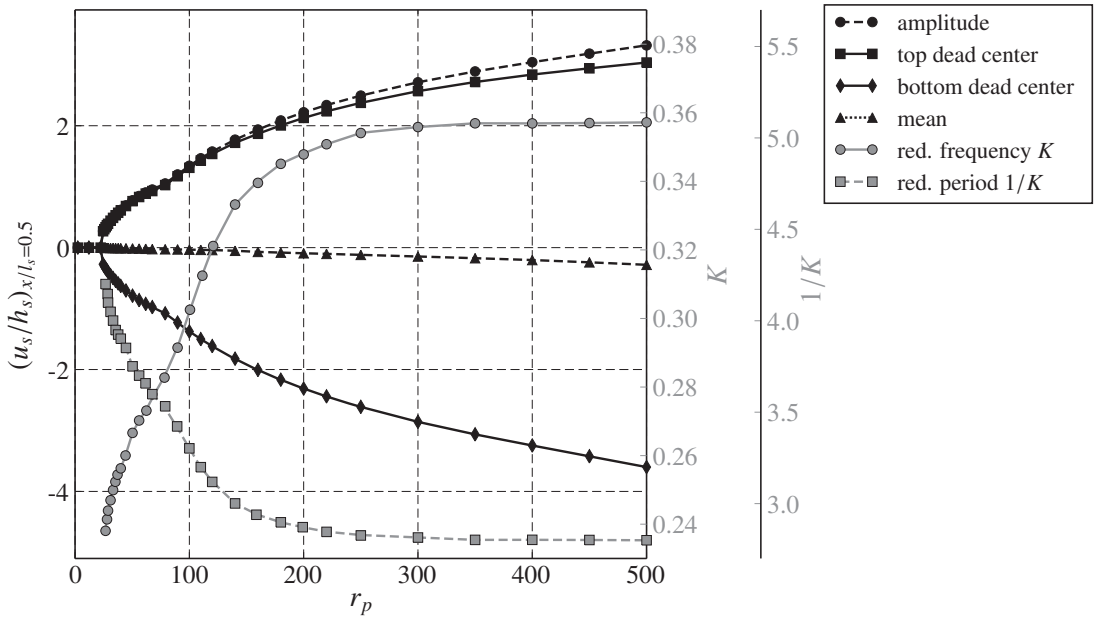

Figure A.6: LCO of the panel at $Ma_\infty = 1.12$, $r_m = 0.1$

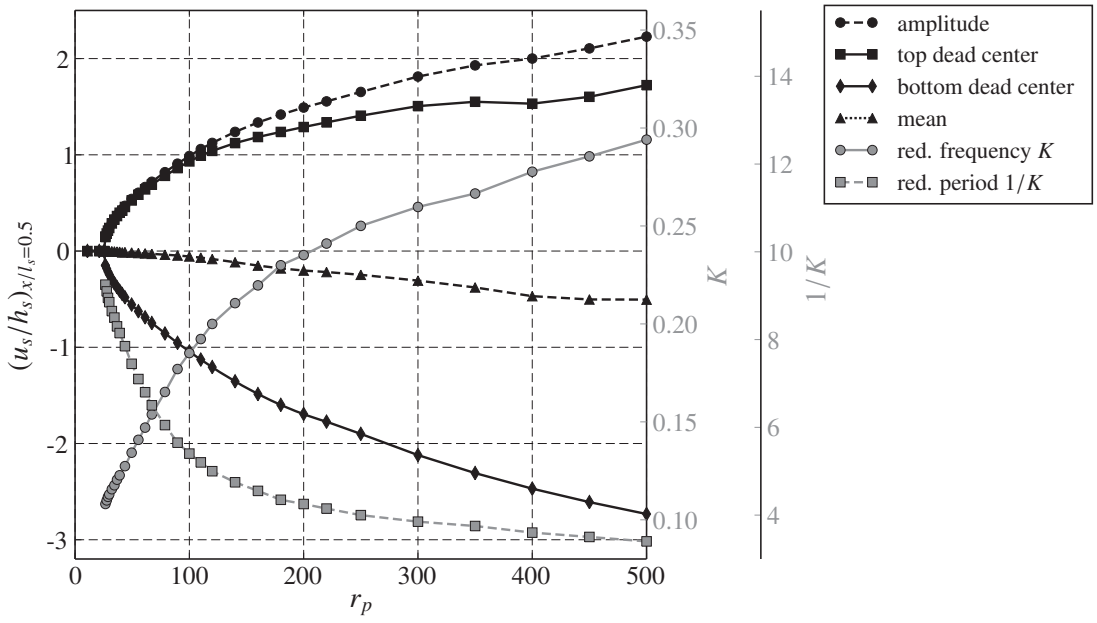

Figure A.7: LCO of the panel at $Ma_\infty = 1.04$, $r_m = 0.20$

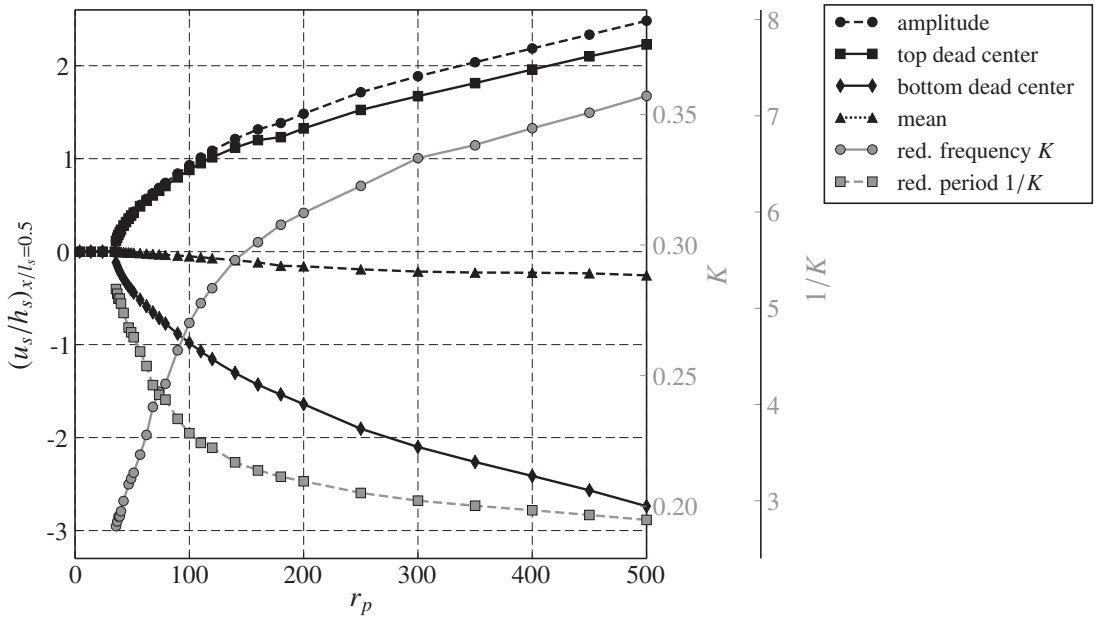

Figure A.8: LCO of the panel at $Ma_\infty = 1.08$, $r_m = 0.20$

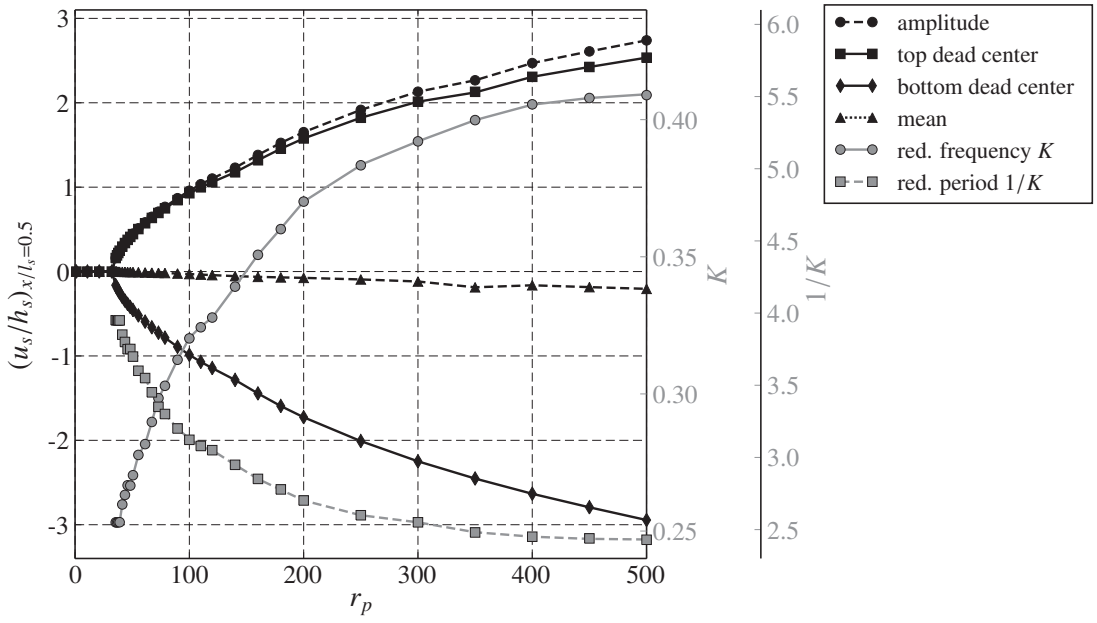

Figure A.9: LCO of the panel at $Ma_\infty = 1.12$, $r_m = 0.20$